Seismic Rock Slope Failure Modes and Time-Dependent Displacements Using Single Block Methods

Matthew D. Gibson

A dissertation
submitted in partial fulfillment of the
requirements for the degree of

Doctor of Philosophy

University of Washington

2015

Reading Committee:

Joseph Wartman, Chair

Steven Kramer

Pedro Arduino

Program Authorized to Offer Degree:
Civil and Environmental Engineering

University of Washington

Abstract

Seismic Rock Slope Failure Modes and Time-Dependent Displacements Using Single Block Methods

Matthew D. Gibson

Chair of the Supervisory Committee:
Associate Professor Joseph Wartman
Civil and Environmental Engineering

Seismically induced rock slope failures have resulted in billions of dollars of economic damage and enormous loss of life throughout the world. Accurate prediction of the triggering and run out of these failures is elusive for a variety of reasons, including knowledge of the physical modes of failure. Simplified tools that are prevalent in soil slope engineering are relatively non-existent in rock slope engineering. Current state of art in rock slope engineering requires complex and computationally expensive numerical models to evaluate the seismic performance or rock slopes, which inhibits extensive evaluations to be conducted.

This research explores the potential failure modes of an idealized rigid rock block and expands the modes typically considered to include not only sliding but also toppling (pure forward rotation), confined toppling (constrained forward toppling) and slumping (combined backward rotation and translation). The yield acceleration (or minimum inertial acceleration to cause block movement) for slumping, similar to toppling, is found to be lower than for pure translational sliding. These yield accelerations indicate the initial modes of rock block failure; however, they do not always predict the ultimate failure mode. To predict the final failure modes, the results of discrete element numerical analyses were compared to pseudo static yield acceleration to develop a seismic failure mode chart based on block geometry and interface friction.

For co-seismic displacement predictions, simplified models predicting ultimate displacement of a mass under seismic conditions are limited to purely translating, sliding blocks (i.e. Newmark's sliding block method). This dissertation introduces additional non-linear, time-dependent models to predict ultimate displacement in toppling and slumping modes as well. Similarities of the dynamic response of rocking, toppling, and slumping systems are exposed and allow knowledge from the well-established literature of rocking blocks to be leveraged. The parameters of these non-linear models are combined such that mapping of more complex systems to these simple models can be performed. Important findings from these new methods are that the magnitude of seismically-induced displacement is dependent on the size and shape of the block (or failure mass) and the displacement dependent yield accelerations. In addition, by establishing a failure criteria for the different modes of failure, ground motion characteristics (mean period and intensity) can be used to predict the likelihood of failure. Design charts are developed to allow seismic toppling and slumping failures to be integrated into PBEE evaluations or real-time regional assessments.

TABLE OF CONTENTS

Page

List of Figures v

List of Tables ix

Acronyms x

Symbols xii

Chapter 1: Introduction 1
- 1.1 Thesis Organization 5

Chapter 2: Seismic Rock Slope Engineering Literature Review 7
- 2.1 Empirical Prediction of Rock Slope Failures During Earthquakes 8
- 2.2 Modes of Failure 10
  - 2.2.1 Mode Determination 12
  - 2.2.2 Example Slopes 15
- 2.3 Seismic Triggering of Rock Slope Failure 16
  - 2.3.1 Empirical Prediction Methods 16
  - 2.3.2 Pseudo-static Limit Equilibrium and Yield Acceleration 18
- 2.4 Displacement Methods 19
  - 2.4.1 Single Block Models 19
  - 2.4.2 Advanced Methods 24

Chapter 3: Pseudo-Static Failure Modes and Yield Accelerations in Rock Slopes . 27
- 3.1 Existing Failure Mode Charts 29
- 3.2 Geometry 32
  - 3.2.1 Fractured Rock Slopes 32
  - 3.2.2 Discrete Rock Blocks 33

3.3 Failure Modes . . . 43
  3.3.1 Static Limit Equilibrium . . . 43
  3.3.2 Pseudo-Static Limit Equilibrium and Failure Modes . . . 46
  3.3.3 Pseudo-Static Failure Mode Transitions . . . 53
3.4 Pseudo-Static Yield Accelerations . . . 55
  3.4.1 Toppling . . . 55
  3.4.2 Sliding . . . 56
  3.4.3 Slumping . . . 57
  3.4.4 Confined Toppling . . . 59
  3.4.5 Interpretation of Yield Equations . . . 60
3.5 Experimental and Numerical Verification . . . 70
  3.5.1 Verification by Centrifuge Experiments . . . 70
  3.5.2 Comparison by DEM (UDEC) Analysis . . . 74
3.6 Application and Examples . . . 78
  3.6.1 Application of Mode and Yield Criterion . . . 78
  3.6.2 Example 1: Isolated Blocks . . . 82
  3.6.3 Example 2: Mount Healy Schist Rock Slope . . . 82
  3.6.4 Example 3: Variable Rock Mass . . . 83
3.7 Discussion and Conclusions . . . 87

Chapter 4: Displacement Response of Toppling Rock Blocks . . . 91
4.1 Seismic Rock Block Toppling Review . . . 92
  4.1.1 Rocking Blocks . . . 93
  4.1.2 Precariously Balanced Rocks . . . 95
  4.1.3 Rock Slope Engineering . . . 96
4.2 Rocking Motion Relative to Toppling Yield Acceleration . . . 98
  4.2.1 Interpretation of Perturbing and Restoring Forces from k_{ri} . . . 103
  4.2.2 Influence of Moment of Inertia, I_i . . . 108
  4.2.3 Visualizing Behavior of Earthquake Ground Motion with k_{ri} . . . 110
4.3 Model for Toppling of Rock Blocks From Slopes . . . 113
  4.3.1 Toppling Block Model Assumptions . . . 114
  4.3.2 Toppling Block Model Equations of Motion . . . 117
  4.3.3 Solution by Numerical Integration . . . 119

4.3.4 Solving for Critical Toppling Yield Acceleration 121
4.3.5 Model Verification 122
4.3.6 Selection of Non-Linear Simulation Over Linear 124
4.3.7 Validation by Centrifuge Modeling 125
4.3.8 Response to Simple Sinusoidal Pulses 127
4.3.9 Response to Earthquake Ground Motion 129
4.4 Effects of Rock Block Geometry on Toppling Model Parameters 129
4.5 Rock Block Toppling Response to Earthquake Ground Motions 133
4.5.1 Earthquake Ground Motion Simulations 133
4.5.2 Simulation Results 136
4.5.3 Reinterpretation of Simulation Data 138
4.6 Example Application - Christchurch 2011 147
4.6.1 Rockfall Survey and Source Geology 147
4.6.2 Analysis 149
4.6.3 Results 151
4.7 Example Toppling Evaluation 154
4.8 Discussion and Conclusion 161

Chapter 5: Displacement Response of Slumping Rock Blocks 164
5.1 Review of Slumping Blocks and Deformation Predictions 166
5.1.1 Slumping 166
5.1.2 General Displacement Methods of Single Block Models 167
5.1.3 Methods for Slumping Failure Prediction 169
5.2 Slumping Behavior of a Rigid Block 170
5.2.1 Equation of Motion 170
5.2.2 Similarity to Other Seismic Displacement Models 177
5.2.3 Behavior of Equation of Motion Parameters 178
5.2.4 Correlation of q^2 and k_s with Geometry and Friction Angle 179
5.2.5 Variability of q^2 and k_s with Block Rotation 183
5.3 Slumping Block Model 183
5.3.1 Solution by Numerical Integration 186
5.3.2 Model Validation 187
5.3.3 Comparison to Sliding Block Analysis 191

5.3.4 Dimensionless Analysis of Slumping Blocks 194
5.4 Slumping Response to Random Earthquake Ground Motions 200
5.4.1 Solving for Critical k_s 200
5.4.2 Solving for Critical k_s at Threshold Behaviors 201
5.4.3 Solving for Critical k_s for Various Block Shapes 203
5.4.4 Earthquake Ground Motion Simulations 205
5.4.5 Simulation Results 208
5.4.6 Reinterpretation of Simulation Data 211
5.5 Multiple Block Systems Represented by Slumping Blocks 219
5.5.1 DEM (*UDEC*) Model as Target Solution 220
5.5.2 Vertically Stacked Rock Blocks 220
5.5.3 Three Horizontally Stacked Rock Blocks 223
5.5.4 Ten Horizontally Stacked Rock Blocks 227
5.6 Discussion and Conclusion 232

Chapter 6: Recommendations for Future Research 236
6.1 Pseudo-Static Failure Modes 236
6.2 Seismically-Induced Toppling Failure 236
6.3 Seismically-Induced Slumping Failure 237
6.4 Seismically-Induced Confined Toppling Failure 238

Bibliography 239

Appendix A: Ground Motions 252

LIST OF FIGURES

Figure Number Page

1.1 Rockfall during 2015 Gorkha earthquake in Nepal 2
1.2 Rockfall during 2011 Canterbury earthquake 3
1.3 Rockfall during 2008 Wenchuan earthquake 4

2.1 Area affected by landslides versus earthquake magnitude 10
2.2 Conceptual blocky failure modes of rock slopes 11
2.3 Rectangular block static stability boundaries and dynamic motion charts. . . 13
2.4 Effective failure modes of a rock mass 14
2.5 Pseudo-static rectangular block failure modes 15
2.6 Complex rock slope pictured after 2007 Pisco, Peru Earthquake 17
2.7 Empirical landslide risk decision tree 18
2.8 Sliding block schematic 20
2.9 Sample calculation of sliding block method 21
2.10 Rectangular rocking block 22
2.11 Example rocking block spectrum 23

3.1 Rectangular block static stability boundaries and dynamic motion charts. . . 30
3.2 Effective failure modes of a rock mass 31
3.3 Pseudo-static rectangular block failure modes 32
3.4 Complex rock slope pictured after 2007 Pisco, Peru Earthquake. 34
3.5 Discrete rock block geometry parameterized by joint spacing and relative fracture angle. 36
3.6 Parallelogram-shaped blocks based on $\frac{S_2}{S_1}$ and γ. 38
3.7 Discrete rock block geometry parameterized by forward and backward block angles, α_1 and α_3. 39
3.8 Parallelogram block shapes based on α_1 and α_3. 41
3.9 Relationship between parallelogram parameter sets. 44
3.10 Static, limit equilibrium, free body diagrams. 45

3.11 Pseudo-static toppling failure mode and failure path. 49
3.12 Pseudo-static confined toppling failure mode and failure path. 50
3.13 Pseudo-static sliding failure mode and failure path. 51
3.14 Pseudo-static slumping failure mode and failure path. 52
3.15 Pseudo-static limit equilibrium failure modes. 54
3.16 Yield accelerations for $\phi = 30°$. 61
3.17 Yield accelerations for $\phi = 40°$. 62
3.18 Yield accelerations for $\phi = 50°$. 63
3.19 Yield accelerations for $\phi = 60°$. 64
3.20 Slumping yield acceleration (k_s) as function of back rotation for single and multiple slumping blocks. 69
3.21 Confined toppling yield acceleration (k_{ct}) as function of forward rotation . . 70
3.22 Block shapes in centrifuge experiments 72
3.23 Typical *UDEC* model geometry for parametric study. 75
3.24 Comparison of predicted failure modes to *UDEC* verification results. 79
3.25 Comparison of predicted yield accelerations to *UDEC* verification results. . . 80
3.26 Example 1: Pseudo-static mode determination for isolated blocks. 83
3.27 Example 2: Pseudo-static mode determination for fractured rock slope. . . . 84
3.28 Example 3: Variable rock mass. 86

4.1 Existing failure mode charts for rock blocks 97
4.2 Asymmetric mass in contact with an inclined plane at two points, O_1 and O_2. 99
4.3 Free body diagram of a mass on an accelerating inclined plane rocking about point O_2. 99
4.4 Force vector diagram illustrating the horizontal pseudo-static rocking acceleration coefficients for the block in Figure 4.3 where $\theta = 0$. 100
4.5 Force vector diagram illustrating the horizontal rocking acceleration coefficient for the block in Figure 4.3 rocking about point O_2. 101
4.6 Comparison between k_h and k_{ri} for a symmetric block on a level plane. . . . 105
4.7 Demonstrating the effects of vertical ground motion for a symmetric rocking block on a level plane. 107
4.8 Interpreting the effects of a symmetric block rocking on a sloping plane ($\beta = 3°$).108
4.9 Influence of block scale on rocking response, I_i vs k_{ri}. 109
4.10 Earthquake example: Large rectangular block 110

4.11 Earthquake example: Small rectangular block 112
4.12 Seated rock block that can only rotate forward. 114
4.13 Solution scheme to determine critical k_r/PGA 122
4.14 Verification of rectangular wave (linear solution). 124
4.15 Comparison of k_r/PGA for the linear and non-linear solution. 125
4.16 Model verification based on centrifuge experiment of rock block toppling . . 126
4.17 Toppling model response to sinusoidal-like ground motion input 128
4.18 Forward toppling response to earthquake ground motion. 130
4.19 Relationship between p^2 and r_3 for parallelograms of various shapes 132
4.20 Simulation results using dimensionless parameters. 137
4.21 Earthquake simulation results for PGA and T_m. 140
4.22 Earthquake simulation results for PGV. 141
4.23 Earthquake simulation results for PGD and T_m. 142
4.24 Comparison of simple simulations to Earthquake simulations. 144
4.25 Earthquake simulation results for each ground motion set. 145
4.26 Earthquake simulation results with and without vertical motions. 146
4.27 Relationship between $\frac{k_r g}{p}$ and the volume of a cuboid block. 150
4.28 Estimated rock block geometry range in Port Hills during the Canterbury earthquakes. 152
4.29 Estimated rockfall depositional size gradation from Canterbury earthquakes. 155
4.30 Estimated frequency of rockfall depositional size from Canterbury earthquakes.156
4.31 Seismic toppling evaluation of Threatening Rock. 158
4.32 Seismic toppling evaluation of block similar to Threatening Rock. 160

5.1 Conceptual, non-fracturing, blocky failure modes 166
5.2 Sample calculation of sliding block method 168
5.3 Slumping block schematic 171
5.4 Free body diagrams for a slumping block 173
5.5 Rigid body accelerations used to relate $\ddot{x}_{cm}$, $\ddot{y}_{cm}$ and $\ddot{\theta}$. 175
5.6 Variability of slumping equation components 179
5.7 Variability of q^2 and k_s, for α_1, α_3 parameter set. 181
5.8 Variability of q^2 and k_s, for $\frac{S_2}{S_1}$, γ parameter set. 182
5.9 Percent change of q^2 and k_s, for α_1, α_3 parameter set. 184
5.10 Percent change of q^2 and k_s, for $\frac{S_2}{S_1}$, γ parameter set. 185

5.11 Geometry used in validation 188
5.12 Validation of slumping block model (SBM) with DEM. 189
5.13 Comparison between slumping and sliding block models. 192
5.14 Comparison between slumping and sliding block models. 193
5.15 Dimensionless evaluation of the effects of block scale. 196
5.16 Dimensionless evaluation of the effects of slope and friction angle. 197
5.17 Dimensionless evaluation of the effects of aspect ratio. 198
5.18 Dimensionless evaluation of the effects of relative fracture angle, γ. 199
5.19 Solution scheme to determine critical k_s/PGA 202
5.20 Slumping block failure criteria. 204
5.21 Influence of geometric parameters and joint friction angle on initial motion parameters. 205
5.22 Simulation results for slumping block failure based on full rotation using dimensionless parameters. 209
5.23 Simulation results for slumping block failure based on heel displacement using dimensionless parameters. 210
5.24 Earthquake simulation results (full rotation failure) for PGA and T_m. 212
5.25 Earthquake simulation results (full rotation failure) for PGV. 213
5.26 Earthquake simulation results (full rotation failure) for PGD and T_m. 214
5.27 Earthquake simulation results (heel displacement failure) for PGA and T_m. . 215
5.28 Earthquake simulation results (heel displacement failure) for PGV. 216
5.29 Earthquake simulation results (heel displacement failure) for PGD and T_m. . 217
5.30 Earthquake simulation results for each ground motion set. 218
5.31 Geometry of three vertically stacked blocks 221
5.32 Example 1: Comparison of *UDEC* to simplified model for three vertically stacked blocks. 224
5.33 Geometry of three horizontally stacked blocks. 225
5.34 Example 2: Comparison of *UDEC* to simplified model for three horizontally stacked blocks 228
5.35 Geometry of ten horizontally stacked blocks. 229
5.36 Example 3: Comparison of *UDEC* to simplified model for ten horizontally stacked blocks. 231

A.1 Histograms of ground motion metadata 254

LIST OF TABLES

Table Number Page

2.1 Types of coseismic landslides 9

3.1 Summary of centrifuge results for single discrete blocks. 73
3.2 Range of parameters used in *UDEC* verification. 74
3.3 Fixed parameters used in *UDEC* verification 76
3.4 Example: Fracture set parameters for variable rock mass. 85

4.1 Possible earthquake simulation combinations. 135
4.2 Toppling simulation summary statistics 136
4.3 Port Hills rockfall abundance surveyed from the Canterbury earthquakes. . . 148
4.4 Assumed distributions of source block volumes and ground motion PGV's . . 153

5.1 Similarity of slumping block equation to other seismic displacement models with a rotation component. 177
5.2 *UDEC* parameters for slumping block validation 188
5.3 Block parameters used in dimensionless evaluations 195
5.4 Possible earthquake simulation combinations. 207
5.5 Slumping simulation summary statistics 208
5.6 *UDEC* parameters for vertically and horizontally stacked block simulations . 220
5.7 Input parameters for the vertically stacked block simulation 221
5.8 Input parameters for the three horizontally stacked block simulation 225
5.9 Input parameters for the ten horizontally stacked block simulation 227

A.1 PEER ground motion metadata 255
A.2 Baker: Broadband ground motion metadata 270
A.3 Baker: Pulse-like ground motion metadata 274
A.4 Spectrally Matched ground motion metadata 278

LIST OF ACRONYMS

Notation	Description
2D	Two Dimensional
3D	Three Dimensional
AP	Associated Press
CAV	Cumulative Absolute Velocity
DDA	Discontinuous Deformation Analysis
DEM	Discrete Element Method
FDM	Finite Difference Method
FEM	Finite Element Method
FS	Factor of Safety
GMP	Ground Motion Parameter
$\mathrm{I_a}$	Arias Intensity
LEM	Limit Equilibrium Method
PBEE	Performance-Based Earthquake Engineering

Notation	**Description**
PBR	Precariously Balanced Rocks
PEER	Pacific Earthquake Engineering Research Center
PFC	Particle Flow Code distributed by Itasca Consulting, Inc.
PGA	Peak Ground Acceleration
PGD	Peak Ground Displacement
PGV	Peak Ground Velocity
PSHA	Probabilistic Seismic Hazard Analysis
SBM	Slumping Block Model
TBM	Toppling Block Model
UDEC	Universal Distinct Element Code distributed by Itasca Consulting, Inc.
WLS	Weighted Least Squares

LIST OF SYMBOLS

Notation	**Description**
$\ddot{\mathbf{u}}_{cm}$	Acceleration vector of a rigid body at its center of mass.
α_1	The backward block angle created by the $\mathbf{r}_1$ vector and a line perpendicular to the base plane.
α_3	The forward block angle created by the $\mathbf{r}_3$ vector and a line perpendicular to the base plane.
$\mathbf{h}$	The vector parallel to the back plane from the heel of the block to the top of the block.
$\mathbf{b}$	The vector parallel to the base plane from the heel of the block to the toe of the block.
β	The primary sub-horizontal angle formed by the base fracture.
C	Center of mass.
F_I	The inertia force acting at the center of mass induced by an earthquake ground motion.

Notation	Description
$\mathbf{R}_I$	The resultant force acting at the center of mass that includes the inertia force induced by an earthquake ground motion.
$\mathbf{N}$	A normal reaction vector acting on a block.
R_{mom}	The restoring moment acting on a toppling block.
τ	The shear force acting on the base of a block.
F_s	Geometric shape factor applied to g/r.
$\mathbf{W}$	The weight vector of a block.
ϕ	The friction angle of a rock joint.
γ	The angle between the base and back fracture.
g	Gravitational acceleration.
$\hat{\mathbf{g}}$	Unit vector in the direction of gravity.
$\hat{\mathbf{g}}_\perp$	Unit vector perpendicular to the direction of gravity.
I_{cm}	Mass moment of inertia about the center of mass.
I_i	Mass moment of inertia about a block corner.
k_h	The horizontal seismic coefficient of a ground motion as a fraction of gravity.

Notation	**Description**
k_{inc}	The incremental horizontal inertial acceleration that induces motion on a block, $k_{inc} = (-\ddot{u}_{hg}/g - k_s)mg\hat{\mathbf{g}}_{\perp}$.
k_r	The critical horizontal acceleration to induce rocking motion.
k_{rs}	The initial critical horizontal acceleration to induce rocking motion.
k_{ct}	The critical horizontal acceleration to induce confined toppling motion.
k_s	The critical horizontal acceleration to induce slumping motion.
k_v	The vertical seismic coefficient of a ground motion as a fraction of gravity.
k_y	The critical horizontal acceleration to induce sliding.
m	Block mass.
$\mathrm{M_w}$	Moment magnitude.
O_1	The block corner at the heel of the block in contact with the base plane.
O_2	The block corner at the top of the block in contact with the back plane.
O_3	The block corner at the toe of the block in contact with the base plane.

Notation	Description
ω	Angular frequency.
p^2	The frequency parameter for the rocking block.
ψ_i	Forward or backward block angle relative to vertical.
q^2	Slumping block dynamic characteristic factor.
$\mathbf{r}_1$	The vector from a single block's center of mass to the uphill contact point on the base plane.
$\mathbf{r}_2$	The vector from a single block's center of mass to the uppermost contact point on the back plane.
$\mathbf{r}_3$	The vector from a single block's center of mass to the downhill contact point on the base plane.
$\mathbf{R}_1$	The reaction vector at the base of the block acting at contact 1.
$\mathbf{R}_2$	The reaction vector at the base of the block acting at contact 2.
$\mathbf{R}_3$	The reaction vector at the base of the block acting at contact 3.
ρ	Mass density.

Notation	**Description**
S_1	The perpendicular distance between the base fractures.
S_2	The perpendicular distance between the back fractures.
θ	The angular displacement.
$\dot{\theta}$	The angular velocity.
$\ddot{\theta}$	The angular acceleration.
θ_c	The critical angular displacement.
θ_n	The normalized angular displacement.
T_m	Mean period as defined by Rathje et al. (1998).
$\ddot{u}_{vg}$	The vertical ground acceleration.
$\ddot{u}_{hg}$	The horizontal ground acceleration.
$\ddot{x}$	The horizontal acceleration of a rock block.
$\hat{\mathbf{x}}$	The horizontal unit vector.
$\ddot{y}$	The vertical acceleration of a rock block.
$\hat{\mathbf{y}}$	The vertical unit vector.
$\hat{\mathbf{z}}$	The horizontal unit vector (in-out of page).

ACKNOWLEDGMENTS

The most important factor in the success of this dissertation is the support of my wife, Claire Gibson. Claire, as an accomplished geotechnical engineer, provided invaluable feedback from countless conversations about toppling and slumping blocks. In addition, she edited this dissertation and cared for our two children, Josephine and Ira, while I worked full-time at Shannon & Wilson and worked on this dissertation during many weekends, evenings, and mornings.

I am very fortunate to have been invited by Joe Wartman (PI) to participate on the NEES Rock Research Project (NSF Grant No CMMI-1156413). Joe challenged me to explain complicated numerical models with simple models which ultimately lead to the topic of this dissertation. This experience has given me a greater appreciation for ability of simple, fundamental engineering concepts to explain complicated processes. I am grateful for the guidance and thesis review provided by Mary MacLaughlin and Dave Keefer (Co-PI's). I am especially thankful to Mary for sponsoring me to visit Montana Tech to work with her research group and their outstanding hospitality during my stay. I owe a debt of gratitude to Kermit Applegate, Lorne Arnold, Jake Dafni, and Sam Sideras for enduring long conversations with me.

I am thankful for Pedro Arduino's suggestion to talk to Peter McKenzie about Python in 2011. Those conversations led me becoming a Python evangelist and resulted in my 4-year-old daughter to coin the phrase "Are you talking about the Python in the pantry, again?".

I am thankful for my colleagues at Shannon & Wilson for their support and wisdom and for the company's support for my three year leave of absence.

Chapter 1

INTRODUCTION

The theory of plate tectonics fundamentally changed our understanding of how the physical environment is formed and reformed. Ironically, this process which produces phenomenal mountain landscapes, also produces powerful ground shaking that leads to their demise. While the prediction of the strength and timing of earthquakes is a challenging task, the consequences of their inevitable arrival are well-known and reiterated on an all to frequent schedule. The consequences of these natural disasters range from the liquefaction of sediments in seemingly benign environments to dramatic landsliding of rock and soil slopes alike. Landslide related natural disasters have caused billions of dollars of economic damage and have been responsible for enormous loss of life throughout the world (Keefer and Larsen, 2007).

Seismically induced rock slope failures have the potential to result in sudden, catastrophic consequences. Although a rock slope failure can be a relatively quick event, the consequences of rock slope failures can be long lasting as they permanently alter the natural environment, such as blocking streams and filling valleys (Hewitt et al., 2008) and destroying the built environment. The following earthquake induced disasters illustrate the impact of rock slope failures during earthquakes:

- **2015 Gorkha earthquake (Nepal) (Chiaro et al., 2015; Moss et al., 2015):** The Gorkha district of Nepal was struck by a series of $M_w=7.8$, $M_w=6.7$, and $M_w=6.8$ earthquakes. These earthquakes resulted in 8,674 fatalities and many more injured. Extensive landsliding and rockfall was observed in the mountainous regions impacting homes and blocking roads, hampering rescue efforts. Figure 1.1 shows an example of rockfall on a local road.

Figure 1.1: Rockfall during 2015 Gorkha earthquake in Nepal

.

- **2010 & 2011 Canterbury earthquake sequence (New Zealand) (Massey et al., 2012, 2014):** This series of earthquakes resulted in more than 5,000 mapped rockfalls among 800+ dwellings in Christchurch, New Zealand. In some cases, homes were struck and/or penetrated by boulders greater than a meter in dimension. Some failures resulted in dislodged building-sized boulders colliding with buildings (Figure 1.2a) or landslides comprised of hundreds of car-sized boulders (Figure 1.2b).

- **2008 Wenchuan earthquake (China) (Tang et al., 2011; Xu et al., 2009):** There were estimated to be over 56,000 landslides resulting in over 250 landslide dams (Figure 1.3a). Damage was caused to a wide variety of civil infrastructure including bridges, buildings, dams, irrigation channels, and entire towns. Over 20,000 deaths were directly attributed to landslides. Large boulders were dislodged from surrounding slopes and displaced to the valley floors (Figure 1.3b).

(a) Photo: Hannah Johnston/Getty Images

(b) Photo: Martin Hunter/Getty Images

Figure 1.2: Rockfall during 2011 Canterbury earthquake

.

(a) Lake formed by rock landslide dam (Photo: AP)

(b) Large rock ejecta (Photo: AP)

Figure 1.3: Rockfall during 2008 Wenchuan earthquake

.

- **1970 Ancash earthquake (Peru) (Plafker et al., 1971; Keefer and Larsen, 2007):** A massive rock slope failure inundated the villages of Yungay and Ranrahirca with the number of fatalities exceeding 25,000. Evidence, common to many natural disasters, indicates that this was not the first and will likely not be the last earthquake induced landslide to hit this area.

Prediction of system behavior to earthquake loading is a complex problem in civil engineering. There is no exception for rock slopes given their inherent natural variability in composition and geometric arrangement. Seismic stability evaluations in geotechnical engineering are common place, however those for rock slopes lag behind relative to other areas of geotechnical and civil engineering (e.g. soil slope stability, liquefaction, and structural response). Seismic rock slopes methods are in great need for advancement to meet the current risk-based seismic engineering environment.

1.1 Thesis Organization

The concepts and methods of analysis presented in this thesis form the beginning of the trek to decipher the seismic response of fractured rock slopes. The following chapter provides a general primer on the landscape of the current state of practice and art of rock slope behavior during earthquakes. Those familiar with rock slope engineering, can likely skip this chapter and move directly to subsequent chapter topics where the current state of research will be reiterated.

Chapters 3, 4, and 5, which constitute the original work of this thesis, were written with the intent for direct submission to peer-reviewed journals and thus are self contained. However, it is beneficial to the reader to move through each chapter in succession as the research concepts build upon each other.

Based on the complex geometric composition of rock slopes, this dissertation focuses on developing a fundamental understanding of the physics dominating rock slope failures. Chapter 3 sets out to expand the identification of pseudo static failure modes and yield accelerations of more diverse discrete rock block shapes compared to current methods that are built on rectangular shapes. Chapter 4 builds on the abundant rocking block literature and modifies it to address seismic rock block toppling failures. Methods are developed to evaluate the time-dependent response of toppling rock blocks. These methods are used to evaluate a large database of ground motions and develop probabilistic failure criteria based on ground motion intensity parameters. Chapter 5 develops and explores a slumping block model and discovers mathematical similarities to the toppling block. As with the toppling rock block, methods are developed for time-dependent ground motion simulations and probabilistic failure criteria are established. Lastly, thoughts of future research opportunities stemming from this dissertation are presented in Chapter 6.

Chapter 2

SEISMIC ROCK SLOPE ENGINEERING LITERATURE REVIEW

There are many factors that may induce rock slope failures, such as ground water flow, precipitation, deteriorating rock fractures, undercutting of slopes, human activity, and earthquakes. The mechanisms of how most of these factors lead to rock slope failures are relatively well understood. However, the methods for predicting these failures, especially for earthquaking loading, are sparse. Compared to seismic soil slope engineering, seismic rock slope engineering lags behind in the ability to identify basic failure mechanisms by simplified methods and provide quantitative, risk-based evaluations.

Seismic slope engineering analyses generally include the following steps to predict performance during earthquakes: determining controlling failure modes, predicting the triggering of motion, estimating displacement during motion, final deformation, and evaluating displacement to natural or artificial failure criteria. For rock slope failures, geometry, persistence, and strength of rock mass discontinuities will play a dominant role (Eberhardt, 2008). These discontinuity characteristics control failure modes such as sliding, toppling, slumping, or variants of these modes (Hoek and Bray (1977), Goodman and Kieffer (2000), and Sitar et al. (2005) among others). Once the likely co-seismic failure modes are identified, the next step is to predict the triggering of slope displacement by specific earthquake scenarios. The earthquake scenarios to be evaluated are usually prescribed by ground motion amplitude and frequency or time histories of ground accelerations. If triggering of slope movement is established to occur during an earthquake, engineers must be able to estimate the potential displacements or magnitude of failure. With displacement predictions, communities and government agencies are able to make risk-based decisions of how to mitigate the consequences of failure either by engineering stabilization solutions or preparing for disaster responses. This final analytical step is arguably the most important, yielding quantitative predictions of failure likelihood that can be ingested in a performance-based earthquake engineering (PBEE) process.

This chapter provides a general overview of seismically induced rock slope failure evidence and the current state of evaluating the failure modes, triggering predictions, and estimates of displacements and consequences of failure. Additional details will be provided in each of the following chapters where necessary. The subject of static slope stability has drawn the attention of many authors (e.g. Hoek and Bray, 1977; Hoek et al., 2000, among others), and in general, will not be repeated here unless the discussion benefits. This is not to say that this text can be read without an understanding of these methods. The reader not familiar in basic rock slope stability methods should refer to the above-mentioned text.

2.1 Empirical Prediction of Rock Slope Failures During Earthquakes

Earthquake induced rock slope failures and resulting landslides are not a new phenomenon. Accounts of these spectacular events have been documented and evaluated throughout the literature (Cluff (1971); Plafker et al. (1971); Wilson and Keefer (1983); Jibson et al. (2006); Keefer et al. (2006); Aydan et al. (2009); Alfaro et al. (2012), among others). The factors that determine the difference between which slopes fail or remain stable are numerous. The first major effort to catalog earthquake induced landslides and their attributes was undertaken by Keefer (1984) who evaluated 40 major earthquake case histories world-wide. From this work, 14 types of rock and soil landslides caused by earthquakes were identified and are summarized in Table 2.1. Landslide types related to rock that were identified include slides, topples, and slumps. Several rock slope characteristics were identified to contribute to their failures with a major factor being the geometry and frictional characteristics of discontinuities and fractures. One relationship uncovered by Keefer is that the area affected by landslides can be related to the earthquake magnitude. This relationship provides an indication of a limiting earthquake intensity to induce slope failures. Keefer's work was followed by Rodríguez et al. (1999)

Table 2.1: Types of coseismic landslides (Keefer, 1984)

Relative abundance of landslides	Landslide type
Very abundant 100,000	Rock falls Disrupted soil slides Rock slides
Abundant 10,000 to 100,000	Soil lateral spreads Soil slumps Soil block slides Soil avalanches
Moderately Common 1,000 to 10,000	Soil falls Rapid soil flows Rock slumps
Uncommon 100 to 1,000	Subaqueous landslides Slow earth flows Rock block slides Rock avalanches

who extended the database to a total of 76 earthquake case histories and whose results reinforced the conclusions of Keefer's work. Keefer (2013) provides the latest summary of these cataloged studies as shown in Figure 2.1

Additional researchers have shown Keefer's relationship to be applicable over a wide range of seismic and geologic settings. For instance, Aydan et al. (2009) provides a well documented case history that summarizes observed sliding, toppling, and slumping failures

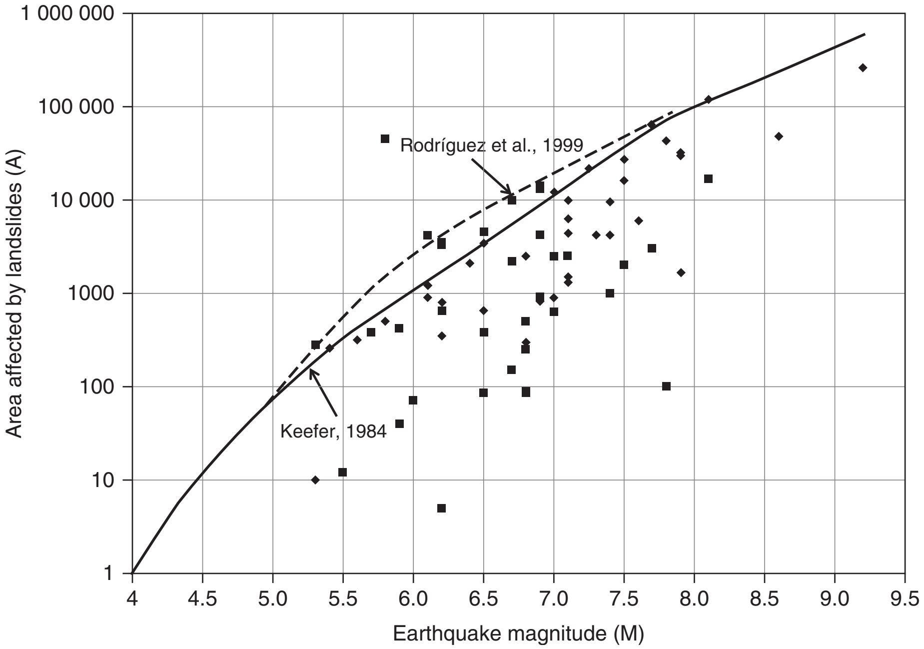

Figure 2.1: Area in square kilometers affected by landslides versus earthquake magnitude (Keefer, 2013)

.

and makes a direct comparison to the findings of Keefer (1984). From these studies it is clear that there is an intimate relationship between earthquakes and slope characteristics.

2.2 Modes of Failure

In order to simplify the infinite number of rock block shapes and potential failure modes, simplified conceptual models are often adopted. An extensive list of conceptual rock slope failure modes are discussed in Goodman and Kieffer (2000). A few of these conceptual examples that demonstrate blocky, non-fracturing failure modes are shown in Figure 2.2. These figures show rock slope failures that consist of one block or a complex network of many blocks. The failures are grouped here into the general categories of dominant failure modes identified by Keefer (1984); sliding, toppling, and slumping. It is interesting to note

(a) sliding (b) sliding

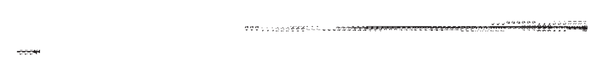

(c) topple (d) topple

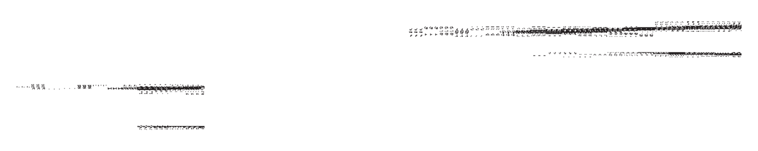

(e) slump (f) slump

Figure 2.2: Conceptual, non-fracturing, blocky failure modes of rock slopes (Goodman and Kieffer, 2000)

that these three categories represent the total possible combinations of translational and rotational rigid body motion with slumping, and as will be shown in Chapter 3, some forms of toppling being the modes that undergo both types of motion. In addition, the failures composed of many blocks appear to be more complex variants of the single block failure modes.

2.2.1 Mode Determination

Kinematic failure modes, such as toppling, sliding, and wedge failure, are generally identified using methods based on stereographic projections (Goodman, 1989). These methods are well established and are integrated into numerous commercially available software programs. However, these methods make a fundamental assumption of a vertical gravity field. It will be shown in the Chapter 3 that this assumption is only appropriate for static loading.

The most prominent design charts currently available for single block failure modes are limited to blocks formed by orthogonal joint sets. A succinct literature review of these charts is discussed by Yagoda-Biran and Hatzor (2013) and is summarized here. Ashby (1971) and Hoek and Bray (1977) presented the first chart (Figure 2.3a) that established the static limit equilibrium failure modes. They also identified dynamic failure modes when the block is in motion relative to the fracture planes. The chart was revised by Bray and Goodman (1981) (Figure 2.3b) based on DEM modeling by Voegele (1979) that indicated that the *sliding* and *sliding & toppling* boundary should be modified. The dynamic failure modes were again modified by Sagaseta (1986) (Figure 2.3c) to reflect the appropriate application of inertial forces.

Modes of failure for discontinuous rock slopes were investigated by Aydan et al. (1989). In this study, rock slopes with various configurations of discontinuities (i.e. through-going or step-wise continuous) were evaluated for sliding, toppling and combined sliding-toppling modes of failure. Tilt tables and base friction machines were used to verify their analysis. The geometries and discretization of modes are shown in Figure 2.4. These studies showed that multiple blocks could combine to form the basic modes identified by the simplified charts.

While these studies discuss dynamic motion, they should not be confused with initiation of motion under seismic forces. These charts instead delineate boundaries between statically stable and unstable, rectangular blocks under gravitational loading. The dynamic motion represents the scenario where a block begins motion in statically unstable conditions. This

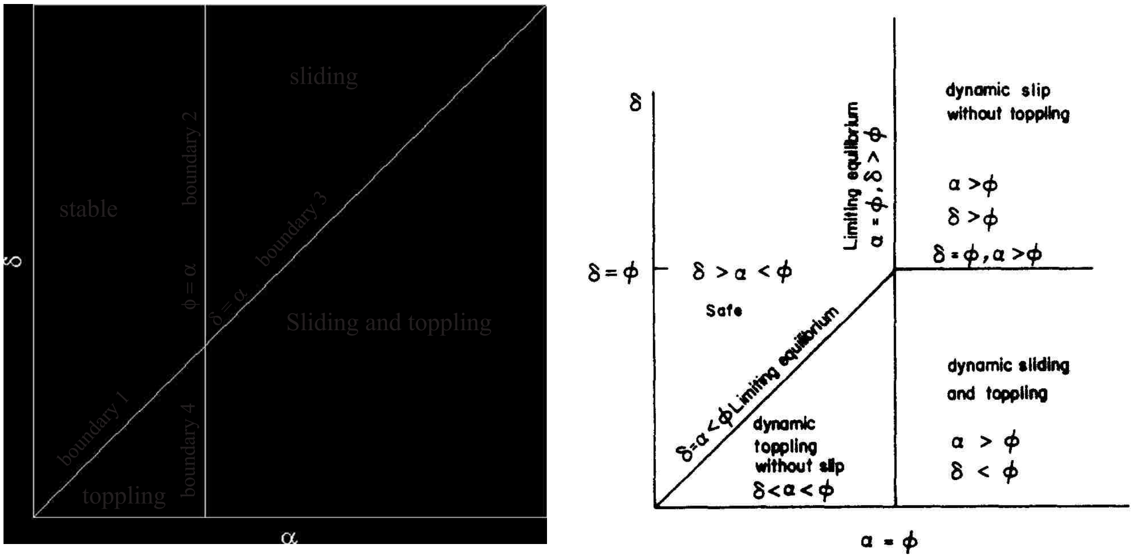

(a) Ashby (1971); Hoek and Bray (1977)

(b) Bray and Goodman (1981)

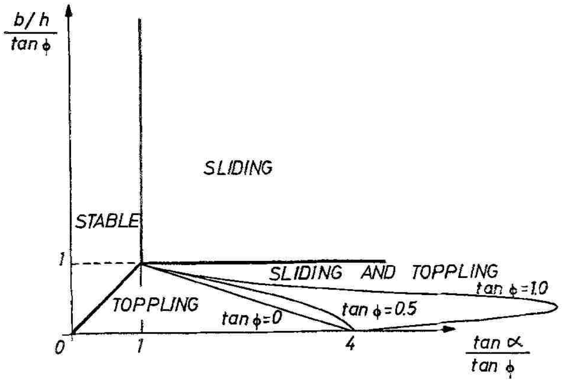

(c) Sagaseta (1986)

Figure 2.3: Rectangular block static stability boundaries and dynamic motion charts. Note that dynamic motion does not equate to seismic failure modes.

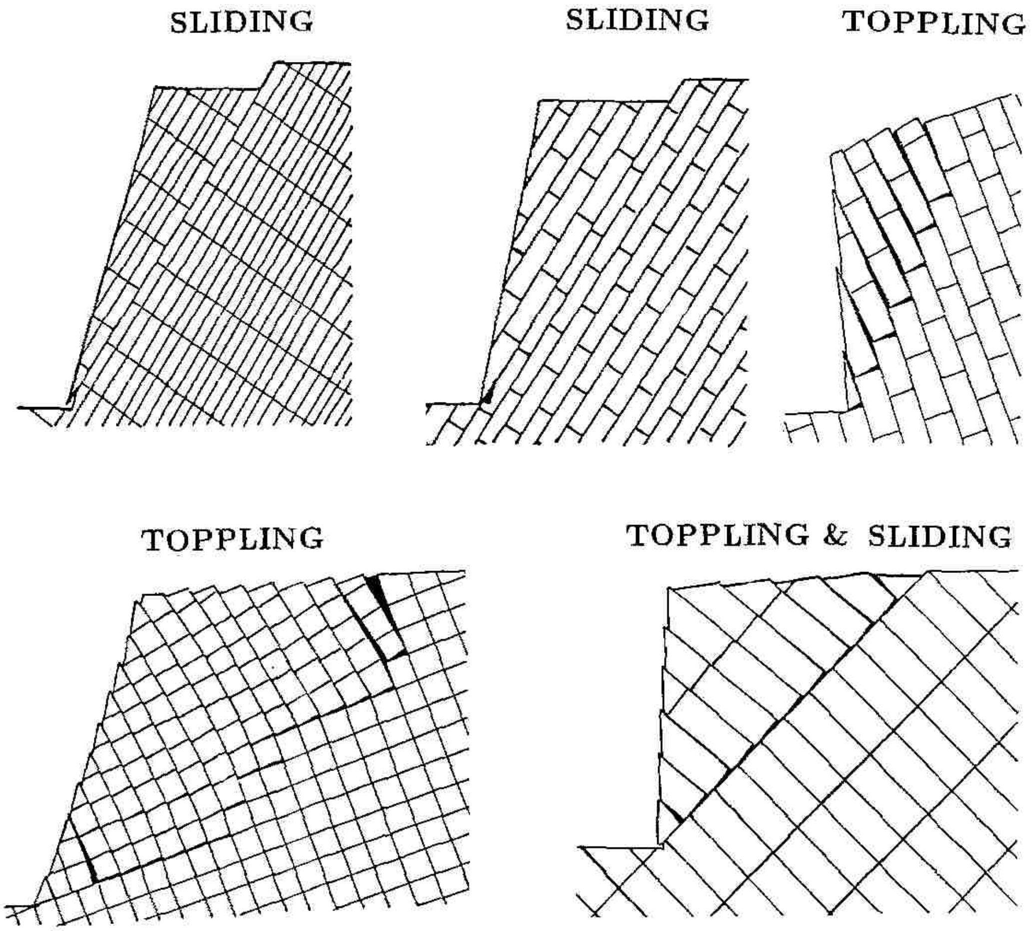

(a) Geometries

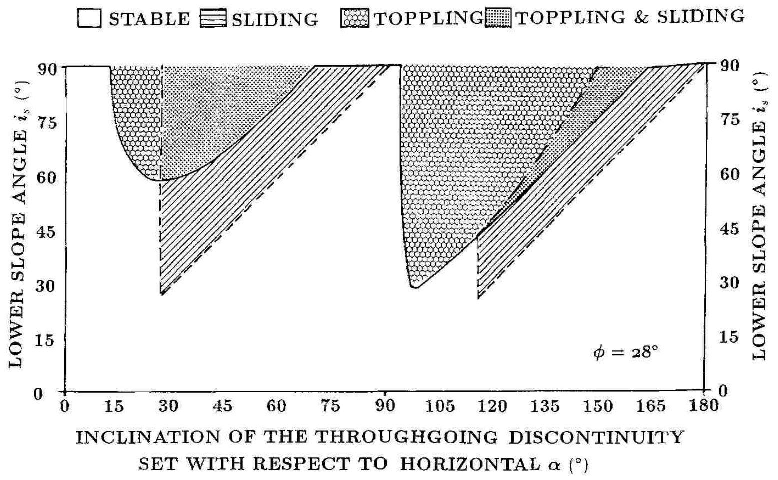

(b) Failure mode chart

Figure 2.4: Effective failure modes of a rock mass (Aydan et al., 1989).

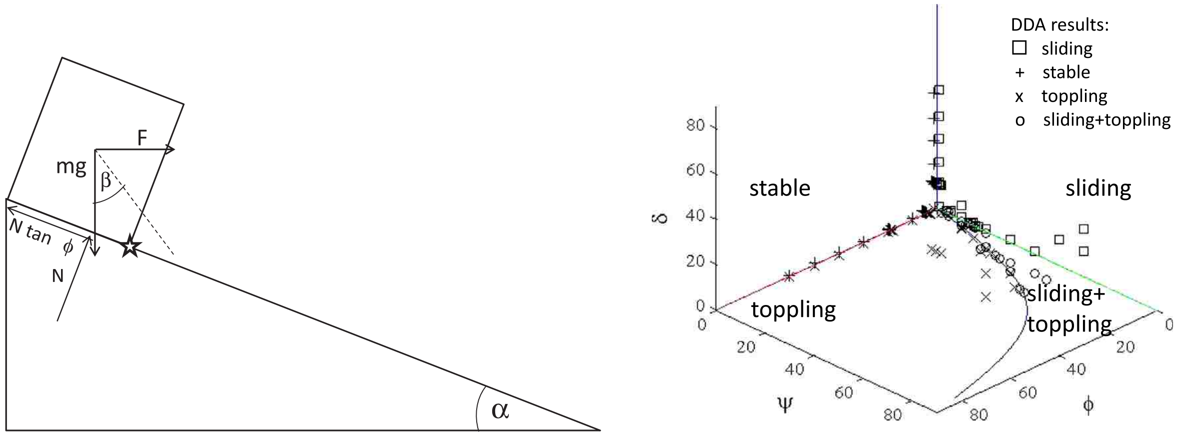

(a) Geometry (b) Geometry

Figure 2.5: Pseudo-static rectangular block failure modes (Yagoda-Biran and Hatzor, 2013).

situation is more representative of blocks whose fractures undergo strength loss rather than experience an inertial loading induced by an earthquake.

Given the earthquake loading limitation, Yagoda-Biran and Hatzor (2013) showed that the seismic inertial force could be thought of as adding additional slope angle to the static charts thus expanding the charts applicability to include earthquake loading. The slope angle, α is effectively increased by the angle, β, formed by the resultant force acting on the block (weight force and inertia force) relative to vertical. The modified chart is shown in Figure 2.5 where the parameter $\psi = \alpha + \beta$. Despite this advancement, this seismic failure chart still possess the primary assumption of its ancestors, namely it is applicable only to rectangular rock blocks.

2.2.2 Example Slopes

An example of a complex slope that could give rise to these modes of failure as they occur in nature is demonstrated through images taken by Wartman (2007) during site reconnaissance of the 2007 Pisco, Peru earthquake (Figure 2.6). These images illustrate the complex network of discontinuities present in natural rock slopes and that there are many opportunities for differing local failure modes to occur within a single slope. In addition, these images reiterate that rock blocks formed by the discontinuities are not restricted to rectangular shapes.

2.3 Seismic Triggering of Rock Slope Failure

The current analytical methods available to evaluate the triggering of seismic rock slope failure can be broken down into two categories: empirical predictive models and pseudo-static limit equilibrium methods (LEM). For the purpose of modern probabilistic seismic risk evaluations and based on the author's experience with methods in soil and slope engineering, the methods in these categories lag behind those used in other areas of civil engineering. In other cases, these methods do not sufficiently capture the basic range of potential failure modes identified by Keefer (1984).

2.3.1 Empirical Prediction Methods

Empirical predictive models for rock slope failures have been derived based on general slope geometric and geomorphological characteristics for landslides observed to fail during earthquakes. Since these models result from observing failures, the ability to predict how likely certain slope parameters predict failure depends on the data collected in the field. It is often the case that rock slope failures are catastrophic, limiting the ability to collect information on the state of the rock slope immediately preceding failure. Therefore, these models tend to be exclusively qualitative and require substantial experience and judgment to be applied.

One of the first methods was developed from Keefer's landslide database (Keefer, 1984) to provide a simple decision making chart as to the level of risk for landsliding (see Figure 2.7). Another type of empirical model, a weighted classification system, was used by Harp and Noble (1993) to evaluate landslides within a specific mountain range. In this model, weights are applied to various slope parameters based on experience to produce a classification system that could be used to evaluate the likelihood of slope failure on a regional scale. The Harp and Noble (1993) model, like the Keefer (1993) model, can only be used for a very coarse,

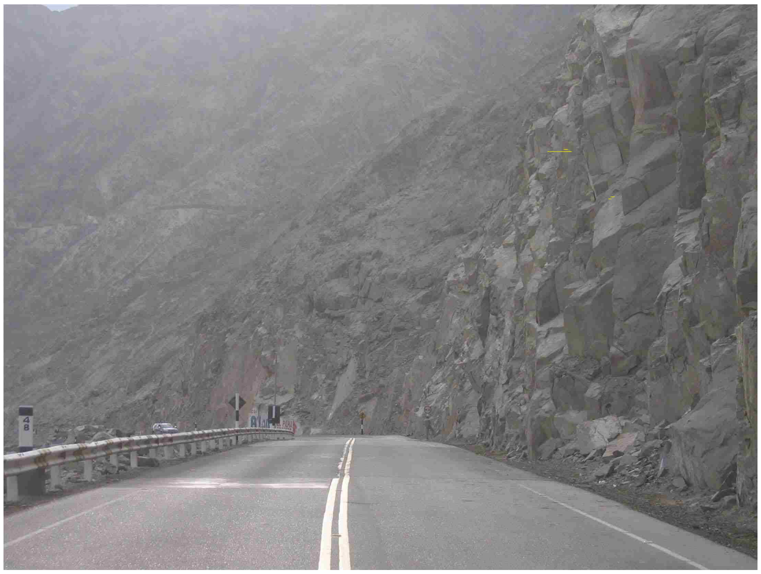

(a) Blocky slope with indications of missing rock blocks where toppling, sliding, and slumping failure modes are suspected.

(b) Blocky slope with indications of rock blocks where sliding and slumping modes are suspected.

Figure 2.6: Complex rock slope pictured after 2007 Pisco, Peru Earthquake (Photos: J. Wartman)

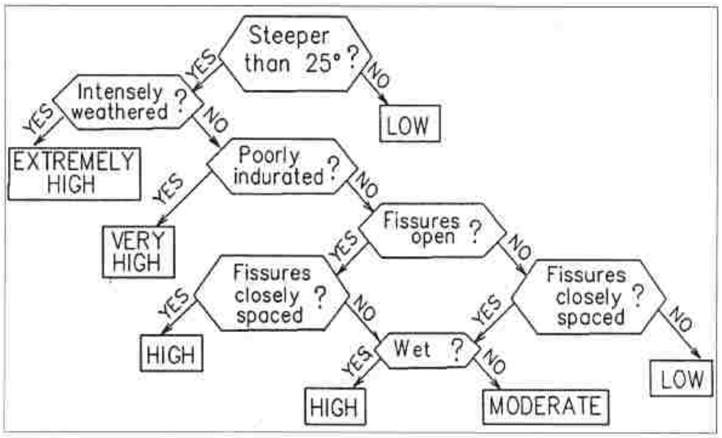

Figure 2.7: Empirical landslide risk decision tree (Keefer, 1993)

qualitative evaluation of landslide risk. While these models can be insightful, additional analysis for specific rock slopes is certain to be required for any engineering application.

2.3.2 Pseudo-static Limit Equilibrium and Yield Acceleration

Pseudo-static LEM methods are well understood and applied throughout civil engineering. These methods approximate dynamic behavior by including a representative inertial force into static analyses methods giving rise to the term pseudo-static. The inertial force is generally a fraction of the static weight and is chosen either based on theory or, more commonly, based on empirical evidence. These forces are then used to determine the minimally stable configuration of geometry and strength (i.e. limit equilibrium).

Pseudo-static LEM is generally used to provide a binary outcome/boundary of whether failure will or will not occur and an estimate of a factor of safety against failure. These methods are often applied to determine a seismic factor of safety for a given applied constant pseudo static inertial acceleration. Alternatively, a critical yield acceleration can be determined which indicate the maximum pseudo-static acceleration that can be tolerated before the onset of failure/motion (or when a factor of safety equals unity). A major limitation of LEM is that it does not provide any indication of displacement or degree of consequences for slope failure required by PBEE analyses.

For a simplified, two-dimensional, rectangular block sliding on a single surface, block toppling about its corner or both, the critical yield accelerations can be easily determined from statics (Sagaseta, 1986). For blocks sliding on multiple surfaces that induce back rotation, such as the slumping block, the problem of resolving the force diagram for stable configurations becomes indeterminate and requires iterative techniques and additional assumptions. Kieffer (1998) provides an iterative technique to determine a factor of safety for single and multiple slumping blocks in which a pseudo static force is included. This method could be used to determine the yield acceleration for many block shapes but would require an iterative analysis for each shape that is not likely to be undertaken by practicing engineers. At this time, there is no closed-form solution for the critical yield acceleration for slumping.

2.4 Displacement Methods

Methods that produce displacement estimates based on analytical models lend themselves to be more useful in seismic risk analyses given their quantitative nature. The complexity of these methods range from single block elements with basic principles of physics to numerical methods incorporating complex contact algorithms. In this section, a review of the most prominent methods is organized based on their level of analytic complexity.

2.4.1 Single Block Models

Methods based on single block models employ basic physics principles applied to simple geometries that are intended to approximate complex systems. Analogous to single degree oscillating systems, single block models can provide a rich understanding of emergent complex behavior resulting from dynamic loading. Single block models are also used to provide a quantitative displacement response to earthquake loading. Depending on the specific formulation of the model, this response can be informative as to the relative magnitude of slope deformation, or damage potential, that can be expected from various earthquakes. For example, Gazetas et al. (2012) used single block models to evaluate the destructiveness potential of the recorded 2011 Christchurch earthquake ground motions.

Sliding Block

Newmark (1965), Goodman and Seed (1966), and Seed and Goodman (1964) made famous the sliding block model to estimate displacements of earth dams and sand embankments from loading by earthquake ground motions. The sliding block (Figure 2.8) is assumed to slide with a rigid, perfectly plastic frictional contact between itself and an accelerating plane. This means that the block's movement is equal to the base plane until the yield acceleration (assumed constant) is exceeded at which time the block begins sliding relative to the plane. The block slides with an absolute acceleration equal to the yield acceleration and continues sliding until the relative velocity between the block and plane equals zero. After the block stops sliding its motion again mirrors the base plane and the cycle of analyzing the yield acceleration repeats. The relative displacement of the block is determined by double integrating the time history of relative acceleration between the block and plane. Strenk and Wartman (2011) provide an illustrative example of the sliding block calculation (see Figure 2.9).

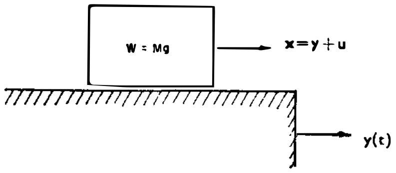

Figure 2.8: Sliding block schematic(Newmark (1965))

The sliding block model has been shown to be applicable to systems that undergo pure translational motion such as tetrahedral wedge sliding (Ling et al. (1997); Aydan et al. (2009); Bakun-Mazor et al. (2011)). Jibson (1993) reinforces the use of the sliding block model for the seismic evaluation of landslides and, in general, indicated that this is the most

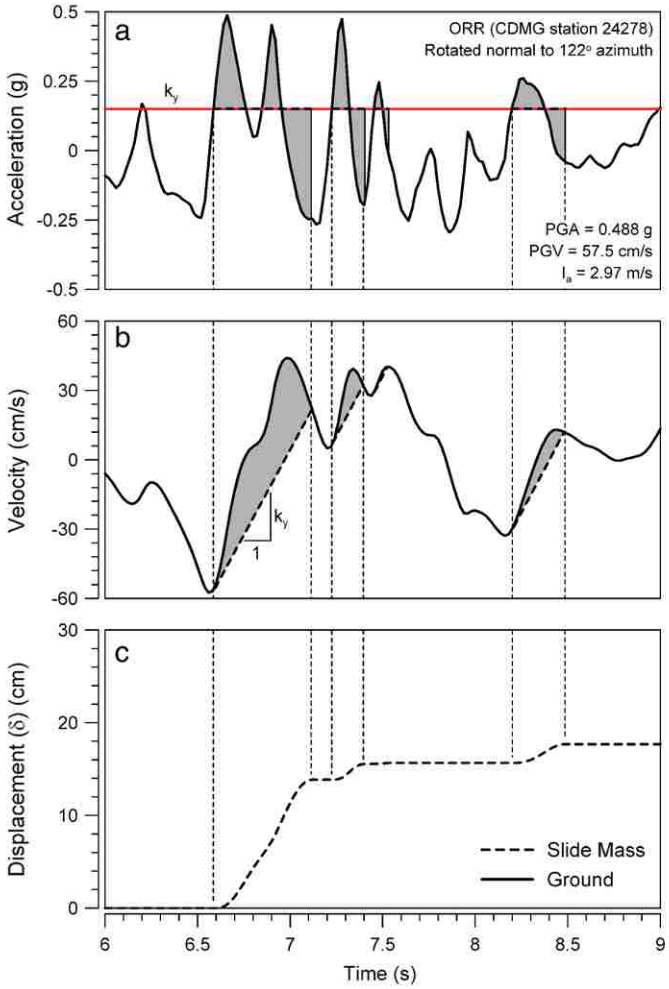

Figure 2.9: Sample calculation of sliding block method (Strenk and Wartman (2011))

commonly used model for assessing the displacement potential of slopes from earthquake ground motions. Kramer and Smith (1997) and Wartman et al. (2003) showed that the rigid assumption limits the applicability of the rigid block and rigid interface to natural soil slopes. To overcome this limitation, Kramer and Smith (1997) described a method to calculate the displacement response of a compliant (flexible) slope on a rigid contact. Based on the author's experience, both the rigid and compliant sliding block system are used widely throughout the geotechnical engineering field.

Rocking Block

The rocking block model consists of a rectangular block on an accelerating plane where the block is allowed to rotate about either of its edges with no sliding allowed (see Figure 2.10). Early use of this model can be traced to Japan in 1881, originating from the desire to back-calculate the peak ground acceleration (PGA) for earthquakes based on overturned tombstones (Ishiyama, 1980). Housner (1963) made this method popular with his analytical evaluation of tall slender structures from the 1960 Chilean earthquake. The general form of this model is comparative to the evaluation of precarious rock blocks (Brune et al. (1996); Shi et al. (1996); Anooshehpoor et al. (2004)). Makris and Konstantinidis (2003) used this model to develop a rocking spectrum, analogous to a traditional single degree oscillator response spectrum, to estimate the toppling potential for various block sizes due to earthquake ground motions (see Figure 2.11).

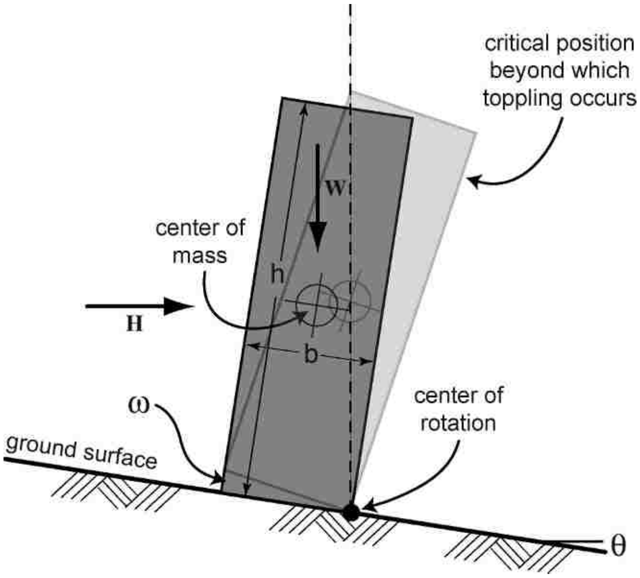

Figure 2.10: Rectangular rocking block (Haneberg (2009))

While the rocking block literature is fairly mature, it does not fit well with the problem of toppling of a rock slope in its current state. For rock toppling applications, Haneberg (2009)

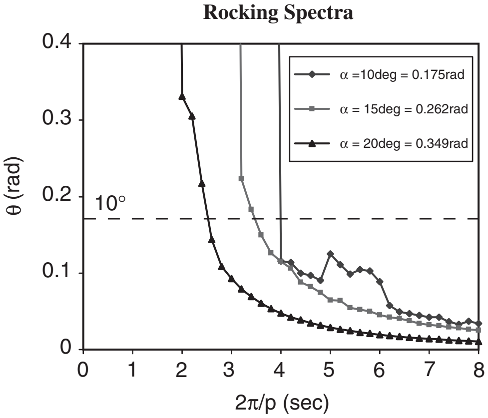

Figure 2.11: Example rocking block spectrum (Makris and Konstantinidis, 2003))

considered a toppling block loaded by a single half-sine pulse. The model was used to develop design charts to determine the required loading (PGA at a given frequency) to overturn a rock block. This work showed that the toppling response of a rock block is sensitive to it's rectangular shape and the loading frequency and amplitude. While the results are intriguing, the underlying assumptions require some scrutiny and the results will be shown in some cases to be conservative. In addition, this method is not capable of evaluating the loading from an earthquake time history. These limitations in the rocking block methods applicability and Haneberg's assumptions will be addressed in Chapter 4.

Slumping Block

There are no known simple single block displacement models known to the author that are capable of predicting seismic deformation of a slumping rock block. Sliding block (translation only) models are more commonly applied to translational and slumping slope failures (Jibson, 1993). However, researchers have shown that ignoring rotation causes displacements to be under predicted (You and Michalowski, 1999; Michalowski, 2007). The consideration of rotation has been studied in soil slopes by many (Sarma, 1981; Chang et al., 1984; Sawada and Nomachi, 1985; Ling and Leshchinsky, 1995; Ling et al., 1997; Siddharthan and El-

Gamal, 1998; Zeng and Steedman, 2000; Michalowski, 2007; Zeng and He, 2013), but these methods have not been translated to rock slopes.

2.4.2 Advanced Methods

Multi-Block Models

Single block models represent simple models evaluated with relatively simple first principles from physics. Their behavior is intentionally limited for ease of calculation and interpretation, however this is not necessarily required. Tonon (2007) presents an incremental-iterative algorithm for analyzing general failure modes of rock blocks subject to generic forces. This model is truly comprehensive with the ability to model large deformations and rotations and non-linear contact behavior between the block and the plane. These attributes make the model capable of detecting any failure mode of the block. However, this model was developed for the situations of the rapid removal of constraints leading to dynamic motion rather than applied earthquake loading; thus it is not easily applied to the earthquake problem.

Another comprehensive model is one developed by Michalowski (2007). This model is capable of evaluating multiple blocks sliding along a curved base plane. Michalowski (2007) concludes that the rotational component of the block's permanent deformation path is important to capture the maximum potential for sliding. While these two methods allow for more detail, the cost of these complex models is the loss of a simple, intuitive model that encompasses the influence of geometry and dynamic response from seismic loading.

Numerical Methods (FEM, FDM, DEM, and DDA)

As with most problems in engineering, advanced numerical methods such as the finite element method (FEM), finite difference methods (FDM), discrete element method (DEM), and discontinuous deformation analysis (DDA) can be used to model blocky systems with complex geometric layouts and fracture constitutive behavior. These methods can be generally parsed into two categories: Continuum and Discontinuum. The applicability of these numerical techniques have been well discussed in the literature (Coggan et al., 1998; Eberhardt, 2003, 2006; Stead et al., 2006; Eberhardt, 2008) and are summarized below.

Continuum models (e.g. FEM or FDM) are most applicable in materials such as massive, intact rocks or heavily jointed rock. Continuum models utilize FEM or FDM to solve the differential equations of equilibrium with various constitutive models to relate stresses and strains. The problem domain is represented by a mesh of elements that assume continuity of displacement across the element. The modeling of intact rocks is generally only valid up to the point of failure. Once failure occurs, the rock forms fractures which produce discontinuous deformations and the assumption of continuous deformation is void. The accuracy and appropriateness of modeling heavily jointed rock is dependent on the information being sought. In general, the calculation of macro scale deformation, stress distribution, and failure location is feasible. However, local details near the fractures would be inaccurate. The ability to model heavily jointed systems would be highly dependent on the choice of constitutive model and selection of model parameters that approximate the global behavior.

DEM and DDA are by far the most popular numerical methods used in rock engineering research and consulting practice given their formulation to specifically evaluate the interaction between multiple rock blocks. Discontinuum models are most applicable when the response of a slope is controlled by the orientation, spacing, persistence and interface response of the rock joints (Einstein et al., 1983). The problem domain is represented by an assemblage of interacting, discrete shapes created by the distribution of fracture geometries. Similar to FEM and FDM used to solve continuum models, discontinuum models utilize the universal distinct element code (UDEC), DDA, or particle flow codes (PFC) to solve the equations of equilibrium and interaction between blocks. These types of models are commonly referred to as DEM. With this type of modeling the accuracy of the model is governed by the appropriate definition of fracture geometry and choice of joint interface constitutive model and parameters. The explicit modeling of the discontinuities provides more realistic distribution of stresses and displacements and in some cases drives the development of the non-linear failure mechanisms and rock mass response (Eberhardt, 2003).

Discontinuum models have been used to evaluate the seismic stability of rock slopes by many researchers (Chuhan et al., 1997; Hatzor, 1999; Havenith et al., 2003; Hatzor, 2003; Bhasin and Kaynia, 2004; Hatzor et al., 2004; Pekau and Yuzhu, 2004; Wang et al., 2006; Wu, 2010). Discontinuum models will be used in this thesis considering that the problems being modeled consist of relatively few distinct blocks. In particular, because of ease of access and familiarity in the rock slope engineering community, the DEM program universal distinct element code *UDEC* will be used for the discontinuum modeling throughout this thesis. The numerical model results will be used for pseudo-static failure mode determinations of rock blocks and non-linear, time dependent, seismic responses of various rock block configurations. In addition, the time dependent solutions from *UDEC* will serve as the target (or known) solutions for various problems evaluated in this thesis.

Chapter 3

PSEUDO-STATIC FAILURE MODES AND YIELD ACCELERATIONS IN ROCK SLOPES

Rock slope failures have contributed greatly to the economic and human loss experienced during seismic events throughout the world. Accounts of these spectacular events have been documented and evaluated throughout the literature (Cluff (1971); Plafker et al. (1971); Wilson and Keefer (1983); Jibson et al. (2006); Keefer et al. (2006); Aydan et al. (2009); Lanzo et al. (2010); Alfaro et al. (2012); Massey et al. (2014), among others). A database of earthquake induced landslide failures compiled by Keefer (1984), and reinforced by others (Rodríguez et al., 1999; Keefer, 2013), clearly indicates that failure modes, observed in the field following earthquakes, include sliding, toppling, and slumping. Methods based on simplified, discrete, single block models such as a rectangular block on a plane or wedge blocks are commonly used to approximate the behavior of rock slopes and determine the factor of safety against failure (Hoek and Bray, 1977; Yagoda-Biran and Hatzor, 2013). These models assume rectangular blocks on a plane or sliding prismatic three-dimensional (3D) wedge blocks. A major limitation common to rectangular and wedge shaped blocks is that the assumed geometry and boundary conditions restrict the potential failure modes to sliding or toppling. This chapter will expand the geometry assumptions so that new failure modes will be kinematically admissible.

In order for additional failure modes to be considered, non-rectangular shapes need to be considered. Kieffer (1998) considered blocks in static loading that are parallelogram in shape and require a second plane to provide static stability and thus fail in a slumping mode of failure (simultaneous sliding and back rotation). While this was a big advance in the evaluation of rock block failure modes, the implementation of this model was limited to factor of safety evaluations against slumping modes of failure. Tonon (2007) introduced a model that is capable of evaluating complex block geometries which does not restrict potential failure modes, however this model requires a block specific evaluation and is most applicable to problems with a quick reduction in strength rather than quick (seismic) loading.

In this chapter a simple, yet broadly applicable, two-dimensional (2D) single block framework is introduced that does not restrict the geometry to orthogonal fracture sets. This formulation allows for the slumping failure mode to naturally occur and can identify a new single block failure mode, confined toppling. Through the use of simple failure mode charts, this framework can be easily applied by a wide range of practitioners including geologists performing pre- and post-failure field reconnaissance and design engineers. In addition to the identification of new failure modes, this formulation allows for the calculation of the corresponding pseudo-static accelerations that lead to block motion. Seismic yield acceleration equations are presented for all four modes of failure: sliding, toppling, slumping, and confined toppling. The equations for slumping and confined toppling are derived for the first time.

Although the model may be simple in its formulation and implementation, it is quite powerful in allowing for significant implications to be developed. Complex shaped blocks can be easily evaluated knowing just their centers of mass and contact points with supporting fractures. The failure mode of discrete rock blocks are shown to not be dependent on the inclination of the primary fracture in which the block rests upon and the scale of the block itself. Seismic failure modes are demonstrated to be different from those induced by static forces alone and can even change modes depending on the amount of displacement during the ground motion. In addition, it is shown that the characteristics of an earthquake ground motion acting on these blocks in combination with geometric variability can influence the abundance of failure types observed in the field. Finally, two example mode and yield acceleration evaluations of actual rock slopes are presented.

3.1 Existing Failure Mode Charts

The most prominent design charts currently available for single block failure modes are limited to blocks formed by orthogonal joint sets. A succinct literature review of these charts is discussed by Yagoda-Biran and Hatzor (2013) and is summarized here. Ashby (1971) and Hoek and Bray (1977) presented the first chart (Figure 3.1a) that established the static limit equilibrium failure modes. They also identified dynamic failure modes when the block is in motion relative to the fracture planes. The chart was revised by Bray and Goodman (1981) (Figure 3.1b) based on DEM modeling by Voegele (1979) that indicated that the *sliding* and *sliding & toppling* boundary should be modified. The dynamic failure modes were again modified by Sagaseta (1986) (Figure 3.1c) to reflect the appropriate application of inertial forces.

Modes of failure for discontinuous rock slopes were investigated by Aydan et al. (1989). In this study, rock slopes with various configurations of discontinuities (i.e. through-going or step-wise continuous) were evaluated for sliding, toppling and combined sliding-toppling modes of failure. Tilt tables and base friction machines were used to verify their analysis. The geometries and discretization of modes are shown in Figure 3.2. These studies showed that multiple blocks could combine to form the basic modes identified by the simplified charts.

While these studies discuss dynamic motion, they should not be confused with initiation of motion under seismic forces. These charts instead delineate boundaries between statically stable and unstable, rectangular blocks under gravitational loading. The dynamic motion represents the scenario where a block begins motion in statically unstable conditions. This situation is more representative of blocks whose fractures undergo strength loss rather than experience an inertial loading induced by an earthquake.

Given the earthquake loading limitation, Yagoda-Biran and Hatzor (2013) showed that the seismic inertial force could be thought of as adding additional slope angle to the static charts thus expanding the charts applicability to include earthquake loading. The slope

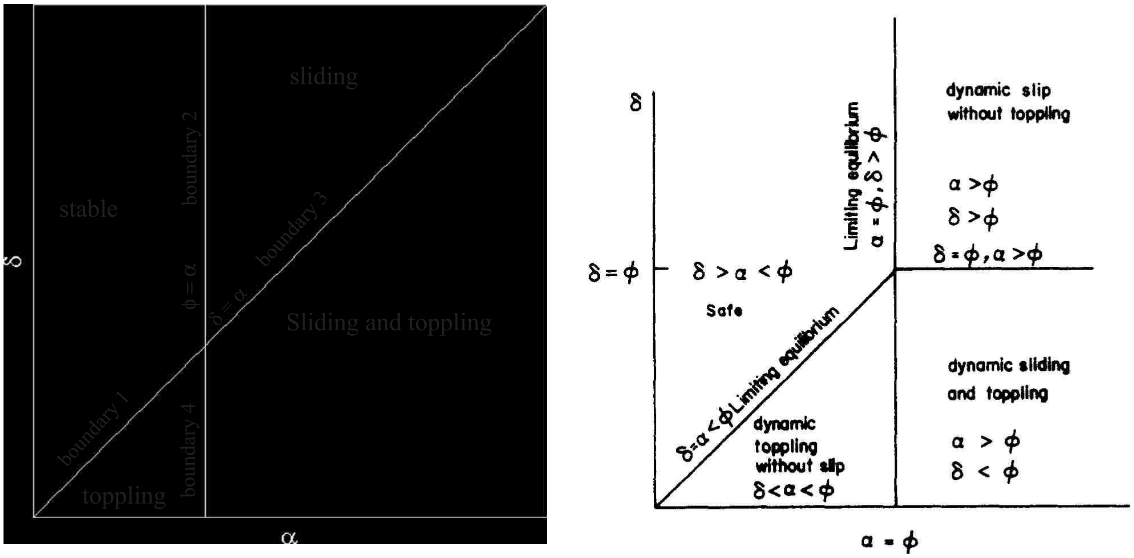

(a) Ashby (1971); Hoek and Bray (1977)

(b) Bray and Goodman (1981)

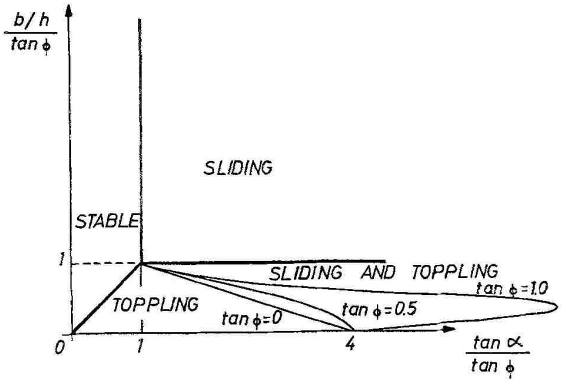

(c) Sagaseta (1986)

Figure 3.1: Rectangular block static stability boundaries and dynamic motion charts. Note that dynamic motion does not equate to seismic failure modes.

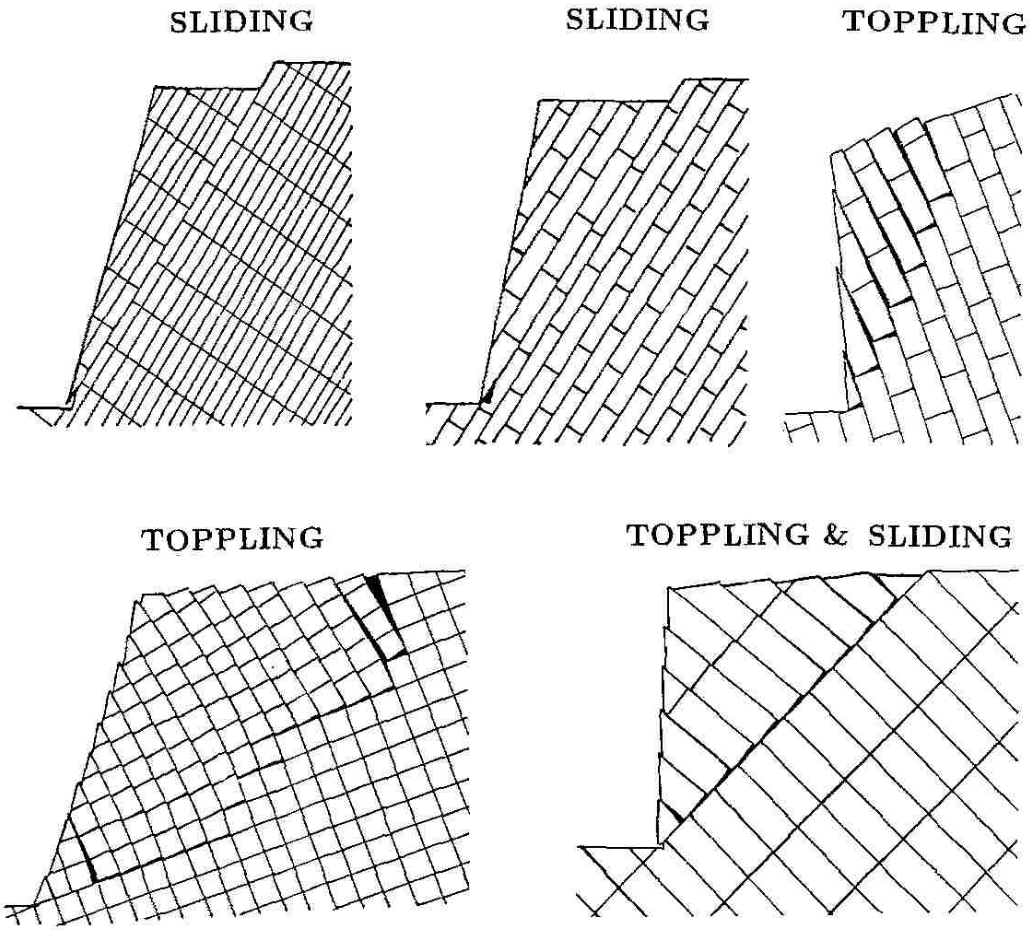

(a) Geometries

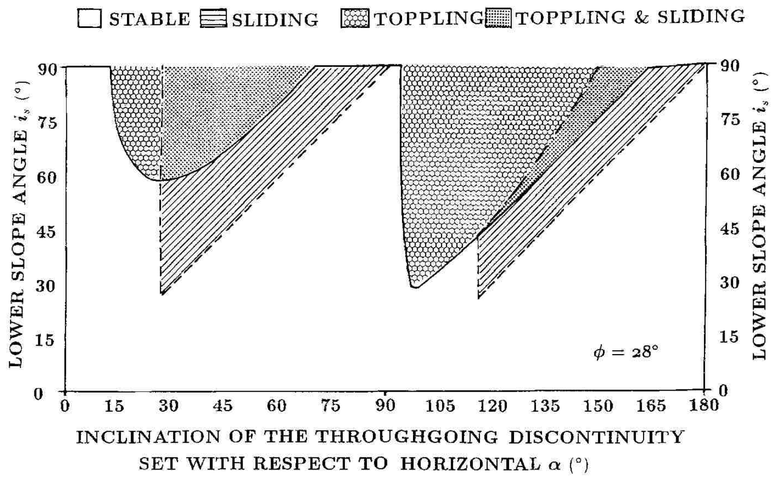

(b) Failure mode chart

Figure 3.2: Effective failure modes of a rock mass (Aydan et al., 1989).

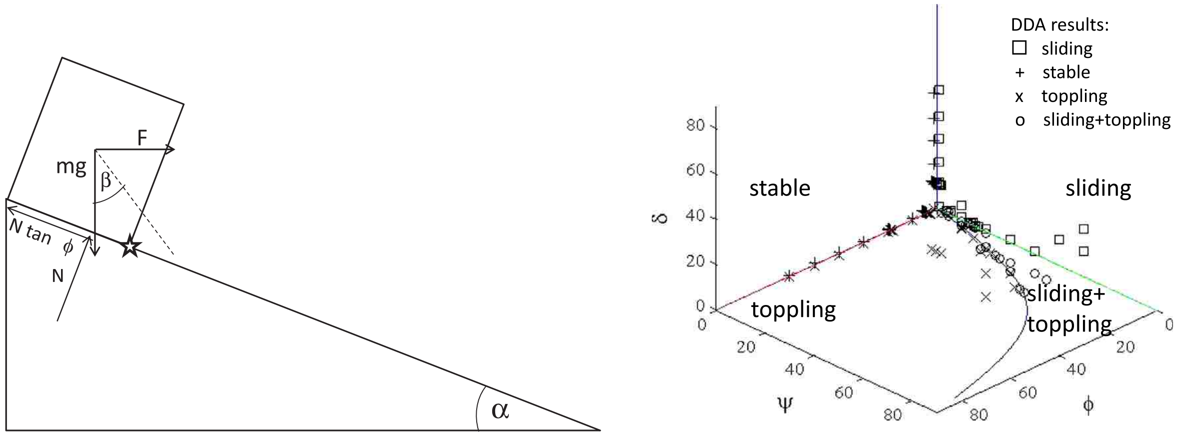

(a) Geometry

(b) Geometry

Figure 3.3: Pseudo-static rectangular block failure modes (Yagoda-Biran and Hatzor, 2013).

angle, α is effectively increased by the angle, β, formed by the resultant force acting on the block (weight force and inertia force) relative to vertical. The modified chart is shown in Figure 3.3 where the parameter $\psi = \alpha + \beta$. Despite this advancement, this seismic failure chart still possess the primary assumption of its ancestors, namely it is applicable only to rectangular rock blocks.

3.2 Geometry

3.2.1 Fractured Rock Slopes

The formation of a fractured rock slope is the result of many complex processes working in seemingly random sequences. Fortunately for the rock slope engineer, the end result of these processes, whether the final result is a slope with a complex failure network or a homogeneous intact rock slope, is the primary concern. On their own, discrete blocks can fail catastrophically and impart great damage to civil structures and result in great loss of life and thus are worthy of analysis. The main focus of this chapter is that of fractured rock slopes and the discrete blocks these fractures form.

The range of discrete rock block geometries found on rock slopes is the result of the intersections formed by fractures throughout the rock mass. In some cases these fracture networks create orthogonal intersections that form rectangular blocks. However, when the fractures intersect each other at arbitrary angles then many more block geometries become possible. As a matter of nomenclature, the fracture set closest to a horizontal orientation is termed the base fracture, while the other fracture set is termed the back fracture. For example, Figure 3.4 slopes in nature with two predominate fracture sets. These figures illustrate slopes where the base fracture set is dipping out of the slope (daylighting fracture) while the back fracture set is oriented either side of vertical. The discrete blocks formed by these intersecting fracture sets at the slope surface are highlighted. If the fractures within each set have strikes that differ by more than 20 degrees, then more general polygons are formed and two dimensional assumptions may no longer apply (Goodman, 1989).

In addition to discrete block failures, these discrete blocks can interact with each other and create complex emergent behavior (Aydan et al., 1989). Similar to discrete blocks, the failure of multi-block slopes during earthquakes can be catastrophic (Massey et al., 2012). Currently, for seismic loading, these slopes are evaluated with either simplified failure charts based on rectangular-shaped blocks (Yagoda-Biran and Hatzor, 2013) or slope specific numerical analyses (Pal et al., 2011; Wu, 2010; Bhasin and Kaynia, 2004; Chuhan et al., 1997).

3.2.2 Discrete Rock Blocks

Throughout civil engineering fundamental exploration of simple systems has provided invaluable insight into complex structures. Examples of simple systems include the single degree of freedom oscillator and the Newmark sliding block (Newmark, 1965). As mentioned previously, rectangular blocks on a slope are commonly used to assess failure modes of rock slopes. The study of simple block geometries will be continued here with an expansion of geometry assumptions.

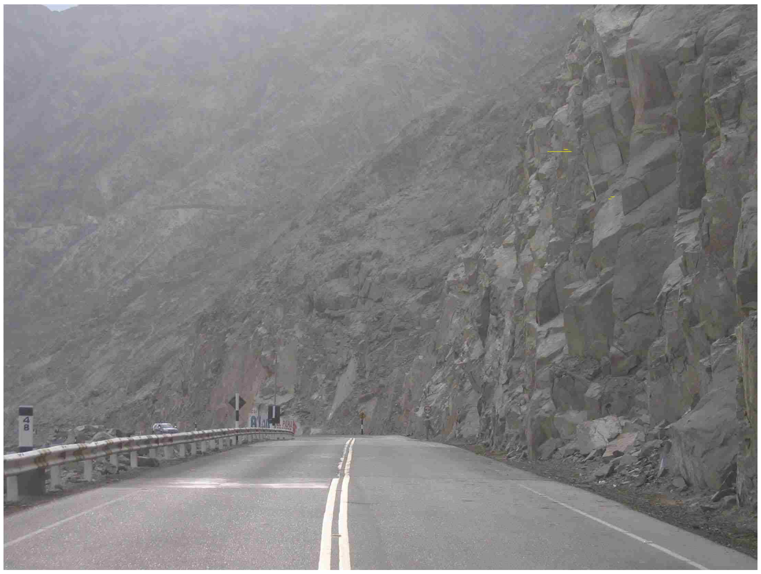

(a) Blocky slope with indications of missing rock blocks where toppling and slumping failure modes are suspected.

(b) Blocky slope with indications of rock blocks where sliding and slumping modes are suspected.

Figure 3.4: Complex rock slope pictured after 2007 Pisco, Peru Earthquake (Photos: J. Wartman).

Block Parameters (Aspect Ratio and Relative Orientation)

First, consider single, discrete rock blocks that are formed on the outer most portions of the slope highlighted in Figure 3.4. The blocks are redrawn in Figure 3.5 with additional geometric detail. The blocks are detailed from the perspective of geologists and engineers who evaluate fracture networks primarily from core logs or surface mapping where relative fracture orientations and fracture spacing are a natural choice of parameters to quantify rock block geometries. The strikes of the fractures within each fracture set are assumed to be within 20 degrees resulting in a parallelogram shape that can be evaluated with 2D assumptions. The block rests on a base fracture plane inclined at an angle β with respect to horizontal. The angle formed between the base and back fracture is termed the relative fracture angle, γ. The perpendicular spacing between the base fractures is denoted as S_1 while the perpendicular spacing between back fractures is denoted as S_2.

The block is assumed to be in contact with the fractures at points 1 and 3, as shown in Figure 3.5. Contact 1 is located at the heel of the block near the intersection of the two fractures and can act either along the base plane or back plane depending on movement of the block. In some cases, contact 1 acts to provide primary weight support by contact with the base fracture while in other cases it acts as a lateral support force through contact with the back fracture. Contact 2 is located along the back fracture and acts as a lateral support force in some circumstances. Contact 3 is located where the toe of the block intersects the base fracture plane and provides primary weight support to the block. Point 4 is not in contact with a fracture but is defined for the purposes of defining the block geometry. The edges of the block are not necessarily assumed to be perfectly planar but it is assumed that the block makes contact with the fractures in only three contact locations.

Three position vectors, $\mathbf{r}_1$, $\mathbf{r}_2$, and $\mathbf{r}_3$, are identified as the vectors from the center of mass, C, to the three corners in contact with the two fracture planes. Since the block is a parallelogram and assuming a uniform density distribution throughout the block, $\mathbf{r}_2 = -\mathbf{r}_3$ and $\mathbf{r}_1 = -\mathbf{r}_4$. With these relationships, the geometry of this 2D discrete rock block is

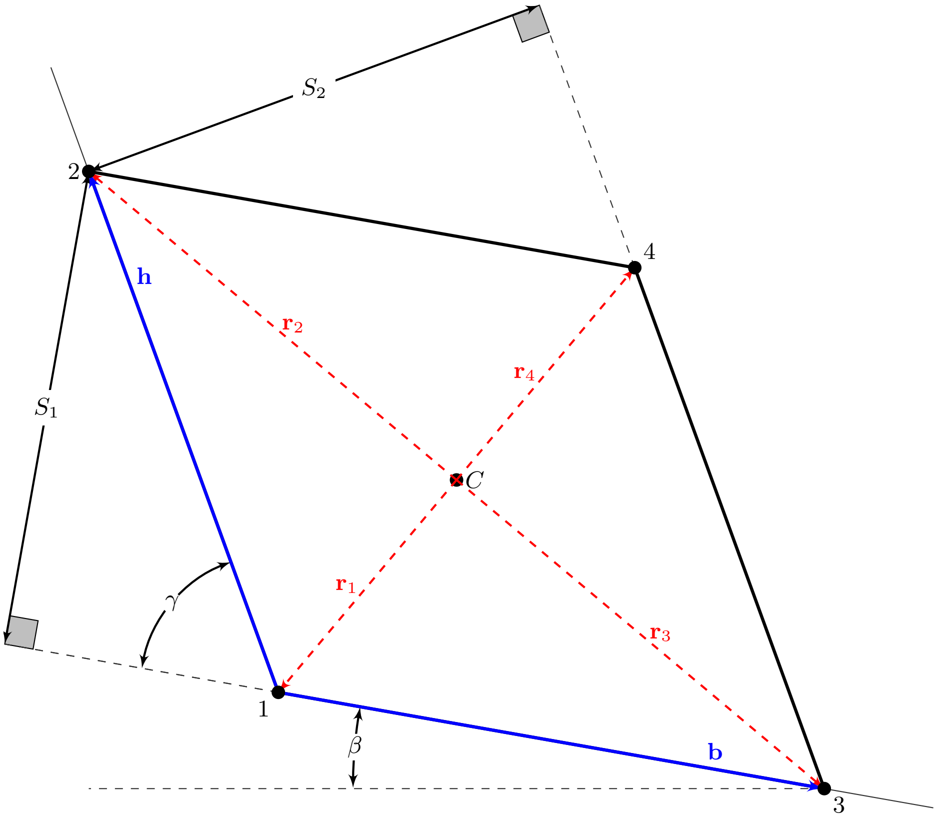

Figure 3.5: Discrete rock block geometry parameterized by joint spacing and relative fracture angle.

completely described by $\mathbf{r}_1$ and $\mathbf{r}_3$. The position vectors will prove to be useful later when pseudo-static failure modes and minimum accelerations levels that initiate failure are evaluated; thus, their relationship with respect to these measured field parameters are explored in some detail here.

The components of the position vectors, relative to a reference frame formed by the base fracture and its normal, can be determined from the parameters S_1, S_2, and γ. To determine the position vector components, the vectors that describe the back and base fracture planes originating at contact 1 (**h** and **b**, respectively) are first described as,

$$\mathbf{b} = \left[\frac{S_2}{\sin(\gamma)}, 0\right] \tag{3.1a}$$

$$\mathbf{h} = \left[-\frac{S_1}{\tan(\gamma)}, S_1\right]. \tag{3.1b}$$

Note that for brevity, the third component of the vector is dropped since it equals zero. Factoring out the length of S_1

$$\mathbf{b} = S_1\left[\frac{S_2}{S_1}\csc(\gamma), 0\right] \tag{3.2a}$$

$$\mathbf{h} = S_1\left[-\cot(\gamma), 1\right]. \tag{3.2b}$$

S_1 is left in the fraction to emphasize the aspect ratio $\frac{S_2}{S_1}$ and scaling effect of S_1. Now, the position vectors can be written in terms of **b** and **h**.

$$2\mathbf{r}_1 = -\left[\mathbf{b} + \mathbf{h}\right] \tag{3.3a}$$

$$2\mathbf{r}_3 = \left[\mathbf{b} - \mathbf{h}\right] \tag{3.3b}$$

Expanding these equations with the components of **b** and **h**,

$$2\mathbf{r}_1 = S_1\left[\cot(\gamma) - \frac{S_2}{S_1}\csc(\gamma), -1\right] \tag{3.4a}$$

$$2\mathbf{r}_3 = S_1\left[\cot(\gamma) + \frac{S_2}{S_1}\csc(\gamma), -1\right]. \tag{3.4b}$$

Since $\mathbf{r}_1$ and $\mathbf{r}_3$ completely describe the geometry of the block, then using equations, the entire shape of a block is described by the fracture spacings and relative fracture angle. A feature of writing the equations in this manner is that the vector components in the bracket describes a unit block, which could be expected since the cross product of two vectors describe the area of a shape. Since both vectors are multiplied by the value of S_1, it acts to scale the fixed geometric shape of the unit block to a given size. With the position vector Equations (3.4a & 3.4b), the shape of the blocks can be visualized based on values of $\frac{S_2}{S_1}$ and γ as shown in Figure 3.6.

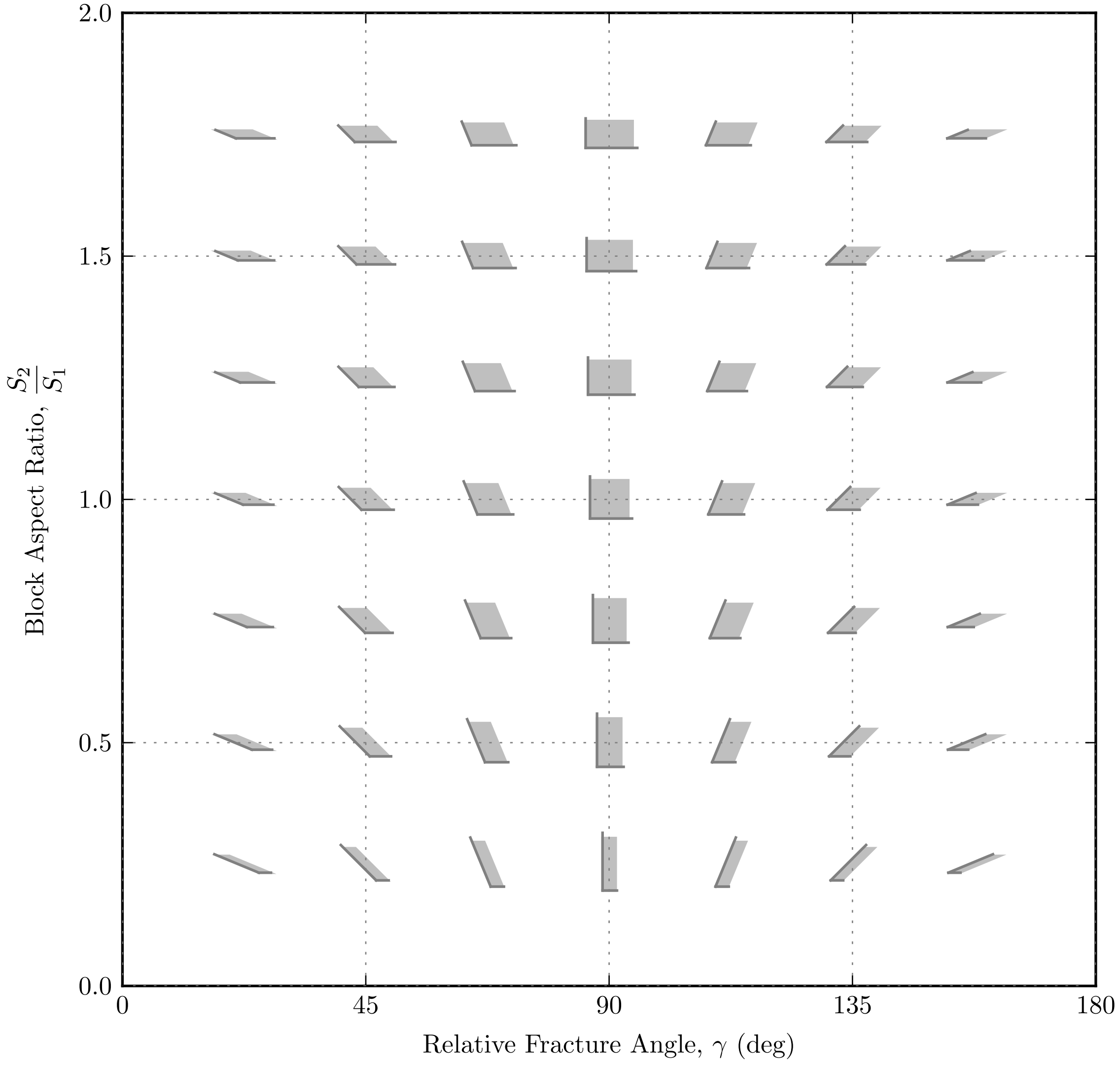

Figure 3.6: Parallelogram-shaped blocks based on block aspect ratio, $\frac{S_2}{S_1}$ and relative joint angle, γ.

Block angle parameters

For reasons that will be made clearer in subsequent sections, it is useful to adopt a different set of parameters to describe the block shape. Figure 3.7 shows the same block as in Figure 3.5 but with this different geometric detailing. The back block angle, α_1, and the forward block angle, α_3, are defined as the angles formed by $\mathbf{r}_1$ and $\mathbf{r}_3$, respectively, as measured with respect to the outward unit normal ($\hat{\mathbf{n}}_{1\perp}$) of the base fracture. These angles are considered positive if the position vector ($\mathbf{r}_1$ or $\mathbf{r}_3$) is oriented downslope of the base fracture normal ($\hat{\mathbf{n}}_{1\perp}$). For the block shown in Figure 3.7, α_1 is negative and α_3 is positive.

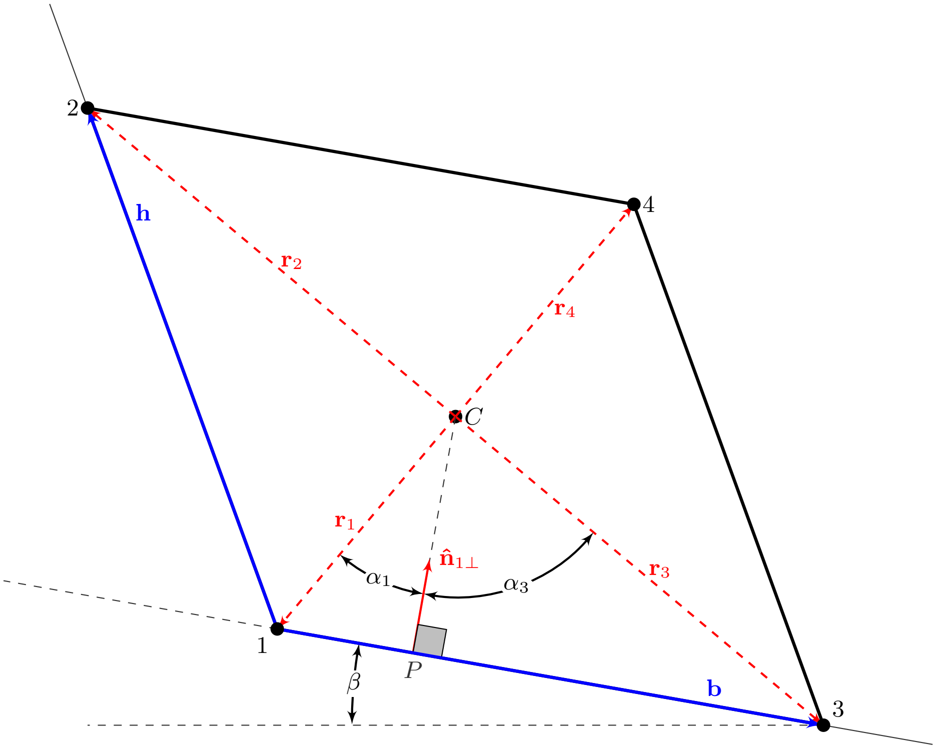

Figure 3.7: Discrete rock block geometry parameterized by forward and backward block angles, α_1 and α_3.

The components of the position vectors are easily determined from these newly defined parameters, α_1 and α_3 as

$$\mathbf{r}_1 = r_1 \left[\sin(\alpha_1), -\cos(\alpha_1)\right] \tag{3.5a}$$

$$\mathbf{r}_3 = r_3 \left[\sin(\alpha_3), -\cos(\alpha_3)\right]. \tag{3.5b}$$

Note that $r_1 = \|\mathbf{r}_1\|$ and $r_3 = \|\mathbf{r}_3\|$ are scalar lengths. These lengths can be related to each other using their relationship to the length of the line from point C to point P.

$$\|C - P\| = r_1 \cos(\alpha_1) = r_3 \cos(\alpha_3) \tag{3.6}$$

Rearranging,

$$r_3 = r_1 \frac{\cos(\alpha_1)}{\cos(\alpha_3)}. \tag{3.7}$$

Substituting equation (3.7) in to equation (3.5b),

$$\mathbf{r}_1 = r_1 \left[\sin(\alpha_1), -\cos(\alpha_1)\right] \tag{3.8a}$$

$$\mathbf{r}_3 = r_1 \frac{\cos(\alpha_1)}{\cos(\alpha_3)} \left[\sin(\alpha_3), -\cos(\alpha_3)\right]. \tag{3.8b}$$

Using these equations, the unit block shape can be completely described by the backward and forward angles. Since all vectors are multiplied by the scalar r_1, it scales the block. As with S_1, various values of r_1 or r_2 only change the overall size of the block and do not change the shape of the block. Based on equations (3.8a) and (3.8b), the shape of the blocks can be visualized based on values of α_1 and α_3 as shown in Figure 3.8. Note that the dashed diagonal line representing $\alpha_1 = -\alpha_3$ describes blocks that are rectangular in shape. This line is also a mirror line separating blocks with shapes leaning forward (left of the dashed line) and blocks leaning backward (right of the dashed line).

Relationships between block parameter sets

For practical purposes, and as will be shown later, it is necessary to be able to work in either parameter set. For this reason, the two parameter sets are mapped to each other using the

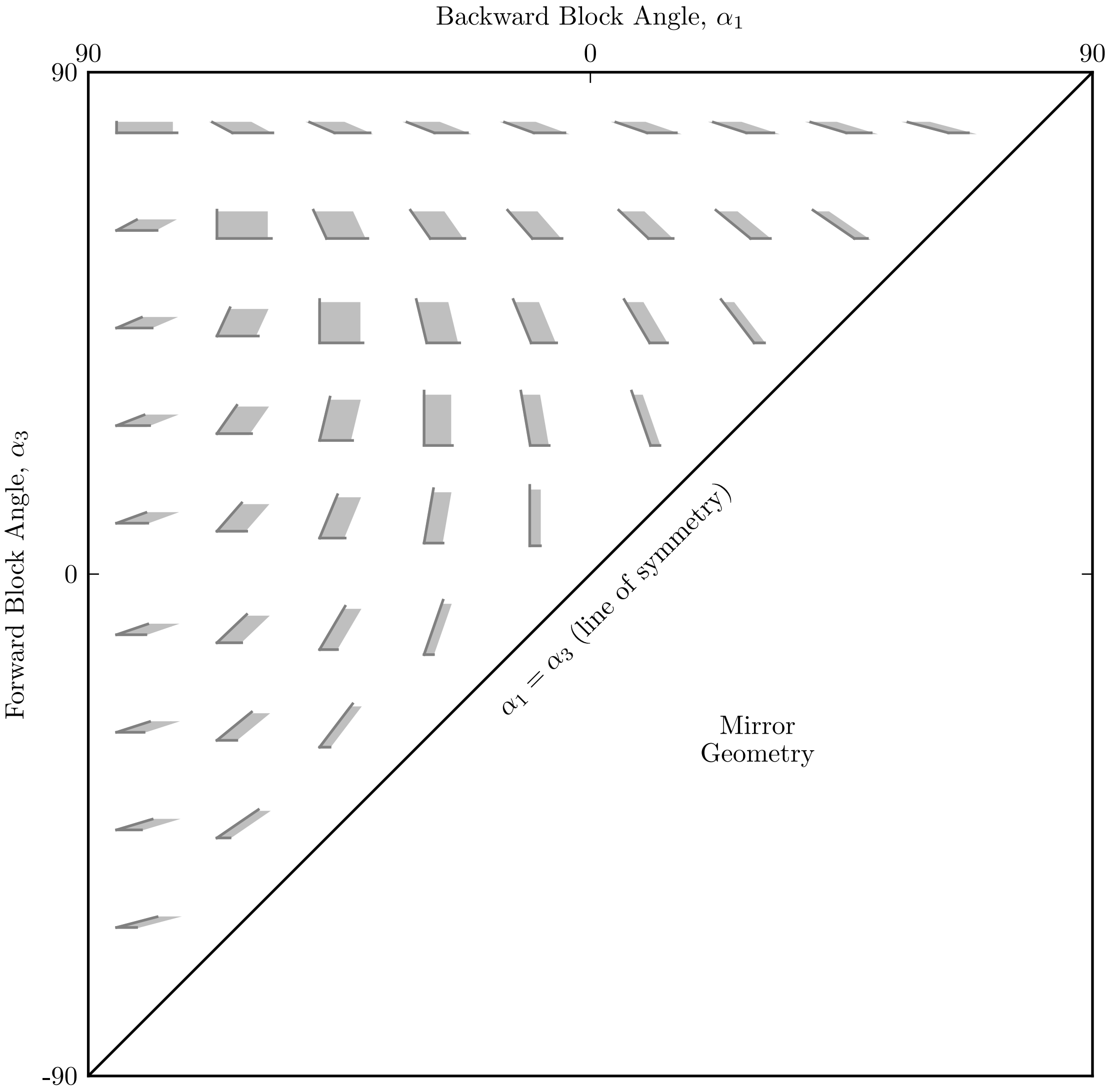

Figure 3.8: Parallelogram block shapes based on the forward and backward block angles, α_1 and α_3.

coordinates of the position vector derived previously. First to determine the relative angle, γ, $\mathbf{h}$ is constructed using $\mathbf{r}_1$ and $\mathbf{r}_3$,

$$\mathbf{h} = -(\mathbf{r}_1 + \mathbf{r}_3). \tag{3.9}$$

Substituting in the components of $\mathbf{r}_1$ and $\mathbf{r}_3$ from Equations (3.8a) and (3.8b),

$$\mathbf{h} = -r_1 \left[\sin(\alpha_1) + \sin(\alpha_3)\frac{\cos(\alpha_1)}{\cos(\alpha_3)}, -\cos(\alpha_1) + \cos(\alpha_3)\frac{\cos(\alpha_1)}{\cos(\alpha_3)} \right]. \tag{3.10}$$

Simplifying and rearranging,

$$\mathbf{h} = r_1 \left[-\cos(\alpha_1)(\tan(\alpha_1) + \tan(\alpha_3)), 2\cos(\alpha_1) \right]. \tag{3.11}$$

The relative fracture angle can now be determined based on the components of $\mathbf{h}$. The negative of the x-component of $\mathbf{h}$ is used since it is negative itself when $\gamma < 90$.

$$\begin{aligned} \gamma &= \tan^{-1}\left(\frac{h_y}{-h_x}\right) \\ \gamma &= \tan^{-1}\left(\frac{2}{-(\tan(\alpha_1) + \tan(\alpha_3))}\right). \end{aligned} \tag{3.12}$$

Now, the fracture spacings can be determined by comparing the y-component of the back vector and the x-component of base vector.

$$b_x = \frac{S_2}{\sin(\gamma)} = r_1 \left(\frac{\cos(\alpha_1)}{\cos(\alpha_3)} \sin(\alpha_3) - \sin(\alpha_1) \right) \tag{3.13a}$$

$$h_y = S_1 = 2r_1 \cos(\alpha_1) \tag{3.13b}$$

Dividing these two equations determines the aspect ratio.

$$\frac{b_x \sin(\gamma)}{h_y} = \frac{S_2}{S_1} = \frac{(\tan(\alpha_3) - \tan(\alpha_1))\sin(\gamma)}{2} \tag{3.14}$$

Alternatively, α_1 and α_3 can be determined from the components of $\mathbf{r}_1$ and $\mathbf{r}_3$ in terms of γ and $\frac{S_2}{S_1}$.

$$\alpha_1 = \tan^{-1}\left(\frac{r_{1x}}{-r_{1y}}\right) = \tan^{-1}\left(\frac{\cot(\gamma) - \frac{S_2}{S_1}\csc(\gamma)}{-1}\right) \tag{3.15a}$$

$$\alpha_3 = \tan^{-1}\left(\frac{r_{3x}}{-r_{3y}}\right) = \tan^{-1}\left(\frac{\cot(\gamma) + \frac{S_2}{S_1}\csc(\gamma)}{-1}\right) \tag{3.15b}$$

From these equations, the contour plots in Figure 3.9 are presented to illustrate the relationship between the two parameters sets.

3.3 Failure Modes

3.3.1 Static Limit Equilibrium

It can be seen that the blocks on the natural rock slopes in Figure 3.4 are not rectangular thus the failure charts in Figure 3.1 are not applicable. To determine the static stability of the blocks in Figure 3.4, three potential free body diagrams in Figure 3.10 are considered. Note that the analysis of non-rectangular discrete blocks in this chapter will concentrate on the pseudo-static limit equilibrium failure modes and not dynamic modes as the previous charts describe. In this Figure, $\mathbf{W}$ is the static weight vector of the block while $\mathbf{R}_1$ and $\mathbf{R}_2$ are the reaction force vectors acting on the block. Note that although it is possible for water pressure to be present within the fractures, the purpose of this work is to evaluate the role that simple fracture geometries and earthquake loading play in the failure of discrete rock blocks. Water pressures acting within the fractures are not considered.

The first state considered (Figure 3.10a) is the scenario where the weight vector is oriented between the position vectors $\mathbf{r}_1$ and $\mathbf{r}_3$. In this case, there is only one reaction force ($\mathbf{R}_1$), which acts at some point located along the base of the block. The exact point where the force acts depends on the geometry and mobilized friction angle and can be determined by projecting $\mathbf{W}$ onto the base plane. In limit equilibrium, the angle the base reaction force forms with the base fracture is equal to the ultimate friction angle. In addition, the block does not require the back plane for stability thus any potential reaction force at contact 2 can be assumed to be zero. This is essentially the classic problem introduced in introductory physics of a block on a frictional plane and is a more general block than the rectangular block considered by most rock slope stability researchers.

The second state considered (Figure 3.10b) is the scenario where $\mathbf{W}$ lies on the upslope side (left in the figure) of $\mathbf{r}_1$. When $\mathbf{W}$ acts, by itself, on the upslope side of $\mathbf{r}_1$, it creates a

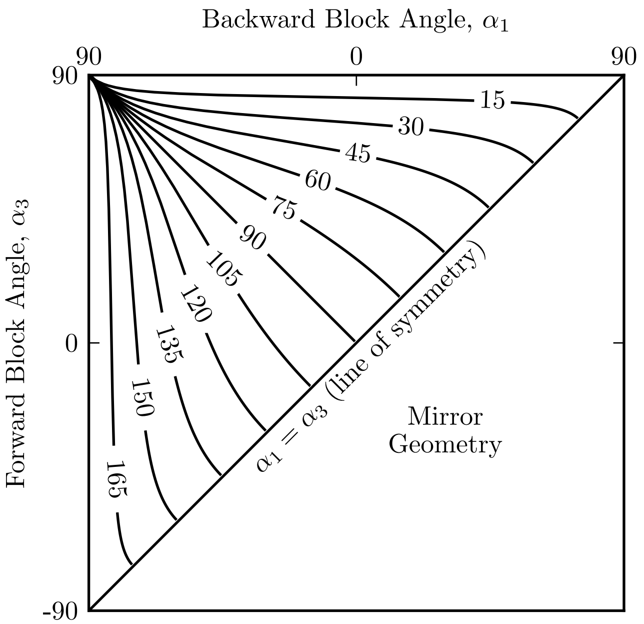

(a) Relative fracture angle, γ, contours

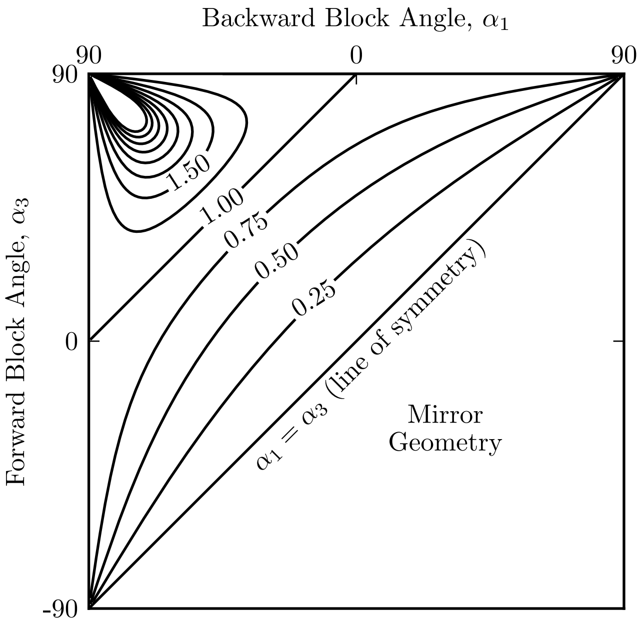

(b) Fracture spacing ratio, $\frac{S_2}{S_1}$, contours

Figure 3.9: Relationship between parallelogram parameter sets.

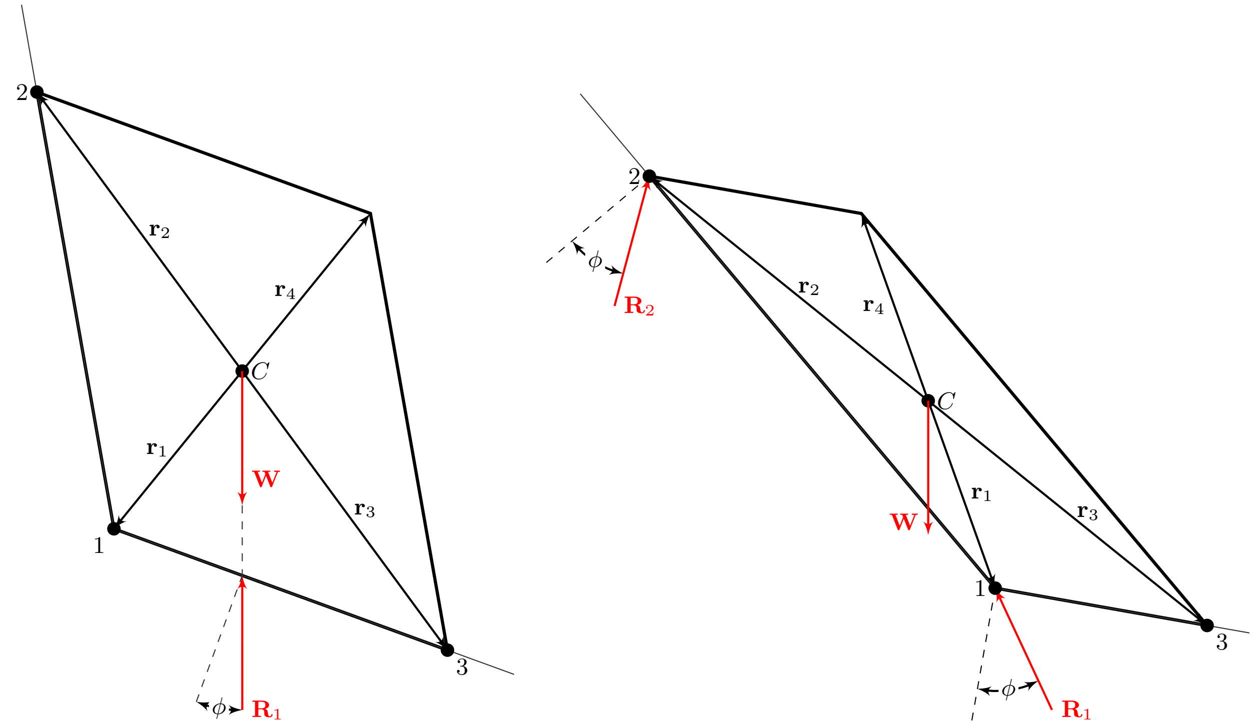

(a) Base supported block

(b) Base and back supported block

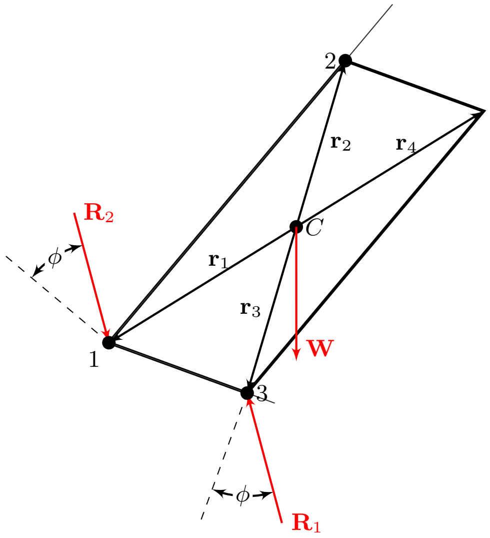

(c) Confined block

Figure 3.10: Static, limit equilibrium, free body diagrams for statically stable block configurations. Note that the scenario (not shown) where the weight vector is outside the toe of the block and the relative fracture angle (γ) is less than 90 degrees is statically unstable.

counter-clockwise torque about the block heel, thus a second reaction force ($\mathbf{R}_2$), is required in addition to $\mathbf{R}_1$ for static stability. Kieffer (1998) investigated this scenario with the assumption that this geometry leads to a slumping mode of failure. As Kieffer (1998) discussed, this system is statically indeterminate given that there are four unknowns (the orientation and magnitude of each reaction force) and only three available equations of motion. Kieffer (1998) introduced a fourth equation, a fictitious support force of zero magnitude applied to the block to produce a statically determinate problem. An iterative calculation was used to determine the mobilized friction angle using the force and moment equilibrium equations. The mobilized friction angle was compared to the ultimate friction angle and a factor of safety against failure was calculated factor of safety, FS= $\phi_{mobilized}/\phi_{ultimate}$.

The third state considered (Figure 3.10c) is the scenario where the back fracture plane forms an acute angle with the base fracture plane from the perspective of the block (i.e. $\gamma > 90$). For the scenario where $\mathbf{W}$ lies within the base of the block, the free body diagram in Figure 3.10a is sufficient. However, when $\mathbf{W}$ is oriented downhill of $\mathbf{r}_3$ (right in the figure), it creates a clock-wise torque about the block toe, thus the block requires support from the back fracture plane to remain stable. Unlike the scenario shown in Figure 3.10b, the reaction forces applied to the block in Figure 3.10c are located at contacts 1 and 3. The reaction force ($\mathbf{R}_2$) on the back fracture plane acts to resist the heel of the block from sliding upward. The reaction force ($\mathbf{R}_1$) on the base plane acts to resist the base of the block from sliding out. Absent of the back plane, a block in this scenario is statically unstable and would topple (or topple & slide) as discussed in Sagaseta (1986). Although this statically unstable scenario was initially evaluated for base friction models (Bray and Goodman, 1981) and is interesting from a dynamics standpoint, it is not likely to be encountered in nature as they will have already failed.

3.3.2 Pseudo-Static Limit Equilibrium and Failure Modes

In this section, the scenario where the discrete block is acted on by seismic forces will be considered. During seismic loading, the ground is assumed to undergo translational displacement in the horizontal and vertical directions. If the ground is assumed rigid, the base and back fractures adopt these same displacements. In addition, assuming that the frictional contacts made between the discrete rock block and two planes and the block itself are also rigid, the block has the same displacements as the supporting fractures.

Applying D'Alembert's principal (Chopra, 2000), the seismic force can be analyzed as an inertial force, $\mathbf{F}_I$, acting at the block's center of mass. This inertial force is equal to the mass of the block multiplied by the magnitude of the ground acceleration, but acts in the opposite direction (i.e. $\mathbf{F}_I = -m\ddot{\mathbf{u}}_g$). The inertial force can then be evaluated along with the other external forces considered in the static equilibrium section in the traditional manner of force and moment equilibrium. This form of analysis is commonly referred to as a pseudo-static analysis. Since earthquake ground motions are commonly expressed in terms of horizontal and vertical accelerations, $\mathbf{F}_I$ is decomposed into horizontal $\left(-\frac{\ddot{u}_{hg}}{g}mg = -k_h mg\right)$ and vertical inertial forces $\left(-\frac{\ddot{u}_{vg}}{g}mg = -k_v mg\right)$, where mg is the weight of the block. For simplicity, these inertial forces will be added to the components of the weight vector to form a new resultant vector ($\mathbf{R}_I = mg\left[k_h \hat{\mathbf{g}}_\perp, (1+k_v)\,\hat{\mathbf{g}}\right]$).

When the block is in force and moment equilibrium and on the verge of motion relative to the base and back fracture planes, then the block is considered at the limit of equilibrium. For the block to be on the verge of motion, then the shear forces acting on the fracture planes must also be at their limit. If a Coulomb sliding law is assumed to describe this limit, then the shear forces along the fractures are $\tau_i = N_i \tan(\phi_i)$. This means that at limit equilibrium, the reaction forces act at an angle of ϕ from a line perpendicular to the plane on which they act. Note that in assuming limit equilibrium, the block acceleration relative to the fracture planes is zero and thus the inertial forces ($\mathbf{F}_I = -m\ddot{\mathbf{u}}_g$) still holds.

Combining pseudo-static forces with the concept of limit equilibrium for blocks formed by two fracture sets of varying orientation, seismic failure modes and the minimum ground motion accelerations that initiate block motion can be determined. Very recently, the Sagaseta (1986) charts were updated to include seismic inertial forces by Yagoda-Biran and Hatzor (2013) where the seismic force is converted to an equivalent base fracture angle. This equivalent angle can be added to the base fracture angle to form a new parameter that replaces the base angle parameter used on the x-axis of the failure chart (Figure 3.3). While this is dynamic motion, it should not be confused with initiation of motion under seismic forces. Since these charts assume rectangular blocks, they have limited applicability to the wider range of geometries observed in nature and preclude the evaluation of some failure modes. To overcome these limitations the free body diagrams of non-orthogonal discrete blocks discussed in the previous section will now be revisited.

Toppling

The first set of free body diagram examines the scenarios where the orientation of $\mathbf{R}_I$ is downhill of, but not equal to $\mathbf{r}_3$. These scenarios can occur for both base supported and base and back supported blocks as shown in Figure 3.11. In order for $\mathbf{R}_I$ to achieve this orientation, the friction limit along the base fracture plane must not have been reached and the block has not slid. With $\mathbf{R}_I$ outside of $\mathbf{r}_3$, the reaction force $\mathbf{R}_3$ acts at the block toe. Sum of moments about the block toe indicates that there is a net clock-wise torque meaning the block's initial motion will be to rotate about the block toe. The trajectory of the block's center of mass follows a circle centered at contact 3 with a radius equal to the length of $\mathbf{r}_3$ as shown in Figure 3.11. This motion can lead to the toppling mode of failure depending on the ground motion magnitude, frequency content, and duration, which will be discussed in subsequent chapters. The toppling mode of failure occurs when the block overturns and does not return to its original static position.

Confined Toppling

The blocks drawn in Figure 3.11 depict blocks formed by fractures with $\gamma <= 90$. As discussed previously, when $\gamma > 90$ the blocks are in a confined scenario where reaction forces act at the heel (contact 1) and toe (contact 3) of the block as shown in Figure 3.12. Like the toppling case described above, the torque created by $\mathbf{R}_I$ creates a tendency for the block to want to rotate about contact 3. However, with the resistance provided at the heel of the

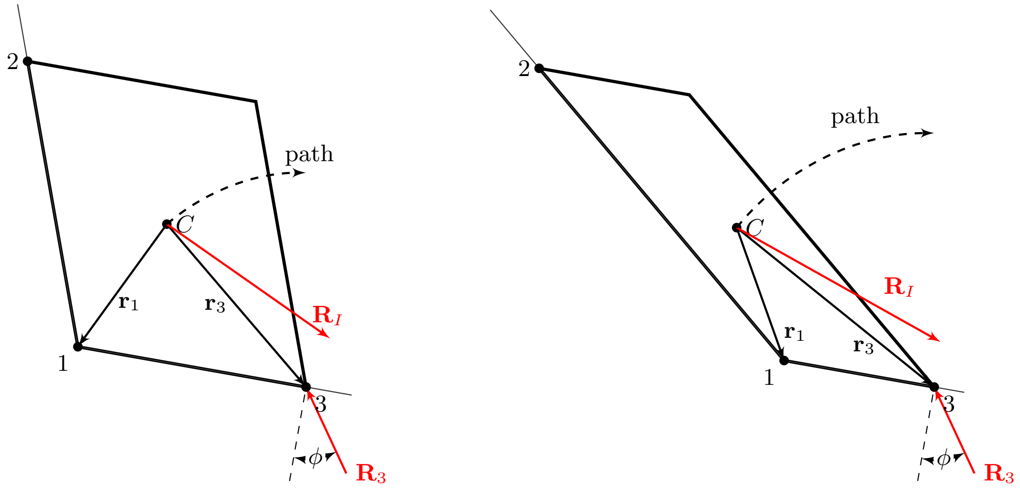

(a) Base supported block (b) Base and back supported block

Figure 3.11: Pseudo-static toppling failure mode and failure path.

block rotation is resisted. When the block is in limit equilibrium, contact 1 will begin to slide up the back fracture plane while contact 3 slides out along the base fracture plane. In order for the block contacts 1 and 3 to slide along the fracture planes as described, the block must also rotate clockwise hence the term confined toppling (see Figure 3.12). Once the block has displaced sufficiently such that the heel can no longer make physical contact with the back fracture, the block will transition into a toppling mode of failure. This loss of contact occurs when the base of the block is perpendicular to the back fracture plane and the path of contact 1 is tangent to the back fracture plane. From trigonometry, this scenario is determined to occur after the block has rotated an angle of $90 - \gamma$.

Sliding

The next set of free body diagrams consider the scenarios where the orientation of $\mathbf{R}_I$ is between $\mathbf{r}_1$ and $\mathbf{r}_3$. As before, these scenarios can occur for both base supported and base and back supported blocks as shown in Figure 3.13. In these scenarios, the friction limit

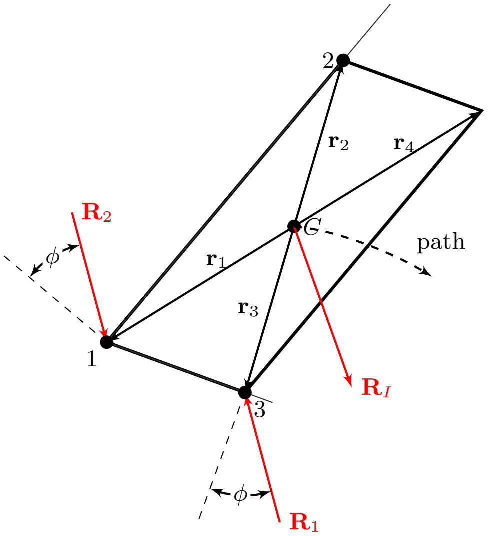

Figure 3.12: Pseudo-static confined toppling failure mode and failure path.

of the base joint has been reached before $\mathbf{R}_I$ exceeded the orientation of $\mathbf{r}_3$ thus averting toppling. The reaction force $\mathbf{R}_1$ acts equal and opposite of $\mathbf{R}_I$. The point at which $\mathbf{R}_1$ acts can be determined by projecting $\mathbf{R}_I$ on to the base plane. Since the friction limit has been reached, $\mathbf{R}_1$ is also oriented at an angle of ϕ relative to the inward normal of the base plane. Since $\mathbf{R}_1$ and $\mathbf{R}_I$ are equal and opposite, $\mathbf{R}_I$ is oriented at the same angle ϕ from the outward normal of the base fracture plane. Or, relative to $\mathbf{W}$, $\mathbf{R}_I$ is rotated at an angle of $\phi - \alpha$ counter-clockwise. While sum of the moments and forces are zero, the amount of shear force on the base fracture plane that can be transmitted to the block by friction is limited to the normal force multiplied by $\tan\phi$. When this frictional force is divided by the mass of the block, the resulting acceleration is constant. This implies that that the acceleration of the block will no longer match that of the joint's acceleration. Relative to the base joint's frame of reference, the block will begin to translate down the base plane as shown in Figure 3.13. This mode of failure is termed sliding. Note, that when the orientation of $\mathbf{R}_I$ is equal to $\mathbf{r}_3$, that the sum of moments are still zero therefore the block will still only slide.

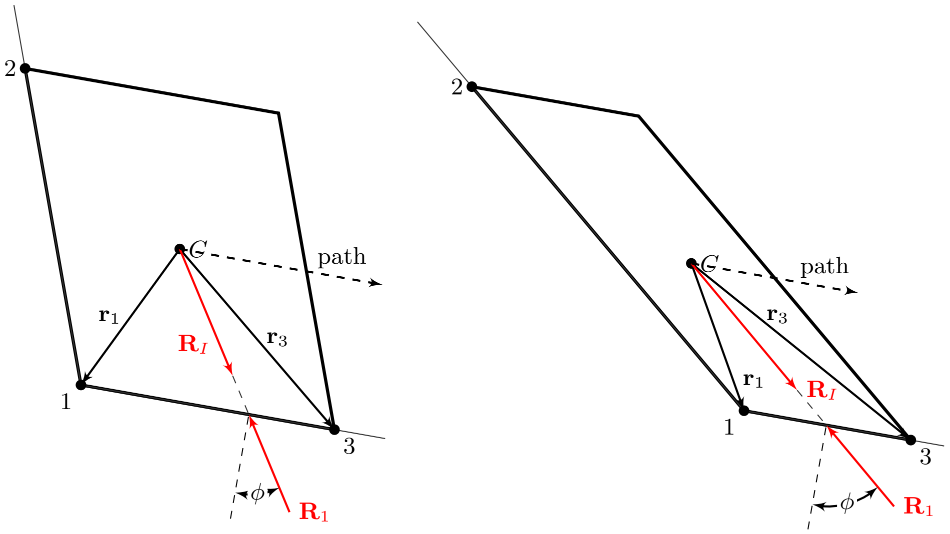

(a) Base supported block (b) Base and back supported block

Figure 3.13: Pseudo-static sliding failure mode and failure path.

Slumping

The final free body diagram considers the scenario where the orientation of $\mathbf{R}_I$ is uphill of $\mathbf{r}_3$. This scenario can only occur when static back-support is provided to the block by the back fracture plane as shown in Figure 3.14. Since back support is required, $\mathbf{R}_2$ must always be positive and non-zero. Considering the block is at limit equilibrium, the friction limit has been reached, thus $\mathbf{R}_1$ and $\mathbf{R}_2$ are oriented at an angle ϕ relative to the inward normal of the respective planes on which they act. Similar to the sliding case, the sum of moments and forces are equal to zero, but since the shear forces are limited by friction, the acceleration of the block will not match the fracture planes' acceleration thus block motion is initiated. The block maintains contact with the base fracture plane at contact 1 and since the block requires back-support it maintains contact with the back plane at contact 2. These two contacts constitute a kinematic constraint and thus constrain the block to have only 1 degree of freedom. With these constraints the block must also rotate counter-clockwise causing motion in the curved path shown in Figure 3.14 (i.e. slumping). The constraints

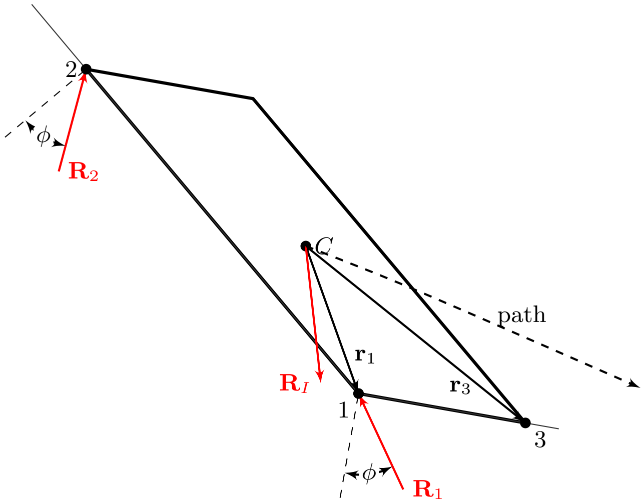

Figure 3.14: Pseudo-static slumping failure mode and failure path.

also allow for the translational degrees of freedom to be related to rotation, thus effectively reducing the total degrees of freedom in the system to one.

Pseudo-Static Limit Equilibrium Limitations

The following limitations apply to the pseudo-static limit equilibrium evaluations above:

- In comparison to an analysis that considers changing ground acceleration (time history analysis), the pseudo-static limit equilibrium analysis represents the mode of movement at the onset of block motion relative to the fracture planes. Describing the changes in block motion throughout a time history analysis is not provided here.

- The vertical acceleration is assumed to not overcome gravity, thus $1 + k_v$ is assumed to be greater than zero meaning that the block stays in contact with at least the base fracture plane and does not eject or jump from the slope.

- These analyses do not provide any indication of displacement or degree of consequences for slope failure, however these subjects will be discussed in subsequent chapters.

3.3.3 Pseudo-Static Failure Mode Transitions

In the previous sections, the combinations of possible inertial force orientations relative to the position vectors were described and shown to indicate the possible pseudo-static modes of failure. There are two transition points that correspond to the scenarios when $\mathbf{R}_I$ is oriented in the same direction as $\mathbf{r}_1$ or $\mathbf{r}_3$. The orientation of $\mathbf{R}_I$ relative to the base plane in these cases is α_1 and α_3, respectively. Since the sliding mode forms the boundary for each transition point, the free body diagram for this mode can be used to evaluate each transition point. As determined before, for sliding, $\mathbf{R}_1$ acts at the angle of ϕ relative to the inward normal of the base plane and since $\mathbf{R}_I$ is equal and opposite it acts at the same angle ϕ relative to the outward normal of the base plane. Therefore, at the transition points, where $\mathbf{R}_I$ has the same orientation as $\mathbf{r}_1$ or $\mathbf{r}_3$, $\alpha_1 = \phi$ or $\alpha_3 = \phi$, respectively. These transitions form the boundaries of slumping to sliding and sliding to toppling. In addition to these transition points, is the scenario where the block undergoes confined toppling. As mentioned before, this scenario arises when the back fracture plane overhangs the block (i.e. $\gamma > 90$) or when $\alpha_1 < -\alpha_3 < \phi$.

With these transition relationships, Figure 3.15a is presented which allows the pseudo-static failure modes to be determined given a known block geometry and joint friction. For comparison purposes, if the back fracture is not present, the chart would reduce to that shown in Figure 3.15b where the slumping and confined toppling are no longer applicable. Note that a line $\alpha_1 = -\alpha_3$ in both charts corresponds to rectangular blocks and is equivalent to the limit equilibrium modes predicted from Figure 3.1 where $\delta = \alpha_3 = -\alpha_1$. The dynamic portions of the Hoek and Bray (1977) family of charts is orthogonal to these new charts and thus not visible.

There are several key observations of this analysis:

- The chart is generic for any block shape since the only geometric information used to determine these failure modes were the position vectors.

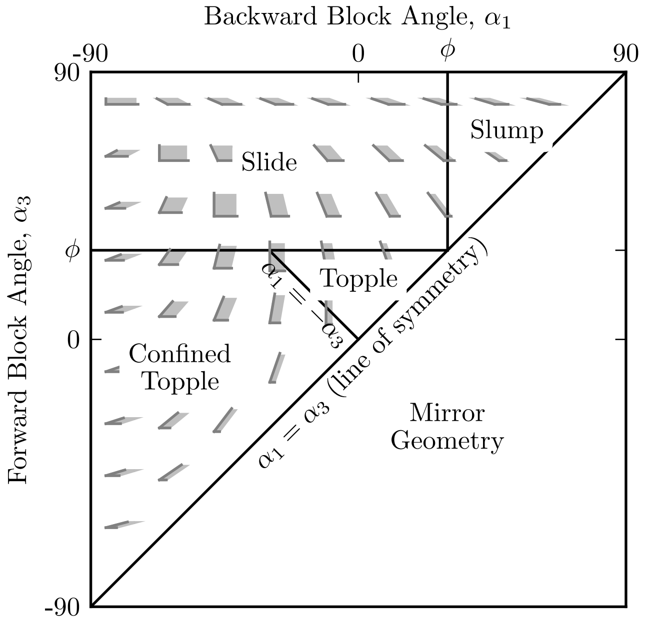

(a) Blocks influenced by both base and back fractures

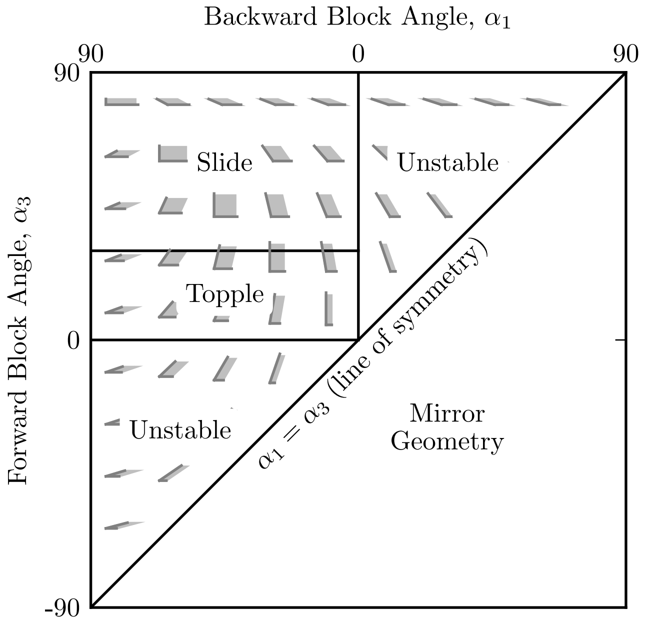

(b) Blocks only supported on the base fracture

Figure 3.15: Pseudo-static limit equilibrium failure modes.

- It is clear from this comparison that rectangular block mode charts are very limited in the geometries they represent and failure modes they predict.

- Since the angle of the base fracture was not used to determine these transition points, the angle of the base fracture does not determine the pseudo-static mode of failure.

- The slumping failure mode for statically loaded blocks is only applicable for seismic loading when the friction angle is greater than α_1 otherwise the block will slide or topple.

3.4 Pseudo-Static Yield Accelerations

For each failure mode identified in Section 3.3.2 and determined from Figure 3.15, a minimum inertial acceleration can be determined which sets the block into motion. This acceleration has been determined by previous researchers for sliding (Seed and Goodman, 1964; Newmark, 1965; Goodman and Seed, 1966) and toppling modes (Sagaseta, 1986; Yagoda-Biran and Hatzor, 2013, among others). For the sake of review and completeness, the derivations of these minimum inertial acceleration equations are presented below. In addition, the minimum inertial acceleration required for slumping and confined toppling motion to initiate is derived for the first time. Lastly, for clarity, the minimum inertial acceleration to initiate the four modes of failure will be given a unique name.

3.4.1 Toppling

The minimum horizontal inertial acceleration required for a block to lift off its base and rotate about its toe has been described by Sagaseta and Yagoda-Biran and Hatzor, among others. This acceleration will be referred to as the static rocking acceleration, k_r. When $\mathbf{R}_I$ is within the base of the block, rotation about the block toe is resisted by the weight of the block. As k_h increases, the line of action of the reaction force, $\mathbf{R}_1$, acting on the base fracture plane and $\mathbf{R}_I$ approach the scenario where they pass through contact 3. Ultimately, the reaction force from the base fracture plane will act at contact 3 while $\mathbf{R}_I$ continues to move beyond (to the right of) contact 3, at which point, rotational motion of the block is initiated. The value of k_h that aligns $\mathbf{R}_I$ with $\mathbf{r}_3$ can be determined by geometry.

$$k_r = k_h = (1 + k_v)\tan(\alpha_3 - \alpha) \tag{3.16}$$

For k_h to reach this value, there needs to be sufficient frictional resistance between the base fracture plane and the block such that sliding does not occur at lower values of k_h.

3.4.2 Sliding

The minimum horizontal inertial acceleration required for a block to begin sliding was brought to mainstream popularity in the civil engineering community by Newmark (1965), Goodman and Seed (1966), and Seed and Goodman (1964). For sliding systems, this acceleration is commonly referred to as the sliding yield acceleration, k_y.

In Newmark (1965), a block sliding on a horizontal plane was evaluated. For this level ground scenario, the normal force N is equal and opposite of $\mathbf{W}$. The maximum sliding resistance available to the block based on a Coulomb sliding law is $\tau = N\tan(\phi) = mg\tan(\phi)$. The horizontal inertial force is counteracted solely by the sliding resistance acting on the block. Therefore, when the block is at a limit equilibrium state, $k_h = \tan(\phi)$. Because the frictional force is at a maximum and no more force can be transferred to the block, the block's inertial force and yield acceleration will remain constant. Generally this is explained in terms of FS in which the yield acceleration is defined as the value of horizontal inertial acceleration which results in a FS$= 1$. As the value of k_h exceeds k_y, the block and fracture planes will have different accelerations resulting in relative movement along the base fracture.

Seed and Goodman (1964) went a step further and evaluated a block acting on an inclined plane. From their work, the equation for the yield acceleration is

$$k_y = k_h = (1 + k_v)\tan(\phi - \alpha). \tag{3.17}$$

3.4.3 Slumping

This section presents the determination of the minimum horizontal acceleration to initiate motion for the slumping case shown in Figure 3.14. Since each reaction force ($\mathbf{R}_1$ and $\mathbf{R}_2$) is comprised of two unknowns, magnitude and orientation, there are a total of four unknowns and thus the system appears to be statically indeterminate. However, as the horizontal acceleration increases so does the angle of the reaction forces relative to the normal vector of each fracture plane. When the block is in a limit equilibrium state, the maximum shear component of each reaction has been reached. For purely frictional behavior this means that the orientation of the reaction force is also limited and forms an angle of ϕ relative to the normal vector of each plane. This assumption reduces the number of unknowns contributed from the reaction forces to two, making the system statically determinate.

The factor of safety approach described in the sliding section is used to solve for the k_h that would result in a FS$=1$. The approach used by Kieffer (1998) to determine the factor of safety of slumping blocks appears similar but is not. In Kieffer's analysis the mobilized friction angle is solved for assuming a fictitious support force and iterating (by changing the friction angle) until that support force is zero. The factor of safety is then calculated as the ratio of the tangents of the peak friction angle to the mobilized friction angle. Iteration is required because Kieffer's equations were transcendental. If Kieffer's method is used for seismic loading, the fictitious force is the inertial force. However, since it is of interest to determine the critical inertial force to induce motion instead of a factor of safety, an iterative method is not necessary. Since the block is in limit equilibrium, the orientation of the reaction forces is fixed. For Coulomb sliding, this orientation is the friction angle. Therefore, all that is required is to consider k_h as a third unknown and use sum of forces and moments to form three equations that can be solved simultaneously.

The three equilibrium equations are shown below, noting that the sum of vector forces contributes two equations.

$$\mathbf{R}_1 + \mathbf{R}_2 + \mathbf{W} + k_h m g \hat{\mathbf{g}}_\perp + k_v m g \hat{\mathbf{g}} = \mathbf{0} \text{ (Sum of forces)} \tag{3.18}$$

$$\hat{\mathbf{z}} \cdot (\mathbf{r}_1 \times \mathbf{R}_1) + \hat{\mathbf{z}} \cdot (\mathbf{r}_2 \times \mathbf{R}_2) = 0 \text{ (Sum of moments about C)} \tag{3.19}$$

Equations 3.18 and 3.19 can be expanded to expose the scalar unknowns R_1, R_2, and k_h:

$$R_1 \hat{\mathbf{R}}_1 + R_2 \hat{\mathbf{R}}_2 + (1 + k_v) m g \hat{\mathbf{g}} + k_h m g \hat{\mathbf{g}}_\perp = \mathbf{0} \tag{3.20}$$

$$R_1 \hat{\mathbf{z}} \cdot (\mathbf{r}_1 \times \hat{\mathbf{R}}_1) + R_2 \hat{\mathbf{z}} \cdot (\mathbf{r}_2 \times \hat{\mathbf{R}}_2) = 0. \tag{3.21}$$

The vector equation, 3.20, can be expanded into the two scalar equations below:

$$R_1 (\hat{\mathbf{R}}_1 \cdot \hat{\mathbf{g}}_\perp) + R_2 (\hat{\mathbf{R}}_2 \cdot \hat{\mathbf{g}}_\perp) + k_h m g = 0 \tag{3.22}$$

$$R_1 (\hat{\mathbf{R}}_1 \cdot \hat{\mathbf{g}}) + R_2 (\hat{\mathbf{R}}_2 \cdot \hat{\mathbf{g}}) + (1 + k_v) m g = 0 \tag{3.23}$$

Solving Equations 3.21, 3.22, and 3.23 simultaneously results in the minimum horizontal inertial acceleration required to initiate block slumping termed the slumping yield acceleration, k_s:

$$k_s = (1 + k_v) \frac{(\hat{\mathbf{R}}_1 \cdot \hat{\mathbf{x}})(\hat{\mathbf{z}} \cdot (\mathbf{r}_2 \times \hat{\mathbf{R}}_2)) - (\hat{\mathbf{R}}_2 \cdot \hat{\mathbf{x}})(\hat{\mathbf{z}} \cdot (\mathbf{r}_1 \times \hat{\mathbf{R}}_1))}{(\hat{\mathbf{R}}_2 \cdot \hat{\mathbf{y}})(\hat{\mathbf{z}} \cdot (\mathbf{r}_1 \times \hat{\mathbf{R}}_1)) - (\hat{\mathbf{R}}_1 \cdot \hat{\mathbf{y}})(\hat{\mathbf{z}} \cdot (\mathbf{r}_2 \times \hat{\mathbf{R}}_2))}. \tag{3.24}$$

Simplifying the equation further by factoring out r_1 and r_2 and multiplying by $(1/r_1)/(1/r_1)$,

$$k_s = (1 + k_v) \frac{\frac{r_2}{r_1}(\hat{\mathbf{R}}_1 \cdot \hat{\mathbf{x}})(\hat{\mathbf{z}} \cdot (\hat{\mathbf{r}}_2 \times \hat{\mathbf{R}}_2)) - (\hat{\mathbf{R}}_2 \cdot \hat{\mathbf{x}})(\hat{\mathbf{z}} \cdot (\hat{\mathbf{r}}_1 \times \hat{\mathbf{R}}_1))}{(\hat{\mathbf{R}}_2 \cdot \hat{\mathbf{y}})(\hat{\mathbf{z}} \cdot (\hat{\mathbf{r}}_1 \times \hat{\mathbf{R}}_1)) - \frac{r_2}{r_1}(\hat{\mathbf{R}}_1 \cdot \hat{\mathbf{y}})(\hat{\mathbf{z}} \cdot (\hat{\mathbf{r}}_2 \times \hat{\mathbf{R}}_2))}. \tag{3.25}$$

The position vectors and magnitudes represent the block geometry while the reaction forces represent limiting resistance (e.g. ultimate friction angle) on the two fracture planes. Furthermore, from the normalization by r_1, it can be seen that the scale of the block does not influence the slumping yield acceleration. In the end, only the block's shape and resistance along the contacts controls the yield acceleration.

3.4.4 Confined Toppling

This section presents the determination of the minimum horizontal acceleration to initiate motion for the toppling case shown in Figure 3.12. As was the case with slumping, each reaction force is comprised of two unknowns, magnitude and orientation, thus there are a total of four unknowns, meaning the system is statically indeterminate. As k_h increases so does the angle of the reaction forces relative to the normal vector of each plane. When the block is in a limit equilibrium state, the maximum shear component of each reaction has been reached. For purely frictional behavior this means that the orientation of the reaction force is also limited and forms an angle of ϕ relative to the normal vector of each plane. As with slumping, this assumption reduces the number of unknowns contributed from the reaction forces to two. The only difference between this case of confined toppling and the case of slumping is that the location of the reaction forces is different. The base reaction force ($\mathbf{R}_1$) is now located at the toe of the block and the back reaction force ($\mathbf{R}_2$) is located at the heel of the block.

The yield acceleration for confined toppling can be solved in the same manner as for slumping. The sum of forces and moment equations are shown below, noting that the sum of vector forces contributes two equations.

$$\mathbf{R}_1 + \mathbf{R}_2 + \mathbf{W} + k_h mg\hat{\mathbf{g}}_\perp + k_v mg\hat{\mathbf{g}} = \mathbf{0} \text{ (Sum of forces)} \tag{3.26}$$

$$\hat{\mathbf{z}} \cdot (\mathbf{r}_1 \times \mathbf{R}_2) + \hat{\mathbf{z}} \cdot (\mathbf{r}_3 \times \mathbf{R}_1) = 0 \text{ (Sum of moments about C)} \tag{3.27}$$

Notice that the only differences between equations (3.27) and (3.19) are the cross products. Since the procedure to solve for the critical k_h is the same as for slumping, $\mathbf{r}_1 \times \mathbf{R}_2$ and $\mathbf{r}_3 \times \mathbf{R}_1$ is substituted for $\mathbf{r}_1 \times \mathbf{R}_1$ and $\mathbf{r}_2 \times \mathbf{R}_2$ in Equation (3.25) and thus the full derivation is not presented. This substitution results in the minimum k_h required to initialize the confined toppling failure mode termed the constrained toppling yield acceleration, k_{ct}:

$$k_{ct} = (1 + k_v)\frac{(\hat{\mathbf{R}}_1 \cdot \hat{\mathbf{x}})(\hat{\mathbf{z}} \cdot (\mathbf{r}_3 \times \mathbf{R}_1)) - (\hat{\mathbf{R}}_2 \cdot \hat{\mathbf{x}})(\hat{\mathbf{z}} \cdot (\mathbf{r}_1 \times \mathbf{R}_2))}{(\hat{\mathbf{R}}_2 \cdot \hat{\mathbf{y}})(\hat{\mathbf{z}} \cdot (\mathbf{r}_1 \times \mathbf{R}_2)) - (\hat{\mathbf{R}}_1 \cdot \hat{\mathbf{y}})(\hat{\mathbf{z}} \cdot (\mathbf{r}_3 \times \mathbf{R}_1))}. \tag{3.28}$$

Simplifying further as before,

$$k_{ct} = (1+k_v)\frac{\frac{r_3}{r_1}(\hat{\mathbf{R}}_1\cdot\hat{\mathbf{x}})(\hat{\mathbf{z}}\cdot(\hat{\mathbf{r}}_3\times\mathbf{R}_1)) - (\hat{\mathbf{R}}_2\cdot\hat{\mathbf{x}})(\hat{\mathbf{z}}\cdot(\hat{\mathbf{r}}_1\times\mathbf{R}_2))}{(\hat{\mathbf{R}}_2\cdot\hat{\mathbf{y}})(\hat{\mathbf{z}}\cdot(\hat{\mathbf{r}}_1\times\mathbf{R}_2)) - \frac{r_3}{r_1}(\hat{\mathbf{R}}_1\cdot\hat{\mathbf{y}})(\hat{\mathbf{z}}\cdot(\hat{\mathbf{r}}_3\times\mathbf{R}_1))}. \tag{3.29}$$

3.4.5 Interpretation of Yield Equations

Initial Yield Acceleration

Unlike the determination of pseudo-static failure modes, the magnitude of the horizontal yield acceleration for each failure mode is dependent on the inclination of the base fracture plane. As Yagoda-Biran and Hatzor (2013) explains, the slope can be thought of as an inertial force itself. A series of contour plots of the pseudo-static yield equations, (3.16), (3.17), (3.25), and (3.29) relative to α_1 & α_3, for friction angles ranging from 30 to 60 degrees are shown in Figures 3.16 through 3.19. A few trends are noted:

- Equation (3.16) shows a near linear relationship relative to α_3, because the tangent function for small angles can be approximated by the angle itself. This apparent linear relationship is especially visible with the increase in base angle. As the base angle approaches α_3, $\alpha_3 - \beta$ becomes small.

- Equation (3.17) is the most familiar in earthquake engineering which indicates for any geometric scenario where sliding controls and when the fracture friction angle and orientation are fixed, the sliding yield acceleration is constant.

- Equation (3.25) is equal to the sliding yield acceleration near the transition boundary ($\alpha_1 = \phi$) and decreases away from the transition boundary. This equation is non-linear, demonstrating a minimum near the middle of the $\alpha_1 = \alpha_3$ boundary. This implies that for a slumping block and given friction angle, there is an unique relative angle and spacing between the base and back fracture planes where the slumping yield acceleration is at its minimum.

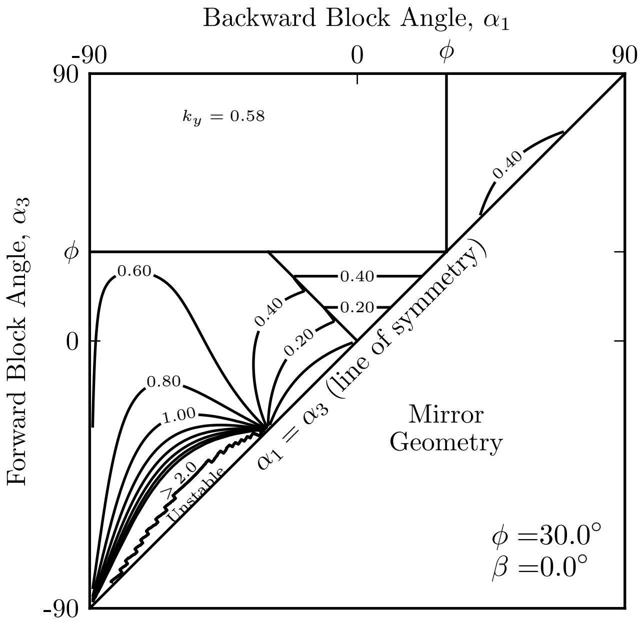

(a) Base fracture angle = 0°

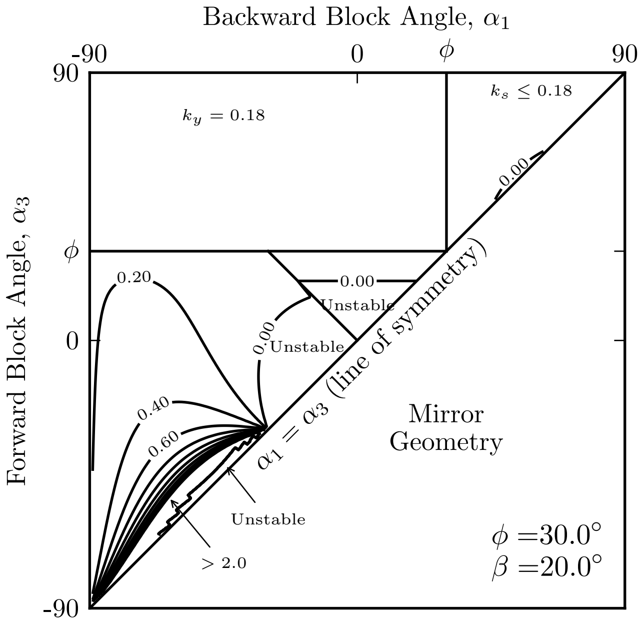

(b) Base fracture angle = 20°

Figure 3.16: Yield accelerations for $\phi = 30°$.

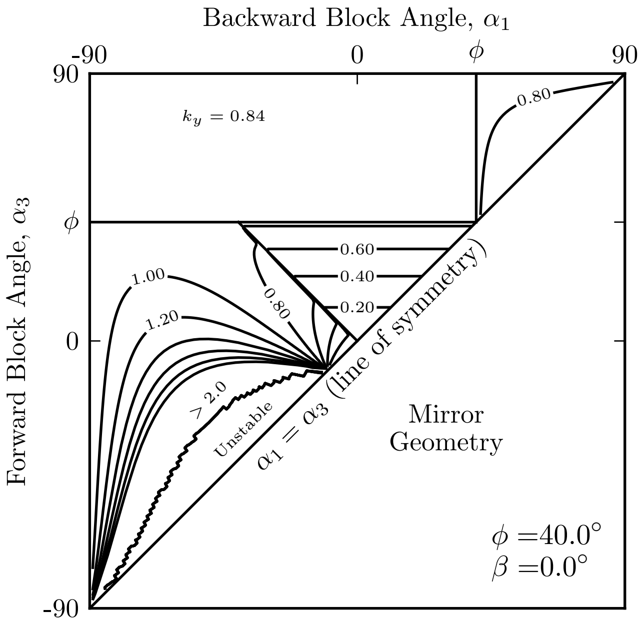

(a) Base fracture angle = 0°

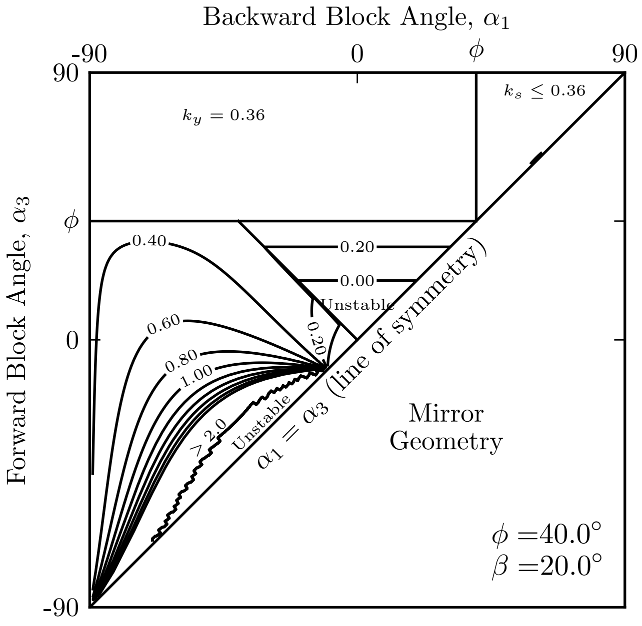

(b) Base fracture angle = 20°

Figure 3.17: Yield accelerations for $\phi = 40°$.

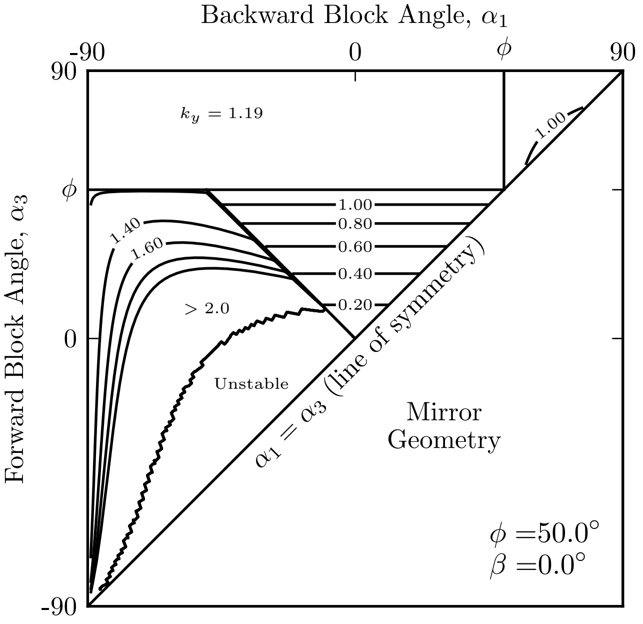

(a) Base fracture angle = 0°

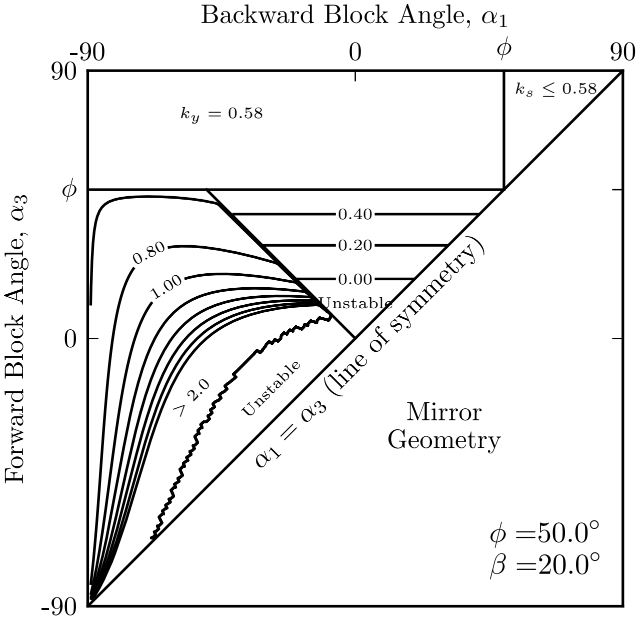

(b) Base fracture angle = 20°

Figure 3.18: Yield accelerations for $\phi = 50°$.

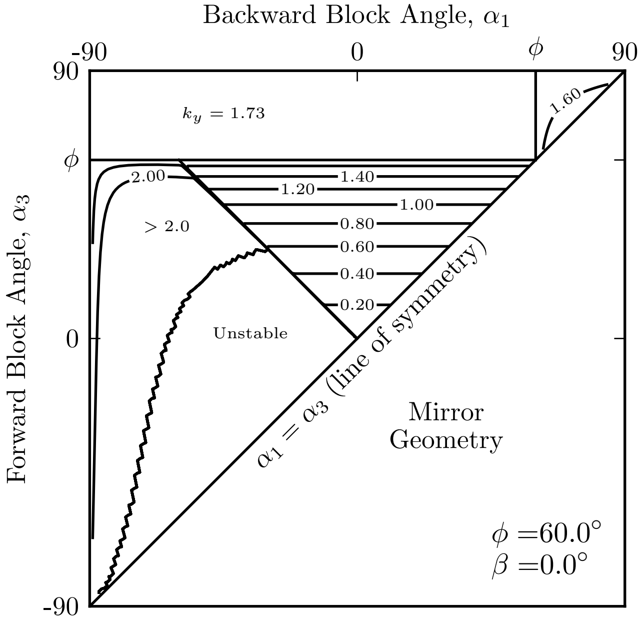

(a) Base fracture angle = 0°

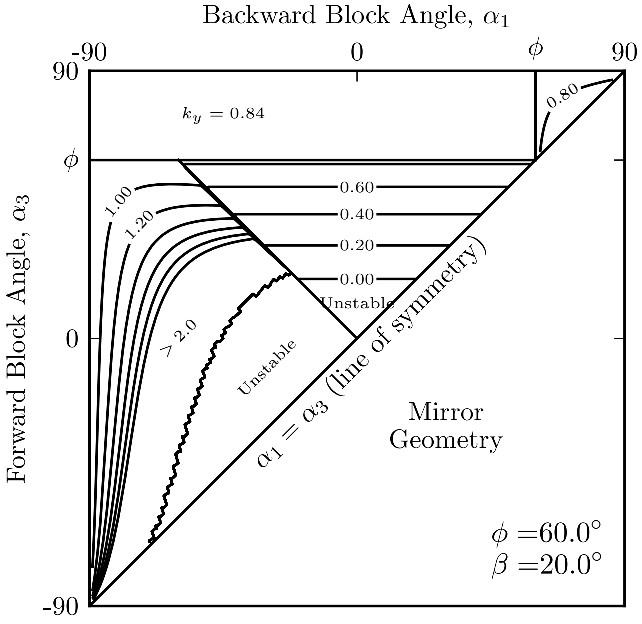

(b) Base fracture angle = 20°

Figure 3.19: Yield accelerations for $\phi = 60°$.

- This observation of a minimum can be rationalized by investigating the effects of changing α_1. As mentioned in Section 3.3.3, when $\alpha_1 < \phi$, the sliding mode controls. As α_1 approaches and exceeds ϕ, support from the back fracture plane is required for static stability. The increase in the normal force on the back fracture plane reduces the normal force on the base fracture plane and since shear resistance is based on this normal force, the same trend occurs. The orientation of the shear resistance on the base fracture plane is the most productive at resisting horizontal acceleration than that of the back fracture plane, therefore the transfer of shear resistance from the base to back fracture plane reduces the overall horizontal resistance of the system. However, as α_3 approaches 90°, the base fracture plane and back fracture plane approach the same angle. Ignoring the fact that the block's volume is also decreasing to zero, in the limit as α_3 approaches 90°, the reaction vectors on both planes approach the same orientation, which is the scenario for the sliding mode of failure, thus k_s approaches k_y.

- The lower yield acceleration of the slumping block keeps in step with that of a log-spiral failure surface (Chang et al., 1984) and multi-block models (Michalowski, 2007). The interesting connection between these previous results and those of the slumping block is that they are all systems undergoing back rotations. The previous discussion regarding the distribution of shear forces on steeper planes provides a clear indicator why these models behave similarly.

- Since the only controlling factor in determining the failure modes is the orientation of $\mathbf{R}_I$ relative to α_1 and α_3, this criterion is applicable to wide array of fracture conditions. This includes fractures with shear resistance described by other models (e.g. Barton-Bandis) or systems with water pressures. For example, if the shear resistance of a fracture set is determined to be some value τ, then ϕ in the equations $\alpha_1 = \phi$ & $\alpha_3 = \phi$ in Figure 3.15 is replaced with an equivalent friction angle $\phi_{eq} = \tau/N$. For a fracture set with shear resistance described by ϕ, C in the Coulomb sense, then,

$$\frac{\tau}{N} = \tan(\phi_{eq}) \tag{3.30}$$

$$\frac{\tau}{N} = \tan(\phi) + \frac{cL}{N}, \tag{3.31}$$

where L is the block base length and N is the normal force. Given the parallelogram shape, $N = \rho g L S_1$, therefore

$$\frac{\tau}{N} = \tan(\phi) + \frac{c}{\rho g S_1}. \tag{3.32}$$

Substituting for S_1,

$$\frac{\tau}{N} = \tan\phi + \frac{c}{2\rho g r_1 \cos(\alpha_1)} = \tan\phi_{eq}. \tag{3.33}$$

An equivalent friction angle is then

$$\phi_{eq} = \tan^{-1}\left(\tan\phi + \frac{c}{2\rho g r_1 \cos(\alpha_1)}\right). \tag{3.34}$$

It can be seen in equation (3.34) that α_1 or α_3 cannot be directly equal to the friction angle. In this case, the modes become a function of the scale of the block.

- For all failure modes, increasing the base angle reduces the magnitude (PGA) of the earthquake that induces motion.

- For the toppling, sliding, and slumping failure modes, as the base angle increases and exceeds the friction angle, the yield equations become negative (white in the figures) which means that the specific geometry is not statically stable. In the case of confined toppling, certain geometries remain statically stable even though the base angle exceeds the friction angle.

Yield Acceleration After Relative Block Movement

Motion of the block relative to the base and back fracture plane can cause changes in the geometries that existed at the point of limit equilibrium and therefore change the failure mode.

For the sliding mode, the block moves downhill of the back fracture plane, however since the resistance to block movement is provided solely by the base fracture plane, this change in geometry does not result in a change to the yield acceleration. This is the same result as for blocks traditionally analyzed by Newmark's method (Jibson, 1993). Reduced yield accelerations associated with block displacement have been considered by some researchers in certain scenarios such as liquefaction and post peak shear resistance but will not be discussed here.

For cases where the blocks require back-support under static conditions but fail in a sliding mode under seismic conditions ($0 < \alpha_1 < \phi < \alpha_3$), the mode of failure can switch from sliding to slumping. This occurs after the block slides and the ground motion reverses direction such that the inertia force is oriented up hill, the forces on the block cause it to rock backward. Since the block has translated away from the back fracture, the block must rotate past its original orientation in order to make contact with the back fracture plane. This additional orientation increases α_1 and α_3 at the same rate. With continued sliding displacement and increased back rotation, α_1 will exceed ϕ and the slumping mode will take over.

For the toppling mode, rotation of the block causes α_3 and α_1 to decrease and thus based on equation (3.16) the rocking acceleration also decreases. However, if the block does not topple, the rocking acceleration does not remain in a decreased state as the block ultimately returns to its initial geometry. Some scenarios can be imagined where the rocking acceleration would remain reduced without the block toppling. For instance, if debris fell between the block and the fracture planes as the block rotated forward, the block would be restricted from returning to its initial geometry and would remain in a rotated state.

When a single block undergoes slumping motion it rotates "backward" causing α_1 and α_3 to increase at the same rate. Since $\hat{\mathbf{r}}_1$ and $\hat{\mathbf{r}}_2$ are dependent on α_1 and α_3 (and tied to the rotation of the block), they change orientation. The relationship between the slumping acceleration and block rotation can be determined by evaluating equation (3.25) with the vectors $\hat{\mathbf{r}}_1$ and $\hat{\mathbf{r}}_2$ rotated at various angles, θ from their initial orientations. The rotation of the block is limited to γ as rotation beyond this point results in the block being oriented such that the plane originally in contact with the back fracture is now in contact with the base fracture plane. In this case, a re-evaluation of the block geometry indicates that the block will slide. An example of the relationship between rotation and slumping yield acceleration is shown in Figure 3.20a. Note that the magnitude of rotation that the block can rotate decreases as the friction angle increases. In addition, the change in yield acceleration decreases as the back fracture orientation approaches that of the base plane, which at its limit is the sliding block scenario.

Another scenario can be envisioned where multiple blocks stacked side-by-side, slump, as typically analyzed by Kieffer. If these blocks are slumping (i.e. rotating backward) at the same time, then the orientation of position vectors and back reaction force for the leading block is changing. An example of varying the orientation of $\hat{\mathbf{R}}_2$ as a percentage of θ is shown line in Figure 3.20b where the trailing block is assumed to rotate a fraction of the amount that the leading block rotates. Notice that the yield acceleration for the leading block in a multi-block system does not decrease as much as for a lone slumping block. Depending on the amount of rotation of the back fracture plane, the yield acceleration can actually begin to to increase, which is generally the case in most complex landslides.

A block with confined toppling motion rotates forward causing α_1 and α_3 to decrease, and for the same reasons as for slumping, the orientation of $\hat{\mathbf{r}}_1$ and $\hat{\mathbf{r}}_2$ also change. Applying equation (3.29) where $\hat{\mathbf{r}}_1$ and $\hat{\mathbf{r}}_2$ are rotated by various angles, θ from their initial orientations results in a decreasing yield acceleration as is shown in Figure 3.21. The block can rotate forward by a maximum amount of $\gamma - 90$ at which time the block has displaced sufficiently such that it loses contact with the back fracture and transitions to a pure toppling mode. At this point, a re-evaluation of failure mode indicates that since α_3 is already negative and there is no longer back support, the block changes to the toppling mode. The yield acceleration instantaneously becomes negative meaning the block is statically unstable. The block can continue to rotate to a total rotation of $180 - \gamma$ before the block contacts the base fracture plane on its outward side.

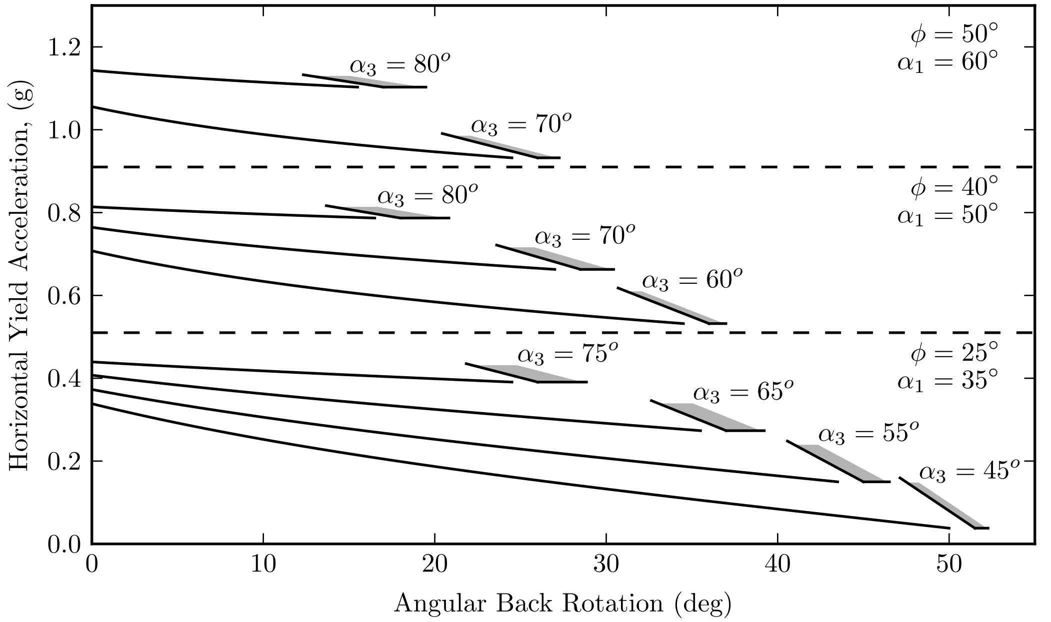

(a) Slumping yield acceleration (k_s) as function of back rotation for various shaped blocks and fracture friction angles.

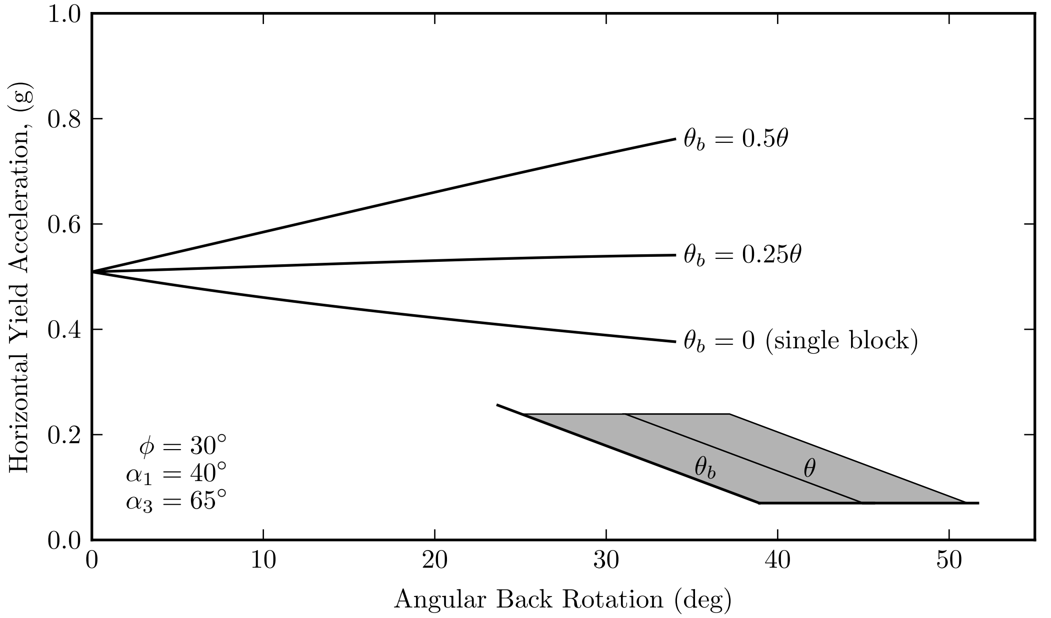

(b) Slumping yield acceleration (k_s) as function of back rotation for leading block in a multi-block system. The movement of the block behind the leading block causes the yield acceleration of the leading block to increase.

Figure 3.20: Slumping yield acceleration (k_s) as function of back rotation for single and multiple slumping blocks.

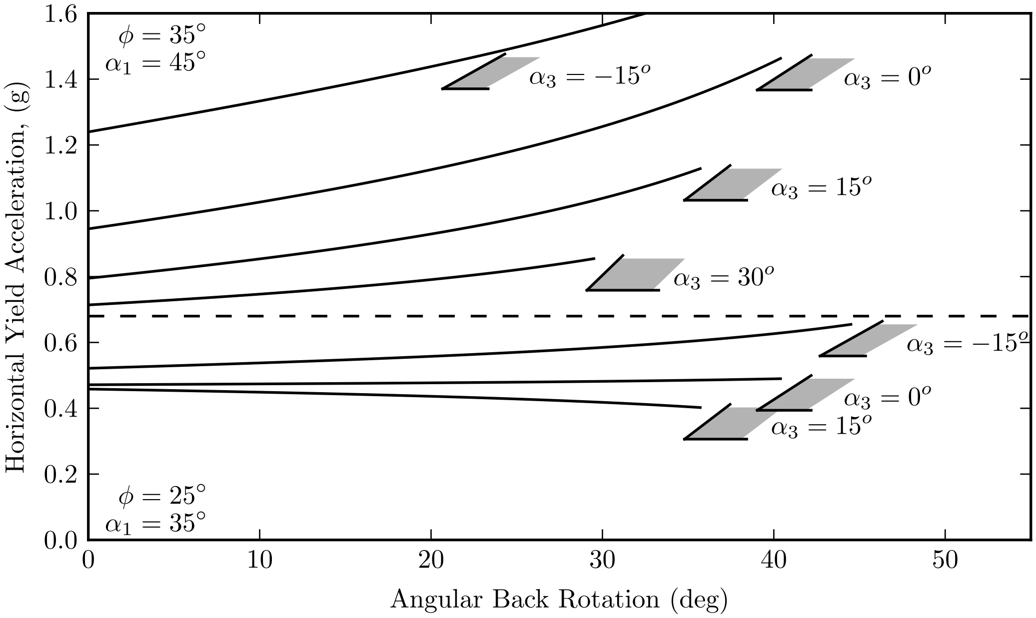

Figure 3.21: Confined toppling yield acceleration (k_{ct}) as function of forward rotation

3.5 Experimental and Numerical Verification

Verification of the failure mode relationships and yield acceleration equations is performed through the use of centrifuge experiments and numerical analysis.

3.5.1 Verification by Centrifuge Experiments

Centrifuge experiments were conducted by Applegate and Wartman (2011, 2012, 2013) in which discrete gypsum blocks of differing geometries were subject to sinusoidal and earthquake like horizontal accelerations. Experiments that tested single blocks were selected and evaluated relative to the analytical failure mode and yield acceleration relationships. The friction angle of the fractures was estimated based on blocks that were designed specifically to slide. In test 11, a sliding block, set on a base fracture plane set to 20 degrees, began sliding at approximately 0.48g's. Applying equation (3.17), the friction angle is back-calculated to be approximately 45.6 degrees. Additional characterization of the blocks are documented in a experimental study by Smith et al. (2013). Although the Smith study found lower friction angles for the blocks, the friction angles measured in the centrifuge was deemed to be more representative of the centrifuge experiments since they were directly measured. The blocks were assumed to behave rigidly for purposes of the evaluations performed in this section.

Centrifuge tests 1, 2, 3, 4, & 11 were selected for analysis as blocks showed signs of motion relative to the base fracture plane based on high speed video observations. Two block shapes were tested, rectangular blocks and parallelogram blocks which were intended to exhibit toppling and slumping failure modes respectively. The geometries of the toppling blocks consisted of rectangular shapes while the blocks that were intended to slump blocks are shown in Figure 3.22. Notice that the slumping blocks that were parallelogram in shape required one modification of cutting the points of the block to prevent them from breaking off. The geometry was reported based on the measurements H and B.

For toppling blocks, $\alpha_3 = \tan^{-1}(B/H)$ and since the block is rectangular, $\alpha_1 = -\alpha_3$. Given the modification to the slumping geometry, S_1 and S_2 are calculated as follows:

$$S_1 = (H + 0.4\sin(45^\circ))\sin(45^\circ) \tag{3.36}$$

$$S_2 = B. \tag{3.37}$$

Based on equations (3.4a) and (3.4b), α_1 and α_3 are calculated as follows:

$$\alpha_1 = \tan^{-1}\left(\frac{r_{1x}}{-r_{1y}}\right) \qquad = \tan^{-1}\left(\cot(\gamma) - \frac{S_2}{S_1}\csc(\gamma)\right) \tag{3.39}$$

$$\alpha_3 = \tan^{-1}\left(\frac{r_{3x}}{-r_{3y}}\right) \qquad = \tan^{-1}\left(\cot(\gamma) + \frac{S_2}{S_1}\csc(\gamma) - 0.4cm\right). \tag{3.40}$$

The results of these experiments compared to the predictions of Figure 3.15 are presented in table 3.1. Excellent agreement was reached for the blocks designed to topple with the deviations in yield acceleration possibly associated to the precision at which the base of the blocks could be made flat such that the outside corners of the blocks were the only contact points with the base fracture plane.

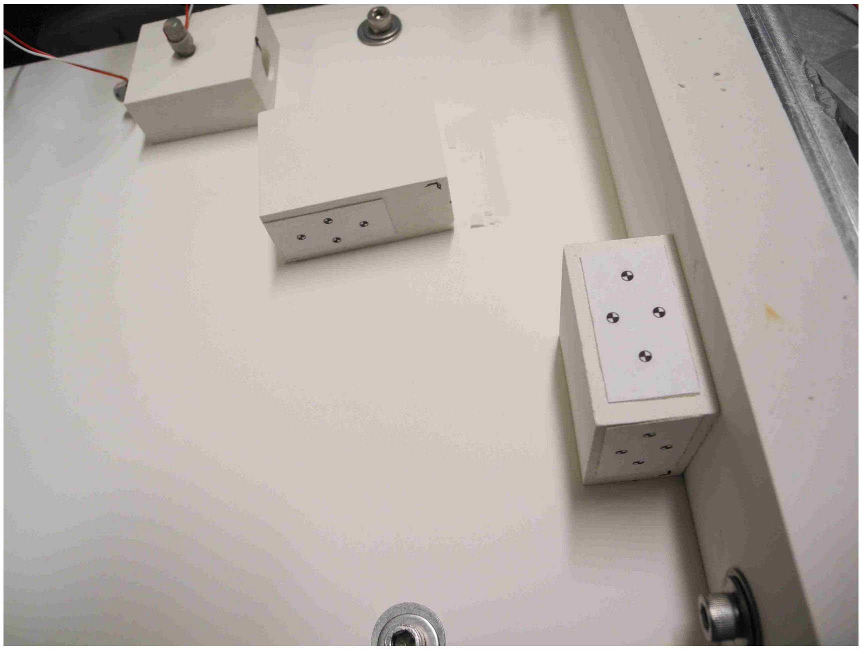

(a) Toppling blocks with varying aspect ratios that represent tests 1, 2, 3, and 4 block geometries.

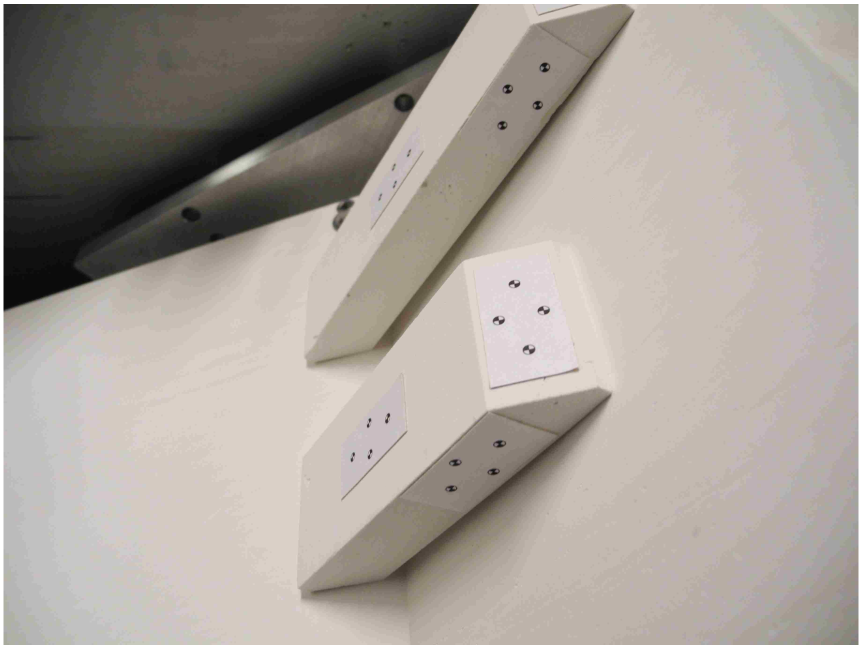

(b) Sliding blocks with varying aspect ratio that undergo sliding in back supported configuration (represents test 11).

Figure 3.22: Block shapes in centrifuge experiments by Applegate and Wartman (2013). See Table 3.1.

Table 3.1: Summary of centrifuge results for single discrete blocks.

Test	B	H	S_1	S_2	α_1	α_3	β	Predicted		Observed	
	(cm)	(cm)	(cm)	(cm)	(deg)	(deg)	(deg)	yield acc.	mode	yield acc.	mode
1	2.57	4.64	-	-	-29.0	29.0	20	0.16	topple	0.22 ± 0.2?	topple?
	2.57	5.74	-	-	-24.1	24.1	20	0.07	topple	0.09 ± 0.2	topple
2	2.57	5.74	-	-	-24.1	24.1	20	0.07	topple	0.07 ± 0.2	topple
	2.57	5.74	-	-	-24.1	24.1	20	0.07	topple	0.07 ± 0.2	topple
	2.57	4.64	-	-	-29.0	29.0	20	0.16	topple	0.18 ± 0.2	topple
3	2.57	4.64	-	-	-29.0	24.1	25	0.07	topple	0.08 ± 0.2	topple
4	2.57	5.74	-	-	-24.1	24.1	25	0.00	topple	0.00 to 0.05	topple
	2.57	4.64	-	-	-29.0	29.0	25	0.07	topple	0.05 to 0.20	topple
11	2.88	10.68	7.75	2.88	25.4	48.4	20	0.48	slide	0.48 ± 0.2	slide*
	2.90	7.20	5.29	2.90	12.6	54.0	20	0.48	slide	0.48 ± 0.2	slide*

* Initial block movement was sliding, then when the ground motion reversed direction, the block went back to a slump-like position as predicted.

The blocks that were initially designed to slump in test 5, actually exhibited the sliding mode as indicated in Table 3.1. The reasons for this discrepancy is that the chamfering of the block corner caused the blocks to be constructed with an α_1 such that the slumping criteria ($\alpha_1 > \phi$) was not met. In addition, the higher observed friction angle observed between the block and fracture plane during the centrifuge testing made slumping criteria more difficult to meet. The sliding, toppling modes and yield accelerations are correctly predicted by the failure mode chart based on the blocks' as-built measurements and measured friction angle in the centrifuge. Although observations of slumping behavior were desired, this test provided the following insight and verification:

- Blocks identified to slump by strength reduction analyses for static loading with ($0 < \alpha_1 < \phi$) will actually slide or topple under seismic loading.

- Once these blocks have translated in the sliding mode, they return to a "slump-like" configuration when the ground motion subsides.

3.5.2 Comparison by DEM (UDEC) Analysis

Since the centrifuge tests could only provide a partial verification of the failure mode chart and yield equations, an extensive parametric analysis was performed using the distinct element method (DEM) as implemented by *UDEC* Version 5.0. A *UDEC* model was developed to verify the failure mode and yield acceleration of single blocks predicted by the pseudo-static mode and yield equations presented in the previous sections of this chapter. A sample of the general model geometry is shown in Figure 3.23 which is based on the geometry shown in Figure 3.7. The base block that forms the base and back fracture planes is modeled as a rigid block with two surfaces on which the discrete rigid block interacts. To simplify modeling, the block is assumed to be a parallelogram. The geometry of the discrete block and the fracture planes are fully described by specifying the block angles and the base angle. The parametric study consisted of the array of parameters shown in Table 3.2.

Table 3.2: Range of parameters used in *UDEC* verification.

Parameter	Vector of values
α_1 and α_3	[-80 to 80, by 10's]
ϕ	[35, 55]
β	[-10, 0, 20]
scale	[1 and 2]

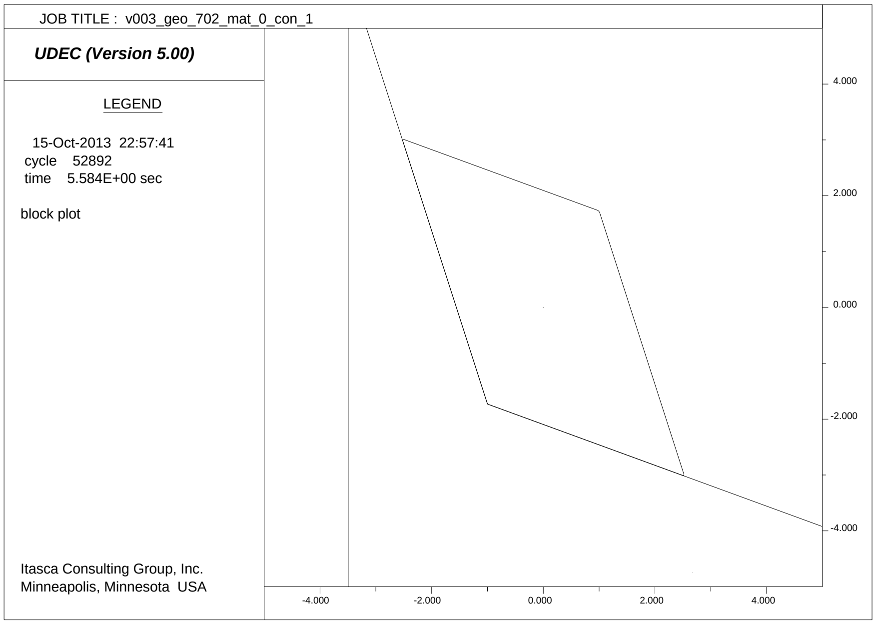

Figure 3.23: Typical *UDEC* model geometry for parametric study.

UDEC is implemented with rounded corners at all block corners to “smooth” calculations and model behavior. The rounding of the block was set to 1% of the smallest block length based on modelling performed by Lanaro et al. (1997). Note that the rounding of the block corner causes the contact points to be slightly shifted, thus the modeled α_1 and α_3 are slightly different than intended. More precise results could be obtained by reducing the rounding percentage, however, this reduction would negatively impact simulation run times and would not change the ultimate conclusions of this analysis.

The joint constitutive relationship used in the model is the Coulomb slip model with cohesion set to zero. A summary of non-default model parameters are shown in table 3.3. Density does not factor into the failure mode and yield equations, but is a necessary parameter to be set in *UDEC* since density is needed for the equations of motion. In addition, the analytical solutions assume rigid contact between the block and fracture planes when

Table 3.3: Fixed parameters used in *UDEC* verification

Rigid block parameters	
Density	2700 kg/m^3
Rounding	1.0%

Joint parameters	
Cohesion	0
Joint Normal Stiffness	6.56e10 N/m
Joint Shear Stiffness	6.56e10 N/m

the shear resistance is below the limit state. However, since *UDEC* solves the equations of motion using springs, joint normal and shear stiffnesses is required, but also does not significantly influence the results so long as the values approximate relatively stiff behavior.

Pseudo-static loading was simulated by first stepping the model to static equilibrium under a vertical gravity field and then applying an additional horizontal component to the gravity field. This method is equivalent to having $\mathbf{W}$ oriented vertically and applying k_h. The magnitude of k_h was increased in 0.01m/s^2 increments. With each horizontal loading increment the model was cycled to equilibrium where equilibrium was determined when the unbalanced forces were less than 1.0Newton. When the translational or rotational components of displacement became unstable, then the model was halted and the current magnitude of k_h was noted, along with the mode of failure. The mode of failure was determined by evaluating the shear (τ_i) and normal (N_i) forces of the i^{th} contacts. The logic used to detect the yield points and failure modes is summarized in pseudo code in Algorithm 1. A contact was deemed to lose contact if the normal force was less than 1 Newton. A contact was deemed slipping if the shear force at the contact was within 0.5% of yield.

Algorithm 1 *UDEC* logic used to detect yield points and failure modes

```
if contact 2 has lost contact then
    if contact 3 is the only contact then
        $mode \leftarrow Topple$
    else if contact 3 is slipping & contact 1 is slipping on base fracture then
        $mode \leftarrow Slide$
    else if contact 3 is slipping & contact 1 is slipping on back fracture then
        $mode \leftarrow Confined\ Topple$
    else
        $mode \leftarrow No\ Failure$
    end if
else if contact 1 & 2 are slipping & contact 3 has lost contact then
    $mode \leftarrow Slumping$
else
    $mode \leftarrow No\ Failure$
end if
```

The failure modes determined from the *UDEC* simulations are summarized in Figure 3.24 by overlaying the results onto the pseudo-static failure mode chart presented previously in Figure 3.15. Notice that although slope angle and block scale was varied, it did not control the mode of failure. Similarly, pseudo-static yield accelerations calculated from the *UDEC* simulations are are summarized in Figure 3.25. The relative error of the results are generally within five percent error with the exception of a few points which are attributed to the rounded corners. The absolute error of the results are less than 0.02g. The slide and slump modes have the lowest absolute error because the yield acceleration is controlled mostly by the frictional resistance on the fracture. *UDEC* underpredicts the yield acceleration for slumping and toppling and overpredicts for the confined toppling modes. In addition, for confined toppling, a few simulations deviated significantly appearing as outliers. These deviations are likely a result of the following:

- The tolerance used in the mode detection algorithm to detect slip, rotation, and lift-off of a block contact.
- The rounding approximation of the block corners used in *UDEC* that cause the position vectors to have a slightly different orientation in comparison to the idealized block model.
- Numerical errors associated with the discrete time stepping scheme in the finite difference calculations of *UDEC* .
- The precision settings used in *UDEC* to detect the creation/deletion of contacts and initiation of sliding.

This error may be undesirable for this comparison modeling, however for problems encountered in nature, the rounded edge may provide a better approximation. In these cases where the corner is rounded, care should be taken when using the simplified block model to correctly identify the contact points and calculation of the position vectors. Overall, the *UDEC* results shown in Figures 3.24 and 3.25 demonstrate excellent agreement and provide confidence not only in the mode and yield acceleration relationships, but in the ability of *UDEC* to capture the initiation of block motion relative to the fracture planes.

3.6 Application and Examples

3.6.1 Application of Mode and Yield Criterion

Application of the pseudo-static failure mode and yield acceleration criterion begins with the task of collecting rock fracture data. A comprehensive procedure for this application is provided below.

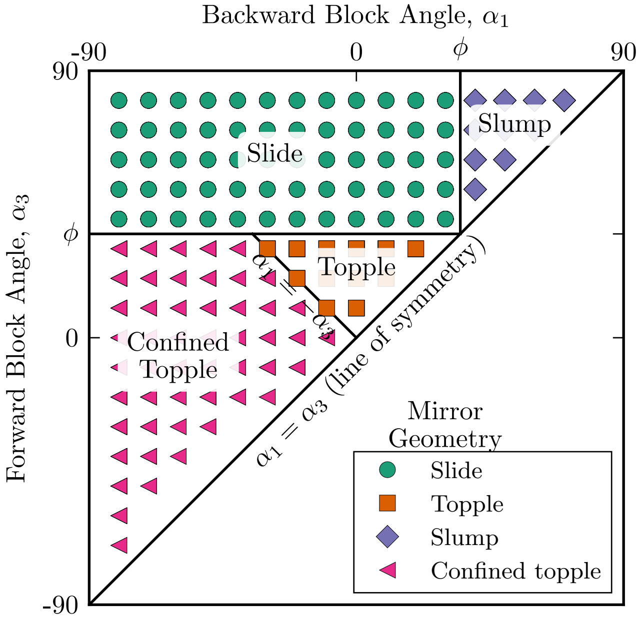

(a) $\phi = 35°$

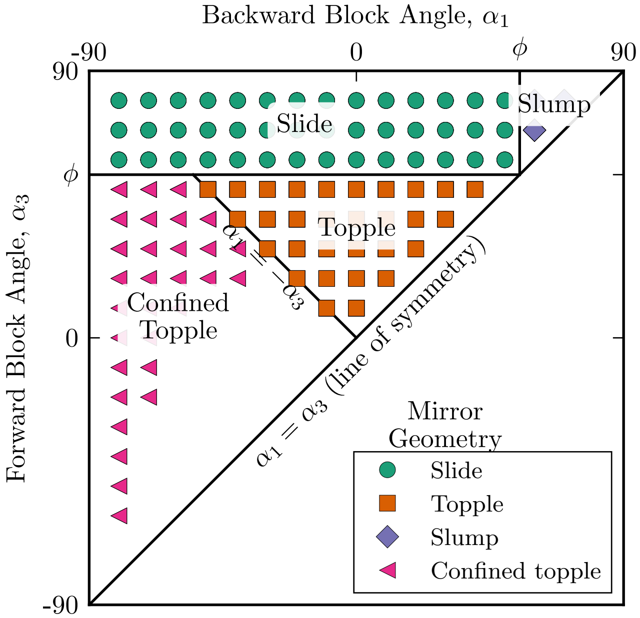

(b) $\phi = 55°$

Figure 3.24: Comparison of predicted failure modes to *UDEC* verification results.

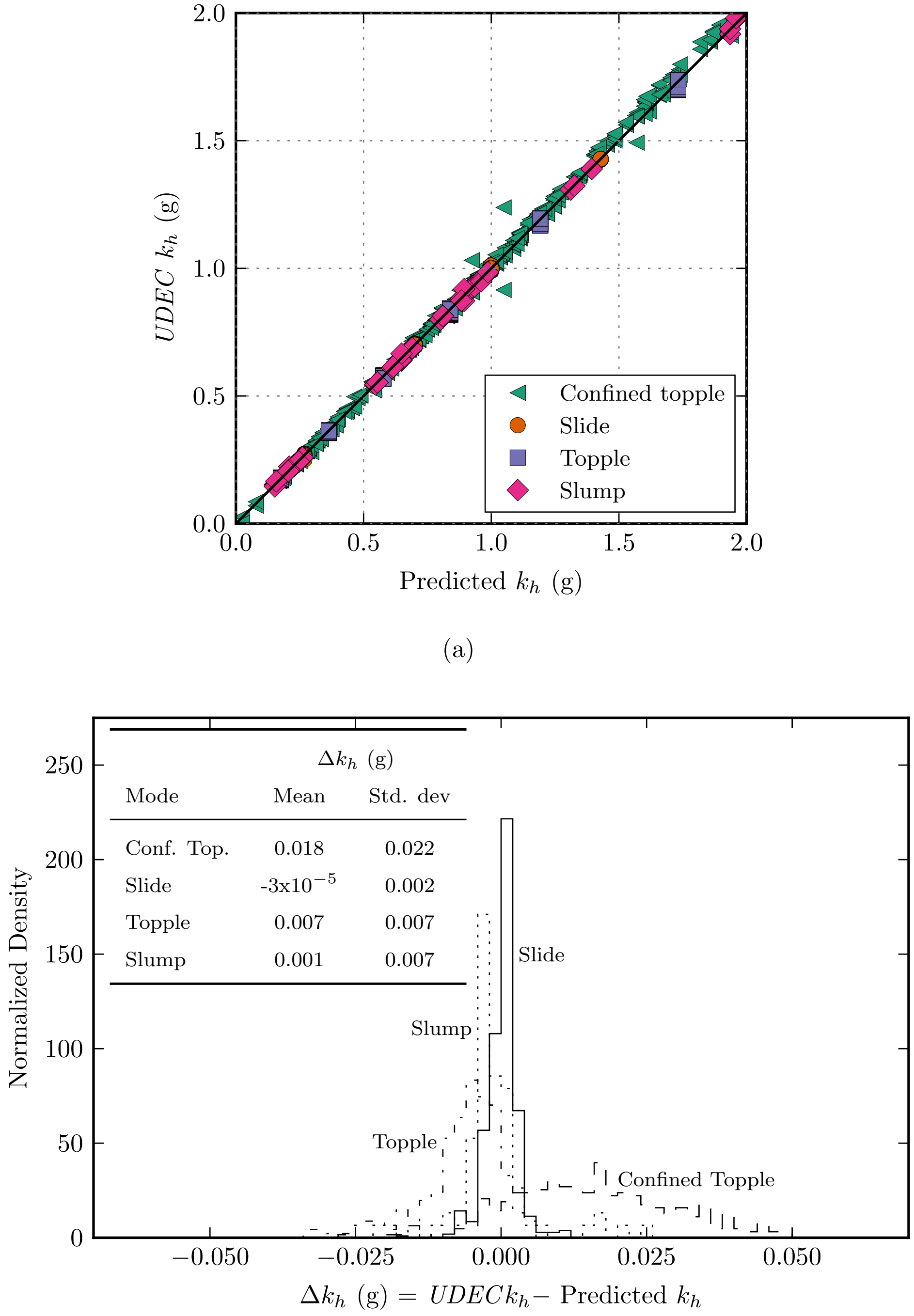

	Δk_h (g)	
Mode	Mean	Std. dev
Conf. Top.	0.018	0.022
Slide	-3x10^{-5}	0.002
Topple	0.007	0.007
Slump	0.001	0.007

(a)

(b)

Figure 3.25: Comparison of predicted yield accelerations to *UDEC* verification results.

1. Collect rock slope fracture data including fracture orientations, dips and spacing.
2. Identify three dominant fracture sets that form release planes and can create discrete rock blocks.
3. Identify the shape of the discrete rock blocks for the two dimensional approximation.
4. Identify the center of mass of the discrete rock block.
5. Calculate geometric parameters α_1 & α_3 and $\mathbf{r}_1$, $\mathbf{r}_2$, & $\mathbf{r}_3$. Recall that these parameters are relative to the fracture with an orientation (positive or negative) nearest to horizontal and the orientation of the open face of the slope.
6. Determine pseudo-static failure mode by plotting α_1 & α_3 on Figure 3.15.
7. Determine pseudo-static yield accelerations using Equations (3.17),(3.16),(3.25), or (3.29).

The above procedure is easy to apply for joint sets that form parallelograms as the geometric relationships derived in this chapter can be used, however, the procedure is not limited to these shapes. Since the failure mode and yield equations were derived based on the position vectors $\mathbf{r}_1$, $\mathbf{r}_2$, & $\mathbf{r}_3$, then blocks of random polygon shape can also be analyzed by identifying the three contact points. Different techniques/relationships for determining the block geometry would be necessary for odd shaped blocks. However, the procedure is limited to blocks that have three contact points with two intersecting fracture planes.

Programs that can perform a comprehensive evaluation of discrete fracture networks, could be used to evaluate and identify discrete rock blocks relative to an open slope face and calculate their potential failure modes and yield accelerations. Simple algorithms could also be developed for use in geographic information system (GIS) programs to provide a regional evaluation of seismic block failure modes and yield accelerations. Site specific ground-based

LIDAR could be used to characterize the jointing in the rock slope and allow for the identification of specific modes and yield accelerations for discrete rock blocks.

3.6.2 Example 1: Isolated Blocks

The first example demonstrates how to identify pseudo-static failure modes of rock blocks on a slope is taken from a fractured rock mass and is shown in Figure 3.26a. Two rock blocks are individually identified and approximated by four-sided polygon shapes. The contact between the rock block and the fractures are identified as points 1, 2, and 3. The position vectors are drawn from the center of mass to contacts 1 and 3. A line is drawn from the center of mass perpendicular to the base fracture. Finally, an inter-fracture friction angle of 40 degrees is assumed. With this information, the blocks' failure modes can be determined by plotting the backward and forward block angles on a failure mode chart with the friction angle set appropriately. Figure 3.26b shows the failure mode chart with the two blocks indicated on it. From the chart it can be seen that the failure modes for each of these blocks is likely toppling. However, notice that the right block is near the boundary between toppling and sliding. Also, if the friction angle happened to be less than assumed, then the left block would undergo a sliding failure.

3.6.3 Example 2: Mount Healy Schist Rock Slope

The second example demonstrates how to identify pseudo-static failure modes of rock blocks on a slope is taken from a slope in Mount Healy, Alaska in a fractured schist and is shown in Figure 3.27a. The same procedures of identifying and approximating rock blocks used in the first example are followed for this example. As before, two blocks are identified for mode analysis. The inter-fracture friction angle is assumed to be 40 degrees. Figure 3.27b shows the failure mode chart with the two blocks indicated. From the chart it can be seen that the failure mode for the right block is sliding while the left block is slumping. Similar to the first example, if the friction angle is lower than assumed, then the right block's failure mode would also be slumping. Recall, that since the right block requires back support under

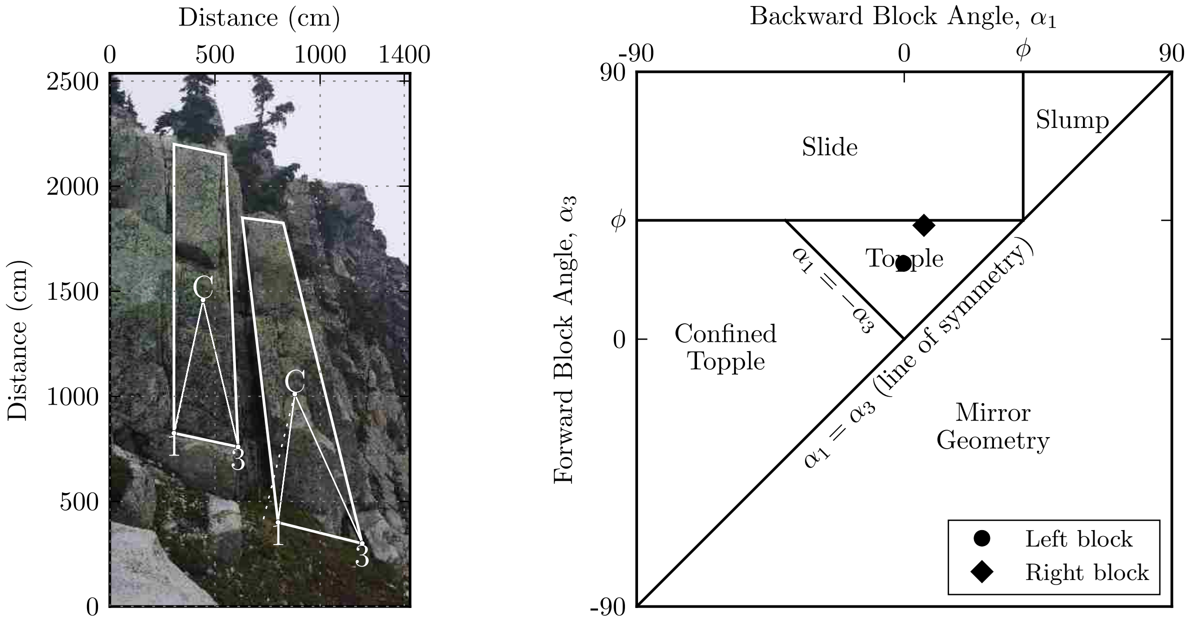

(a) Photo by Brett Campbell

(b) Seismic failure mode chart

Figure 3.26: Example 1: Pseudo-static mode determination for isolated blocks.

static forces, even though the block will initially slide in an earthquake, when the block's motion stops, it will rotate back against the back fracture in a slump position. After several cycles of this behavior, the block will be rotated back sufficiently such that in the next and subsequent cycles of earthquake loading, the block will undergo slumping failure. This mode path is shown on Figure 3.27b.

3.6.4 Example 3: Variable Rock Mass

The third example is presented, as a simple demonstration, of how this procedure can be used for a set of fracture data. Assume that the fracture statistics shown in Table 3.4 have already been determined. The friction angle describing the shear resistance between the fracture planes and discrete block is assumed to be $\phi = 40°$. Fracture set 1 is identified as the base fracture plane since its orientation is nearest to horizontal. For this example, 20,000 random

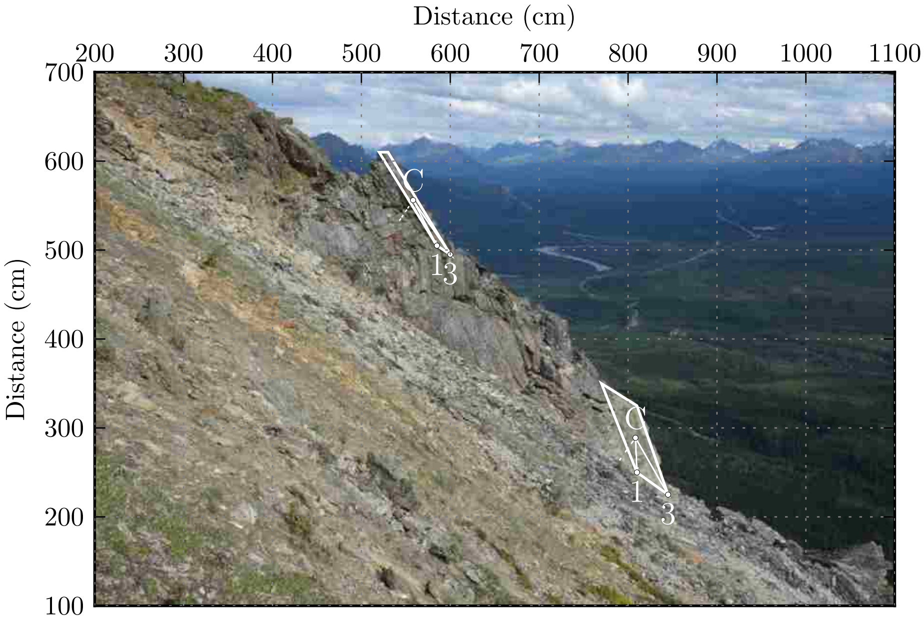

(a) Photo by J. Wartman

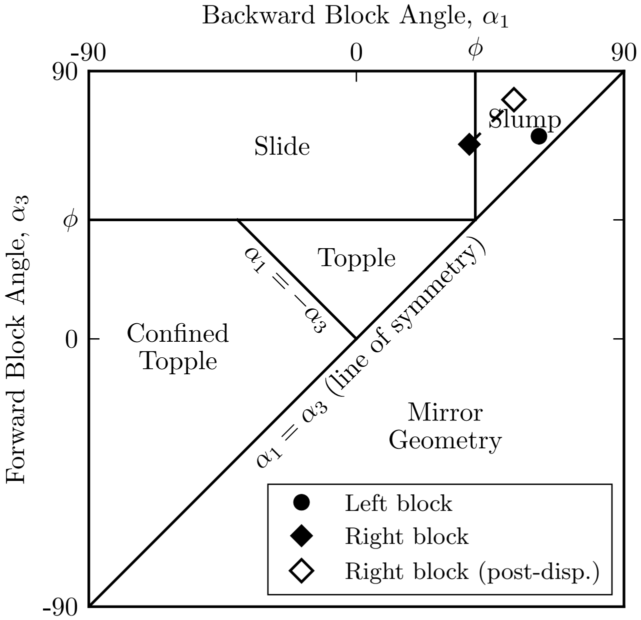

(b) Seismic failure mode chart. As the right block displaces the mode changes from sliding to slumping.

Figure 3.27: Example 2: Pseudo-static mode determination for fractured rock slope.

Table 3.4: Example: Fracture set parameters for variable rock mass.

Fracture Set	Parameter	Mean	Standard deviation
1	Orientation	20.0	5.0
	Spacing (or S_1)	1.0	0.1
2	Orientation	45.0	5.0
	Spacing (or S_2)	0.6	0.1

realizations of each parameter based on the fracture statistics are evaluated. The parameters α_1 and α_3 are determined by calculating γ (subtracting the orientation of fracture set 1 from set 2) and then applying Equations (3.15a) and (3.15b). A two-dimensional histogram of the failure modes determined from α_1 and α_3 is shown in Figure 3.28a. The mean α_1 and α_3 for the data set is indicated by the red dot. Although the mean falls within the sliding mode of failure, the variability in fracture geometry makes it possible for both sliding and slumping modes to occur. The histogram is not circular in shape since the distributions are Gaussian only in γ and $\frac{S_2}{S_1}$.

The yield acceleration of each sample is then calculated and parsed based on the specific mode of failure. Histograms and cumulative distributions of the yield accelerations for each mode of failure is shown in Figure 3.28b. Both plots indicate that if all samples are realized then more slides than slumps would be expected. This would only occur if the horizontal PGA (HPGA) of an earthquake exceeded approximately 0.4g's. If the HPGA of an earthquake was less than approximately 0.4g's then the analysis suggests that slumps would be the most abundant failure mode observed in the field.

While different trends would be seen for the geometry of different fracture sets, an interesting implication can be drawn from this specific example. Most earthquake reconnaissance occurs for large magnitude earthquakes which also typically have large PGA's. Since the

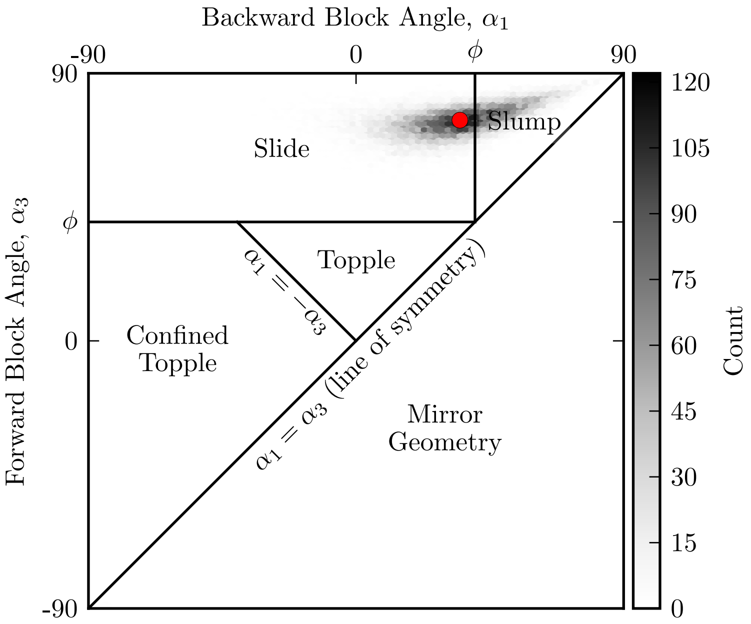

(a) 2D histogram of expected failure modes. The mean α_1 and α_3 for the data set is indicated by the red dot.

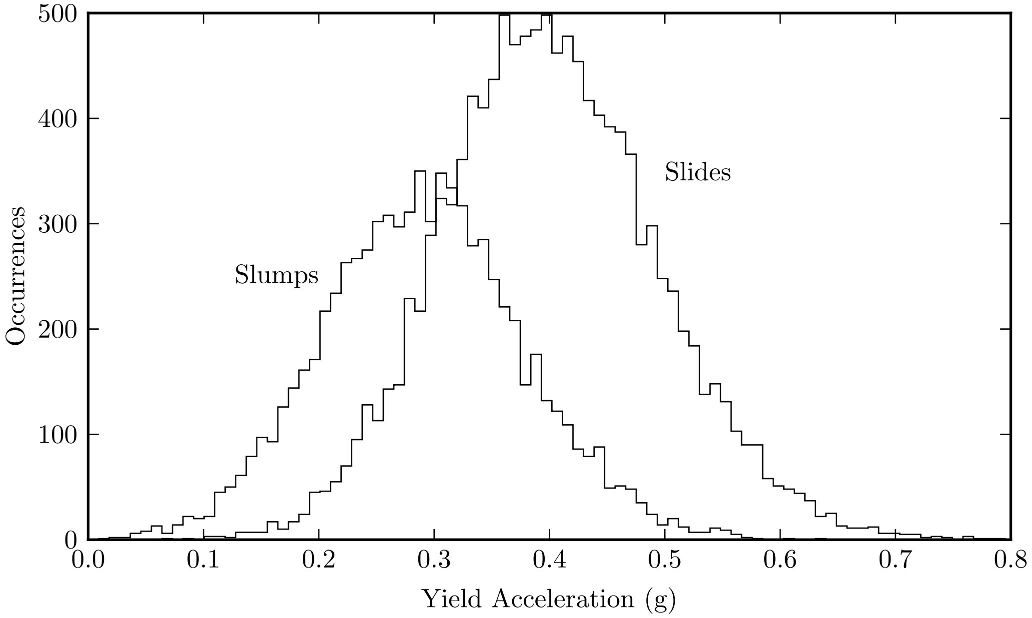

(b) Histogram of each mode occurrence.

Figure 3.28: Example 3: Variable rock mass.

cumulative plot in Figure 3.28b indicates that the abundance of a failure mode depends on PGA, then empirical relationships based on earthquake reconnaissance of large earthquakes would be potentially biased in their prediction of the dominant failure mode of rock blocks for specific geometries. Although these trends are interesting, they are not conclusive since there are additional factors that influence the failure of discrete blocks such as time dependent behavior that will be further evaluated in subsequent chapters.

3.7 Discussion and Conclusions

The relationships and examples presented in this chapter allow for a substantial expansion of the understanding of rock block failures during earthquakes. The mode chart presented in Figure 3.15 expands the identification of potential pseudo-static failure modes for blocks that includes those formed by non-orthogonal fracture sets. The chart is generic for any block shape since the only geometric information used to determine these failure modes were the position vectors. With non-orthogonal fractures, the geometry for the slumping failure mode is now delineated. In addition, a new static and seismic failure mode, confined toppling, is identified. Some of the key inferences that can be drawn from this formulation to determine pseudo-static failure modes include:

- The angle of the base fracture is not needed to determine the pseudo-static failure mode for blocks on a frictional fracture plane.

- The scale of a block does not contribute to the determination of failure mode or yield acceleration when the fracture's shear resistance is described by a friction only relationship. However, this is not the case for blocks having fracture shear resistance that is best described by friction and cohesion parameters, such as rocks types where fracture gouge forms or chemical bonding occurs.

- Although blocks with $0 < \alpha_1 < \phi$ require back support and are determined by Kieffer (1998) to slump under static loading, during seismic loading a subset of these blocks do not slump and either slide or topple.

- The failure mode for statically determined slumping blocks are not necessarily applicable to blocks under seismic loading.

- Since the only controlling factor in determining the pseudo-static failure mode is the orientation of $\mathbf{R}_I$ relative to α_1 and α_3, this criteria can be applied to other scenarios where the shear resistance of the fracture planes described by any means or additional external loading such as water pressures are considered. This task can be made easier by evaluating the sliding free body diagram at the two transition points to determine the set of values that best describes the transition points for all modes.

- The orientation of fracture sets relative to an open slope face and the friction angle of the fractures are the main determinants of the seismic mode of failure.

The lower bound seismic accelerations that initiate block motion relative to the fracture planes supporting the block were evaluated. The yield acceleration equations for slumping and confined toppling were derived for the first time. The yield accelerations for toppling, confined toppling and slumping show a non-linear relationship with their geometry whereas the yield acceleration for sliding is constant. Between the sliding, toppling and slumping failure modes, the sliding yield acceleration is always the greatest, however, the confined toppling yield acceleration can exceed all three. Key inferences drawn from the yield equations include:

- The pseudo-static modes can change because of slight changes in geometry or friction angle whereas the yield accelerations are equal at the sliding/slumping, sliding/toppling, and sliding/confined toppling transition points. The exceptions to this rule are the transition points from toppling to confined toppling where a discontinuous change in yield acceleration occurs and confined toppling yield acceleration is greater than toppling yield acceleration.

- Although slumping may resemble sliding in that shearing occurs on the fractures and it may be tempting to use the sliding yield acceleration as a proxy, there is significant differences between the two. For example the sliding yield acceleration for a given ϕ is the upper bound value for blocks that slump, a similar conclusion as Michalowski (2007). Once relative block motion takes place, the slumping, toppling, and confined toppling yield accelerations begins to decrease where as the sliding yield acceleration remains constant. Slumping, toppling, and confined toppling motion involves rotation which will make the displacement response dependent on the block's moment of inertia. In addition, slumping and confined toppling block follows a curved path whereas the path for a sliding block is linear. Thus, global displacement of a slumping or confined toppling block will depend on the non-linearity of the curved path, which itself is dependent on the geometry of the block.

- Blocks that are predicted to fail in the confined toppling mode and with $\alpha_3 < 0$ (meaning the center of mass overhangs the block toe) fail catastrophically once the block rotation exceeds $90 - \gamma$ since the block no longer experiences resistance from the back fracture plane and is in a precarious position.

- The likelihood of a mode occurring is based on the likelihood of a specific joint orientation, spacing, and open slope face orientation. As different rock types might have different typical geometries of joint set formation, different types of rocks may have different dominant modes of failure under seismic loading. For example, in rocks that typically show columnar jointing, such as basalts the expected modes of failure will be sliding or toppling depending on the relative spacing of those fractures. In rocks such as slates that have relatively small fracture spacing and secondary joints at conjugate angles, slumping and sliding failures would be expected. Geologic locations on a regional scale may also pay an important role in the expected failure modes since the rocks would be subject to similar geologic processes that may cause similar fracture sets.

Chapter 4

DISPLACEMENT RESPONSE OF TOPPLING ROCK BLOCKS

Rock slope failures have contributed greatly to the economic and human loss experienced during seismic events throughout the world. Accounts of these spectacular events have been documented and evaluated throughout the literature (Cluff (1971); Plafker et al. (1971); Wilson and Keefer (1983); Jibson et al. (2006); Keefer et al. (2006); Aydan et al. (2009); Lanzo et al. (2010); Alfaro et al. (2012); Massey et al. (2014), among others). A database of earthquake induced landslide failures compiled by Keefer (1984), and reinforced by others (Rodríguez et al., 1999; Keefer, 2013), clearly indicates that failure modes, observed in the field following earthquakes, include sliding, toppling, and slumping. Rock fall failures experienced during the recent (2010 to 2011) sequence of earthquakes in Christchurch, New Zealand highlights the magnitude of destruction to the built environment and forced abandonment of a large area of settled land (Massey et al., 2014).

Methods for seismic triggering of rock slope failures rely on charts for rectangular blocks that are applicable to only sliding and toppling modes (Yagoda-Biran and Hatzor, 2013) and was expanded for irregularly shaped blocks applicable to four failure modes (sliding, toppling, slumping, and confined toppling) in Chapter 3. Simplified, seismically-induced displacement methods, used to evaluate rock slope failure scenarios in a performance-based earthquake engineering (PBEE) framework, are commonly limited to a sliding block that is used to represent all modes (Jibson, 2011). However, the toppling mode of failure fundamentally differs from sliding block models in several ways. First, the toppling mode involves rotation of the rock mass while the sliding model is translational. Second, the sliding block model is used to assess damage potential based on accumulated displacement; however, the response of a typical toppling block is expected to result in failure or relatively no movement. Lastly, the rotational response of a rock is expected to be dependent on the size and contact conditions of the rock.

In this chapter, the well-researched rocking block model is modified and applied to the toppling of rocks slopes during earthquakes. Rocking block equations are re-derived with reference to the critical acceleration that initiates toppling. The assumptions made in deriving the equations of motion are evaluated relative to centrifuge testing. Parametric analyses are performed and consist of the excitation of a broad range of slumping block geometries by 527 unique recorded earthquake ground motions from the Pacific Earthquake Engineering Research Database (PEER) database. The results of a parametric study which considers varying block shapes subject to horizontal and vertical earthquake ground motions are presented. Relationships in the literature for rock block toppling under simplified loading are shown to be representative of block behavior when subject to earthquake ground motions by utilizing the mean period ($\mathrm{T_m}$) and intensity measures such as peak ground velocity (PGV) of the earthquake. The results of this parametric study are used to statistically predict the failure of slumping blocks based on basic ground motion parameters (PGA, PGV, PGD, $\mathrm{T_m}$) and block and joint interface characteristics. A new relationship is presented that segregates the block and earthquake parameters giving rise to a probabilistic state parameter. This parameter can be used to predict the likelihood of rock block toppling failure during a given earthquake. The characteristics of the ground motion acceleration pulses that lead to overturning are discussed. A simple chart-based method and equations are presented for the evaluation of seismic rock block toppling failures. Finally, this method is used to explore and offer potential explanations for observations of rockfall during the 2011 Canterbury earthquake sequence.

4.1 Seismic Rock Block Toppling Review

In this section the reader is presented with a summary on the current literature of predicting rock toppling during seismic events. Detailed review of key aspects of the literature will be provided throughout the chapter when necessary.

4.1.1 Rocking Blocks

As shown in Figure 3.4, it is common to find blocks on slopes that are bounded by other blocks and thus they must fail by toppling forward (assuming another mode of failure does not control). This forward toppling failure mode is one of the primary failure modes for the generic rocking block and has been extensively researched. This existing research forms a fundamental basis of this chapter and the evaluation toppling of rock blocks under seismic loading.

A mass in contact with a plane at two distinct points (i.e. a rocking block) represents a system encountered in many branches of engineering and architecture. The rocking block literature is relatively mature, indicated by the use of these systems in Japan in 1881 with the desire to back-calculate the peak ground acceleration (PGA) for earthquakes based on overturned tombstones (Ishiyama, 1980). Examples of some of these systems include mechanical equipment (Makris and Konstantinidis, 1998), museum pieces (Di Egidio and Contento, 2009), ancient structures (Hinzen, 2009), water towers (Housner, 1963), and precarious rocks (Brune et al., 1996), among others. Many researchers (e.g. Housner (1963), Aslam et al. (1978), Yim et al. (1980), Ishiyama (1982), Hogan (1989), among others) have shown by analysis and experiment that the response of the rocking block is sensitive to its physical characteristics and initial conditions, which often gives rise to complex non-linear and even bifurcating behavior.

Forward Toppling by Simple Pulse Ground Motions

Rocking blocks have been evaluated throughout the literature for simplified (sinusoidal) and complex ground motions. Solutions to these problems are obtained either by numerical integration or closed-form methods of the linearized equation of motion. However, linearization introduces error into these solution and can significantly effect the outcome (Allen and Duan, 1995). Results of these analyses have been interpreted using techniques ranging from statistics (Yim et al., 1980), dynamical chaos theory such as state planes and Poincaré maps

(Hogan, 1989), approximation with simplified ground motion pulses (Makris and Konstantinidis, 1998), characterizations with a rocking spectrum (Makris and Konstantinidis, 2003), evaluating "resonating" input motions to maximize energy input (Dejong, 2009), integrating earthquake ground motions (Gelagoti et al., 2012), and parametric experiments (e.g. Aslam et al. (1978), Wong and Tso (1989), Winkler et al. (1995), Taniguchi (2004) and Peña et al. (2008)).

For the closed-form, linearized equations of motion, several pulse-like dynamic loadings have been considered. Single cycle, half and full sine pulse motions are the most prevalent throughout the literature. One of the first to consider the half sine pulse loading was Housner (1963) who incorrectly assumed (Shi et al., 1996) that failure occurred by the end of the pulse. Anooshehpoor et al. (1999) described the boundary of when rocking failure occurred relative to the end of the pulse. Up to this point all concentration had been paid toward the minimum acceleration required to overturn a block, which required rocking behavior of the block. The boundaries of minimum acceleration to induce failure by either forward toppling or rocking were shown by Zhang and Makris (2001). They showed that the forward toppling mode had a higher critical toppling acceleration than for block rocking.

Housner (1963) evaluated ground motions with a sine pulse shape, while Yim et al. (1980) evaluated rectangular pulses. Both were later shown to have incorrectly characterized the critical toppling acceleration. The correct solution to the half-sine pulse loading was presented by Shi et al. (1996). This was followed by the correct solution to the full-sine pulse (Anooshehpoor et al., 1999). The list of solutions for pulses was expanded by Makris and Roussos (2000) to include other cycloidal motions (using hyperbolic trig functions) along with the sine and half-sine pulses. The solutions for the full sine and half sine pulses were again studied by Dimitrakopoulos and DeJong (2012) however, this time by using exponential functions. Finally, Voyagaki et al. (2013b) introduced lobe type pulses which could represent a wide range of pulse shapes from triangular to full square pulses.

Toppling From Earthquake Ground Motions

Substantial research effort has also been applied toward the toppling of rocking blocks by earthquake ground motions. The chaotic and sensitive nature of the rocking block's response has been well documented (Yim et al., 1980; Hogan, 1989; Allen and Duan, 1995, e.g.) severely hampering the use of deterministic analyses. However, when viewed from a probabilistic point of view and evaluating many earthquake loadings, trends begin to emerge and probabilistic predictions can be attempted, although they are still imprecise (Yim et al., 1980).

A probabilistic view was taken by Purvance (2005) who took a statistical look at precariously balanced rocks (PBR's) by executing a large number of simulations of various block sizes and synthetic earthquake motions with carefully controlled characteristics. This research showed trends of PGA and PGV relative to block shape. Others have also shown general trends with ground motion intensity measures like PGA, PGV, Arias Intensity (Im), and cumulative absolute velocity (CAV) (Sorrentino et al., 2006; Gazetas et al., 2012).

4.1.2 Precariously Balanced Rocks

In the study area of paleoseismology, toppling blocks have been utilized for the purpose of estimating the characteristics of past ground motions. This concept was introduced by Brune et al. (1996) who hypothesized the concept of using the rocking block model to evaluate precariously balanced rocks of a known age found in select geologic regions to be an indicator of the likelihood of earthquake accelerations. Subsequently, Brune and his research group expanded the rocking block model understanding and applied it to precariously balanced rocks (i.e. asymmetric blocks on an oscillating inclined plane) (Shi et al., 1996; Anooshehpoor et al., 1999; Anooshehpoor and Brune, 2002; Anooshehpoor et al., 2004; Purvance, 2005).

4.1.3 Rock Slope Engineering

For static evaluation of block stability, the most commonly used charts to determine toppling failure are those by Bray and Goodman (1981) shown in Figure 4.1a. For seismic triggering evaluation, Yagoda-Biran and Hatzor (2013) adapted these chart solutions by converting earthquake ground accelerations into a pseudo slope angle which could then be used in combination with static parameters to predict the dynamic mode of failure of a rectangular block (Figure 4.1b). In Chapter 3 a new chart (Figure 3.15) was presented to allow for the determination of seismic failure modes of various two dimensional (2D) block shapes. However, the charts in Figure 4.1 are limited to a pseudo-static understanding (i.e. triggering) of block toppling by earthquake ground motion and are not capable of making a prediction of whether a specific ground motion would result in a toppling failure. In addition, the size and shape of the block is not accounted for and will be shown to be a significant non-consideration.

Haneberg (2009) presented an analysis in an effort to understand the interaction of a rock block shape with the frequency and amplitude content of an earthquake ground motion. This analysis includes the following assumptions:

1. The motion of the center of mass of a toppling block is of the form $\ddot{\theta} = A\sin(2\pi ft)$, where $\ddot{\theta}$ is the angular acceleration of the block about its toe, A is the amplitude of loading, and f is the frequency of loading.

2. The block fails within the first lobe (half cycle) of a sine wave (i.e. time at failure= $1/2f$).

3. The block fails when the center of mass is past the toe of the block.

This work showed that the toppling response of a rock block is sensitive to its shape and the ground motion frequency and amplitude. While the results are intriguing, the underlying assumptions require some scrutiny. It is clear from the rocking block literature that

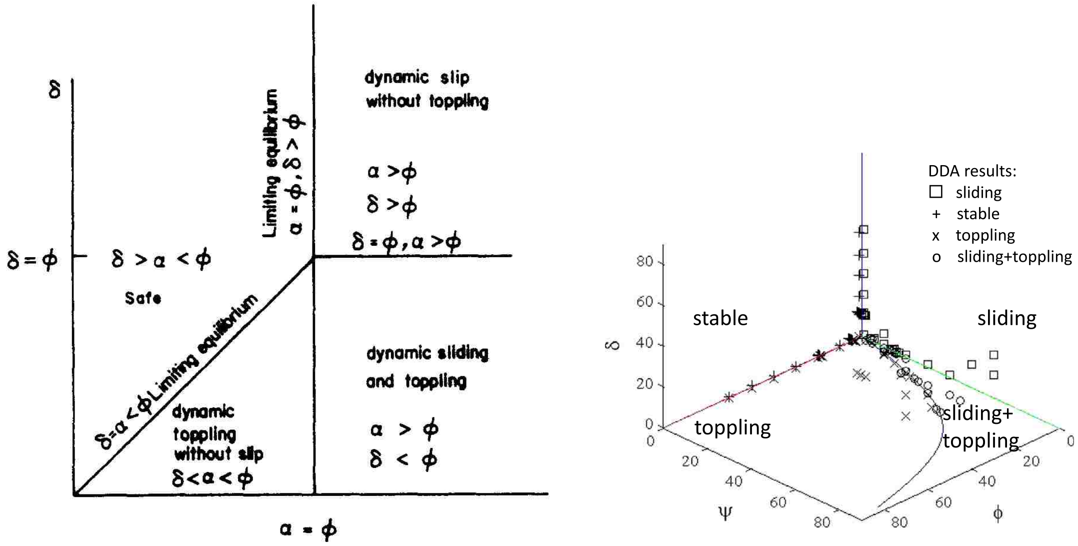

(a) Static (Bray and Goodman, 1981)

(b) Seismic: rectangular (Yagoda-Biran and Hatzor, 2013)

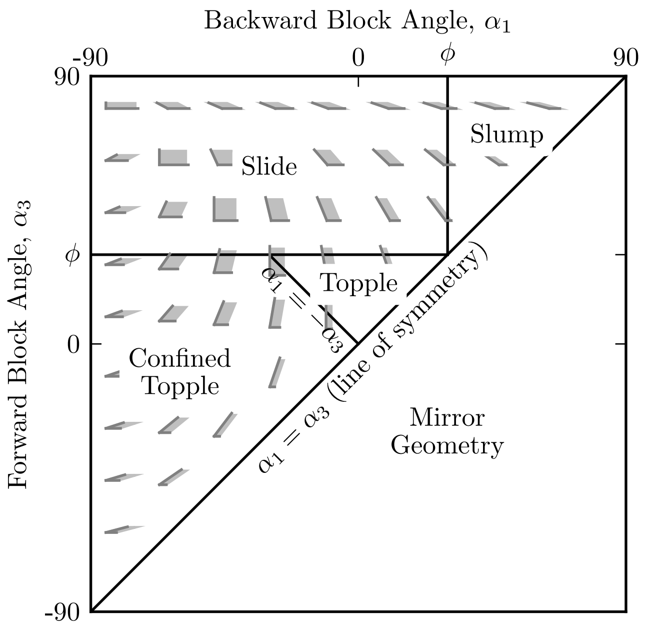

(c) Seismic: any 2D shape (Ch 3)

Figure 4.1: Existing failure mode charts for rock blocks

Assumption 1 (the center of mass acceleration as equal to a sinusoidal ground acceleration) is incorrect. The inertial acceleration that the block feels as the slope accelerates produces a torque on the block about its toe, thus motion of the center of mass is the result of angular motion. Angular motion in this case would be a function of the ground motion, the moment arm from the block toe to the center of mass, and the moment of inertia about the toe. Assumption 2 ignores the fact that the block can have momentum at the end of the first half cycle which can cause the block to continue on the path to overturning even though the ground motion has ceased (Shi et al., 1996). Assumption 3 is correct for the ground motion considered which has only a single lobe of perturbing acceleration. However, outside this specific case, such as for earthquake ground motions, this assumption incorrect (Voyagaki et al., 2013b).

4.2 Rocking Motion Relative to Toppling Yield Acceleration

In this section, the traditional equations of motion for a toppling block will be rewritten in terms of the toppling yield acceleration k_r. Writing the equations of motion in this fashion allows for a more intuitive visualization of rocking block behavior. In addition it allows for an analogy to be made to the Newmark sliding block model when this model applied to toppling rock blocks.

Consider a two-dimensional, asymmetric, rigid mass on a rigid, oscillating plane inclined at an angle β from horizontal (Figure 4.2). The mass is in contact with the plane at two points, O_1 and O_2. Let $\mathbf{r}_1$ and $\mathbf{r}_2$ be the respective vectors from O_1 and O_2 to the center of mass. The angles formed by $\mathbf{r}_1$ and $\mathbf{r}_2$ with respect to a vertical plane passing through each base point are ψ_1 and ψ_2, respectively. Clockwise, in-plane rotation of the block about point O_2 constitutes positive angular displacement, $+\theta$, while counter-clockwise rotation about O_1 constitutes negative angular displacement, $-\theta$.

The forces acting on the block include the gravitational force (mg), the horizontal inertial force ($k_h mg$), and the vertical inertial force ($k_v mg$). These forces, normalized by the gravitational force, are shown in Figure 4.3. The frictional force acting between the plane

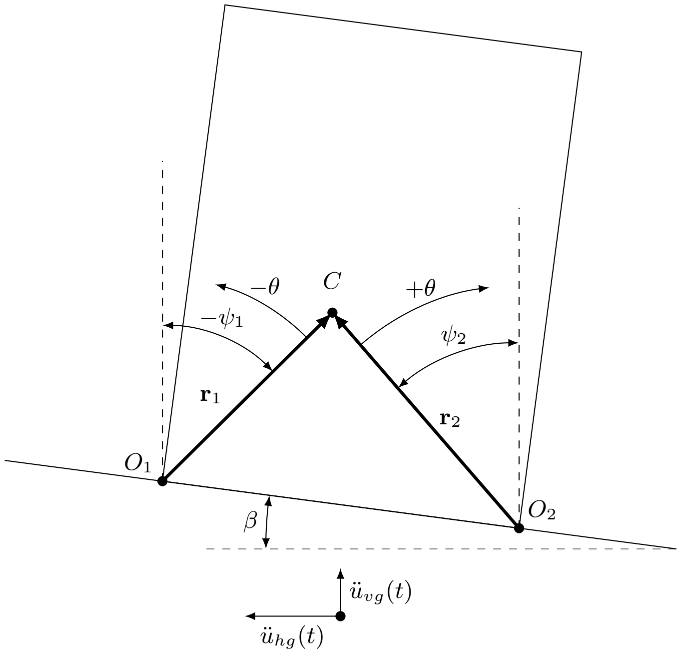

Figure 4.2: Asymmetric mass in contact with an inclined plane at two points, O_1 and O_2.

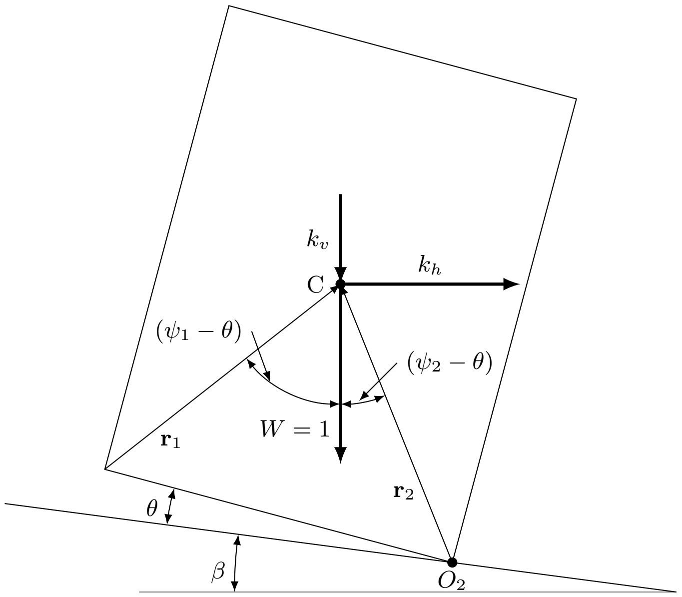

Figure 4.3: Free body diagram of a mass on an accelerating inclined plane rocking about point O_2.

and block is omitted since the force passes through each edge of the block and would result in zero moment.

For simplicity, the subscript i will be used to refer to rotations about point O_i and block properties and motion relative to the i-th rocking corner (Shi et al., 1996). Assuming zero vertical ground motion and no sliding between the plane and the block, block rocking motion will begin when the horizontal inertial acceleration coefficient, $k_h = \ddot{u}_{hg}/g$ exceeds the horizontal pseudo-static rocking acceleration coefficient, k_{rsi}. This acceleration can be defined by the block geometry such that $k_{rsi} = \tan(\psi_i)$. Considering further the inertial reaction to the vertical inertial acceleration coefficient, $k_v = \ddot{u}_{vg}/g$, rocking motion will begin when k_h exceeds $(1 + k_v)\, k_{rsi}$. For the case where $\theta = 0$, the vector force diagram shown in Figure 4.4 illustrates these threshold coefficients for rocking on edges 0_1 and O_2.

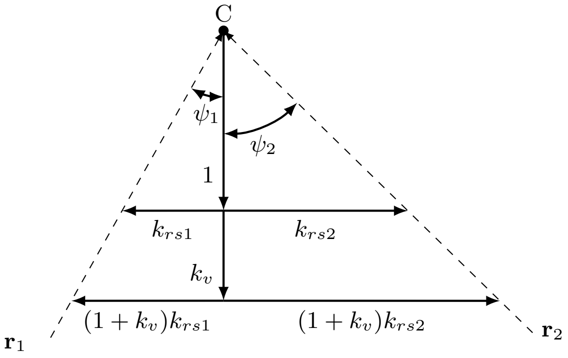

Figure 4.4: Force vector diagram illustrating the horizontal pseudo-static rocking acceleration coefficients for the block in Figure 4.3 where $\theta = 0$.

The left-hand vector force diagram in Figure 4.5 resulting from the free body diagram in Figure 4.3 allows for the traditional equations of angular motion to be derived as

$$I_i\ddot{\theta} = \underbrace{mgk_h}_{\text{horizontal force}} \underbrace{r_i \cos(\psi_i - \theta)}_{\text{moment arm}} - \underbrace{mg(1 + k_v)}_{\text{vertical force}} \underbrace{r_i \sin(\psi_i - \theta)}_{\text{moment arm}} \tag{4.1}$$

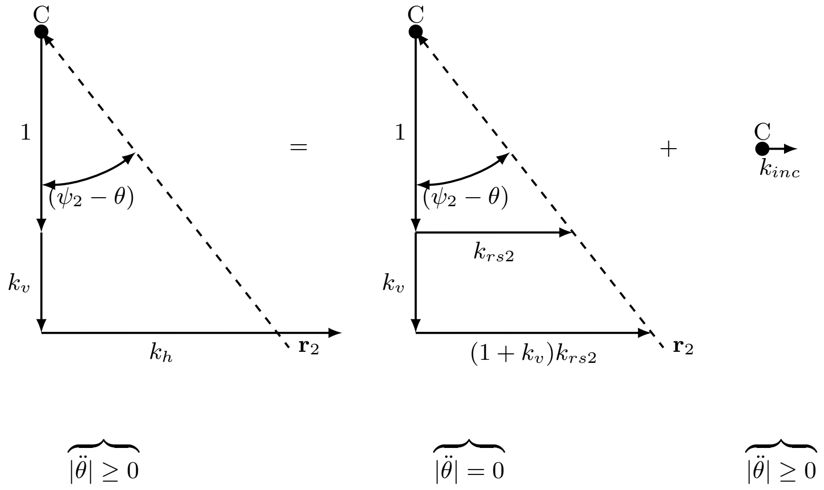

Figure 4.5: Force vector diagram illustrating the horizontal rocking acceleration coefficient for the block in Figure 4.3 rocking about point O_2.

where I_i is moment of inertia about point O_i and $\ddot{\theta}$ is angular acceleration. This equation is generally rewritten by substituting $p_i^2 = mgr_i/I_i$, yielding

$$\ddot{\theta} = p_i^2 k_h \cos(\psi_i - \theta) - p^2(1 + k_v)\sin(\psi_i - \theta) \tag{4.2}$$

The parameter p has the units of $1/s$ and can be thought of as a frequency parameter of the block (Housner, 1963). Evaluating Equation (4.2) requires solving a non-linear, discontinuous, second order, differential equation. Since a closed form solution cannot be obtained for this equation, most of the research into rocking blocks have taken the approach to linearize this equation assuming $\sin(\psi - \theta) \approx \psi - \theta$ and $\cos(\psi - \theta) \approx 1$ for small angles of ψ resulting in:

$$\ddot{\theta} = p_i^2 k_h - p_i^2(1 + k_v)(\psi_i - \theta) \tag{4.3}$$

For a block that rocks from edge to edge, Equation (4.3) could also be rewritten for motion when the block is rotating about O_1 by substituting the subscripts. Furthermore, Shi et al. (1996) went on to derive the behavior of a generic asymmetric block when it transitions from rocking about O_2 to O_1 by defining a coefficient of restitution using the conservation of angular momentum (as was originally done by Housner (1963)) to relate the angular velocity before and after impact. The coefficient of restitution will be discussed further in Section 4.3.1.

Alternatively, the force diagram could be split into two sets of forces that produce zero and non-zero net torques (or angular acceleration), respectively. To facilitate splitting the forces into two sets, k_{rsi} is examined. As the mass rotates about either base point, it can be seen that k_{rsi} is only applicable when $\theta = 0$. A more general term, *instantaneous horizontal rocking acceleration coefficient* (k_{ri}), is used to define the horizontal inertial acceleration coefficient (assuming $k_v = 0$) that produces zero net torque and thus zero angular acceleration acting on the block for all θ.

$$k_{ri} = \tan(\psi_i - \theta) \tag{4.4}$$

The left side of the force vector diagram in Figure 4.5 is now broken down into two sets of normalized forces. The first set of forces are $W = 1$, k_v, and $(1 + k_v)k_{r2}$ whose resultant acts along $\mathbf{r}_2$ and thus result in zero angular acceleration. The second set of forces includes the remaining normalized incremental inertial acceleration force (k_{inc}), which results in non-zero angular acceleration. Since the equations of rotational motion need only consider the portion of the force diagram that results in a non-zero angular acceleration, the motion of the rocking block can now be written in terms of a single force. From the right side of force vector diagram in Figure 4.5 it can be seen that $k_{inc} = k_h - (1 + k_v)k_{r2}$. Accounting for rocking on either edges, k_{inc} is expressed as

$$k_{inc} = k_h - (1 + k_v)k_{ri} \tag{4.5}$$

which creates a non-zero torque of $\mathbf{r}_i \times mg\mathbf{k}_{inc}$. The parameter k_{ri} is defined as the *state variable* that allows the block behavior relative to the input motion to be visualized. An alternative equation of motion can now be stated as

$$I_i\ddot{\theta} = \underbrace{mgk_{inc}}_{\text{Force}}\underbrace{r_i\cos(\psi_i - \theta)}_{\text{Moment Arm}} \tag{4.6}$$

where $r_i\cos(\psi_i - \theta)$ will be referred to as the moment arm, R_{mom}.

Equation (4.6) has been derived relative to a horizontal force that causes zero torque. In general, the derivation could be made relative to a force with any particular fixed orientation. The horizontal orientation was chosen because in the simplified case when there is only horizontal loading, k_{rsi} remains constant. This orientation is familiar and the visualization described in subsequent sections is more intuitive. If the orientation is not fixed and taken, for example, at an orientation perpendicular to $\mathbf{r}_i$, then the interpretation would be complicated by a vector that changes orientation since $\mathbf{r}_i$ varies with θ. It is noted that by multiplying the right hand side of Equation (4.6) by $\cos(\psi_i - \theta)/\cos(\psi_i - \theta)$ and rearranging terms it can be shown to be equivalent to the well-established Equation (4.1).

4.2.1 Interpretation of Perturbing and Restoring Forces from k_{ri}

In order to understand the behavior of a rocking block it is important to know whether the net forces are acting on the block as either perturbing or restoring forces. A perturbing and restoring force is one that produces $\ddot{\theta}$ away from and toward the static equilibrium configuration, respectively. This section is dedicated to understanding how k_{ri} allows for these forces to be interpreted. The relationship of how these two forces lead to or prevent toppling of blocks is demonstrated by example in subsequent sections.

Of all terms in Equation (4.6), k_{inc} is the only term that may be positive or negative and thus determines the sign of $\ddot{\theta}$ of the block. However, the sign of k_{inc} alone does not give a direct indication of whether the net force acting on the block at any given time is perturbing or restoring in nature. To determine the nature of the net force, the sign of k_{ri} relative to k_{inc} needs to be evaluated. When these two parameters (and by association $\ddot{\theta}$ and θ) are of the same sign, then the net force is perturbing and when they are of opposite sign the net force is restoring.

While a plot of $\ddot{\theta}$ and θ versus time could reveal the nature of the net force, it is more instructive to plot k_h and $(1 + k_v)k_{ri}$ versus time because the block response can be directly compared to u_{hg}. The usefulness of interpreting the rocking block response in this manner is demonstrated through three loading and geometric cases. For reference, the equations of motions for all examples in this section were solved using a forward Euler finite difference method along with a predictor-corrector method to resolve block impacts. Although more rigorous methods of numerical integration can be used for more accuracy, they are not necessary to demonstrate the use of the state parameter and methods of interpretation described in this paper.

Case 1: $\beta = 0$, $u_{hg} = f(t)$ *and* $u_{vg} = 0$

For simplicity, assume that $\ddot{u}_{hg}(t) = \frac{1}{2}\sin(4\pi t)$, $\ddot{u}_{vg}(t) = 0$ and $\beta = 0$. Since it was assumed earlier that there is no sliding between the block and the plane, $k_h = u_{hg}$. Also, since $k_v = 0$, then $(1 + k_v)k_{ri} = k_{ri}$. Figure 4.6 shows a plot of k_h and k_{ri} versus time. It is also useful, for reference, to plot a horizontal line at the constant value of k_{rs} for each block edge. Recall that when the block is rocking on edge O_2, k_{ri} is positive and when the block is rocking on edge O_1, k_{ri} is negative. Rocking motion begins when k_h first exceeds the bounds of k_{rsi}, which, for this example, happens to be in the positive direction. As implied by Equation (4.5), when the block is on edge 2 and $k_h > k_{ri}$, k_{inc} is positive and the net force is perturbing. When $k_h < k_{ri}$, k_{inc} is negative and the net force is restoring. This interpretation is mirrored about the x-axis when the block is rocking on edge O_1. This means when $k_h < k_{ri}$, k_{inc} is negative and the net force is perturbing and when $k_h > k_{ri}$, k_{inc} is positive and the net force is a restoring force.

As indicated by Equation (4.4), k_{ri} is dependent on θ and ψ_i, therefore, it provides an analog to θ and its time derivatives. The relative magnitude of θ and R_{mom} can be estimated based on the deviation of k_{ri} relative to k_{rsi}. When the block is in the seated, equilibrium position, $k_{ri} = k_{rsi}$ meaning that $\theta = 0$ and R_{mom} is at its minimum. As the block rocks away from the equilibrium position, $|k_{ri}|$ decreases and thus $|\theta|$ and R_{mom} increase. When $k_{ri} = 0$ then θ has reached the toppling angle, ψ_i, and R_{mom} is at its maximum. If the block does not topple then the block begins rocking back toward the equilibrium position. In this case, k_{ri} begins increasing until its value is equal to k_{rsi} at which point the block will undergo a rocking impact and switch rocking edges. These relationships are also shown in

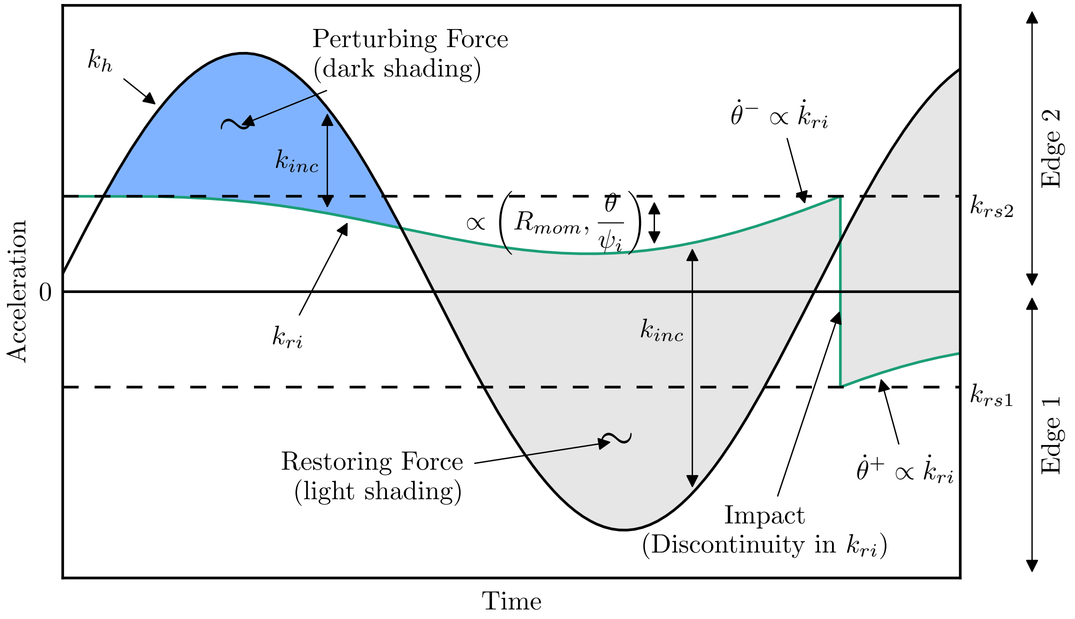

Figure 4.6: Comparison between k_h and k_{ri} for a symmetric block on a level plane. The motion of the plane consists of $\ddot{u}_{hg}(t) = \frac{1}{2}\sin(4\pi t)$ and $\ddot{u}_{vg}(t) = 0$.

Figure 4.6. From these relationships, a sense of the magnitude of the perturbing or restoring torque, $k_{inc} \times R_{mom}$, and thus $\ddot{\theta}$ can be visualized by interpreting the relative magnitudes of k_{inc} and R_{mom}.

Parameter k_{ri} is always non-zero, except when the block reaches the critical toppling angle, ψ_i, at which time $k_{ri} = 0$ where the block is in a precarious position and will most likely topple. However, there are two cases in which k_{ri} can equal zero or appear to equal zero, but the block does not topple. The first case is shown toward the right hand side of the plot in Figure 4.6 and corresponds to a rocking impact as the block switches rocking edges. At this moment the plot of k_{ri} forms a vertical line and appears to momentarily equal zero, which is not the case. This vertical line is actually a discontinuity point in the plot of k_{ri} and the value of k_{ri} remains non-zero but switches sign. The second, and more rare case, was reported by Plaut et al. (1996) where the block may rotate beyond ψ_i momentarily without the result of toppling. Although not shown in Figure 4.6, in this scenario the plot of k_{ri} would momentarily cross and then return about the x-axis (acceleration= 0) at subvertical and likely near horizontal orientations. A plot of this nature would likely take the form of an extrema in a parabolic function.

As indicated previously, k_{ri} is also an analog for the time derivatives of θ. The general slope of k_{ri} is related to $\dot{\theta}$. This is informative in providing a relative indication of $\dot{\theta}$ throughout rocking and more importantly, before and after an impact. The coefficient of restitution, e, can be visualized as a change in slope of $\dot{\theta}$ before and after impact. For $e = 1$, $\dot{\theta}^- = \dot{\theta}^+$, while for $e < 1$, $\dot{\theta}^- > \dot{\theta}^+$, where the superscripts "$-$" and "+" indicate the moments before and after impact, respectively. As will be discussed in later sections, understanding $\dot{\theta}$ before and after impact is crucial in explaining the toppling behavior of blocks.

Case 2: $\beta = 0$, $u_{hg} = f(t)$ *and* $u_{vg} = f(t)$

This next example explores the effects of a vertical motion which can be clearly seen in Equation (4.5). The vertical motion essentially acts to create an effective, instantaneous change of k_{ri} or for $\theta = 0$, k_{rsi}. A change in k_{rsi} means that the block takes on instantaneous attributes of broader or more slender blocks throughout the vertical motion. The effects of the vertical motion are illustrated in Figure 4.7, where the rocking response of a symmetric block to horizontal and vertical earthquake motions is shown. The horizontal (North) and vertical ground motion were taken from station TCU075 of the 1999 Chi Chi, Taiwan earthquake (PEER, 2010). Parameters k_h, k_{ri}, and $(1 + k_v)k_{ri}$ are plotted versus time to allow for interpretation of R_{mom}, θ, and $\dot{\theta}$ and k_{inc}, respectively, as described in previous sections. An effective increase in $|k_{ri}|$ reduces $|k_{inc}|$ if it is a perturbing force and increases $|k_{inc}|$ if it is a restoring force. In this example, before and after impact, the effective $|k_{ri}|$ is increased by the upward vertical ground motion to a point higher than the original k_{rsi} which creates a larger restoring force than would have occurred without vertical motion. Of course, the opposite could have occurred if a downward vertical motion had occurred at the time before and

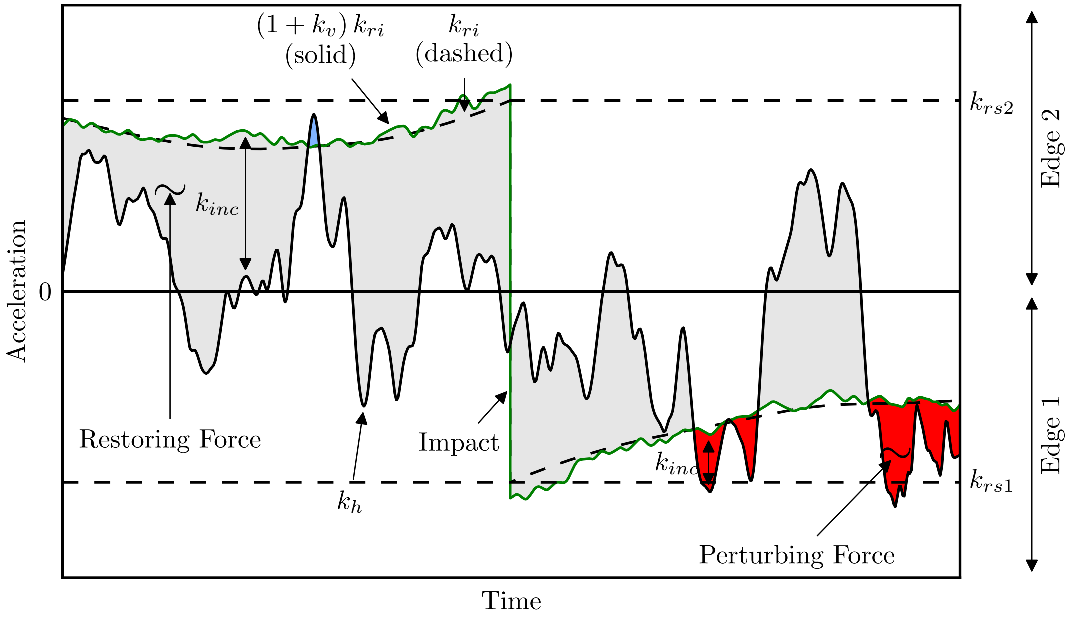

Figure 4.7: Demonstrating the effects of vertical ground motion for a symmetric rocking block on a level plane. The motion of the plane is based on the 1999 Chi-Chi earthquake.

after impact. Ostensibly, the influence of vertical motion does not appear to be significant and k_{ri} appears to be a reasonable approximation for $(1+k_v)k_{ri}$. While it may seem to be a reasonable approximation, had the vertical motion been different, it would have caused dramatically different behavior by changing the instance and quantity of impacts. These differences would change the path of behavior. The vertical ground motion can now be seen as a another source of non-linearity in which the timing of the interaction between k_{ri} with k_h, and therefore the overall response, is altered.

Case 3: $\beta \neq 0$, $u_{hg} = f(t)$ *and* $u_{vg} = 0$

This final example examines the scenario where the block is on an inclined plane and $\ddot{u}_{hg} = \sin(t)$. From Figure 4.2, ψ_i is dependent on β. With any non-zero β, k_{rs1} will no longer

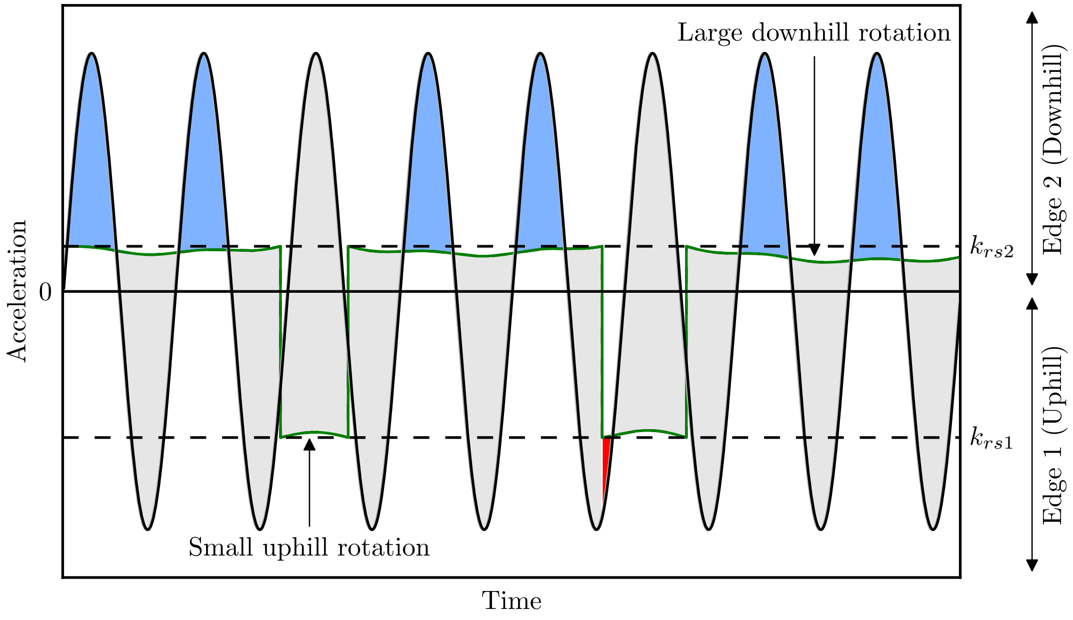

Figure 4.8: Interpreting the effects of a symmetric block rocking on a sloping plane ($\beta = 3°$). The motion of the plane consists of $\ddot{u}_{hg}(t) = \sin(t)$ and $\ddot{u}_{vg}(t) = 0$.

be equal in magnitude to k_{rs2} and k_{inc} and k_{ri} will be substantially effected. Figure 4.8 illustrates the effect of slope angle on the analysis of a rocking block. For rocking in the uphill direction, k_{rs} and k_r are increased relative to the level ground scenario ($\beta = 0$). During a given ground motion, the larger k_{ri} in the uphill direction will reduce the magnitude of perturbing forces and increase the magnitude of restoring forces, along with reducing uphill rotations. The opposite effects are seen for downhill rotations as a result of a reduced k_{ri} relative to the level ground scenario.

4.2.2 Influence of Moment of Inertia, I_i

Makris and Konstantinidis (1998) made the observation that small scale blocks (small I_i) are sensitive to peak ground accelerations, while large scale blocks (large I_i) are more sensitive

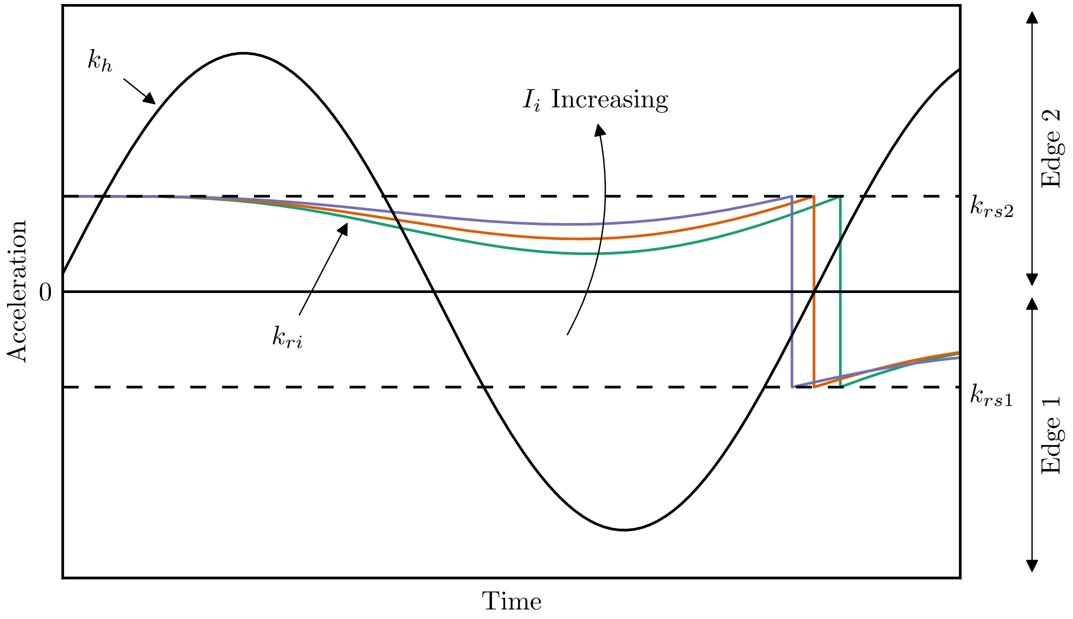

Figure 4.9: Influence of block scale on rocking response, I_i vs k_{ri}.

to incremental ground velocity. This can be explained by examining Equation (4.6) where it can be seen that $\ddot{\theta}$ is inversely proportional to I_i. The influence of I_i can be seen in k_{ri} in the form of an increasingly "muted" response to loading as I_i increases. This muted response can have many secondary consequences on the system such a decrease in θ for many systems for a given loading. The effects of scale are shown in Figure 4.9 where a higher I_i decreases the rocking period and causes impacts to take place sooner. With broadband motions, like earthquakes, a higher I_i can work for either stability or instability as it tends to preserve the current state of $\dot{\theta}$. If the block system is near the static equilibrium position and moving slowly (small $|\theta|$ & $|\dot{\theta}|$) (a common position since nearly all practical systems analyzed start at static equilibrium) then a large I_i will tend to keep the block stable. If the ground motion loading causes the block to accumulate significant rotation (high $|\theta|$) with slow motion (low $|\dot{\theta}|$), then the large I_i tends to hold the block in a sensitive position where a small change

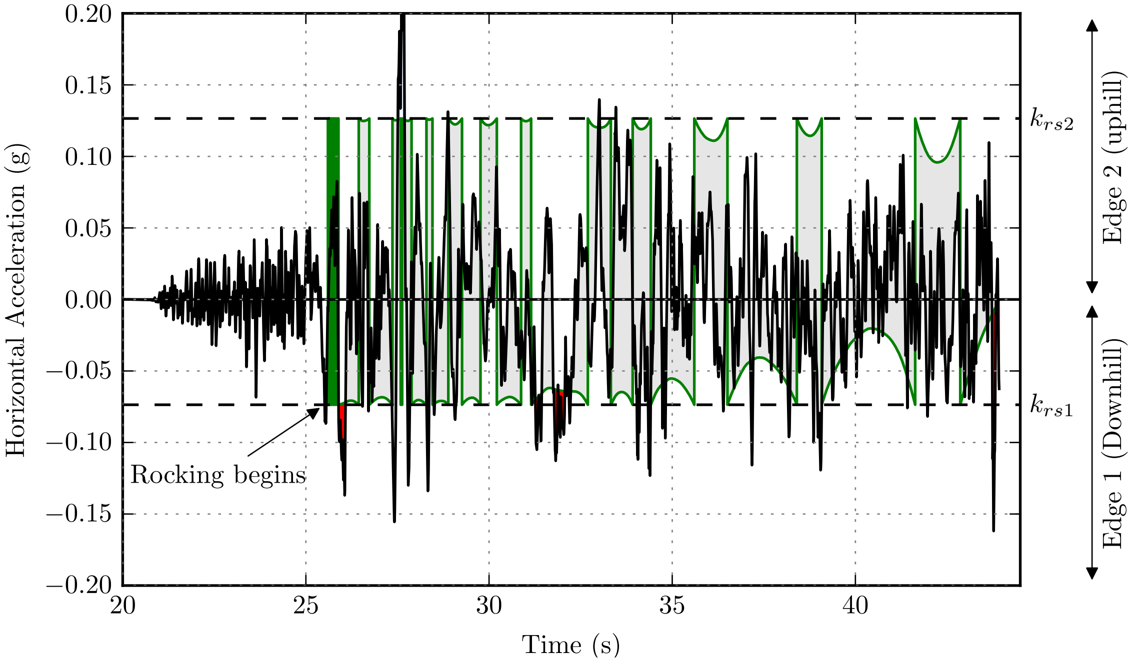

Figure 4.10: Earthquake example: Rectangular block with aspect ratio (base/height)=0.1, height=10.0m, $\beta = -1.5°$, input motion=1999 Chi Chi earthquake.

in θ could result in toppling. When the block manages to accrue significant speed (high $|\dot{\theta}|$) toward toppling, a large I_i will mute $\ddot{\theta}$ which reduces the tendency of the block to reverse direction and avoid a toppling result. Thus, a large I_i value serves, in effect, as a non-linear, low-pass filter of the ground motion. For small I_i, acceleration pulses that exceed k_{rsi} result in high $|\ddot{\theta}|$ and $|\dot{\theta}|$, which often results in near instantaneous overturning if the pulse is of sufficient duration.

4.2.3 Visualizing Behavior of Earthquake Ground Motion with k_{ri}

An application of the use of k_{ri} to visualize and explain the behavior of a rocking block on an inclined plane with an earthquake input motion is shown in Figure 4.10. In this case, a slender rectangular block with an aspect ratio (base/height) equal to 0.1 and height equal to 10 meters is modeled on a plane inclined at an angle of $\beta = -1.5°$. With $\beta < 0$, edge 1 is now on the downhill side of the block, thus $k_{rs1} \approx -0.074$ and $k_{rs2} \approx 0.127$. As with the examples before, horizontal lines are plotted at these k_{rsi}values. The inclined plane is accelerated according to the TCU075-N component of the 1999 Chi Chi earthquake. Assuming no sliding between the block and the plane, k_h equals the input time history applied to the plane. The equations of motion are solved, then the time history of k_h and k_{ri} are added to Figure 4.10. According to the rules applied in the previous sections, interpretation of the block rocking response can now be made.

Rocking of the block begins with an inertial acceleration pulse in the downhill direction. k_{inc} resulting from this acceleration pulse produces a perturbing force that is relatively small and of short duration. Consequently, the block rocks back and forth at high frequency and low amplitude, until the next downhill k_h that exceeds k_{rs1} arrives and instigates a more substantial rocking amplitude. For the next five seconds of ground motion, the block's maximum downhill θ changes little with small perturbing forces and restoring forces that are similar to those under only the influence of gravity. At 32 seconds, there is a set of k_h pulses that exceed k_{ri}, which increases θ and prolong the rotated state of the block. In the next five seconds, the maximum rotation of the block in both the downhill and uphill directions builds more rapidly, primarily under the influence of large restoring forces. At about 36.5 and 38.5 seconds, the block is rotated in the uphill direction and the restoring forces are larger than those caused by gravity. These large restoring forces create large $|\dot{\theta}|$ before the impacts. As the block rotates in the downhill direction at about 37.5 and 40.5 seconds, the restoring forces are smaller than those caused by gravity resulting in large $|\theta|$. This combination of events leads to an increase of $|\dot{\theta}|$ through the impacts and larger overall $|\theta|$. As the block goes through the last impact before toppling, it can be seen that the previous $|\theta_{max}|$ and $|\dot{\theta}^{-}|$ are relatively large compared to previous impacts. After the last impact, there is a mix of small restoring and perturbing forces that result in high frequency $\ddot{\theta}$ in both directions, which do little in the way of reducing $|\dot{\theta}|$ and thus the block overturns.

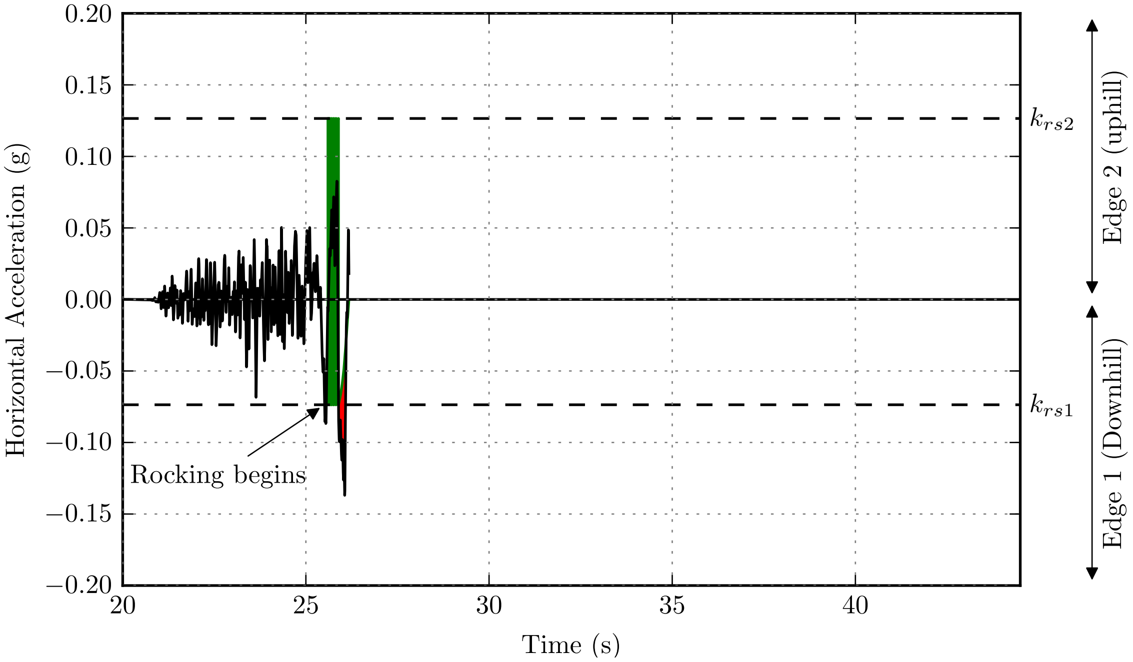

Figure 4.11: Earthquake example: Rectangular block with aspect ratio (base/height)=0.1, height=0.5m, $\beta = -1.5°$, input motion=1999 Chi Chi earthquake.

This case illustrates the mechanisms leading to the overturning of the block. The perturbing forces serve to overcome the first criteria of block overturning, that being exceeding k_{rsi} to begin the block rocking. Once rocking, the influence of the restoring forces take over to increase the rocking amplitude and rocking speed of the block with each subsequent impact. The block rocks until the combination of restoring and perturbing forces in the downhill direction produce an insufficient $\ddot{\theta}$ to reduce and reverse $\dot{\theta}$ and thus the block overturns. When this example is rerun for a smaller scale block with a height = 0.5 meters (Figure 4.11), toppling occurs primarily as a result of the initial inertial forces that produce large angular acceleration because of the reduced moment of inertia of the block.

The result of this previous example may seem counter intuitive at first, but can be understood by envisioning a free rocking block with different initial conditions. If the initial conditions of a free rocking block are set with a large enough non-zero θ or $\dot{\theta}$, the restoring force (gravity) will not be sufficient to prevent the block from overturning in the opposite direction. Each rock of the block throughout the ground motion can be thought of as essentially a small free rocking experiment with an initial θ or $\dot{\theta}$ and restoring force that is more or less than the static gravitational restoring force.

4.3 Model for Toppling of Rock Blocks From Slopes

The equations of motion derived in the previous section are applicable to a 2D rigid block that rocks back and forth on two corners. As mentioned in Section 4.1, in the realm of paleoseismicity, these equations have been used to evaluate precarious (free-standing) rock blocks (PRB's) in nature to estimate ground motion parameters of paleo-earthquakes. As Brune et al. (1996) discusses, PRB's are a relatively special formation that occur in arid regions that have been geologically "quiet" (e.g. no glaciation, earthquakes, and avalanches) for at least 10,000 years. While the use of PRB's is useful for paleoseismology constraints on earthquakes, the occurrence of PRB's in rock slope engineering is not very common. A more common configuration is that of rock blocks that can not rotate backward or are "seated" on fractured rock slopes as shown in Figures 3.4 and 4.12.

The motion of a PRB during forward toppling is similar to "seated" blocks albeit with some key differences. In this section, the full rocking block equations are modified to form a *Toppling Block Model (TBM)*, derived from the traditional rocking block model, that is suitable for rock falls that originate from seated blocks toppling forward. Furthermore, the parameters of these equations are explored in the context of rock block geometries studied in Chapter 3. Since rock blocks rarely conform to the slender assumption used for rocking blocks, the non-linear equations of motion are required. These are solved numerically in a robust manner using event detections to handle the discontinuous nature of the equations. Furthermore, an algorithm is developed to determine the minimum acceleration to induce forward toppling failure given loading by an earthquake ground motion. This algorithm will be used in Section 4.3.1 for simulations of rock block toppling by earthquake ground motion.

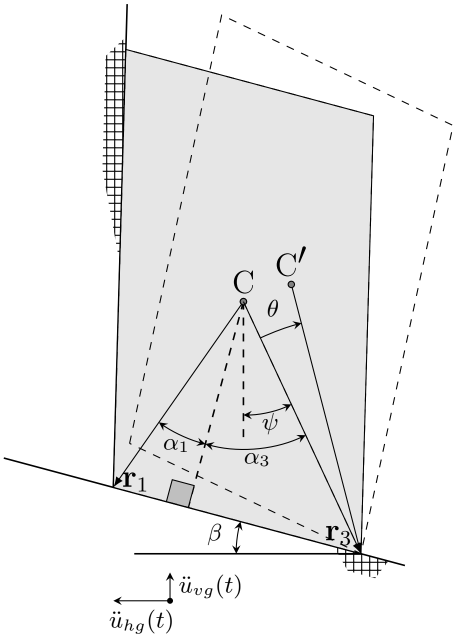

Figure 4.12: Seated rock block that can only rotate forward.

4.3.1 Toppling Block Model Assumptions

The TBM is derived from the rocking block model with additional assumptions in order to approximate the response of a rock block toppling from a slope face. The additional assumptions are as follows:

1. The block has been identified by pseudo-static methods (see Chapter 3) to have a critical failure mode of toppling.
2. The only permissible modes of rigid body motion are rest and rotation about the downhill corner.
3. If the block does not fail and returns to its equilibrium position, its motion stops (i.e. the block does not rebound), therefore it only rocks in the forward direction.
4. There is zero interaction and resistance from any neighboring blocks

The first two assumptions made for the TBM are discussed in more detail below. As a reminder, the assumptions associated with traditional rocking block model remain:

1. The block and fractures are rigid.
2. Impacts occur instantaneously meaning that the bottom of the block is flat or concave causing the point of rotation to change instantaneously.
3. Block motion is 2D in-plane rigid body motion with loading in-plane.
4. The block rotates about a point meaning the block corner is not rounded and does not undergo degradation during rotation.
5. There is zero resistance to rotation about the toe of the block (i.e. a perfect hinge).

Assumption: Rest or Rotational Motion Only

Ishiyama (1982) described various modes of block motion that are possible for a block resting on a plane, which include:

Rest & Rotation. These modes are allowed.

Slide. The pure slide mode has already been excluded by the assumption that the block has been identified by pseudo-static methods to topple ($k_{rs} < k_y$).

Slide-rotation. During base excitation, when pure rotation is the mode of block movement, the inertial acceleration of the block is not limited and is allowed to increase (unlike the case of sliding where base isolation occurs). This means that the remaining block motion that could violate the assumption of pure rocking is that of simultaneous sliding and rocking. Although one might expect the block to begin sliding once k_y is exceeded, this is not the case. Depending on the ratio of k_r to k_y, k_y to PGA, $\ddot{\theta}$, and θ the block will enter a slide-rock mode as some value of k_h greater than k_y Sagaseta

(1986), Shenton III (1996), Pompei et al. (1998), Zhang and Makris (2001), Taniguchi (2002), and Yagoda-Biran and Hatzor (2013), each describe various combinations of horizontal and vertical ground acceleration, friction coefficient, block width to height ratio, and reaction forces to form a criteria of when slide-rock would begin. In general, the block will enter the slide-rock mode at a ratio of k_h to k_y of between one and four.

Translation-jump & Rotation-jump. The jump modes, which occur when $k_v < 0$, are explicitly not analyzed in this thesis.

Assumption: Block Motion Stops Upon Impact With Seat

Obviously, for the rigid blocks shown in Figure 3.4, the block is incapable of rocking back and forth between its toe edge and heel edge like the traditional toppling block because of the kinematic barrier of the back fracture. This barrier means that the impact created by the block returning to its original position is made different by the presence of the back fracture and thus the continuation of motion before and after impact needs to be reevaluated. For the traditional rocking block, the block instantaneously transitions from rotating about one corner to rotating about the other edge. For example from edge O_1 to O_2 as shown in Figure 4.2 or vice versa. Housner (1963) showed for rectangular blocks ($\psi_2 = -\psi_1$), that the change in kinetic energy (i.e. $\Delta\dot{\theta}$) after the impact can be directly related to the geometry of the block through conservation of angular momentum and assuming a perfectly inelastic collision (a smooth transition from edge to edge). The angular velocity after impact considering only geometry was shown to be

$$\dot{\theta^+} = \left(1 - \frac{mr^2}{I_{cm}}(1 - \cos(2\psi))\right)\dot{\theta^-} \tag{4.7}$$

Equation (4.7) always results in a lower post impact angular velocity continuing in the same direction. Shi et al. (1996) performed a similar analysis for asymmetric blocks showing that the asymmetric shape of a block changes the reduction of angular velocity depending on the direction of rocking.

Considering the block returning to a seated position, the only option for the block to continue motion is for it to transition from rotating about its toe to rotating about the top corner in contact with the back fracture. Just before the impact, the velocity vector at the center of mass, $\dot{\mathbf{u}}_{cm}$, is pointing in toward the seat oriented perpendicular to $\mathbf{r}_{toe/cm}$, thus $\dot{\mathbf{u}}_{cm} = r\dot{\theta}$. Following the same procedure as Housner, the angular momentum about the top corner of the block before impact is

$$H_{tc}^{-} = H_{cm} + \mathbf{r}_{cm/top} \times m\dot{\mathbf{u}}_{cm} \tag{4.8}$$

$$H_{tc}^{-} = \dot{\theta}^{-}(I_{cm} - mr^2), \tag{4.9}$$

where I_{cm} is the moment of inertia about the center of mass. Just after the impact, if the block attempts to transition to rotating about the top corner, $\dot{\mathbf{u}}_{cm}$ will reverse direction, therefore the angular momentum after the impact is

$$H_{tc}^{+} = H_{cm} + \mathbf{r}_{cm/tc} \times m\dot{\mathbf{u}}_{cm} \tag{4.10}$$

$$H_{tc}^{+} = \dot{\theta}^{+}(I_{cm} + mr^2). \tag{4.11}$$

From these two equations the angular velocity after the impact is determined as

$$\dot{\theta}^{+} = \left(\frac{I_{cm} - mr^2}{I_{cm} + mr^2}\right)\dot{\theta}^{-}. \tag{4.12}$$

For parallelogram shapes, I_{cm} is equal to a fraction of mr^2, therefore the numerator will always be negative. This means that the angular velocity of the block after the impact tries to rotate the block back into the seat essentially keeping the block pinned into the seat. Repeating this analysis assuming that the pivot point of the block transitions back to the toe yields the same result of an angular acceleration in the direction of rotating the block into the seat. From this logic, it is assumed that the when the block impacts the seat, it will come to rest.

4.3.2 Toppling Block Model Equations of Motion

With the above assumptions, the toppling block model is developed in the rigid plastic framework similar to the Newmark sliding block model, meaning that the block remains at rest relative to the base until the base acceleration exceeds the rocking criteria. Once in motion, the block remains in motion as long as the block is rotated away from its static position ($\theta > 0$). The non-linear equations of motion for a forward toppling block are written as:

$$\ddot{\theta} = p^2 \cos(\theta_c - \theta)\,(\ddot{u}_{hg} - (1 + k_v)k_r) \qquad \text{when, } \ddot{u}_{hg} > (1 + k_v)k_r \text{ or } \theta > 0 \tag{4.13}$$

$$\ddot{\theta} = 0 \qquad \text{all other times,} \tag{4.14}$$

where the critical angle $\theta_c = \psi = \alpha_3 - \beta$ and $k_r = \tan(\theta_c - \theta)$. These equations are similar to the equations for the sliding block model which are

$$\ddot{x} = \ddot{u}_{hg} - (1 + k_v)k_y \qquad \text{when, } \ddot{u}_{hg} > ky \text{ or } \dot{x} > 0 \tag{4.15}$$

$$\ddot{x} = 0 \qquad \text{all other times,} \tag{4.16}$$

where x is relative to the base. However, there are few differences to note:

1. The critical acceleration k_r for toppling is non-linear and dependent on geometry and friction while k_y for sliding is constant and dependent only on friction.

2. The toppling equation is scaled by p^2 which will result in different responses depending on the geometry of the block, while the response in the sliding block model is scale independent for Coulomb-friction surfaces.

3. The toppling block motion does not stop until the block returns to its initial position, while the sliding block motion does not stop until the relative velocity between the block and base fracture is zero.

4. The final outcome for the toppling model is either a block that is at rest in its initial state or a block that has toppled. The sliding block model results in some permanent displacement.

4.3.3 Solution by Numerical Integration

Given that these equations are non-linear and discontinuous, they will need to be solved by numerical methods. Many researchers attempt to solve these equations using a numerical integrator which assumes continuity, such as Matlab's ODE45 solver. While their simulations may be stable (in that a solution is calculated), error is introduced every time integration is performed across a discontinuity in the equations and grows as the time step of integration increases. Alternatively, if care is taken to have an integration point on each side of the discontinuity, then the errors associated with integration can be reduced and larger time steps can be taken without introducing significant error. This is the approach taken for the simulations presented in this chapter. The equations of motion are solved by using the Sundials Fortran solver, CVode, interfaced with Python using the package Assimulo (Fredriksson et al., 2014; Andersson et al., 2015). Assimulo provides an interface to specify discontinuities through events that will be detected by the numerical solver. When an event is detected, changes to the equations of motion or model state are necessary. In this scenario, the numerical integrator stops and reevaluates the previous time step at finer increments until the location of the discontinuity in time is determined within a specified error. In the mathematical literature this is referred to as root finding.

There are several states of the model that are monitored for events as follows:

Event 1 $[\ddot{u}_{hg} > (1 + k_v)k_r]$**:**

This fundamental event is triggered when the ground motion exceeds the block's rocking acceleration and the nonzero equations of motion should be used. If the ground motion falls below the rocking acceleration there is no effect on whether the equations of motion should be switched or not. Ceasing of rocking motion depends on Event 2 described next.

Event 2 $[\theta]$**:**

Once rotational motion of the block begins as described by Event 1 then the block will have a positive angular displacement. As long as θ is positive, the block is on edge and should remain in motion. When θ decreases to zero, meaning the block is back to its original static configuration, then the block's angular displacement and velocity are set to zero. The equations of motion are set to zero if at the same time the ground motion is also below the rocking acceleration.

Event 3 $[k_r < \ddot{u}_{hg,restore,remaining}$ **AND** $\dot{\theta} > 0]$**:**

Voyagaki et al. (2013a) shows that the block's instantaneous equilibrium position occurs when

$$g \sin(\psi - \theta(t)) = \ddot{u}_{hg}(t) \cos(\psi - \theta(t)), \tag{4.17}$$

linearized as

$$\theta(t) = \psi - \ddot{u}_{hg}(t)/g. \tag{4.18}$$

Note that although this criteria has been linearized, it still indicates that the block can rotate beyond θ_c and be brought back by downhill ground motion. As a reminder, downhill ground motion will create an inertial force in the uphill direction. If the notation of k_r is used, then the criteria for instantaneous equilibrium without linearization becomes

$$k_r = \frac{\ddot{u}^+_{hg}(t)}{g} \tag{4.19}$$

where $\ddot{u}^-_{hg}(t)/g$ is the peak down hill acceleration. Furthermore, if the entire ground motion is considered, then the block is not guaranteed to overturn until at any point in time k_r is less than the peak down accelerations remaining in the time history and the block has a forward velocity $\dot{\theta} > 0$). This event is based on this criteria which signals that the block is in an irrecoverable position and terminates the simulation. It is possible that overturning is inevitable at an earlier point in time, however, that cannot be determined without also evaluating the frequency of the motion.

4.3.4 Solving for Critical Toppling Yield Acceleration

As was previously discussed, the minimum peak acceleration magnitude that will overturn a block has been sought after since the beginning of the rocking block literature. Generally, this is accomplished by performing a series of simulations in which the peak amplitude of a signal, such as a sine wave that lasts for one cycle, is increased until overturning of the block is detected. This approach is sound, except for the case of earthquake ground motions where it is desired to keep the input signal fixed. In this case, k_{rs} can be systematically reduced until a block exhibits overturning (threshold) response in a similar approach that was pioneered for earth dams by Makdisi and Seed (1978). When this approach is applied for sliding block models, the threshold response becomes asymptotic relative to changes in the critical acceleration (Strenk and Wartman, 2011). This behavior has also been shown to be true for the rocking block (Sorrentino et al., 2006).

To search for this asymptote, it is necessary to make small changes in k_{rs} between successive simulations, however these small steps can result in a large number of simulations. Optimization can be gain by taking large steps in k_{rs} while the threshold response is small and then decreasing the steps in k_{rs} as the change in threshold response becomes relatively large. Initial simulations are performed at high values of k_{rs}/PGA to establish an initial trend, in this case $k_{rs}/PGA = [0.99, 0.95]$. From this point spline interpolation $\log(\theta_n)$ vs k_{rs}/PGA is used to predict the next target simulation point based on a series of preset target θ_n values, where $\theta_n = \theta/\theta_c$. It is inevitable that the asymptote will be "overshot" and in the case of toppling blocks which means large irrecoverable angular displacements. In this scenario, it is useful to "backup" the search by increasing k_{rs} in very small increments until the block exhibits a non-overturning response again. Lastly, since some changes in k_{rs} may result in large unexpected changes in the threshold response, it is prudent to "fill-in" simulations between this large jump. Figure 4.13 demonstrates this concept by example. The initial points represent the initial stepping by reducing k_{rs}/PGA until the failure farthest failure point is reached. At this time k_{rs}/PGA is increased in very small increments producing

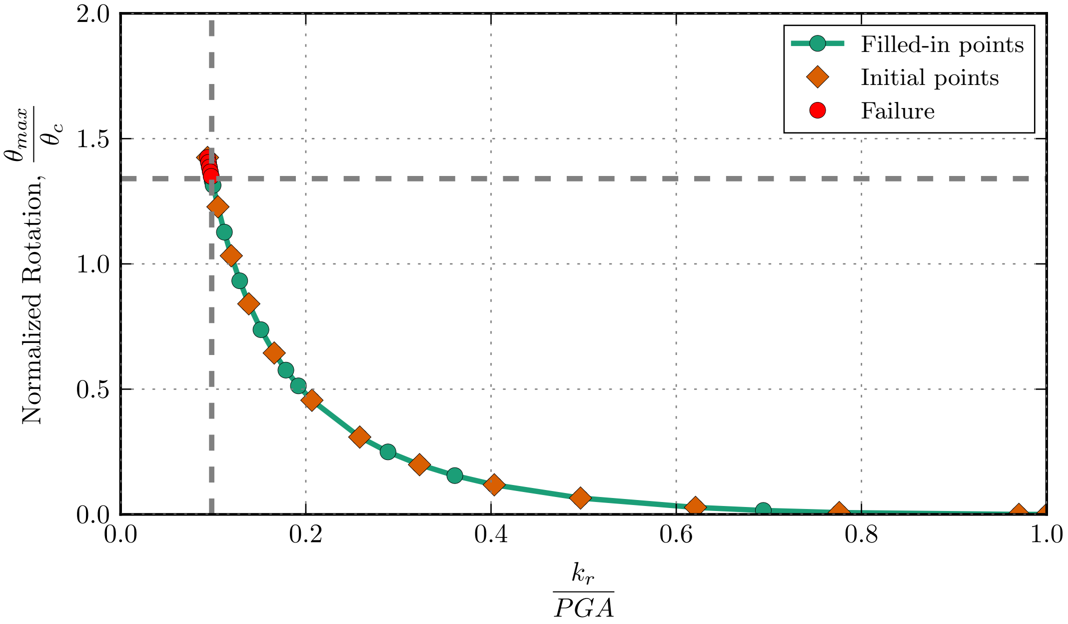

Figure 4.13: Solution scheme to determine critical k_r/PGA

more failure points until a non-failure point is found. Finally, simulations at the green circle points are performed to provided better definition of the curve. The horizontal and vertical dashed lines mark the parameters which represent the interpreted boundary between failure and stability.

4.3.5 Model Verification

Model verification was performed by comparing the results of the numerical model developed above with published closed-form solutions for blocks to illustrate over rotation and correct prediction for various pulses. Closed-form solutions are only available for the linearized form of the rocking equations. For the purpose of verification, the equations of motion in the toppling model are set to linear mode which makes $k_r = \tan(\theta_c - \theta) \approx \theta_c - \theta$ and the moment arm factor $\cos(\theta_c - \theta) \approx 1$. Note that although k_r is linearized in the equations of motion, results are still presented in terms of $k_{rs} = \tan(\theta_c)$ There are many researchers who have presented closed-form solutions to the rocking block equations subject to various simplified loading (e.g. Housner (1963); Yim et al. (1980); Shi et al. (1996); Anooshehpoor et al. (1999); Makris and Roussos (2000); Zhang and Makris (2001); Özer and Alışverişci (2005); Dimitrakopoulos and DeJong (2012); Voyagaki et al. (2013b,a)). Voyagaki et al. (2013a) will be used for verification since it provides the most comprehensive set of closed-form solutions for various pulse loadings and also includes the ability for rotation beyond θ_c.

Consider the closed form solution for the normalized peak amplitude (θ_n) and critical k_{rs}/PGA to a rectangular wave from Voyagaki et al. (2013a):

$$\frac{\psi}{PGA} = \left(1 - e^{-f}\right)^2 \tag{4.20a}$$

$$\theta_n = 1 + \frac{e^{2f} - \left(1 - 2e^{f} + 2e^{3f}\right)^{1/2}}{\left(e^{f} - 1\right)^2} \tag{4.20b}$$

where $f = \frac{1/2}{p}T$. If Equation (4.20a) is written in terms of k_{rs}, then:

$$\frac{k_{rs}}{PGA} = \frac{\tan\left(\left(1 - e^{-f}\right)^2 PGA\right)}{PGA} \tag{4.21}$$

Now consider a series of blocks with $p^2 = [1.0, 1.7, 2.8, 4.6, 7.7, 12.9, 21.5, 35.9, 59.9, 100.0]$ subject to a rectangular wave with peak amplitude, $PGA = 1$, and period, $T = 1/3$. The minimum value of k_{rs}/PGA determined from the asymptote search compared to the closed-form solution is shown in Figure 4.14. The red dotted line and dots represents the predicted boundary made by Voyagaki for the linearized solution. For these simulations as k_{rs}/PGA gets larger the blocks are also becoming less slender. Excellent agreement is seen between the numerical simulations using the search algorithm and the closed-form, analytical solution. From this plot, the "excess" rotation ($\theta_{max}/\psi > 1$) for a full rectangular pulse can be seen by the end of the plot lines that indicate where the block became unstable as predicted by Voyagaki et al. (2013a). Notice for non-slender blocks that as $k_r/PGA \rightarrow 0$, θ_{max}/ψ does

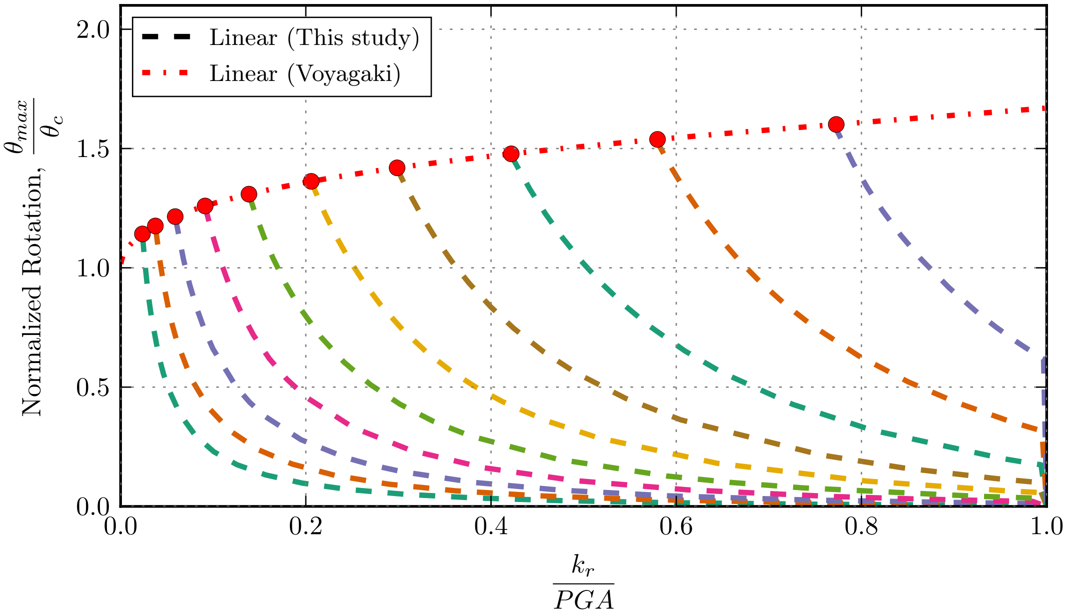

Figure 4.14: Verification of rectangular wave (linear solution).

not approach zero. This is because the moment arm for the block should be $\cos(\psi)$ which is less than the linearized ψ.

4.3.6 Selection of Non-Linear Simulation Over Linear

The linear solution to rocking blocks is used throughout the literature since most researchers limit their research to slender blocks. For the evaluation of rock block toppling in slopes, the slender block assumption will be violated quite often; therefore, it is necessary to use a non-linear solution. A comparison between the non-linear and linear solution is shown in Figure 4.15. The solid and dashed lines represent the non-linear and linear numerical solutions, respectively. As expected, as the blocks become non slender, the linear solution becomes inaccurate and unconservative, predicting higher $\frac{k_r}{PGA}$ than the non-linear solution. These results verify the conclusion made by Dimitrakopoulos and DeJong (2012) who showed

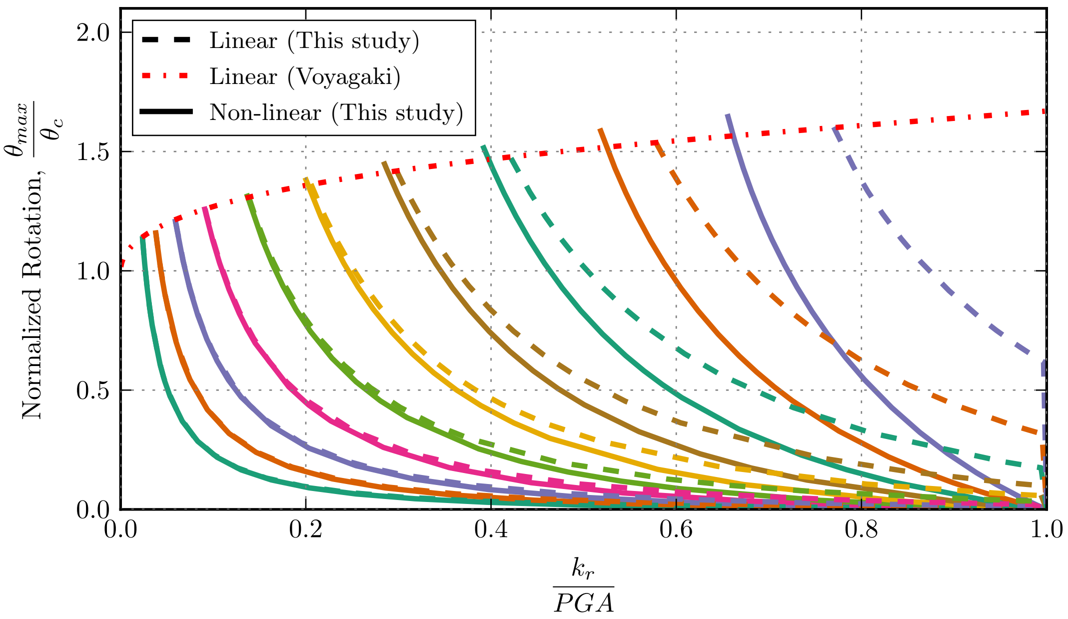

Figure 4.15: Comparison of k_r/PGA for the linear and non-linear solution.

through dimensionless analysis that it was necessary to use the non-linear equations in order to accurately predict self-similar response for rocking blocks.

4.3.7 Validation by Centrifuge Modeling

Validation of the toppling block model is based on centrifuge experiments conducted by Applegate and Wartman (2011, 2012, 2013). Horizontal and vertical accelerations of as measured by accelerometers at the base of the ramp are shown in Figure 4.16a. The block response as modeled with the toppling block model is shown in Figure 4.16b. Overturning occurs at about four seconds into the time history which matches the response in the centrifuge as confirmed by high speed video evidence.

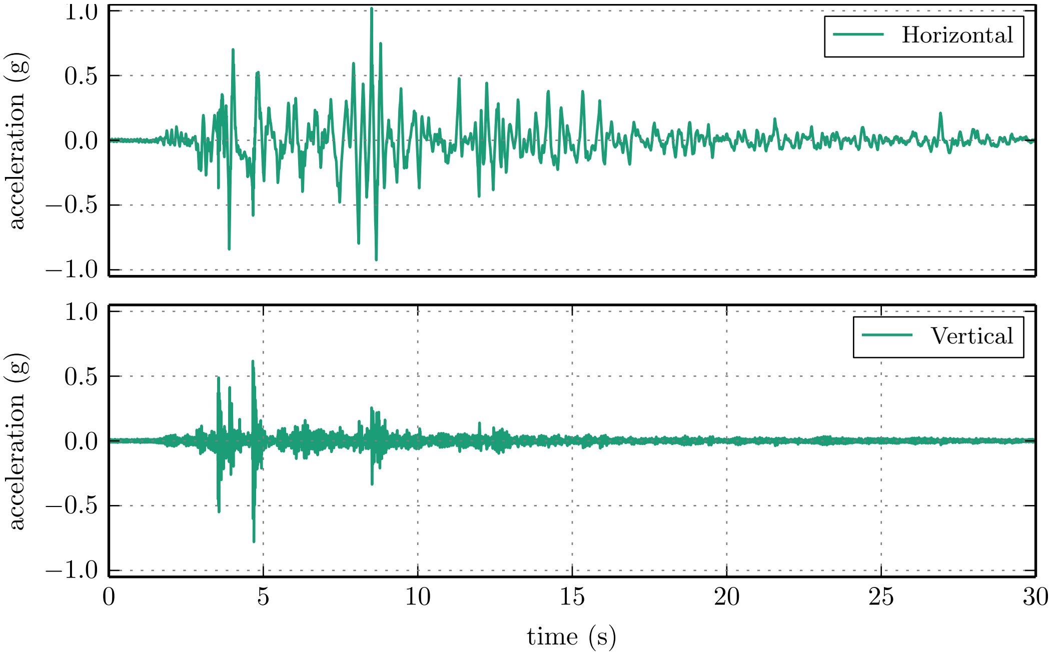

(a) Measured base fracture accelerations in centrifuge

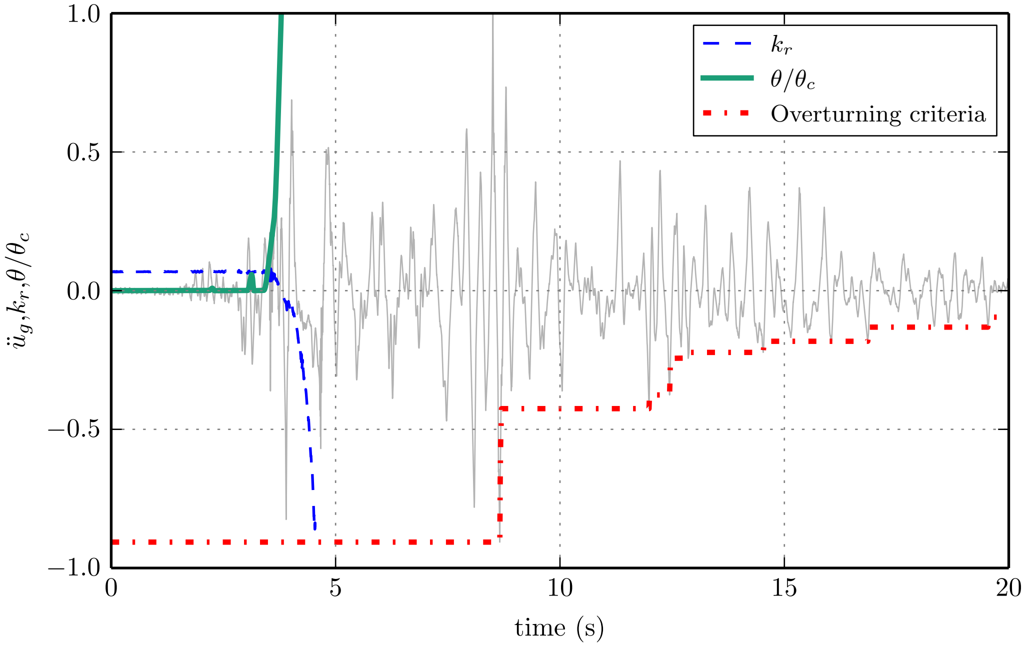

(b) Toppling block response

Figure 4.16: Model verification based on centrifuge experiment of rock block toppling (File: *Topple 25deg Kocaeli 1bl* from Applegate and Wartman (2013)).

4.3.8 Response to Simple Sinusoidal Pulses

The model performance is demonstrated by evaluating a rock block given simple ground motion loadings approximated by a sinusoidal-like shape as shown in Figure 4.17. The first half of the sinusoidal shapes have a peak acceleration amplitude in the uphill direction (PGA^+) of 1.0g and period of 0.5 seconds. The second half have a varying degree of amplitude ranging from 0 to 1.5g. The upper bound of 1.5g ($\approx 1/0.65$) was chosen based on the widely prevalent use of 0.65 in geotechnical earthquake engineering. After one period (or one cycle) of motion, the ground motion is set to zero for five additional seconds to allow the block to "finish" its motion. These loading pulses are shown in Figure 4.17a as the solid lines labeled by the magnitude of the reversals.

Consider a block with the property, $p^2 = 2$ and property k_{rs} set such that the approximate maximum amplitude of rocking is achieved without toppling. For each of the sine pulses shown, the critical value of k_r is different resulting essentially into the analysis of blocks that become progressively more slender as the reversal increases. The normalized angular displacement ($\theta_n = \theta/\theta_c$) and angular velocity response is shown in Figures 4.17b and 4.17c. As Voyagaki et al. (2013b) discussed, these examples illustrate that the blocks are capable of rotating beyond θ_c if sufficient downhill acceleration occurs while the block is in that precarious position. It is interesting to note that only for reversal pulses greater than $-0.65PGA^+$ does the block rotate beyond θ_c and return safely to the seated position. In addition, if the reversal pulse were allowed to increase without limit ($PGA^- \to \infty$) then the equations of motion would allow $\theta \to \infty$ and still allow the block to return to its seat. Naturally, any rotation calculated beyond the amount that results in the block fully overturned onto its face is meaningless. Also if the rotation exceeds a point such that block's pseudo-static failure mode in the opposite direction is sliding then the block will not be able to rotate back to its seat.

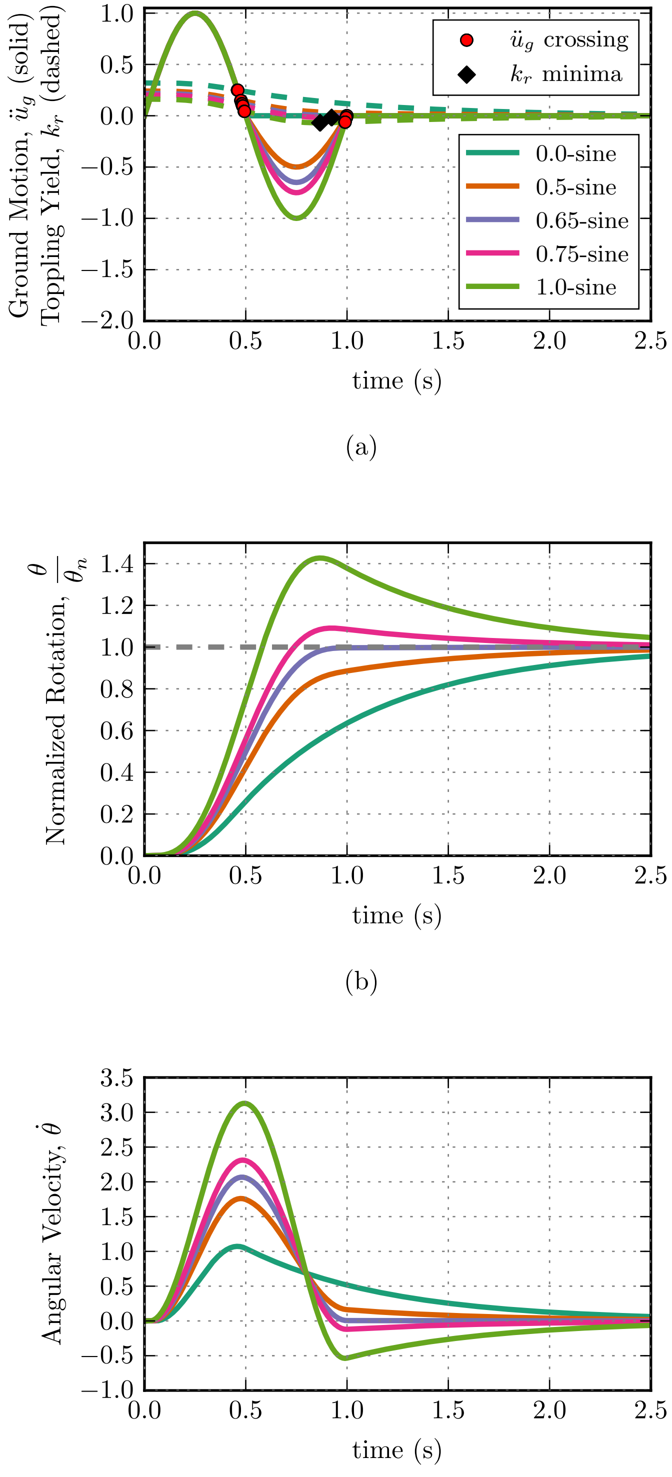

(a)

(b)

(c)

Figure 4.17: Toppling model response to sinusoidal-like ground motion input

4.3.9 Response to Earthquake Ground Motion

The response of a forward toppling rock block to a sample earthquake ground motion is shown in Figure 4.18. In each plot, the block's response from several simulations are shown as the block's k_r is gradually decreased until a failure condition is reached. In one case (Figure 4.18d), two failure simulations are shown to illustrate that for very small changes is k_r the block can fail at different moments in the time history. From a deterministic point of view, this represents the chaos that is expected from toppling rock blocks. It is also interesting to see that for large blocks that react slowly because of their large moment of inertia that their subcritical response easily spans many pulses of velocity while smaller blocks rarely span multiple pulses. Ultimately, when compared to both the acceleration and velocity time histories it can be seen by inspection that the largest ground motion pulses lead to overturning of the block.

4.4 Effects of Rock Block Geometry on Toppling Model Parameters

It is quite common, given the wide range of the number, orientation, and spacing of fractures in any particular rock slope to have block shapes that vary greatly. Therefore it is prudent to evaluate how the parameters of p^2, α_3, and block scale, represented by r_3, interact.

To investigate this relationship, first consider a rectangular shape. It was discussed previously that $p^2 = \frac{3g}{4r_3}$, therefore p^2 is only a function of r_3 which can be thought of as the scale of the block. Note that there is no dependence on the slenderness of the block. This result is expected if the definition of mass moment of inertia in Equation (4.22) is considered for a rigid body,

$$I_p = \int \rho(r) r^2 dA \tag{4.22}$$

where, I_p is the mass moment of inertia about some point p, r is the vector from the point of rotation to a point p on the body. If the density and the shape is considered constant then $\rho(r) = m/A$, so m/A can be brought outside the integral resulting in Equation (4.23)

$$I_p = m/A \int r^2 dA. \tag{4.23}$$

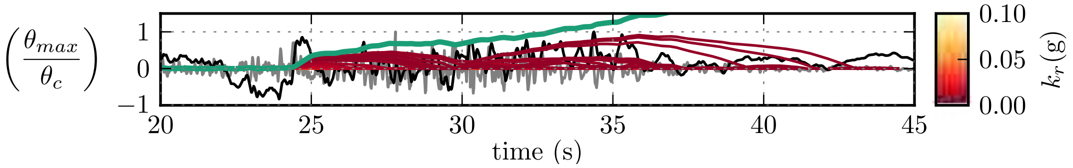

(a) $\omega_m/p = 49.6$ at $k_r/k_{max} = 0.017$

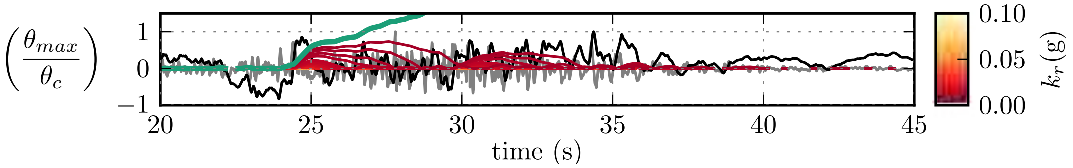

(b) $\omega_m/p = 28.1$ at $k_r/k_{max} = 0.035$

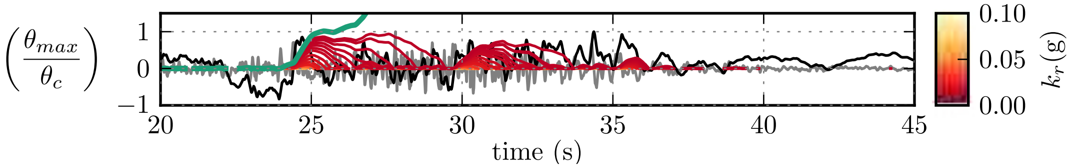

(c) $\omega_m/p = 15.9$ at $k_r/k_{max} = 0.061$

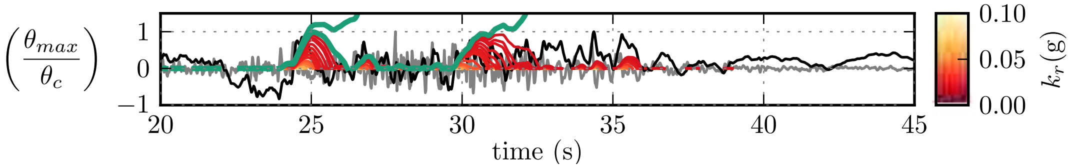

(d) $\omega_m/p = 9.0$ at $k_r/k_{max} = 0.102$

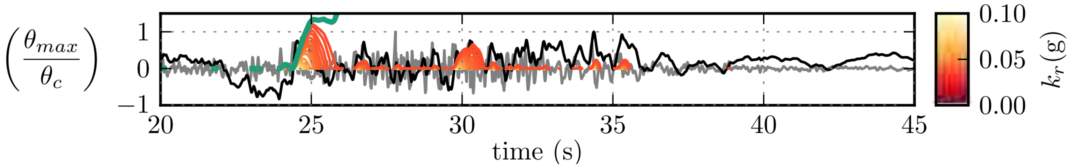

(e) $\omega_m/p = 5.1$ at $k_r/k_{max} = 0.186$

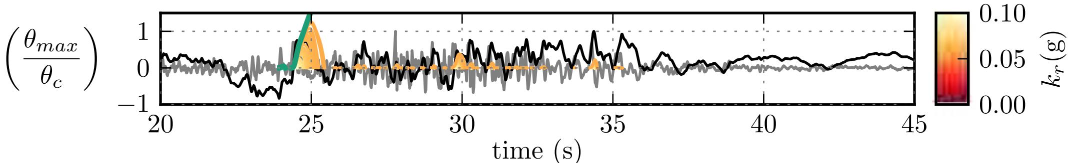

(f) $\omega_m/p = 2.9$ at $k_r/k_{max} = 0.309$

Figure 4.18: Forward toppling response to earthquake ground motion. The dark time history is the velocity normalized to PGV while the gray time history is the acceleration normalized to PGA. The yellow to red lines represent the block's rotational response as the block's k_r is reduced until failure occurs. The failure run is shown as the thick green line.

If it is assumed that $f_s\mathbf{r} = r_3\hat{\mathbf{r}}$, where $f_s = \frac{r_3}{||\mathbf{r}||}$, then

$$I_p = mr_3^2/A \int \frac{\hat{\mathbf{r}}^2 dA}{f_s}. \tag{4.24}$$

Since the length of $\hat{\mathbf{r}} = 1$, the integral evaluates to $\frac{A}{F_s}$, thus

$$I_p = \frac{mr_3^2}{F_s} \tag{4.25}$$

where F_s is the sum of $\frac{r_3}{r}$ which is solely dependent on the shape. Alternatively, I_p of an N-sided polygon can be calculated using the known vertices $P_1 \ldots P_n$ as

$$I_p = \frac{m}{6} \frac{\sum_{n=1}^{N} \|\mathbf{P}_{n+1} \times \mathbf{P}_n\| ((\mathbf{P}_{n+1} \cdot \mathbf{P}_{n+1}) + (\mathbf{P}_{n+1} \cdot \mathbf{P}_n) + (\mathbf{P}_n \cdot \mathbf{P}_n))}{\sum_{n=1}^{N} \|\mathbf{P}_{n+1} \times \mathbf{P}_n\|} \tag{4.26}$$

If the point p is considered the point about which the block would topple, then the calculation of p^2 is

$$p^2 = \frac{mgr_3}{I_p} = \frac{mgr_3F_s}{mr_3^2} = \frac{gF_s}{r_3} \tag{4.27}$$

Note that there is no dependence on the slenderness. This equations means that for a constant shape, p^2 only changes as the scale of the block changes. Comparing this equation to that of the rectangle by Housner (1963), it can be seen by inspection that $F_s = 3/4$.

Since the pseudo-static yield accelerations were evaluated previously for parallelogram shapes, p^2 will be evaluated numerically for these same shapes. The parallelogram can be completely described by the angles α_1, α_3, and either r_1 or r_3. Figure 4.19 presents the results of calculating p^2 for parallelograms for the parameter ranges of α_3 = [5°,25°,45°], 10 values of α_1 between $-\alpha_3$ and α_3, and r_3 = [0.1m,1.0m,10.0m,100.0m]. It can be seen that p^2 is relatively constant for a constant scale r_3, similar to the rectangular block. There is some variance with α_1, where the maximum deviation in p^2 relative to the special case where the parallelogram is equivalent to a rectangle is approximately 0.01%, 2.26%, 6.61% for $\alpha_3 = 5°, 25°, 45°$, respectively. The F_s for these blocks ranges between 3/4 and 1. In most cases this error is small enough that r_3 of the parallelogram could be used to calculate p^2

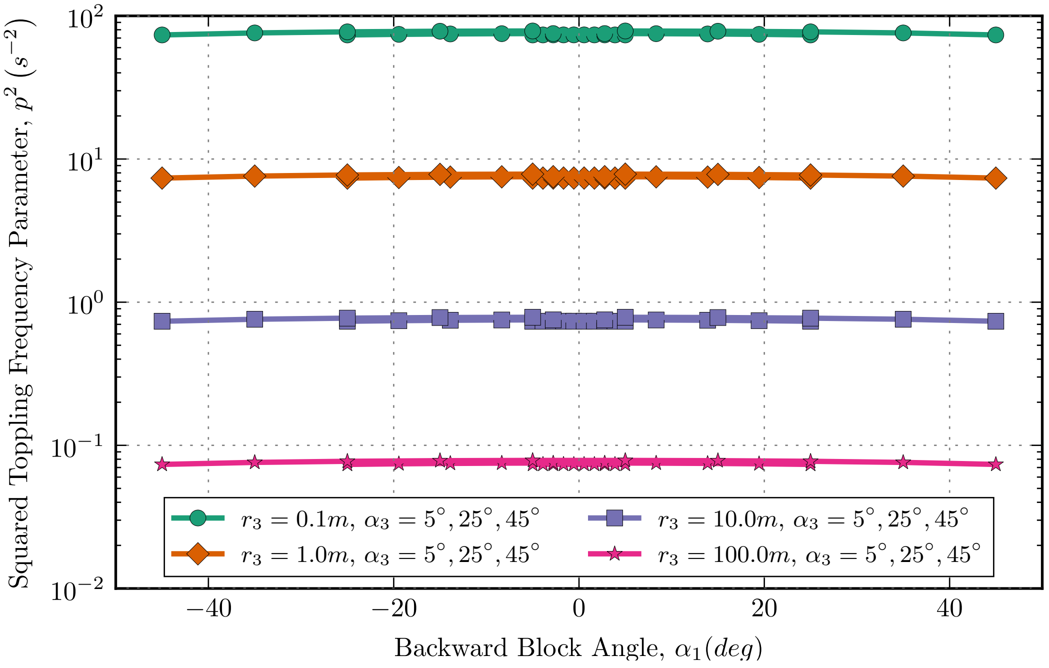

(a) Relationship of block parameters to the block frequency parameter, p^2

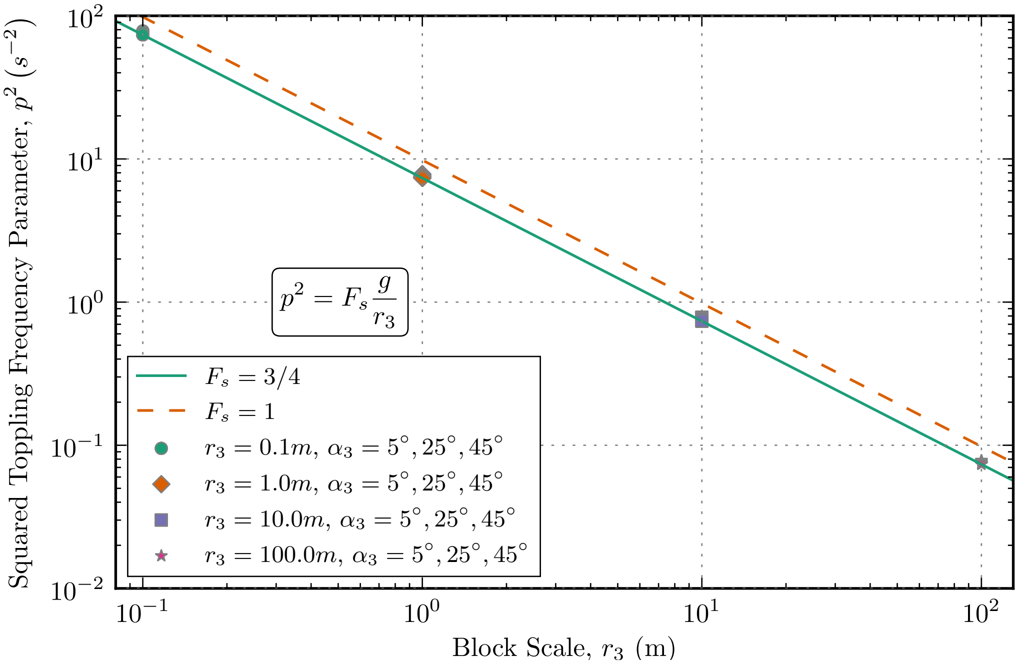

(b) Relationship of block scale to the block frequency parameter, p^2

Figure 4.19: Relationship between p^2 and r_3 for parallelograms of various shapes (See Chapter 3).

directly based on the rectangle formula. However, it is relatively trivial to calculate the exact p^2. A similar calculation performed for various trapezoidal shapes, indicates that $2 \leq F_s \geq 5$. In any case, this result shows that many shapes have similar p^2 such that it is not necessary to evaluate every possible block shape but the range of possible p^2.

The implication of this discussion, is that if the joint structure of a slope is relatively constant, then for blocks whose primary failure mode is toppling, only one calculation per shape is necessary to determine F_s. This factor could be applied to all similar shapes on the slope. In subsequent sections, it will be come evident that this knowledge will allow for the analysis of a rock slope system with two block parameters, two earthquake parameters, and a design chart.

4.5 Rock Block Toppling Response to Earthquake Ground Motions

In this section, a parametric analysis is performed with the toppling block model in which p^2 and the earthquake ground motion are varied. Since p^2 was previously related to various geometries it is only necessary to evaluate a representative range of p^2, not an infinite number of different block shapes and associated parameters. For each parametric combination, the search algorithm outlined in the previous section is used to find the critical k_r/PGA that results in toppling.

4.5.1 Earthquake Ground Motion Simulations

Earthquake Time Histories

Unique earthquake time histories (537 horizontal motions and 104 vertical motions) were selected from various sources. Additional information about the ground motions (e.g. magnitude, distance, PGA) is provided in Appendix A. In general, several suites of ground motions were selected as follows:

PEER

This set of motions consist of 427 horizontal components and 104 associated vertical motions (when available). They include all the motions from the PEER strong ground motion database (PEER, 2010) with a site shear wave velocity greater than 600m/s. The shear wave velocity boundary was chosen with the idea that the time histories would be more related to rock-like geologic profiles.

Baker

Broadband and pulse-like motions (40 each) were selected based on sets 2 and 3 of the motions developed by Baker et al. (2011). The purpose of these motion sets is to assess whether the spectral shape of a ground motion produces a unique signature in the results.

Spectrally Matched

This set of 30 motions were spectrally matched and developed by Astaneh (2013) and are unpublished. The purpose of this motion set is to assess whether spectrally matched motions produce a different response pattern than unmatched motions.

All motions were derived from the PEER database and thus are associated to a NGA reference number. Eight combinations of each ground motion set were evaluated and consisted of two horizontal components, horizontal with and without vertical, and horizontal time history polarity. The possible combinations are summarized in Table 4.1 below. In some cases, when the complimentary vertical motion for a ground motion set was not available or inconsistent with the horizontal components (i.e. different signal length) then the horizontal with vertical combinations were omitted.

Geometries

A range of values for $p^2 = [30.0, 10.0, 3.0, 1.0, 0.3, 0.1]\left(\frac{1}{sec^2}\right)$ were chosen to represent a range of block sizes. For rectangular blocks, this would represent a range of $||\mathbf{r_3}|| = [0.25, 0.74, 2.45, 7.36, 24.53, 73.57](m)$, respectively. For parallelogram blocks with α_3 from

Table 4.1: Possible earthquake simulation combinations.

Combination	Component	Vertical	Polarity
1	1	No	Forward
2	1	Yes	Forward
3	2	No	Forward
4	2	Yes	Forward
5	1	No	Reverse
6	1	Yes	Reverse
7	2	No	Reverse
8	2	Yes	Reverse

0 to 45°, $||\mathbf{r_3}|| \approx [0.33, 0.98, 3.27, 9.81, 32.7, 98.1](m)$, respectively. For each value of p^2, simulations for each of the eight combinations per ground motion were performed.

Simulations

For each time history and geometry combinations, the search algorithm described in Section 4.3.4 was used to determine the critical k_r that results in toppling. The total number of combinations totaled $11,278$ requiring a total number of simulations of $259,749$ to determine the critical k_r. For computational purposes, the lower limit of k_r/PGA was set to 0.01. The relationships of $\frac{k_r}{PGA}$ versus $\frac{\theta}{\theta_c}$ were recorded for each simulations. In addition the entire time dependent response of each simulation was recorded. The results of these simulations were parsed and uploaded to a MYSQL database for further processing and visualization. In some cases for very large blocks (low p^2), the limit set on k_r/PGA ended the simulations before the critical k_r could be determined. In these scenarios the results of these simulations were recorded but omitted from the evaluation of "failed" blocks. Table 4.2 summarizes some basic statistics about the number of combinations that determined a critical k_r.

Table 4.2: Toppling simulation summary statistics

	PEER	Baker-Broadband	Baker-Pulse	Spectrally-Matched
Total simulations	7029	1848	1882	355
Simulations with vertical	2258	912	929	0
Simulations w/o vertical	4771	936	953	355
Unique NGA motions	222	40	40	30
Unique earthquakes	222	40	40	30
Unique horizontal motions	427	80	80	30
Unique vertical motions	104	39	39	0

4.5.2 Simulation Results

A histogram of the results from all ground motion sources plotted in terms of the typical dimensionless parameters for rocking blocks (k_r/PGA and ω_m/p) are shown in Figure 4.20. The non-linear simulation data is compared to the closed-form solutions of the linear equations of motion for various pulse shapes by Voyagaki et al. (2013b). For each plot, the safe zone (the zone where combinations of block and ground motion parameters result in no toppling) is located above the data/lines. The data does not coalesce along a line for two reasons:

1. The ground motion parameters $\omega_m = 2\pi/T_m$ and PGA are being used as proxies for motion frequency and amplitude, which is an approximation for an earthquake.

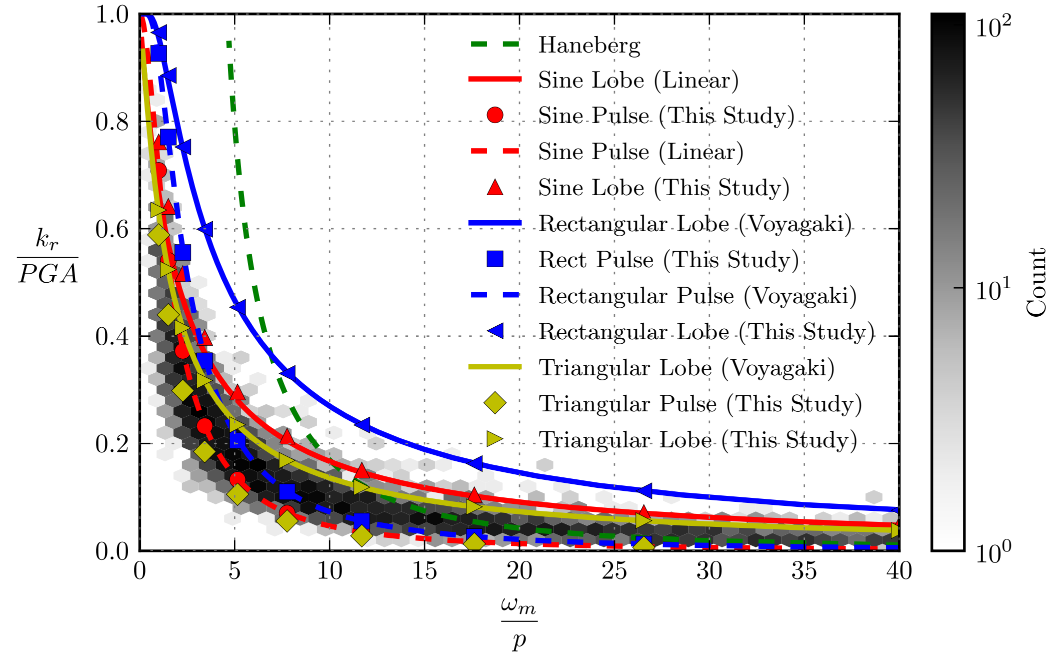

(a) linear space

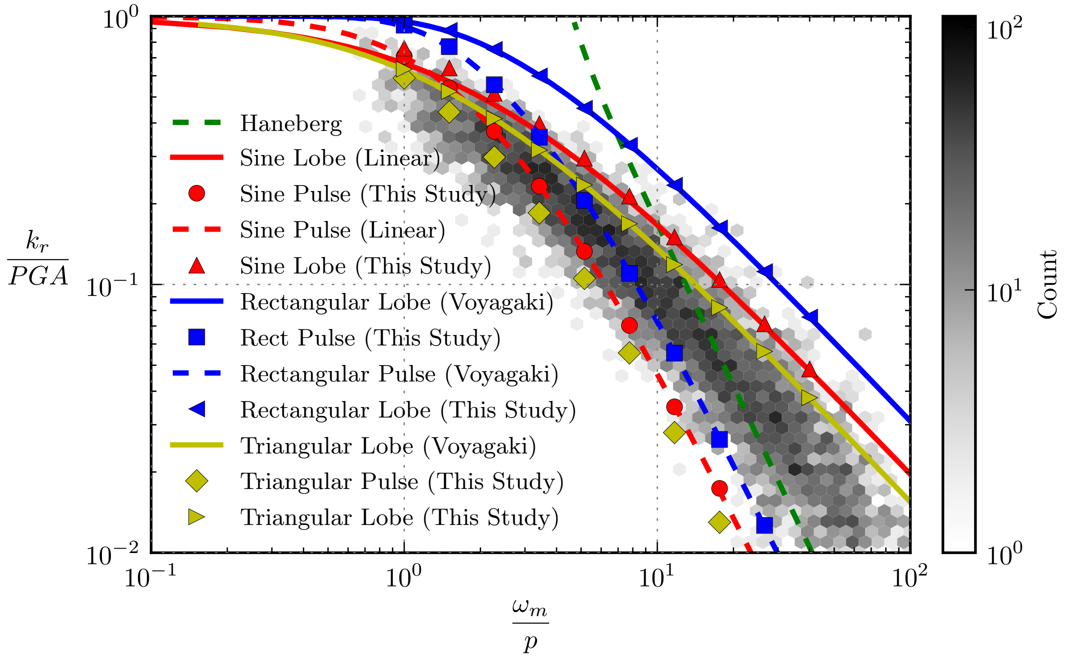

(b) log space

Figure 4.20: Simulation results using dimensionless parameters.

2. As Makris and Roussos (2000) indicated, small blocks (large p^2) react more to acceleration pulses while large blocks (small p^2) react more to accumulated acceleration (i.e. velocity pulses).

A rectangular lobe motion represents the maximum amount of energy that can be exerted for a motion with a fixed period and amplitude since the acceleration is instantaneously at its maximum for the entire period. If the ground motion's PGA and $\mathrm{T_m}$ is conservatively assumed to be in the form of a rectangular lobe, then the rectangular lobe represents the upper bound of the data as shown in Figure 4.20. It can be seen that when evaluating the density of the data, the triangular and sine lobe performs rather well at bounding the bulk of the data. Intuitively it is expected that a sine lobe would provide a more meaningful upper bound and indeed seems to represent an approximate $+2\sigma$ boundary of the data. The triangular lobe falls closer to the mean of the data possibly because it is more representative of an acceleration pulse that may rise and drop quickly, especially when the ground motion signal is discretized at fixed time steps. The equation by Haneberg coalesces around the other equations plotted for large frequencies or small block sizes, however it conservatively diverges for low frequencies or larger blocks.

4.5.3 Reinterpretation of Simulation Data

Although the closed-form solutions for simple pulses are non-linear in both linear and log space, the simulation data (k_r/PGA versus ω_m/p) appears to be approximately linear in log space as shown in Figure 4.20b. Based on the visually apparent linear relationship shown in Figure 4.20b, it will be assumed that k_r/PGA has a linear relationship with ω_m/p in log space (i.e. $\log \frac{k_r}{PGA} = C + M \log \frac{\omega_m}{p}$). With an assumed linear relationship, it is possible to rearrange the terms of the linear equations below

$$\log \frac{k_r}{PGA} = C + M \log \frac{\omega_m}{p} \tag{4.28}$$

Dropping the constant, C and pulling M into the log(), which inverts the fraction on the right side since M is negative,

$$\log \frac{k_r}{PGA} = \log \frac{p^M}{\omega_m^M} \tag{4.29}$$

where the absolute value of M is now being used for M. Now rearranging the terms so that all the block parameters and earthquake parameters are on separate sides of the equation

$$\log \frac{k_r}{p^M} = \log \frac{PGA}{\omega_m^M}. \tag{4.30}$$

Finally, applying the common dynamics relationship for simple harmonic acceleration, velocity, and displacement amplitudes of trigonometric functions, $A = V\omega = D\omega^2$ yields

$$\log \frac{k_r}{p^M} = \log \frac{PGA}{\omega_m^M} = \log PGV = \log PGD\omega_m. \tag{4.31}$$

Equation (4.31) now suggests that the critical block parameters (k_r and p) can be directly related to the ground motion parameters to be used in a predictive manner.

Assuming M=1, the simulation data is now replotted in Figures 4.21 through 4.23 in light of the relationships in Equation (4.31). For each parameter, a hexbin plot of the data with the counts of each bin colored in a log scale is shown. Histograms of the ground motion and block parameters are plotted along the abscissa and ordinate axis to further illuminate the density of the data. Furthermore, histograms of each ground motion set are shown. The variability of the results visually appear to increase with the increase in each ground motion parameter (GMP). For this reason a weighted linear least squares (WLS) fit was performed on each data set for each GMP. Since the variance is unknown, the weights used for each fit were determined by an iterative evaluation of the fitted variance. First the data was split into bins and the variance of each bin calculated as shown in Figures 4.21a to 4.23a. From these plots, the relationship between the GMP and variance was determined to be linear relative to PGA and PGV and quadratic relative to PGD. After applying weights, the mean WLS fit is plotted as a solid line, while the 2.5% and 97.5% probability of failure lines are dashed. The resulting regression equations are shown in each figure.

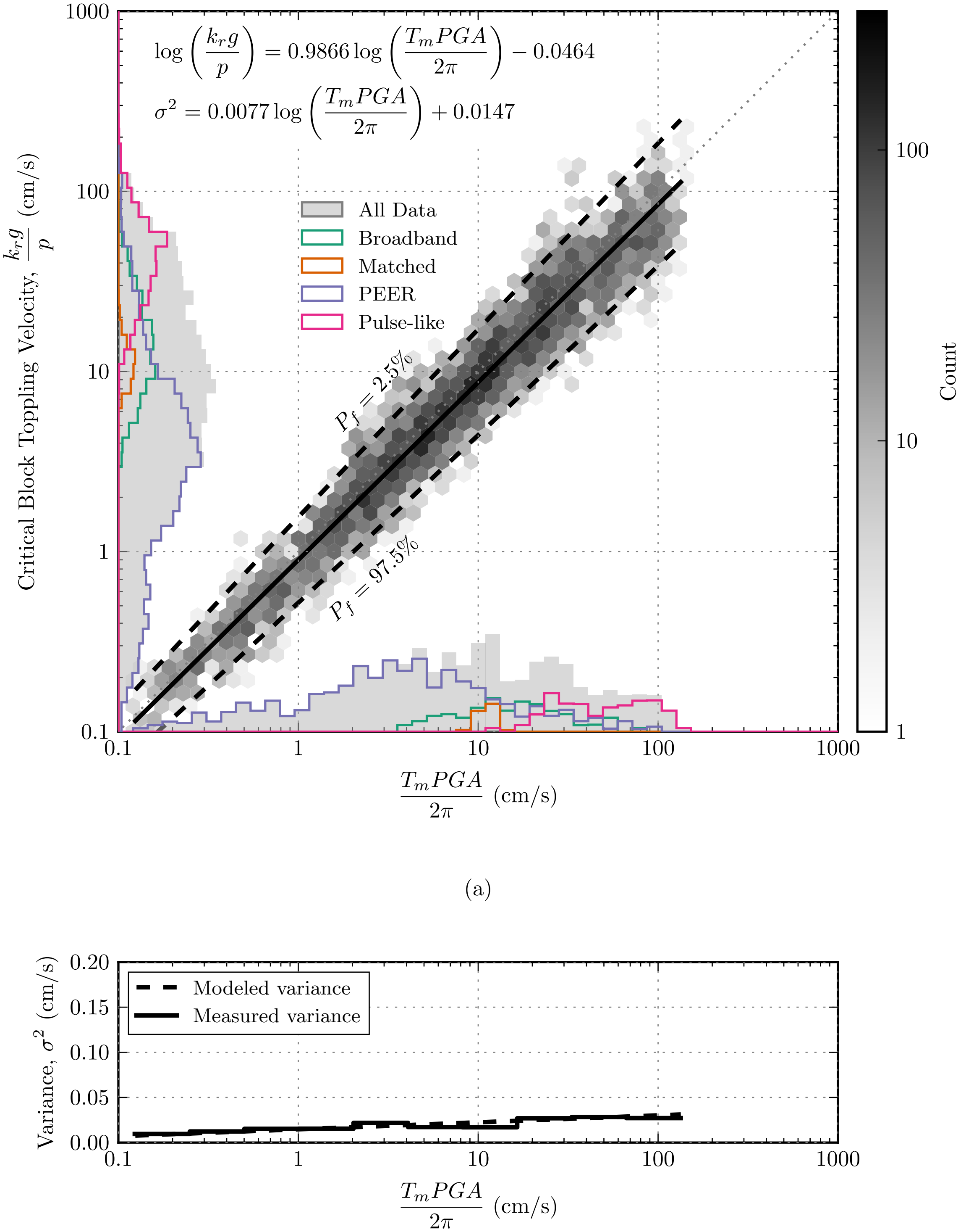

(a)

(b)

Figure 4.21: Earthquake simulation results for PGA and T_m.

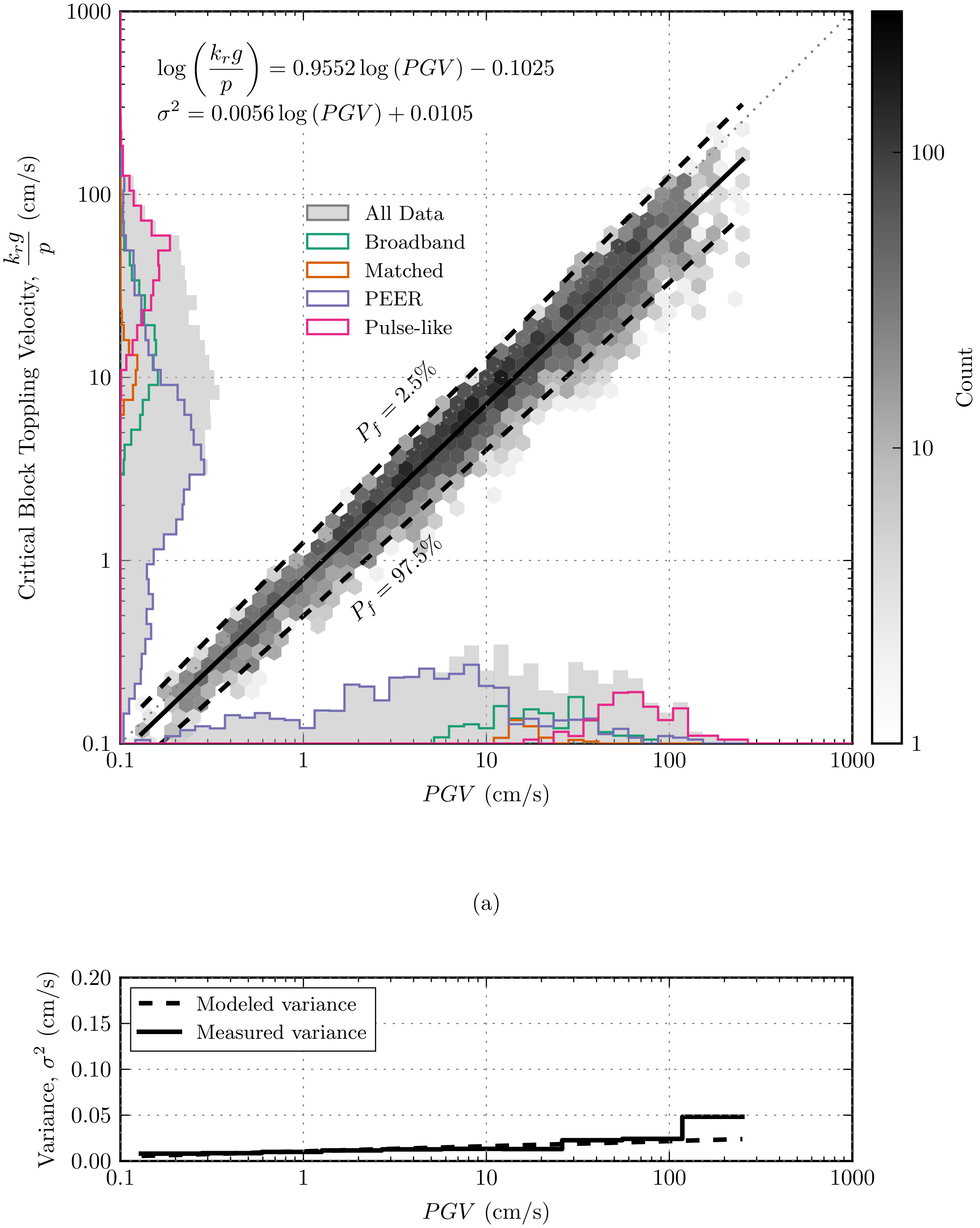

(a)

(b)

Figure 4.22: Earthquake simulation results for PGV.

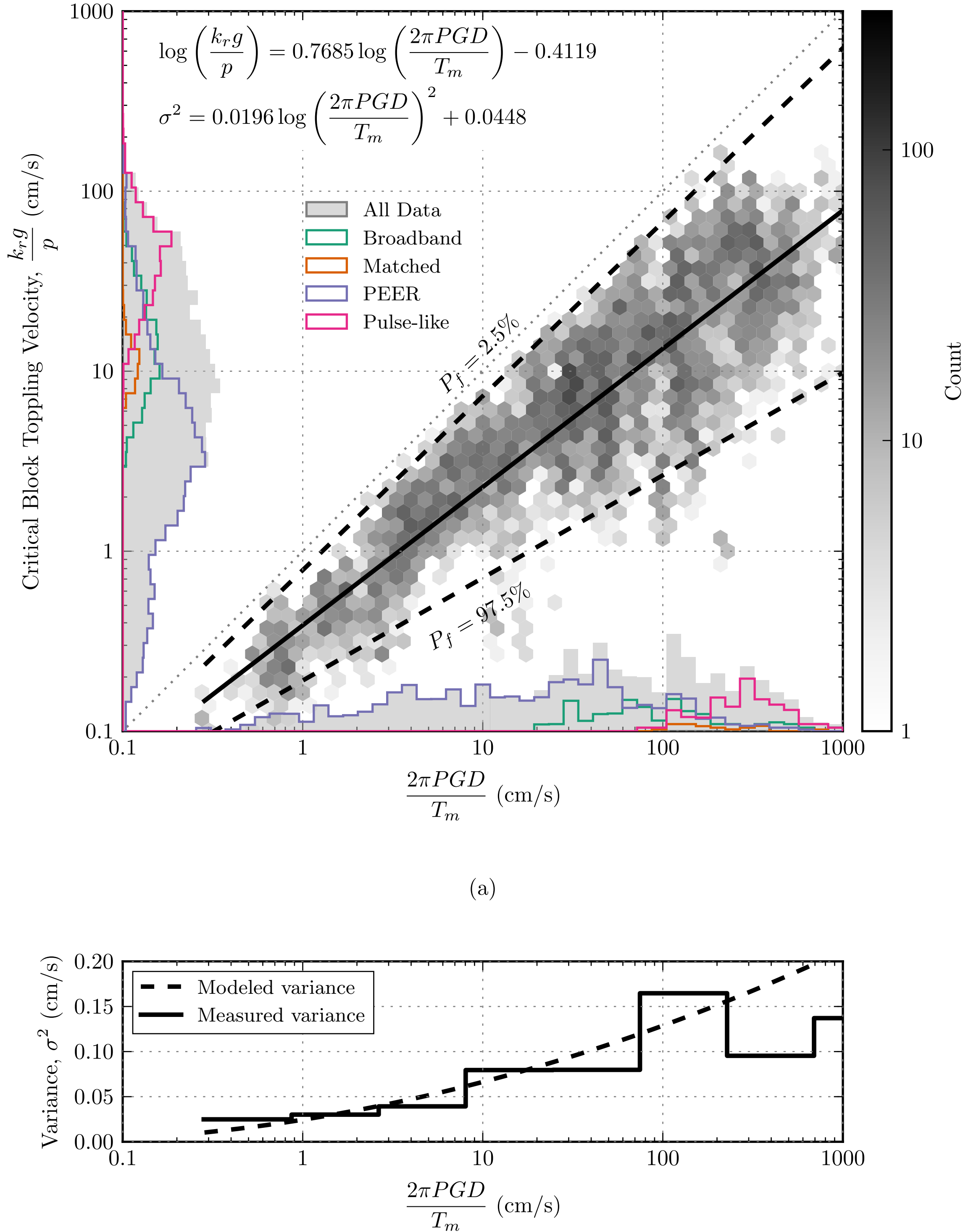

(a)

(b)

Figure 4.23: Earthquake simulation results for PGD and T_m.

These plots in Figures 4.21 through 4.23 confirm that for practical purposes the critical block size can be linearly related to the ground motion parameters. The parameters PGV and $T_m PGA/2\pi$ are the best predictors of the boundary between safe blocks and blocks that will overturn. By visual inspection, it appears that PGV has the more defined boundary and is consistent with recommendations by Sorrentino et al. (2006). The parameter $2\pi PGD/T_m$ also shows a linear trend along the upper boundary however the variance increases dramatically with increase in PGD making it the least skillful predictor overall. It is interesting to see that there is virtually a 1:1 relationship between the block shape and PGV. For this reason, $k_r g/p$ is now referred to as the critical block toppling velocity.

In order to further understand the reason for the variability, simulations with simple sine wave, rectangular, and triangular pulse loadings are performed. Figure 4.24 shows the comparison to the probability of failure boundaries from the earthquake simulations. Both sets of results have similar variability. The primary reason for this agreement is that the period of the simple pulses was limited to the variability in the ground motions (i.e. $\mathrm{T_m}$=0.07-1.7 seconds). If larger periods are used then the simple motion results extend downward. Furthermore, it can be seen that with changes in PGA, the results shift down and to the left along the same path as the earthquake simulations. The results of the earthquake simulations, segregated by ground motion set, are shown in Figure 4.25 along with the WLS fit for all the data combined. It appears that differences in the ground motion set does not impact the likelihood of failure. These comparisons highlight the fact that it is the randomness of the ground motion and banded frequency content that focus the results in the linear relationship shown by the earthquake simulations.

Results for Vertical Motions

The previous results are now plotted with and without the vertical motions as shown in Figure 4.26. The histograms of the input and output are very similar in shape and extent. This plot suggests that the consideration of vertical motion in a probabilistic sense does not

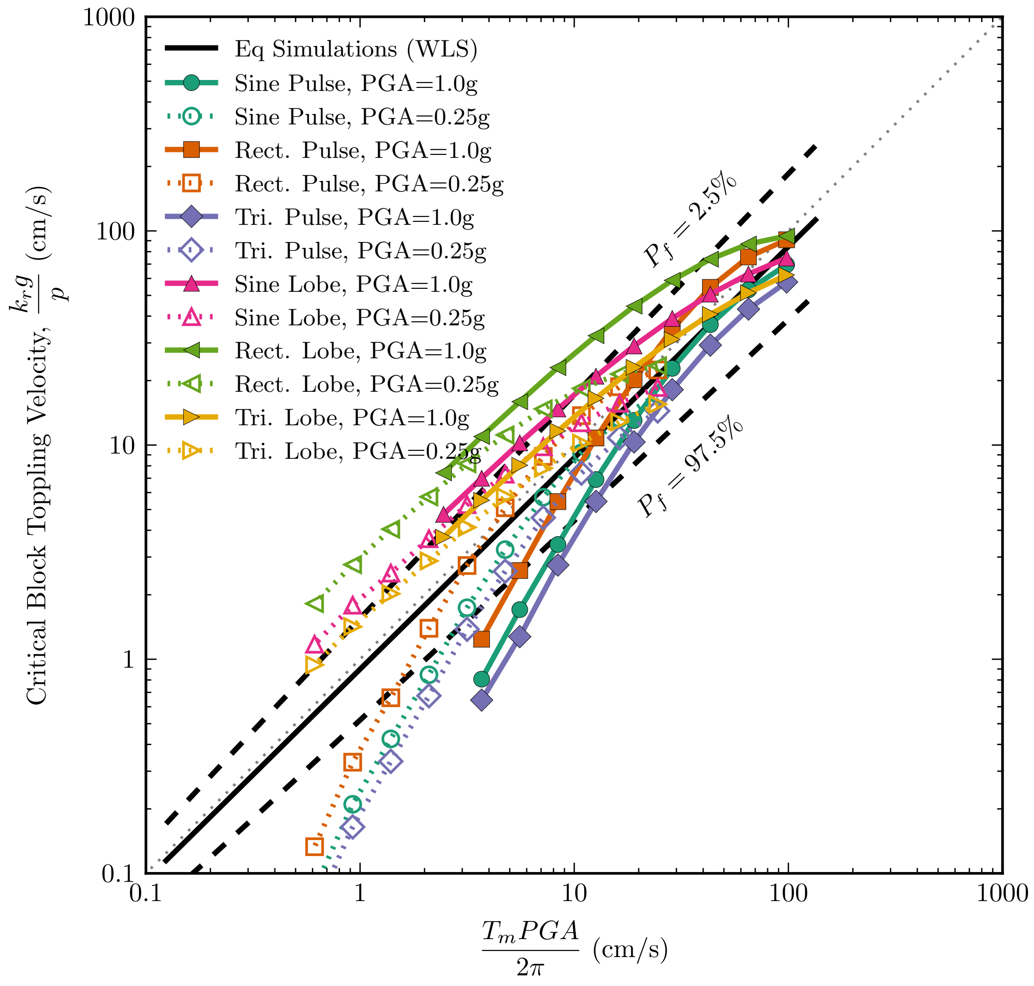

Figure 4.24: Comparison of simple simulations to Earthquake simulations.

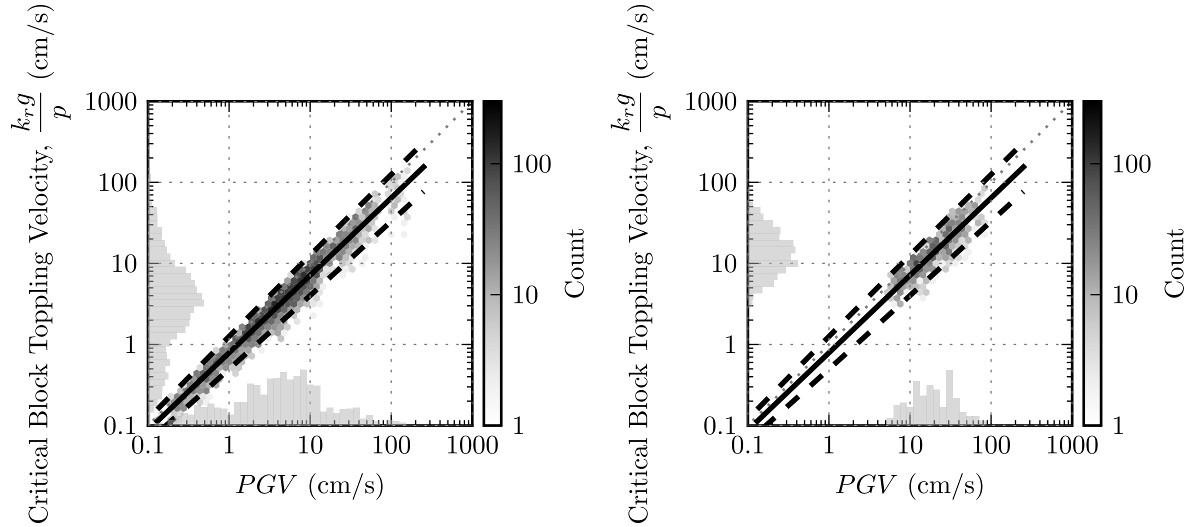

(a) PEER ground motion set

(b) Broadband ground motion set

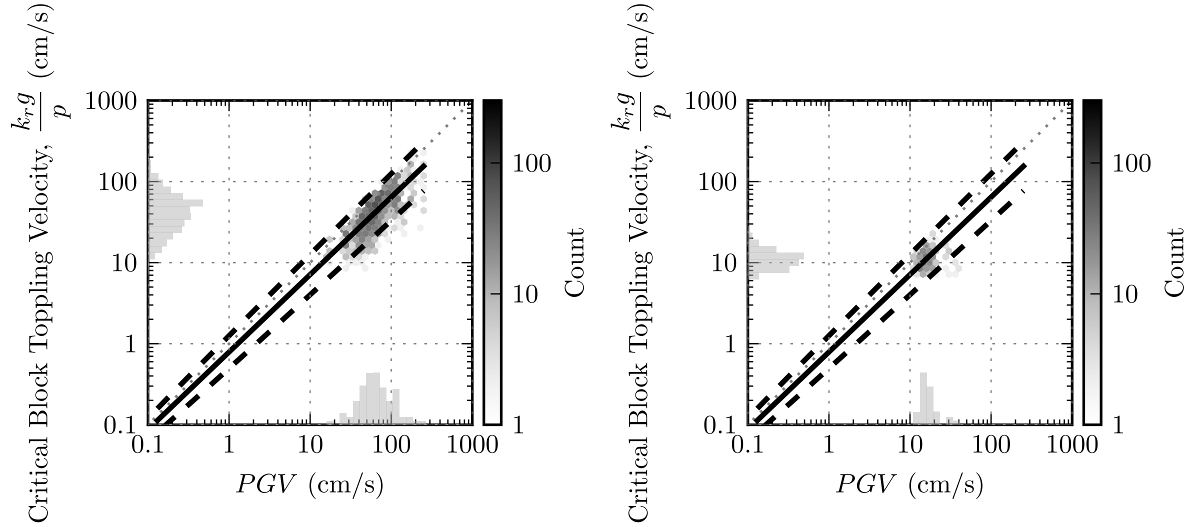

(c) Pulse-like ground motion set

(d) Matched ground motion set

Figure 4.25: Earthquake simulation results for each ground motion set.

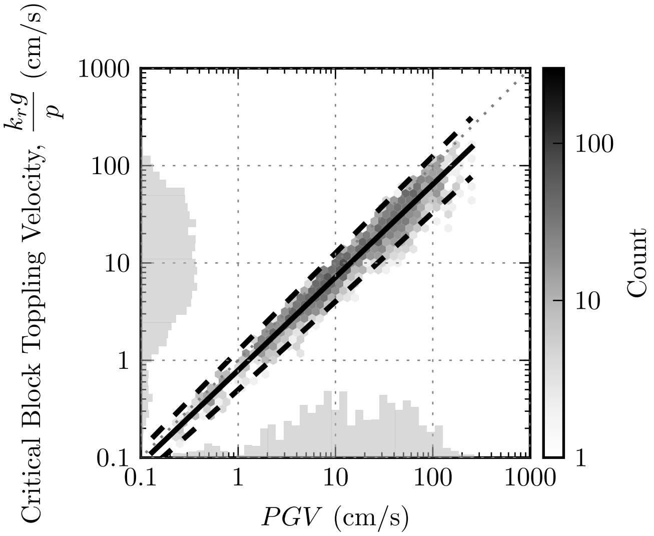

(a) With vertical motion

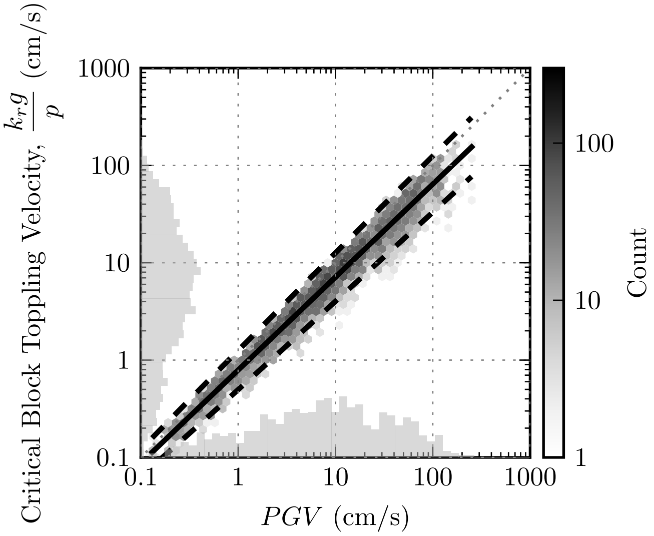

(b) Without vertical motion

Figure 4.26: Earthquake simulation results with and without vertical motions.

change the outcome. Of course on a case-by-case, deterministic basis, the vertical motion will change the outcome of the analysis.

4.6 Example Application - Christchurch 2011

The usefulness of the toppling block relationships presented previously is now demonstrated by evaluation of earthquake induced rock toppling case history. From September 2010 to December 2011, a series of earthquakes ranging in moment magnitude of 5.9 to 7.1 occurred near the city of Christchurch, New Zealand (Bradley et al., 2014). Geotechnical failures ranged from liquefaction in the valley sediments to rockfall in the Port Hills area southeast of the city.

4.6.1 Rockfall Survey and Source Geology

Following the earthquakes, the Christchurch city council and GNS Science conducted damage surveys which included the mapping and measurement of rockfall throughout the Port Hills area (Massey et al., 2014). The abundance of surveyed rockfall relative to the many earthquake events is summarized in Table 4.3. The ground motion characteristics (PGA and PGV) are also presented in Table 4.3 for two nearby ground motion stations. Heathcote Valley School (HVSC) ground motion station is a shallow soil site and Lyttleton Port (LPCC) ground motion station is a rock site. Each station is located at the base of the hills and are located on the East and West flanks of Port Hills, respectively. In the rockfall survey study, a relationship between boulder volume and boulder abundance was developed in which the mean boulder size was $\approx 1m^3$ while the 95^{th} percentile size was ≈ 3 m^3.

The source rock type of these rockfalls is primarily the blocky, basalt lava flow and breccia of the Lyttleton Volcanic Group (Massey et al., 2014). In his master's thesis, McDowell (1989) characterized slopes and geology within Port Hills area. For lava formations, he notes that the top surface of blocks dip at about 30° matching surrounding slopes and is formed with perpendicular joints. In some areas, McDowell indicates that jointing or fractures were blast induced from mining operations around the Port Hills area. Within the loess

Table 4.3: Port Hills rockfall abundance surveyed from the 2010-2011 Canterbury earthquake sequence.

Date (NZ)	Moment[1] Magnitude	PGA[1] (g)	PGV[1] (cm/s)	GeoNet Strong Motion Site	Rockfall[2] Abundance
4 Sept 2010	7.1	0.61	28.8	HVSC	Few
		0.29	19.1	LPCC	
22 Feb 2011	6.2	1.41	81.4	HVSC	Widespread
		0.92	45.6	LPCC	
13 June 2011	6.0	0.91	53.3	HVSC	Many
		0.64	32.6	LPCC	
23 Dec 2011	5.9	0.44	22.3	HVSC	Some
		0.44	22.8	LPCC	

[1] Per Bradley et al. (2014).

[2] These are descriptive terms used by Massey et al. (2014). They indicated that a majority of the rockfall observed occurred during the 22 February 2011 earthquake. The descriptions for rockfall abundance is interpreted as Few < Some < Many < Widespread.

formations, he notes that planes in which toppling occurs are typically about 20°. From this information, an evaluation of the expected abundance of boulder sizes deposited as a result of earthquake rock toppling can be performed.

4.6.2 Analysis

Geometry

First the general geometry of the source rock blocks is estimated. Since it was previously shown that all parallelograms of a constant scale and α_3 have approximately equal p^2, then a cubic geometry can be assumed to determine the volume of the block. The cuboid shape is chosen because of the ease of relating block dimensions to its volume. Assume a cuboid, where all sides are perpendicular, the two base widths (b) are equal but not necessarily equal to the height (h).

$$r_3 = |\mathbf{r}_3| \tag{4.32}$$

$$b = 2r_3 \sin(\alpha_3) \tag{4.33}$$

$$h = 2r_3 \cos(\alpha_3) \tag{4.34}$$

The volume (V) in terms of $\mathbf{r}_3$ and α_3 is

$$V = b^2 h \tag{4.35}$$

$$V = 8r_3^2 \sin^2(\alpha_3)\cos(\alpha_3). \tag{4.36}$$

Rearranging the relationship for rectangles, $p^2 = 3g/4r_3$ to $r_3 = 3g/4p^2$, combining into the volume equation and solving for p,

$$V = \frac{9g^2 \sin^2(\alpha_3)}{2p^4} \tag{4.37}$$

$$p = \left(\frac{9g^2 \sin(2\alpha_3)}{2V}\right)^{1/4}. \tag{4.38}$$

Assuming that the cuboid is a cube ($\alpha_3 = 45°$) and the slope angle is 20°, then $k_r = \tan(25°)$. It could also be reasonable to assume that the base joint angle is zero. In this scenario, for k_r to remain the same value, then $\alpha_3 = 25°$ translating to a height to width ratio of about $2:1$, which is also a reasonable assumption. Combining this range of k_r with Equation 4.38, the relationship between $k_r g/p$ and block volume range between $0.01m^3$ and $100m^3$ is shown in Figure 4.27.

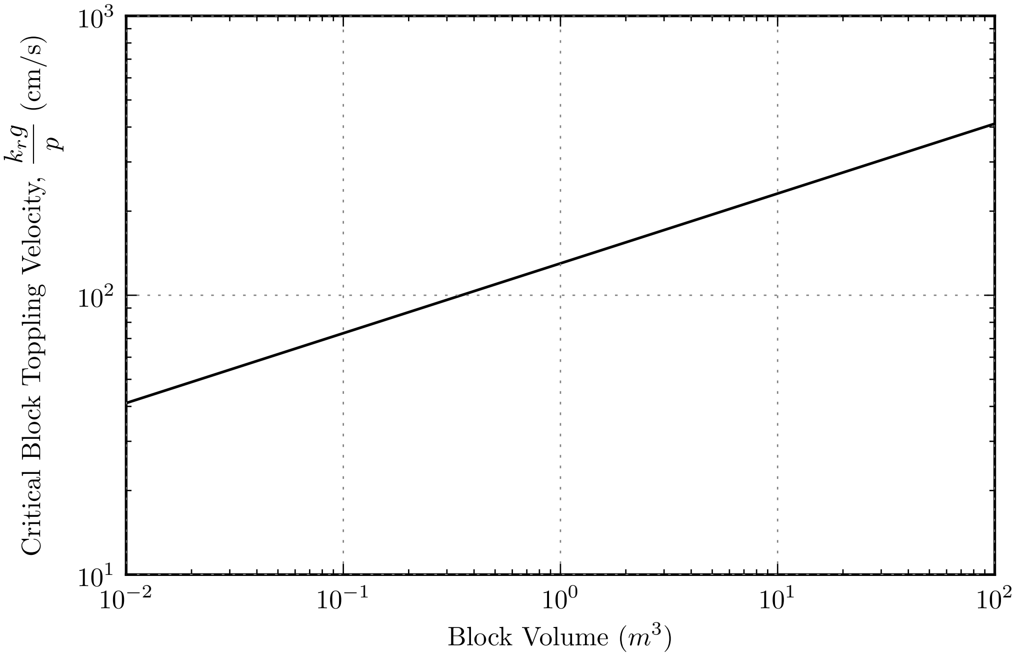

Figure 4.27: Relationship between $\frac{k_r g}{p}$ and the volume of a cuboid block.

Ground Motions

The ground motions recorded in the 21 February earthquake were previously summarized in Table 4.3. The PGV at the LPCC station is lower than that of the HVSC station and is possibly attributed to the source to site distance and directivity of the ground motion toward Christchurch. These two stations will be assumed to give a range of typical ground motions experienced at the base of Port Hills. Since most of the rockfall originated from well above these stations, it would be expected that the ground motions in these source areas would be amplified relative to the measuring stations due to topographic amplification (Ashford et al., 1997; Harp and Jibson, 2002; Murphy, 2006). Analytical, numerical and experimental data of topographic amplification indicates that for peaks with 30° to 45° slopes, an amplification of 100% to 200% is possible. (Pagliaroli et al., 2011) This is also supported by recent centrifuge data of dense soil slopes (Dafni and Wartman, 2014). An amplification factor of 1.5 is assumed for the upper bound PGV used in this analysis.

4.6.3 Results

The block volume ranges indicated above, represented by $k_r g/p$'s, along with the estimated PGV ranges are plotted relative to the confidence intervals determined from the toppling model simulations in Figure 4.28. It can be seen that the intersection of the 2.5% confidence line with the maximum assumed PGV limits for the 22 February earthquake indicates a maximum block volume of approximately $20 - 30m^3$ which is near the top range of block sizes surveyed. The remaining earthquakes, 13 June 2011, 4 September 2010, 23 December 2011, progressively increment to the left in the plot because of smaller observed PGV. The reduced PGV indicates that the maximum block size being triggered would decrease and an increasing number of blocks would not fail. This result supports the qualitative observation of rockfall abundance observed after each earthquake.

Furthermore, a lower bound critical block velocity means there is a corresponding minimum PGV of about 20 cm/s for which topples would have been observed. The minimum PGV translates to the toppling being limited in areal extent. Given the other ground motion parameters that could be used, a minimum PGA and $\mathrm{T_m}$ is also implied. Massey et al. (2014) observed that rockfall was not observed for PGA's of less than 0.3g. Assuming mean period of about 0.3 secs (Bradley et al., 2014), then $T_m PGA/2\pi \approx 14$cm/s which is close to the minimum PGV indicated above. These results illustrate how the rock geometry/geology can control the lower and upper bound accelerations observed at rockfall sites.

This analysis can be taken a step further by assuming a distribution of source block sizes and PGV's and then using the probability of failure determined from the toppling block simulations to estimate the likelihood for a given block to fail. To demonstrate this concept, four sets of analyses were performed in which a uniform and normal distribution for each block size and PGV were assumed. The input assumptions are summarized in Table 4.4. A

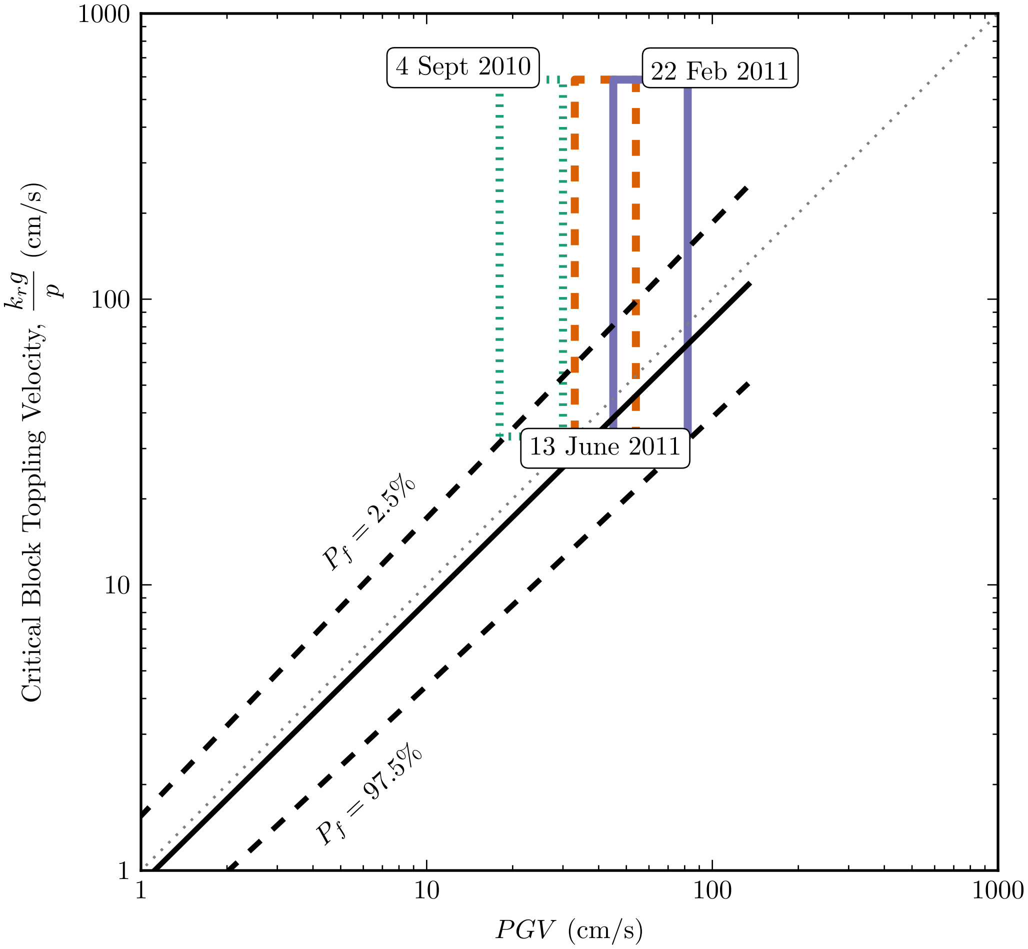

Figure 4.28: Estimated block geometry range for rock blocks in the Port Hills area exposed to estimated PGV values during the Canterbury earthquakes along with the 2.5% and 97.5% confidence intervals determined from toppling model simulations.

Table 4.4: Assumed distributions of source block volumes and ground motion PGV's

Analysis	Block Volumes (m^3)	PGV (cm/s)
1	Uniform: min=0.01 max=1000	Uniform: min=18 max=164
2	Uniform: min=0.01 max=1000	Log Normal: $\mu = 70$ $\sigma = 10^{0.12}$
3	Log Normal: $\mu = 10$ $\sigma = 10^{1.0}$	Uniform: min=18 max=164
4	Log Normal: $\mu = 10$ $\sigma = 10^{1.0}$	Log Normal: $\mu = 70$ $\sigma = 10^{0.12}$

Monte Carlo simulation was performed for each permutation of these assumptions in which the sampled block size and PGV was evaluated for probability of failure.

The resulting gradations of fallen rock from these analysis are shown in Figure 4.29. These results illustrate that for toppling modes the ground motion characteristics act to segregate the source rock based on its geometric properties and the earthquake parameters. This similarity can also be seen when plotted in the form of a histogram for block sizes in Figure 4.30. The shape of the predicted size distribution curves to the surveyed curves is remarkable. In some instances, the simulated data departs from the surveyed data for block volumes between 1 and $10m^3$, which is attributed to sampling bias as indicated by Massey et al. (2014). The influence of the existing source rock and PGV distributions can be seen to shift the curves from right to left. Given the likely sampling bias for small blocks (<1 m^3), it is not possible to conclude which scenario of PGV or source rock is more or less likely. However, these results suggest that the block shapes and earthquake characteristics contribute significantly to earthquake induced rock topples. Although a specific block shape and slope angle was assumed and has not been directly verified, these results illustrate that a similar regional analysis could be easily performed. Furthermore, with site-specific information, the analysis could be used to more definitively conclude the role of earthquake induced toppling in the site's overall rockfall hazard.

4.7 Example Toppling Evaluation

The following steps describe the procedures to evaluate the likelihood of toppling failure of a single block from seismic loading.

1. Determine the expected direction of block movement. For rock blocks on a slope this direction is generally away from the slope. More precisely for a toppling block, it is the direction in which the block will rotate about one of its edges away from the slope. It is possible that there will be multiple edges where rotation is kinematically admissible. It is recommended to evaluate all permissible edges.

2. Set up problem geometry parallel to the direction of block motion such that 2D assumptions are most applicable.

3. Outline the geometry of the shape taking note of contact points between the shape and its foundation.

4. Determine the contact points between the block and the supporting fractures.

5. Confirm that toppling is the controlling mode of failure (See Chapter 3).

6. Calculate the toppling yield acceleration, k_r with respect to the overturning point.

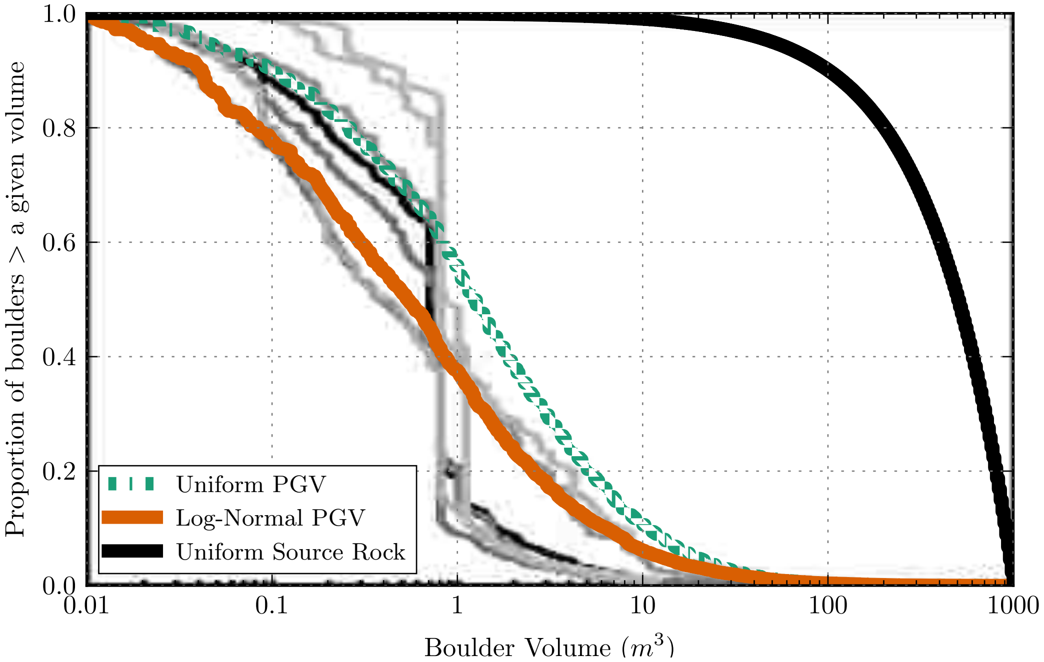

(a) Uniform source rock

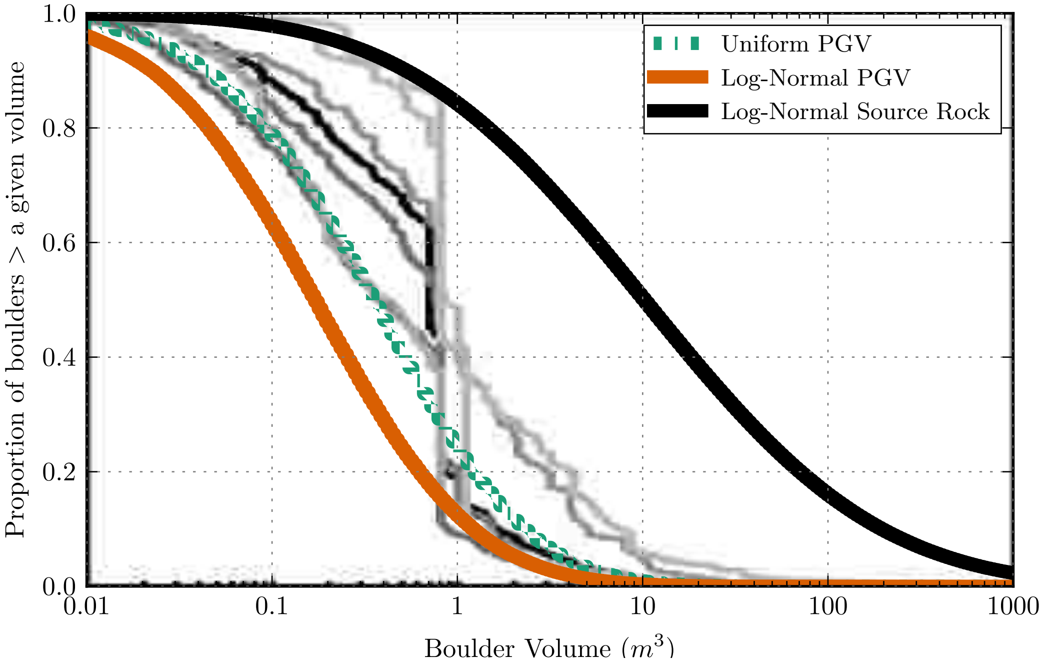

(b) Log-Normal source rock

Figure 4.29: Estimated rockfall depositional size gradation based on uniform and log-normal source rock distribution. Survey data collected for the Canterbury earthquakes is shown in gray for comparison (Massey et al., 2014).

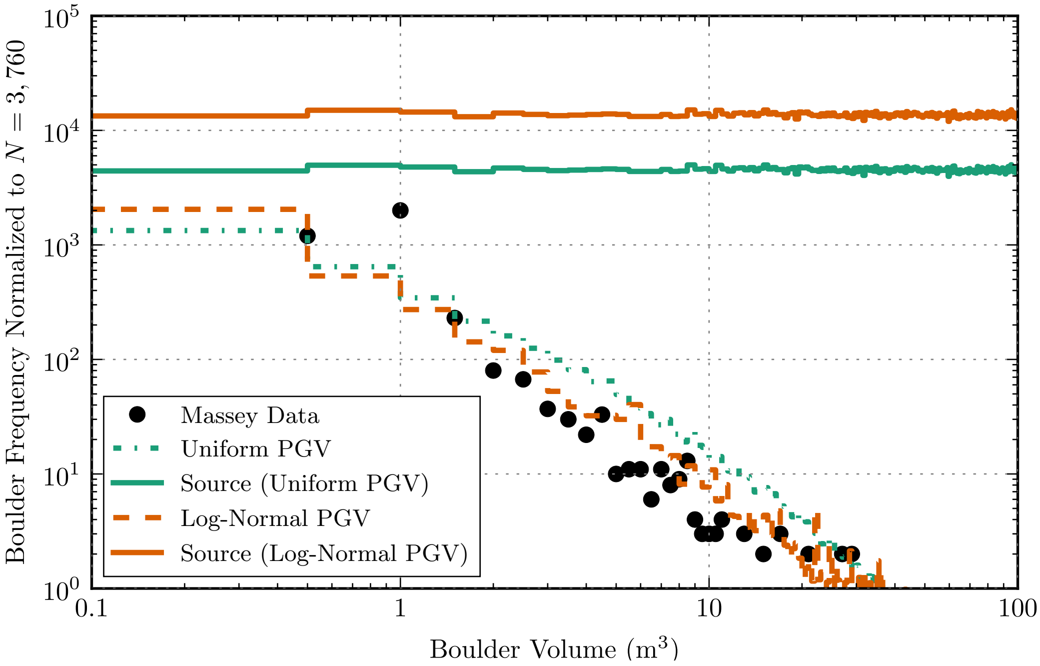

(a) Uniform source rock

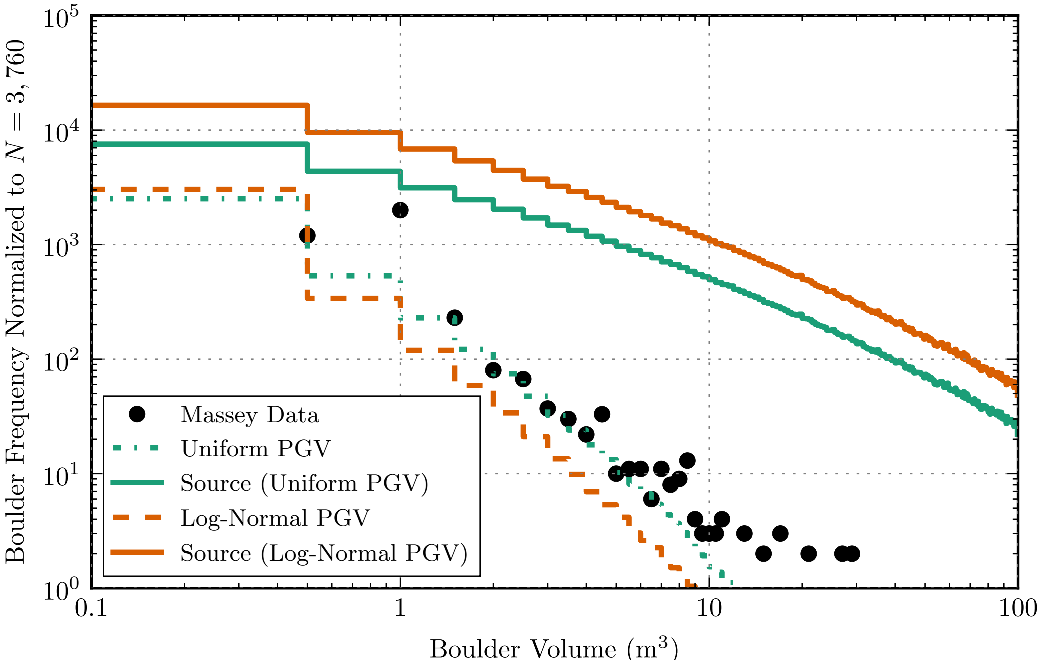

(b) Log-Normal source rock

Figure 4.30: Estimated frequency of rockfall depositional size based on uniform and log-normal source rock distribution compared to survey data collected for the Canterbury earthquakes (Massey et al., 2014). Survey data approximated from publication figures.

7. Determine if toppling will be triggered based on the calculated k_r. If not then the analysis ends here with a block that does not topple.

8. Calculate p^2 with respect to the overturning point. Note that this value changes depending on the overturning point being evaluated.

9. Calculate $k_r g/p$.

10. Determine the probabilistic or deterministic likelihood of toppling using either charts or evaluating a specific ground motion.

    A Determine ground motion parameters (PGA, PGV, PGD, and T_m) and then use charts (Figures 4.21 through 4.23) to determine the likelihood of toppling. This is only necessary if a specific hazard is to be evaluated.

    B Perform the non-linear, time history analysis using the Python package developed in this thesis.

A simple example is now presented to illustrate the use of the above-described procedures. The geometry for the example is drawn from Threatening Rock, a large monolithic rock in the Chaoco National Park in New Mexico that failed in 1941. Although Threatening Rock failed from erosional and rainfall processes, it still provides an interesting academic exercise (Schumm and Chorley, 1964).

According to Schumm and Chorley (1964), Threatening Rock is approximately 40 feet wide, 100 feet tall, and 150 feet long. The first step in the example is to determine the geometric properties of the block as shown in Figure 4.31. The shape is approximated with a polygon, in this case a quadrilateral. The overturning point is shown as point "O". The p^2 parameter with respect to point "O" is calculated with knowledge of the block's vertices to be approximately 0.43s^2. The yield acceleration is determined based on the orientation of the vector r_3 and is $k_r = \tan^{-1}(r_{3x}/r_{3y}) = 0.128g$. Entering Figure 4.21 with the ratio $k_r g/p = 191$cm/s, the block is predicted to not overturn if $T_m PGA/2\pi \leq 190$ cm/s, while

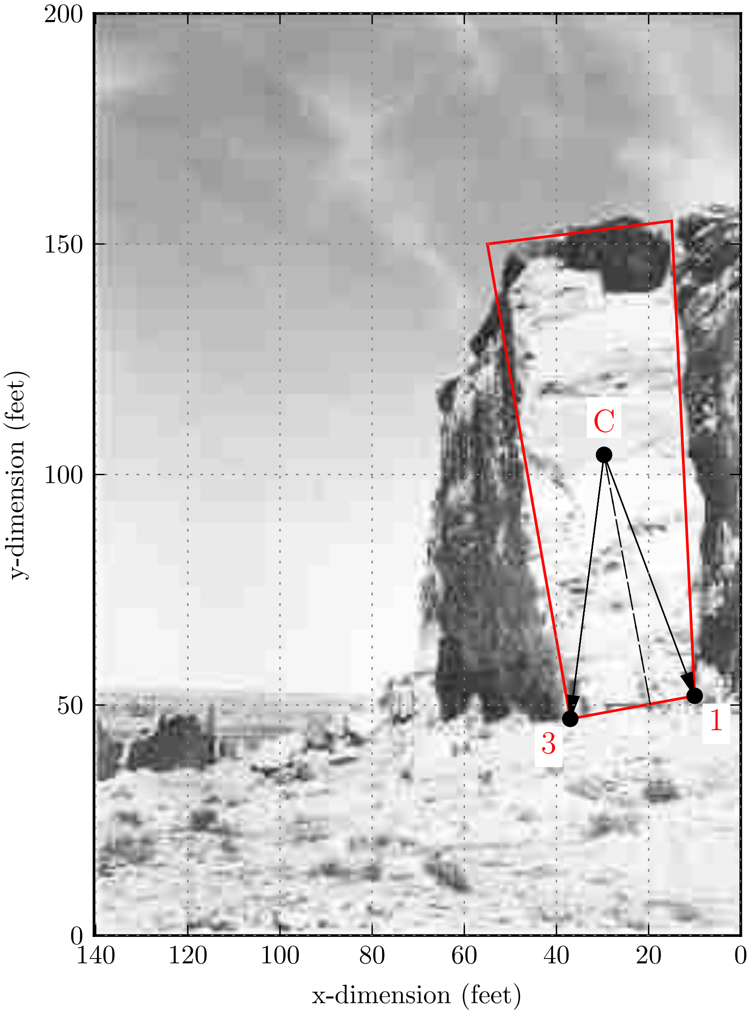

Figure 4.31: Seismic toppling evaluation of Threatening Rock.

it has a 100% chance of overturning if $T_m PGA/2\pi \geq 500$ cm/s. According to the 2008 USGS PSHA for a return period of $2,475$ and $4,950$ years, the PGA for the Chaoca canyon is approximately $0.07g$ and $0.125g$, respectively. Assuming a typical mean period from the PEER database (0.07s to 1.7s), the $T_m PGA/2\pi$ ranges from 0.76 to 2.4 cm/s. Based on this analysis, it would require a relatively rare seismic event to trigger motion and even if the motion was triggered it is not likely that Threatening rock would have been overturned by a seismic event.

As mentioned previously, Threatening Rock failed in 1941, therefore the likelihood of seismic failure is not observable. However, the geology in the Chaoco Canyon is known for geologic formations similar to Threatening Rock. For example, consider the rock in Figure 4.32 observed by visitors to the National Park. Following the same procedures as before, the actual rock block is approximated by a polygon shape. The yield acceleration, 0.095g, and frequency parameter, 0.42 s^{-2}, is smaller than the original Threatening Rock. Entering Figure 4.21 with the ratio $k_r/p = 143$ cm/s, the block is predicted to not overturn if $T_m PGA/2\pi \leq 140$ cm/s, while it has a 100% chance of overturning if $T_m PGA/2\pi \geq 300$ m/s. From this analysis, this block is more likely (than Threatening Rock) to have toppling motion triggered and possibly fail. However, given the return periods of the estimated motion, the likelihood of failure by seismic motion is still rare.

Alternatively the velocity range determined from the ground motion parameters can be thought of as a velocity hazard at the site. In order for Threatening Rock's or another large rock's critical block velocity to fall below these values, the block would need to be severely undermined to reduce k_r and/or be much smaller in size. This highlights the role that earthquakes play in the lasting existence of these geologic formations. It suggests that larger, more ominous rocks are more likely to be observed than smaller ones. This knowledge and analysis procedure could be used for paleoseismic studies in similar geologic environments.

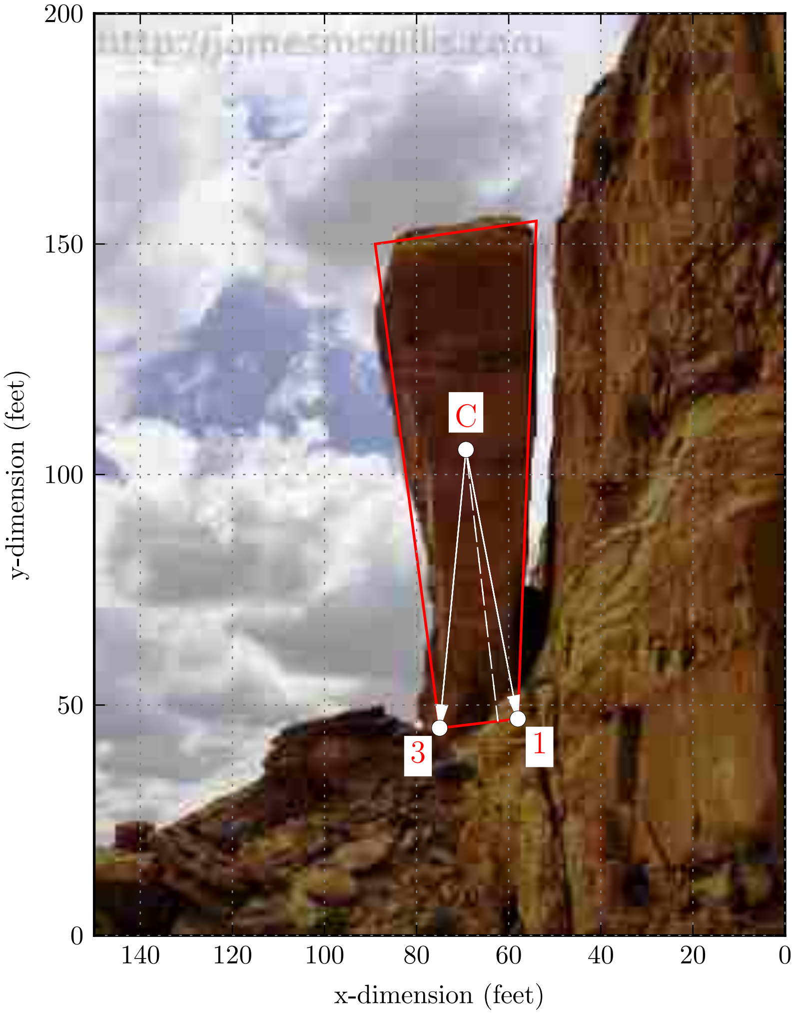

Figure 4.32: Seismic toppling evaluation of block similar to Threatening Rock.

4.8 Discussion and Conclusion

In this chapter, the extensive rocking block literature has been leveraged to develop a model adapted to seismically induced rock block toppling problems. The rocking block equations of motion were reformulated in terms of the toppling yield accelerations. Assumptions appropriate for rock block toppling were added and evaluated to constrain the rocking equations. The resulting rock block toppling model numerically solves the non-linear, discontinuous equations of motion for a given rock geometry relative to earthquake ground motion time history input.

An extensive, robust parametric study was conducted to evaluate numerous geometric rock shapes relative to over 800 earthquake time history records. Assumptions of these simulations include: (1) 2D in-plane motion, (2) Loading in-plane, (3) Zero corner roundness or degradation, (4) Zero resistance about toe of block, (5) Zero resistance along the sides of the block, and (6) Vertical motion (up) $< 1g$ (i.e. blocks do not jump). This study has resulted in the following advances in seismically induced rock block toppling analysis:

1. Various shaped parallelogram blocks have been evaluated to show that for a given block shape, k_r and p^2 have little variability. This means that representative values can be used to approximate a wide range of block shapes in a toppling evaluation.

2. Simulation results were interpreted such that block and earthquake parameters are segregated, which allows for PBEE or reliability analyses to be easily performed.

3. An essentially, statistically linear (safe) boundary between toppling and non-toppling blocks has been found.

4. The response threshold of toppling blocks is shown to be dependent on earthquake magnitude and frequency parameters. The various sources and factors that influence earthquake time histories (e.g. fault type, Magnitude, and distance) are only important

in so much as those sources/factors influence peak acceleration, velocity, or displacement amplitude and mean period of the motion.

5. The safe boundary is virtually invariant relative to the inclusion of vertical motions. However, vertical motion does change the outcome on a earthquake by earthquake and block by block basis.

6. The safe boundary implies that the block parameter can be used as a statistical state parameter for rock block toppling. The block parameter is termed the critical block toppling velocity and is expressed as $k_r g/p$. Commonly used ground motion parameters, PGA, PGV, PGD, and $\mathrm{T_m}$, are used to represent the earthquake.

7. The behavior of a forward toppling block is better behaved than rocking block relationships because the non-linearity of the impact (coefficient of restitution) is removed.

8. According to Kounadis et al. (2012), multiple block systems failing in the forward mode (no impacts) behave as a single block so the method could be applied to multiple block systems. As blocks are stacked on top of each other, the k_r of the system is reduced since the width of the stack does not change but the distance from the center of mass to the block toe increases. On the other hand, the frequency parameter, p^2, is increasing, meaning stacked blocks can cause otherwise stable blocks to fail.

9. Through the Christchurch example, the toppling block model is shown to be useful for regional analyses. The parametric study results were used to show that block geometries and earthquake parameters act together to form the observed size distribution of failed rock blocks. Note that these results were obtained without the Christchurch ground motions being used in the parametric study.

10. Another example of Chaoca Canyon illustrates how the toppling block model could be used for paleoseismic studies. The toppling block failure relationships are able to

predict minimum amplitude and period of the earthquake instead of just a minimum amplitude predicted by methods for precarious rocking blocks. In addition, the toppling block model would not be restricted to the very limited geologic locations that are home to precarious blocks.

11. Design charts and regression equations are provided to allow for quick assessment of earthquake rock block toppling failure.

Chapter 5

DISPLACEMENT RESPONSE OF SLUMPING ROCK BLOCKS

Rock slope failures have contributed greatly to the economic and human loss experienced during seismic events throughout the world. Accounts of these spectacular events have been documented and evaluated throughout the literature (Cluff (1971); Plafker et al. (1971); Wilson and Keefer (1983); Jibson et al. (2006); Keefer et al. (2006); Aydan et al. (2009); Lanzo et al. (2010); Alfaro et al. (2012); Massey et al. (2014), among others). The static stability of rock slopes is often evaluated using single block models (sliding, toppling, and slumping described in Ashby (1971); Hoek and Bray (1977); Bray and Goodman (1981); Sagaseta (1986); Kieffer (1998)) and are intended to represent the range of more complex behavior described in Goodman and Kieffer (2000). Methods for seismic triggering of rock slope failures rely on charts for rectangular blocks that are applicable to only sliding and toppling modes (Yagoda-Biran and Hatzor, 2013) and was expanded for irregularly shaped blocks applicable to four failure modes (sliding, toppling, slumping, and confined toppling) in Chapter 3. Simplified, seismically-induced displacement methods, used to evaluate rock slope failure scenarios in a performance-based earthquake engineering (PBEE) framework, are limited to a sliding block that is used to represent all modes (Jibson, 2011). The sliding block model, however, has limited abilities to predict the actual observed failures without extensive judgment of yield acceleration (Dreyfus et al., 2013). In addition, the internal structure of rock slopes has been identified as a key player in defining threshold behavior (Harp and Wilson (1995); Sitar et al. (2005)), yet the sliding block model has no means to capture this influence. While the new toppling model presented in Chapter 4 independently captured the toppling mode of failure, the slumping mode remains unaddressed. The slumping mode of failure has the potential to capture a non-linear yield acceleration dependent on fracture strength and structure (Chapter 3, Michalowski (2007)) Currently, rock slope engineering problems rely on more complex, site specific methods such as numerical models to estimate seismic displacements (Eberhardt, 2003).

In this chapter, a slumping block model is developed, investigated, and implemented to overcome the mode and analytical limitations and provide a means to estimate seismic slumping displacements. The equations of motion for a rigid slumping block displacing on two fracture planes are derived. A robust algorithm is developed to numerically solve the non-linear, discontinuous equations of motion for time dependent loading by an earthquake. Features of these equations are explored with dimensionless parameters to understand which parameters have the greatest influence over the response of slumping blocks. Similarities between the slumping block and rocking block equations are found. Sliding block models are shown to only capture the center of mass displacement with a well-chosen yield acceleration, which is not parallel to the typically assumed base fracture plane. The yield acceleration of a slumping block, which is dependent on its absolute displacement and boundary conditions, is shown to either decrease or increase depending on whether it acts alone or in a group of neighboring blocks.

Parametric analyses are performed and consist of the excitation of a broad range of slumping block geometries by 427 unique recorded earthquake ground motions from the PEER database. The results of this parametric study are used to statistically predict the failure of slumping blocks based on basic ground motion parameters (PGA, PGV, PGD, $\mathrm{T_m}$) and block and joint interface characteristics. It is shown that as slumping blocks increase in size, the likelihood of failure decreases under a given earthquake. In addition, the parametric results suggest that a static factor of safety near unity is required for large slopes to undergo significant slumping deformation during earthquakes. Finally, the slumping block model is used to understand the behavior of more complex arrangements of rock blocks that exhibit slumping failure. A promising path forward is exposed for use of the slumping block model to predict complex slope slumping failures.

5.1 Review of Slumping Blocks and Deformation Predictions

In this section the reader is presented with a summary on the current literature of slumping blocks and the prediction of rock slumping displacements during seismic events. Additional details of relevant literature will be provided throughout the chapter when necessary.

5.1.1 Slumping

Rock slumping has been thoroughly described by Kieffer (1998). In this description, Kieffer separates slumps into five classes; (1) flexure slumping, (2) block flexure slumping, (3) block slumping, (4) kink band slumping, and (5) toppling induced slumping. The classes of slumping considered in this chapter are shown in Figure 5.1. According to Kieffer (1998), slumping of the types shown in Figure 5.1 can be typically found in strong and hard slates, phyllites, schists, gneiss, granite and layered sedimentary rocks. While these images illustrate slumps

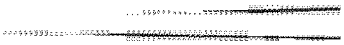

(a) Flexural slumping

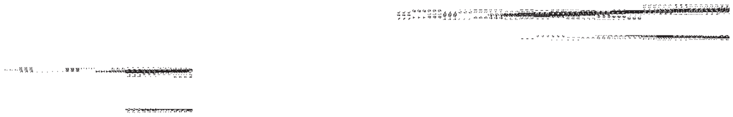

(b) Block slumping

(c) Block flexure slumping

Figure 5.1: Conceptual, non-fracturing, blocky failure modes (after Goodman and Kieffer (2000)).

comprised of multiple blocks, rock slumping failures can simply be a single block dislodging from a rock slope. For the purposes of this chapter a slumping block or slumping failure will primarily refer to a single block that displaces along two fractures by translating and rotating backward. However, examples will also be presented to illustrate how the single slumping block can approximate multiple block systems.

5.1.2 General Displacement Methods of Single Block Models

Methods based on single block models employ basic physics principles applied to simple geometries that are intended to approximate complex systems. Analogous to single degree oscillating models, single block models can provide a rich understanding of emergent complex behavior resulting from dynamic loading (Kramer and Smith, 1997; Gazetas et al., 2012). Single block models can provide an assessment tool to quantify failure potential from earthquake loading as shown in Chapter 4 and summarized in Jibson (2011).

In general, the author is unaware of any empirical methods for slumping failure modes in rock slopes that account for the rotational response of the failure mass. Sliding block models are the most commonly used models for assessing the displacement potential of slopes from earthquake ground motions. Newmark (1965), Goodman and Seed (1966), and Seed and Goodman (1964) brought fame to the sliding block model by estimating displacements of earth dams and sand embankments from earthquake loading. The sliding block model has been shown to be applicable to rock systems that undergo pure translational motion such as tetrahedral wedge sliding (Aydan et al., 2009; Bakun-Mazor et al., 2011). In these models, a block is assumed to slide with a rigid, perfectly plastic frictional contact between itself and an accelerating plane. This means that the block's movement mimics the base plane until the yield acceleration is exceeded and the block begins sliding relative to the plane. The block slides with an absolute acceleration equal to the yield acceleration and continues sliding until the relative velocity between the block and sliding plane equals zero. After the block stops sliding it motion again mimics the base plane and this logical cycle repeats. The relative displacement of the block is determined by double integrating the time history of relative acceleration between the block and plane. The equations of motion for the sliding block model is summarized with Equation 5.2

$$\ddot{x} = \left(\frac{\ddot{u}_{hg}}{g} - (1 + \frac{\ddot{u}_{vg}}{g}) k_y \right) g \qquad \text{for } \ddot{u}_{hg} > k_y \text{ or } \dot{x} > 0 \tag{5.1}$$

$$\ddot{x} = 0 \qquad \text{for } \ddot{u}_{hg} \leq k_y \text{ and } \dot{x} = 0 \tag{5.2}$$

An illustrative example of the sliding block calculation is shown in Figure 5.2. Jibson (1993) describes the use of this model for the seismic evaluation of landslides. A comprehen-

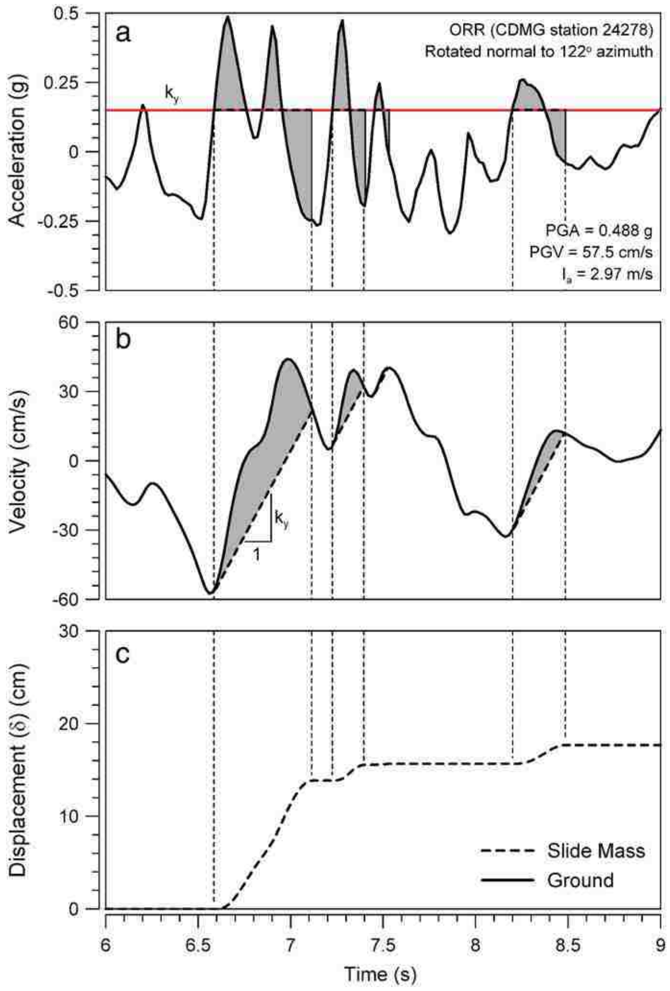

Figure 5.2: Sample calculation of sliding block method (Strenk and Wartman (2011))

sive summary of existing sliding block models and their predictions is provided by Meehan and Vahedifard (2013)

As was shown in Chapter 3, the slumping block yield acceleration is dependent on the moment of inertia of the block. This inevitably means that a displacement method for slumping blocks will require the rotation of the block to be accounted for. A similar conclusion was made by Prater (1979) for soil slopes excited by earthquake ground motion and sliding on a logarithmic failure plane. In this soil case, he states that the motion is dependent on the moment of inertia and calculation of the rotational motion is required. Once set in motion, the failing mass continues to rotate until the rotational velocity of the mass becomes zero. This is the same concept as used to evaluate a sphere sliding on a surface and rotating backward. Finally, after the relative behavior is determined for a given earthquake ground motion, suitable numerical integration techniques can be used to determine total displacements.

The consideration of rotation has been studied by many (Sarma, 1981; Chang et al., 1984; Sawada and Nomachi, 1985; Ling and Leshchinsky, 1995; Ling et al., 1997; Siddharthan and El-Gamal, 1998; Zeng and Steedman, 2000; Michalowski, 2007; Zeng and He, 2013). All except Siddharthan and El-Gamal (1998) neglect the changing position, compliant behavior, and effects on the normal forces of the failure mass. These exclusions are shown by Siddharthan and El-Gamal (1998) to be unconservative assumptions.

5.1.3 Methods for Slumping Failure Prediction

Sliding block (translation only) models are commonly applied to translational and slumping slope failures (Jibson, 1993). The sliding block model is used to develop regression models and empirical relationships for slopes in various geomaterials (Bartlett and Youd, 1992; Jibson, 1993, 2007; Saygili and Rathje, 2008; Rathje and Antonakos, 2011). These regression models typically relate ground motion intensity measures (e.g. PGA, PGV, M_w, and Distance) to a translational displacement response. However, researchers have shown that ignoring rotation causes displacements to be under predicted (You and Michalowski, 1999; Michalowski, 2007).

This under prediction was attributed to a reduction in yield acceleration, although it will be shown later that the displacement constraints formed by the fractures also contributes to these differences. In addition, Meehan and Vahedifard (2013) showed that these and other models consistently underpredicts the deformation measured in the field. Comparison of empirical models to field data have been performed by Dreyfus et al. (2013) and concluded that the yield acceleration of the slope and the triggering earthquake intensity are key factors in predicting performance of slopes during earthquakes. Another limitation to empirical regression models is that they represent the site specific characteristics of the included data thus making it difficult to extrapolate the results to other sites.

At the computational extreme, numerical models (e.g. discrete element method (DEM) and discontinuous deformation analysis (DDA)) can be used, however, these analyses are usually very site specific and thus the results are difficult to generalize. Prediction of slope movement have also been developed based on numerical models that evaluate general slope shapes excited by various earthquake ground motions (Makdisi and Seed, 1978; Bray and Travasarou, 2009).

5.2 Slumping Behavior of a Rigid Block

In this section, the displacement behavior of a slumping block will be investigated. As discussed in Chapter 3, the slumping block differs from a sliding block since it is in contact with multiple planes which constrain its motion. This difference results in a block that must undergo translational and rotational motion simultaneously in order for displacement of the block to occur. An illustration of a slumping block at positions before and after motion has occurred is shown in Figure 5.3. From this understanding of a slumping block's motion, the equations of motion for a slumping block can be derived.

5.2.1 Equation of Motion

Consider a rigid block in two-dimensional (2D) plane motion relative to a rigid, oscillating base. The base is formed by two fracture planes referred to as the base and back fracture

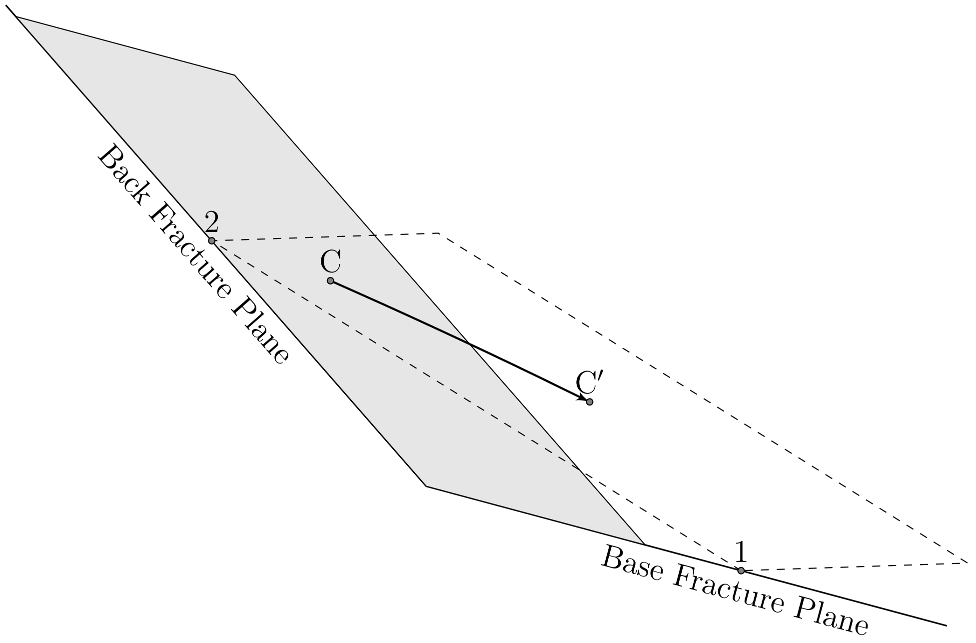

Figure 5.3: Slumping block schematic

planes. The geometry of the block relative to the fracture planes is assumed appropriately such that the slumping mode of movement controls (see Chapter 3). Finally, the block is assumed to be statically stable. It is this last assumption where the slumping block deviates from a sliding ladder in friction contact that are always assumed to begin in a statically unstable condition (Majumdar and Roy, 2012). As was shown in Chapter 3, this assumption means that the block remains in contact with the base and back fractures at contact points 1 and 2 at all times, unlike the sliding ladder. Should the slumping yield acceleration decrease to a value less than zero, then it is possible that the block may come out of contact with the back fracture. However, from an engineering standpoint, this discrepancy is generally uninteresting since block failure is guaranteed.

The free body diagram of a block in motion relative to the base is shown in Figure 5.4a. The forces acting on the block ($\mathbf{R}_1$, $\mathbf{R}_2$, W, $-m\ddot{u}_{vg}$ and $-m\ddot{u}_{hg}$) are shown in red. The resultant force and torque acting on the block ($I\ddot{\theta}$ and $m\ddot{u}_{cm}$) are shown in green. It is of primary interest to determine $I\ddot{\theta}$ and $m\ddot{u}_{cm}$ which represent the motion of the block.

In order to further simplify the free body diagram in Figure 5.4a, the principle of superposition is used. In Chapter 3, a free body diagram was evaluated to determine the slumping yield acceleration and is shown on the left side of Figure 5.4b. Subtracting this free body diagram from the diagram in Figure 5.4a, results in the remaining free body diagram on the right of Figure 5.4b. Since the free body diagram on the left side of Figure 5.4b is at limit equilibrium ($I\ddot{\theta} = m\ddot{u}_{cm} = 0$), then $I\ddot{\theta}$ and $m\ddot{u}_{cm}$ for the free body diagrams in Figure 5.4a and the right side of Figure 5.4b must be equal. Separation of these forces simplifies the equations of motion and will be shown later to be a critical step in forming a comparison to rock blocks that facilitates further investigation.

The equations for sum of forces and moments about the center of mass for the free body diagram on the right side of Figure 5.4b, noting that the sum of vector forces contributes two equations, are

$$\Delta\mathbf{R}_1 + \Delta\mathbf{R}_2 + (-\ddot{u}_{hg}/g - k_s)mg\hat{\mathbf{g}}_{\perp} = m\ddot{\mathbf{u}}_{cm} \tag{5.3a}$$

$$(\mathbf{r}_1 \times \Delta\mathbf{R}_1) + (\mathbf{r}_2 \times \Delta\mathbf{R}_2) = I_{cm}\ddot{\theta}. \tag{5.3b}$$

Assuming a set of orthogonal basis vectors ($\hat{\mathbf{x}} = \hat{\mathbf{g}}_{\perp}$ and $\hat{\mathbf{y}} = \hat{\mathbf{g}}$), factoring out ΔR_1, ΔR_2, r_1, and r_2, and substituting $mk^2 = I_{cm}$, where k = radius of gyration, yields

$$\Delta R_1\left(\hat{\mathbf{R}}_1 \cdot \hat{\mathbf{x}}\right) + \Delta R_2\left(\hat{\mathbf{R}}_2 \cdot \hat{\mathbf{x}}\right) + k_{inc}mg = m\ddot{x}_{cm} \tag{5.4a}$$

$$\Delta R_1\left(\hat{\mathbf{R}}_1 \cdot \hat{\mathbf{y}}\right) + \Delta R_2\left(\hat{\mathbf{R}}_2 \cdot \hat{\mathbf{y}}\right) = m\ddot{y}_{cm} \tag{5.4b}$$

$$\Delta R_1 r_1\left(\hat{\mathbf{r}}_1 \times \hat{\mathbf{R}}_1\right) + \Delta R_2 r_2\left(\hat{\mathbf{r}}_2 \times \hat{\mathbf{R}}_2\right) = mk^2\ddot{\theta} \tag{5.4c}$$

where $k_{inc} = -\ddot{u}_{hg}/g - k_s$.

Acceleration Constraints

In this form these equations have five unknowns: ΔR_1, ΔR_2, $\ddot{x}_{cm}$, $\ddot{y}_{cm}$, and $\ddot{\theta}$. However, since the motion of the block is constrained by the back and base fracture planes, $\ddot{x}_{cm}$ and

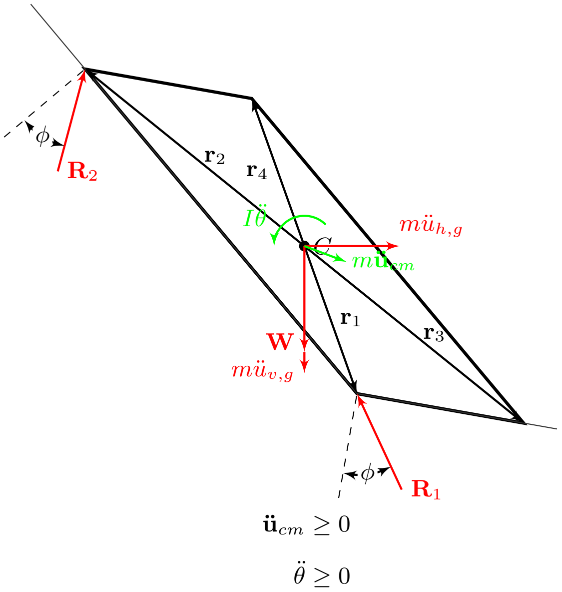

(a) Free body diagram - all forces

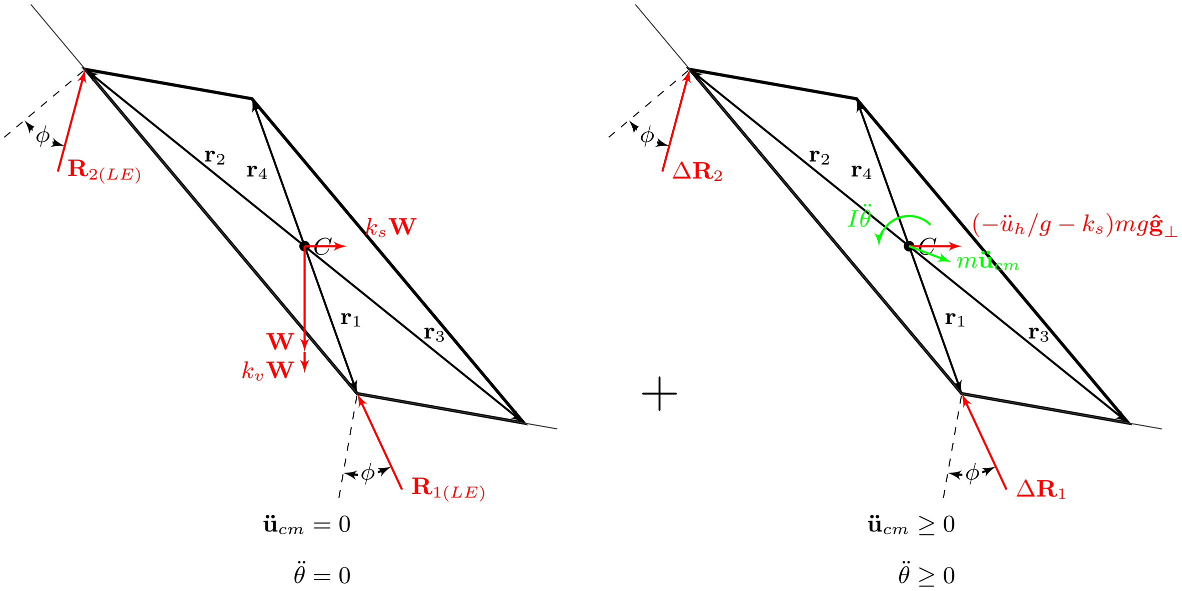

(b) Free body diagram - Superposition

Figure 5.4: Free body diagrams for a slumping block

$\ddot{y}_{cm}$ can be related to $\ddot{\theta}$. This relationship reduces the total unknowns to three ΔR_1, ΔR_2, and $\ddot{\theta}$ making the system statically determinant. The relationship between $\ddot{x}_{cm}$, $\ddot{y}_{cm}$ and $\ddot{\theta}$ is determined by evaluating the relative accelerations of points on the rigid body (1, 2, and C$'$) as shown in Figure 5.5a. First, the acceleration of contact point 2 relative to contact point 1 ($\mathbf{a}_{2/1}$), is determined using the relationship $\mathbf{a}_2 = \mathbf{a}_1 + \mathbf{a}_{2/1}$ as shown in the left vector diagram in Figure 5.5b. A difference in $\mathbf{a}_2$ and $\mathbf{a}_1$ is contributed solely to angular acceleration, thus $\mathbf{a}_{2/1} = l\ddot{\theta}$. Since the orientations of $\mathbf{a}_1$ and $\mathbf{a}_2$ act parallel to the base and back fracture planes and $\mathbf{a}_{2/1}$ acts perpendicular to the back of the block, the law of sines can be used to determine their magnitudes as

$$\frac{\sin(90-\theta)}{||\mathbf{a}_1||} = \frac{\sin(\gamma)}{l\ddot{\theta}} = \frac{\sin(90-\gamma+\theta)}{||\mathbf{a}_2||}. \tag{5.5}$$

Therefore,

$$||\mathbf{a}_1|| = l\ddot{\theta}\frac{\cos\theta}{\sin\gamma} \tag{5.6a}$$

$$||\mathbf{a}_2|| = l\ddot{\theta}\frac{\cos(\gamma-\theta)}{\sin\gamma}. \tag{5.6b}$$

The acceleration of the center of mass is obtained by evaluating its relationship to $\mathbf{a}_1$ with the equation $\ddot{\mathbf{u}}_{cm} = \mathbf{a}_1 + \mathbf{a}_{cm/1}$. As with $\mathbf{a}_{2/1}$, the magnitude of $\mathbf{a}_{cm/1}$ is attributed to the block's angular acceleration. Given that the orientation of $\mathbf{a}_{cm/1}$ is perpendicular to $\mathbf{r}_1$, $\mathbf{a}_{cm/1} = ||\mathbf{r}_1||\ddot{\theta}$. From the vector diagram shown in Figure 5.5b, the center of mass acceleration is

$$\ddot{\mathbf{u}}_{cm} = l\ddot{\theta}\frac{\cos\theta}{\sin\gamma}\hat{\mathbf{a}}_1 + ||\mathbf{r}_1||\ddot{\theta}\hat{\mathbf{a}}_{cm/1} \tag{5.7a}$$

$$\begin{aligned}\ddot{\mathbf{u}}_{cm} &= l\ddot{\theta}\frac{\cos\theta}{\sin\gamma}\left(\cos(\beta)\hat{\mathbf{x}} - \sin(\beta)\hat{\mathbf{y}}\right) \\ &\quad + ||\mathbf{r}_1||\ddot{\theta}\left(-\cos(\alpha_1-\beta+\theta)\hat{\mathbf{x}} - \sin(\alpha_1-\beta+\theta)\hat{\mathbf{y}}\right).\end{aligned} \tag{5.7b}$$

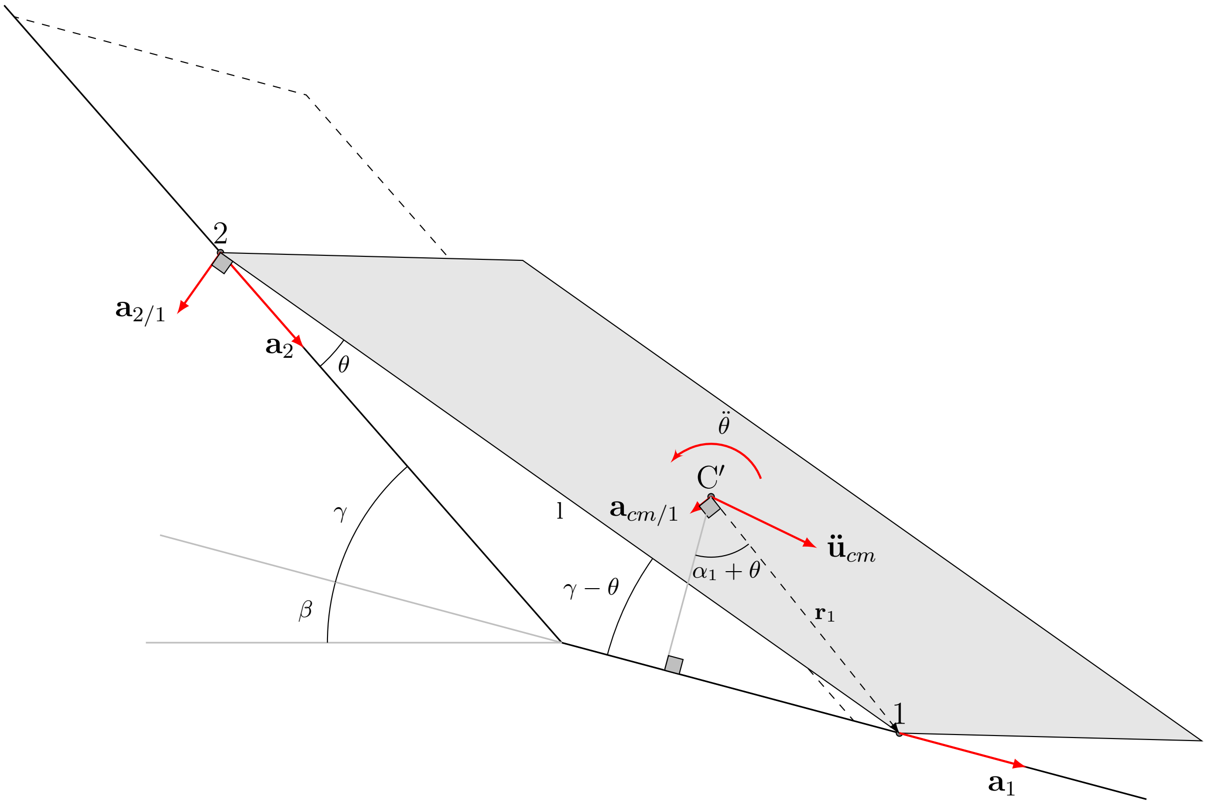

(a) Rigid body accelerations for constrained motion

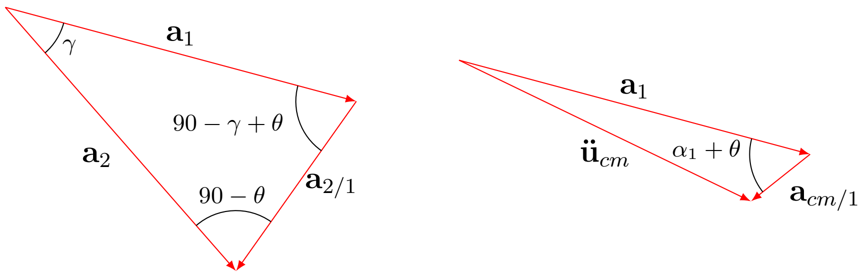

(b) Relative accelerations of the rigid body

Figure 5.5: Rigid body accelerations used to relate $\ddot{x}_{cm}$, $\ddot{y}_{cm}$ and $\ddot{\theta}$.

Substituting the components $\hat{\mathbf{x}}$ and $\hat{\mathbf{y}}$ for $\ddot{x}_{cm}$ and $\ddot{y}_{cm}$, respectively, from this equation into equations 5.4a to 5.4c yields

$$\Delta R_1 \left(\hat{\mathbf{R}}_1 \cdot \hat{\mathbf{x}}\right) + \Delta R_2 \left(\hat{\mathbf{R}}_2 \cdot \hat{\mathbf{x}}\right) + k_{inc} m g = m X_c \ddot{\theta} \tag{5.8a}$$

$$\Delta R_1 \left(\hat{\mathbf{R}}_1 \cdot \hat{\mathbf{y}}\right) + \Delta R_2 \left(\hat{\mathbf{R}}_2 \cdot \hat{\mathbf{y}}\right) = m Y_c \ddot{\theta} \tag{5.8b}$$

$$\Delta R_1 r_1 \left(\hat{\mathbf{r}}_1 \times \hat{\mathbf{R}}_1\right) + \Delta R_2 r_2 \left(\hat{\mathbf{r}}_2 \times \hat{\mathbf{R}}_2\right) = m k^2 \ddot{\theta} \tag{5.8c}$$

where, the constraints imposed by the base and back fractures, X_c and Y_c, are

$$X_c = \quad l \frac{\cos\theta}{\sin\gamma} \cos(\beta) - ||\mathbf{r}_1|| \cos(\alpha_1 - \beta + \theta) \tag{5.9a}$$

$$Y_c = -l \frac{\cos\theta}{\sin\gamma} \sin(\beta) - ||\mathbf{r}_1|| \sin(\alpha_1 - \beta + \theta). \tag{5.9b}$$

Constrained Equations of Motion

Solving these three equations for the three unknowns, ΔR_1, ΔR_2, and $\ddot{\theta}$ yields the equation of angular motion for the slumping block and the dynamic change in reaction force magnitudes.

$$\ddot{\theta} = \frac{g k_{inc} A}{Y_c A + X_c B + k^2 C} \tag{5.10a}$$

$$\Delta R_1 = \frac{-m g k_{inc} \left[\left(\hat{\mathbf{R}}_2 \cdot \hat{\mathbf{y}}\right) k^2 - \left(\hat{\mathbf{r}}_2 \times \hat{\mathbf{R}}_2\right) B r_2\right]}{r_1 \left(Y_c A + X_c B + k^2 C\right)} \tag{5.10b}$$

$$\Delta R_2 = \frac{m g k_{inc} \left[\left(\hat{\mathbf{R}}_1 \cdot \hat{\mathbf{y}}\right) k^2 - \left(\hat{\mathbf{r}}_1 \times \hat{\mathbf{R}}_1\right) B r_1\right]}{r_1 \left(Y_c A + X_c B + k^2 C\right)} \tag{5.10c}$$

where,

$$A = \frac{r_2}{r_1} \left(\hat{\mathbf{R}}_1 \cdot \hat{\mathbf{y}}\right) \left(\hat{\mathbf{r}}_2 \times \hat{\mathbf{R}}_2\right) - \left(\hat{\mathbf{R}}_2 \cdot \hat{\mathbf{y}}\right) \left(\hat{\mathbf{r}}_1 \times \hat{\mathbf{R}}_1\right) \tag{5.11a}$$

$$B = \left(\hat{\mathbf{R}}_2 \cdot \hat{\mathbf{x}}\right) \left(\hat{\mathbf{r}}_1 \times \hat{\mathbf{R}}_1\right) - \frac{r_2}{r_1} \left(\hat{\mathbf{R}}_1 \cdot \hat{\mathbf{x}}\right) \left(\hat{\mathbf{r}}_2 \times \hat{\mathbf{R}}_2\right) \tag{5.11b}$$

$$C = \left[\left(\hat{\mathbf{R}}_1 \cdot \hat{\mathbf{x}}\right) \left(\hat{\mathbf{R}}_2 \cdot \hat{\mathbf{y}}\right) - \left(\hat{\mathbf{R}}_1 \cdot \hat{\mathbf{y}}\right) \left(\hat{\mathbf{R}}_2 \cdot \hat{\mathbf{x}}\right)\right] \frac{1}{r_1}. \tag{5.11c}$$

If these parameters are further consolidated into a single parameter, then Equation 5.10a can be simplified to the form

$$\ddot{\theta} = q^2 \left(k_{inc}\right) \tag{5.12}$$

where

$$q^2 = \frac{gA}{Y_cA + X_cB + k^2C}. \tag{5.13}$$

Equation 5.12 in its condensed form is remarkably similar to the rocking block equation (Equation 4.2) and possesses the same units. The significance of this similarity will be expanded in Section 5.3.4.

5.2.2 Similarity to Other Seismic Displacement Models

The form of Equation 5.12 is similar to other seismic displacement models. In particular, the differences can be narrowed down to variations in the parameter q^2. Table 5.1 shows the equivalent q_2 for derivations of slope displacements assuming a log-spiral failure surface. In addition, Siddharthan and El-Gamal (1998)(circular failure surface for dry cohesionless slopes) and Zeng and He (2013) (circular failure surface for saturated clay slopes) show potential to be written in the form of the slumping block Equation 5.12. However, the equations would need to be reworked considerably and is beyond the scope of this discussion. These similarities may make it possible to apply the results shown later in this chapter to

Table 5.1: Similarity of slumping block equation to other seismic displacement models with a rotation component. The specific references should be consulted for the meaning and expansion of all symbols.

Failure type	Reference	equivalent q^2
Log-Spiral	Prater (1979) (equation 18)	$\frac{M_g+M_c}{I}$
Circular	Sarma (1981) (equation 3)	$\frac{gWd\sin\theta_o+\theta}{I}$
Log-Spiral	Chang et al. (1984) (equation 27)	$\frac{g\gamma[r_o^3(f_4-f_5-f_6)+Xpr_o^2f_q]}{W_3l^2}$
Log-Spiral	Ling and Leshchinsky (1995) (equation 12)	$\frac{gR_{cg,y}}{R_{cg}^2}$
Log-Spiral	Ling et al. (1997) (equation 7)	$\frac{g\cos\beta_{cg}}{r_{cg}}$

slopes of a wide variety of geometries and strength that undergo rotation and translational motion.

5.2.3 Behavior of Equation of Motion Parameters

Equation 5.12 is a function of the block geometry, fracture interface strength limit, and the orientations of the base and back fractures. In order to investigate the behavior of slumping blocks under seismic excitation, it is desirable to have a comprehensive understanding of the effect that differing block and fracture geometries and friction angles have on the parameters of Equation 5.12. As the block displaces during seismic excitation, it translates and rotates backward. Consequently, the block's geometric vectors will also rotate causing the parameters in the equations of motion to change.

The changes to the equations of motion invoked as the slumping block rotates are now evaluated. Consider a slumping block with parameters $\alpha_1 = 65°$, $\alpha_3 = 75°$, scale $= 1$ meter, and $\phi = 55°$. This block has a relative fracture angle, $\approx \gamma = 19°$, which is also equal to the maximum rotation the block can undergo before the block is fully rotated onto its back. Figure 5.6 shows the percent change of the components of Equation 5.10a $(A, B, C, X_c, Y_c, k^2, k_s)$ as the block displaces toward a slumping failure $(\theta/\gamma = 1.0)$. Obviously, k^2 remains constant since it is a property of the block shape. The parameter C is a function of the orientations of the reaction forces acting relative to the base and back fractures. Since the orientation of the base and back fractures and the friction coefficient along the fractures are held constant in this example, C is also constant. Using the definitions of A and B above and recalling Equation (3.25), it can be seen that $k_s = (1 + k_v)A/B$. The parameters A, B, X_c, Y_c, k^2, k_s are all functions of the geometric unit vectors $\hat{\mathbf{r}}_1$ or $\hat{\mathbf{r}}_2$ and thus change with θ. Also shown in Figure 5.6 as thicker lines, are the simplified parameters from Equation 5.12, k_s and q^2. The percent change for these two parameters is modest in comparison with the other parameters shown. Figure 5.6 provides a positive indication that the consolidation of the equation of motion to the form in Equation (5.12) was appropriate. Additional support of this consolidation is provided in subsequent sections.

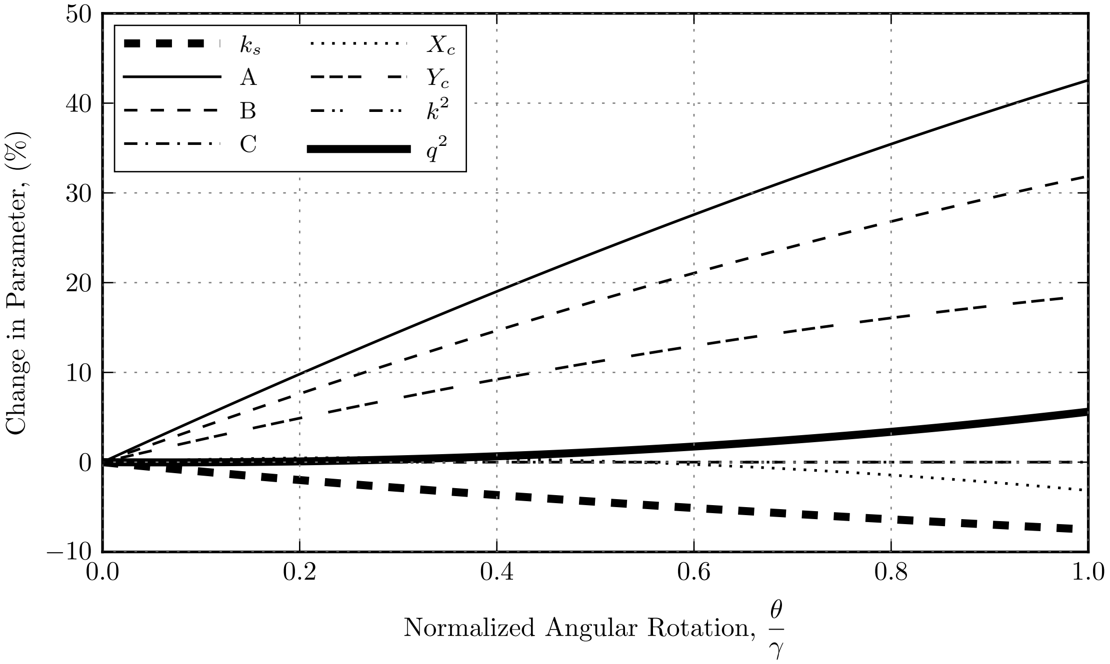

Figure 5.6: Variability of slumping equation components in Equation 5.10a. The parameters k_s and q^2 are highlighted as they will be shown as important predictors of seismic behavior.

5.2.4 Correlation of q^2 and k_s with Geometry and Friction Angle

The relationship between the parameters q^2 and k_s and the block geometry and fracture interface friction angle is evaluated for the full possible rotation of the block. Recall, that the two sets of parameters that can be used to describe a parallelogram are α_1, α_3 and $\frac{S_2}{S_1}$, γ (see Section 3.2). Two base slumping blocks are evaluated with each of the defining parameters varied individually holding all others constant. For the α_1, α_3 set, the base slumping block parameters are $\alpha_1 = 55°$, $\alpha_3 = 75°$, scale$= 1.0m$, slope$= 0°$, $\phi = 45°$. For the $\frac{S_2}{S_1}$, γ set, the base slumping block parameters are $\frac{S_2}{S_1} = 0.1$, $\gamma = 20°$, scale$= 1.0m$, slope$= 20°$, $\phi = 40°$. Figures 5.7 and 5.8 present the results of the α_1, α_3 and $\frac{S_2}{S_1}$, γ sets, respectively. Each figure shows values of q^2 and k_s calculated for all possible block rotations

($\theta = 0$ to γ) for various geometric parameters. These figures illustrate which geometric parameters have the largest influence over q^2 and k_s.

The influence of the geometric parameters on k_s were evaluated in Chapter 3 and are discussed again here. The parameters with the biggest influence over k_s are the slope angle and friction angle. An increase in slope angle results in an increase in driving force and reduction in normal forces, and by relation, reduction in resisting forces, causing $k_{s,0}$ to decrease. An increase in ϕ also results in an increase in resisting forces causing $k_{s,0}$ to increase. Increases in α_3 and s_2/s_1 and decreases in α_1 and γ also cause k_s to increase. The change in these parameters effectively move the block's center of mass relative to a distance perpendicular to the back fracture plane. Changing the center of mass location changes the moments acting on the block and thus the distribution of normal forces acting on each fracture plane. As the center of mass moves further from the back fracture plane, k_s increases.

From Figures 5.7 and 5.8 it can be seen that the parameter with the largest influence on variability in q^2 is the scale of the block. This variability is expected since the constraints X_c, Y_c, and k^2/C have units of length. An order of magnitude increase in scale results in an order of magnitude increase of q^2. To a lesser degree, the parameters α_3, α_1 and $s_2/s_1, \gamma$ also change the values of q^2 as they control the shape of the block and orientation of the fracture planes.

Based on the relationships between geometry on k_s and q^2, the following conclusions can be made:

- The scale of the block is strongly correlated to q^2 while it has zero correlation with k_s.

- Parameters representing the shape of the block have comparable correlation between both q^2 and k_s.

- Friction angle and slope angle are strongly correlated with k_s and weakly correlated with q^2.

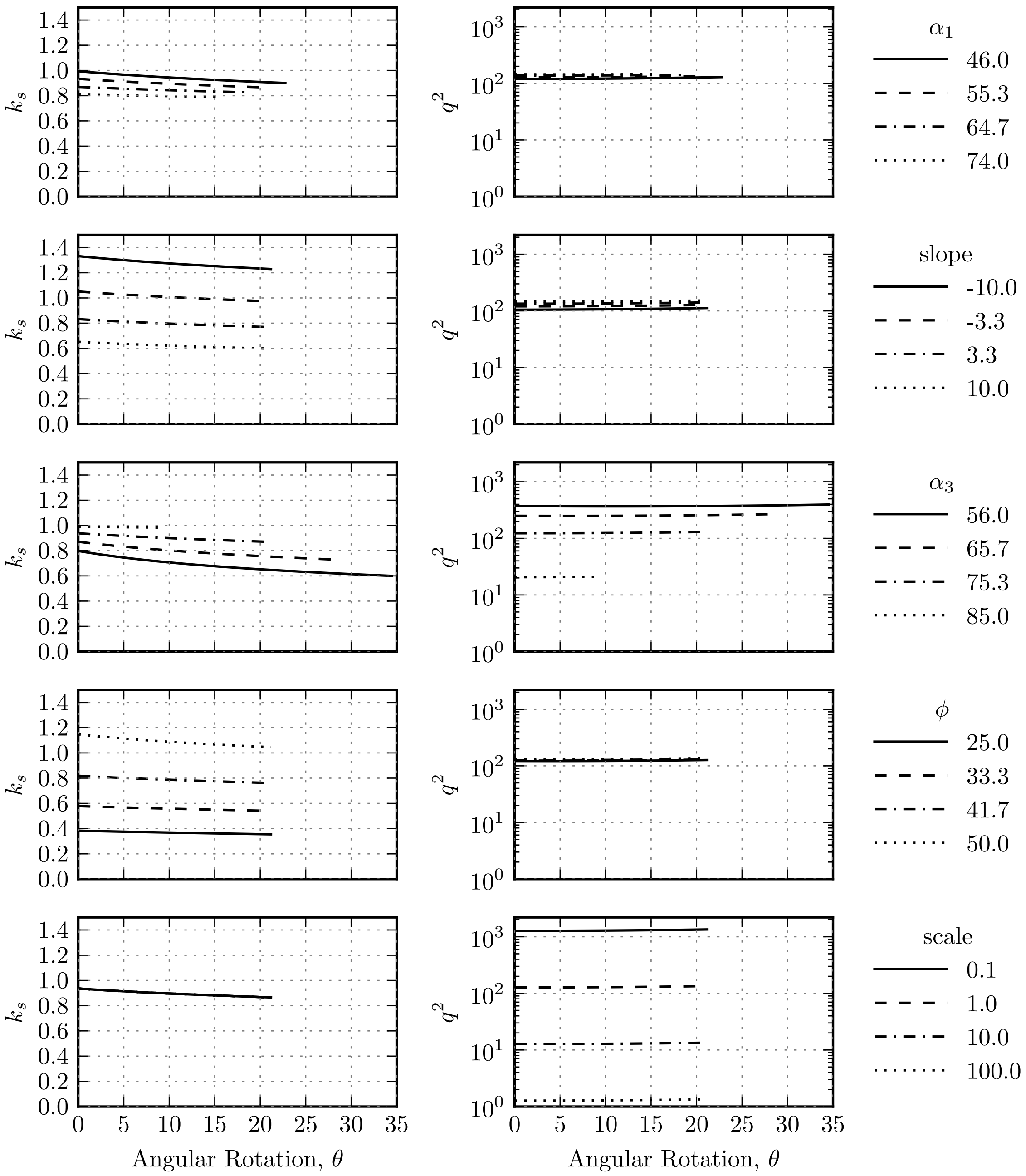

Figure 5.7: Variability of q^2 and k_s, for α_1, α_3 parameter set. The $\frac{S_2}{S_1}$, γ parameter set is held constant.

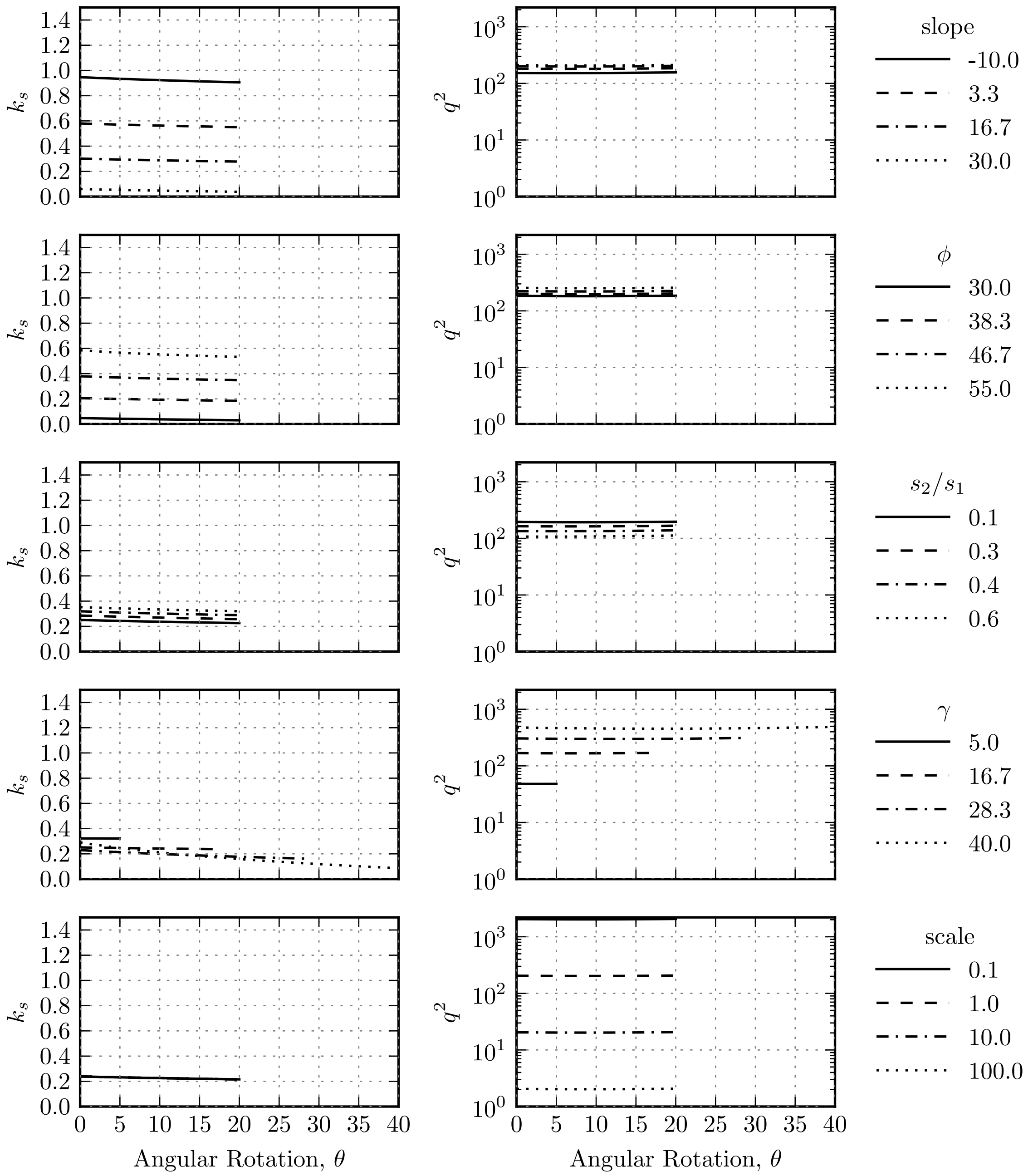

Figure 5.8: Variability of q^2 and k_s, for $\frac{S_2}{S_1}$, γ parameter set. The α_1, α_3 parameter set is held constant.

5.2.5 *Variability of q^2 and k_s with Block Rotation*

If, over a wide range of geometric parameters, the parameters, q^2 and k_s, demonstrate similar behavior as the block rotates, then it may be possible to use their values at $\theta = 0$ to represent their characteristic behaviors during seismic excitation. The data shown in Figures 5.7 and 5.8 is now replotted with θ normalized by the maximum rotation, γ, and the percent change in k_s and q^2. For the parameter k_s, the change in k_s as θ increases is plotted, thus $\Delta k_s = (k_{s,\theta}/k_{s,0} - 1) * 100\%$. For the parameter q^2, the percent change in the value is plotted, thus $\Delta q^2 = (q_\theta^2/q_0^2 - 1) * 100\%$. These plots are shown in Figures 5.9 and 5.10 for the α_1, α_3 and $\frac{S_2}{S_1}$, γ sets, respectively. The plots where the geometric parameters which influence k_s the most (β and ϕ) show consistent responses in both k_s and q^2. Based on these observations, if the shape is held constant, then k_s and q^2 are represented well by their $\theta = 0$ values. The parameters that influence shape the most show less consistency. Because of this inconsistency, blocks of different shapes will likely have different dynamic responses. The largest divergences occur when the block goes from a skinny slumping block to a fat slumping block. The wider the slumping block the more non-linearity in the response of the block. In addition, a block with a large angle to rotate through (large γ) also exhibits high non-linearity. This behavior similar to the rocking block problem.

5.3 *Slumping Block Model*

With the slumping block equations established, termed the Slumping Block Model (SBM) is presented. The SBM is formed in a rigid-plastic model framework similar to that of the Newmark sliding block and toppling block model presented in Chapter 4. This model represents the fundamental behavior of a simultaneously translating and rotating rigid block. Furthermore, the SBM model will be used in Section 5.5 to serve as a proxy for more complex systems.

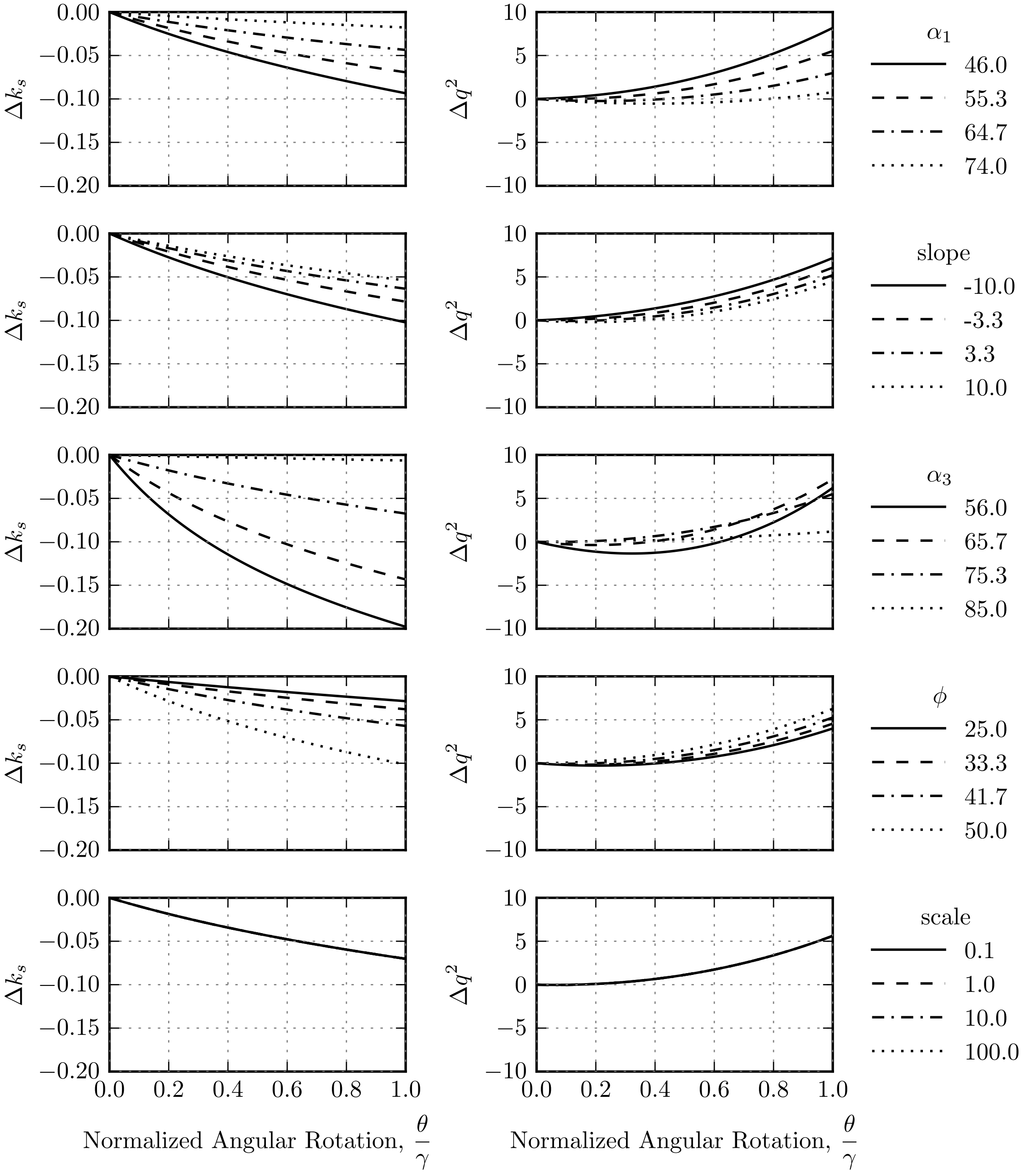

Figure 5.9: Percent change of q^2 and k_s, for α_1, α_3 parameter set.

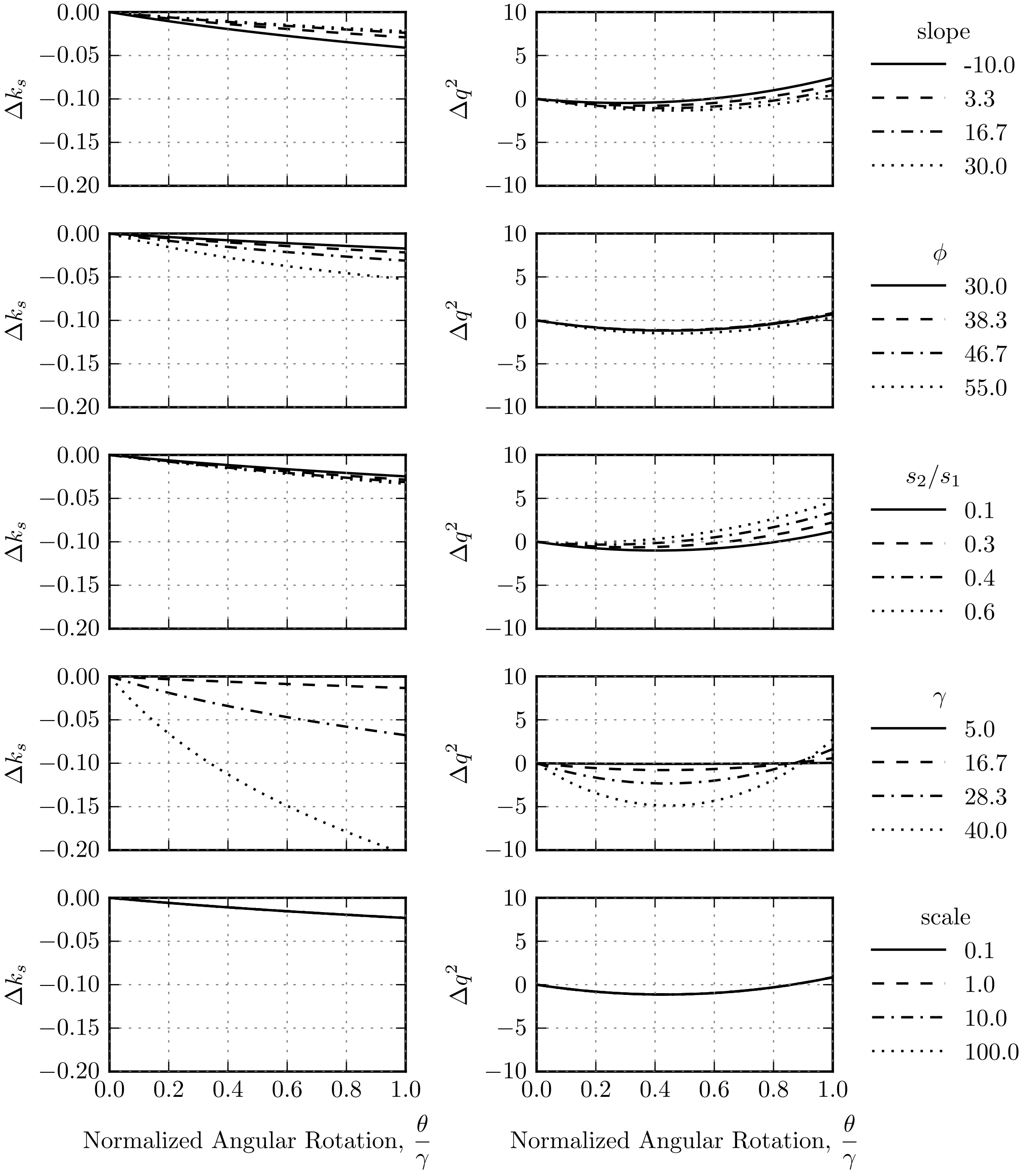

Figure 5.10: Percent change of q^2 and k_s, for $\frac{S_2}{S_1}$, γ parameter set.

5.3.1 Solution by Numerical Integration

Given that the slumping equations are non-linear and discontinuous, they will need to be solved by numerical methods. It is common for equations such as these to be solved using a numerical integrator that assumes continuity, such as Matlab's ODE45 or Python's ODEINT functions that utilize legacy FORTRAN solvers. While a solution may be calculated, these simulations may not be stable. Error is introduced where time integration is performed across a discontinuity in the equations and grows as the time step of integration increases. Alternatively, if care is taken to have an integration point on each side of the discontinuity, then the errors associated with discontinuity can be reduced and larger time steps can be taken reducing error and simulation time. This is the approach taken for the simulations presented in this chapter.

The equations of motion are solved by using the Sundials Fortran solver, CVode, interfaced with Python using the package Assimulo (Fredriksson et al., 2014; Andersson et al., 2015). Assimulo provides an interface to specify discontinuities in the equations of motion through event detection by the numerical solver. When an event is detected, changes to the equations of motion or model state are necessary. In this scenario, the numerical integrator stops and reevaluates the previous time step at finer increments until the location of the discontinuity in time is determined within a specified error. In mathematical terms this is referred to as root finding.

There are several states of the model that are monitored for discontinuous events as follows:

Event 1 - Yield acceleration exceeded $[\ddot{u}_{hg} > (1+k_v)k_s]$**:**

> This event is triggered when the ground motion exceeds the block's critical slumping acceleration and the nonzero equations of motion should be used. If the ground motion falls below the slumping acceleration there is no effect on whether the equations of motion should be switched or not. Ceasing of rocking motion depends on event 2 described next.

Event 2 - Angular velocity approaches zero [$\dot{\theta} \to 0$]:

Once motion of the block begins as described by event 1 then the block will have a positive angular velocity. As long as $\dot{\theta}$ is positive, the block remains in motion. When $\dot{\theta}$ decreases to zero, the block no longer has motion relative to the base plane. The block's angular displacement and velocity are set to zero. The equations of motion are set to zero if, at the same time, the ground motion is also below the slumping acceleration.

Event 3 - Full rotation occurs [$\theta = \gamma$]:

This event triggers the end of the simulation when the block has fully rotated backward. In all cases, once the block has rotated onto its back, the new mode of failure is sliding. Although not evaluated in this chapter, if this event occurs before the time history is complete and the base fracture plane is long enough, the movement of the block could be evaluated using a traditional sliding block analysis.

5.3.2 Model Validation

Model validation was performed by comparing results of the slumping model with results from simulations using the DEM software *UDEC*. The test block geometry consists of a parallelogram ($\gamma = 30°$, $s_2/s_1 = 0.1$, scale=$91.47cm$) founded on an inclined base fracture plane ($\alpha = 20°$) and joint interface friction angle of $\phi = 31°$ as shown in Figure 5.11. The *UDEC* parameters used in this simulation are summarized in Table 5.2.

UDEC uses springs to calculate reaction forces between blocks thus sudden changes in accelerations will induce transient oscillations into the model. Since the slumping model is a rigid-plastic model, for comparison purposes, these transient oscillations are undesirable. Therefore it is necessary to gradually increase the loading amplitude. The inclined plane is accelerated with a ground motion represented by a constant frequency (1hz) sine wave with an amplitude that linearly increases from zero to a peak amplitude of 0.2g's over two cycles and then remains at 0.2g's until the block fails.

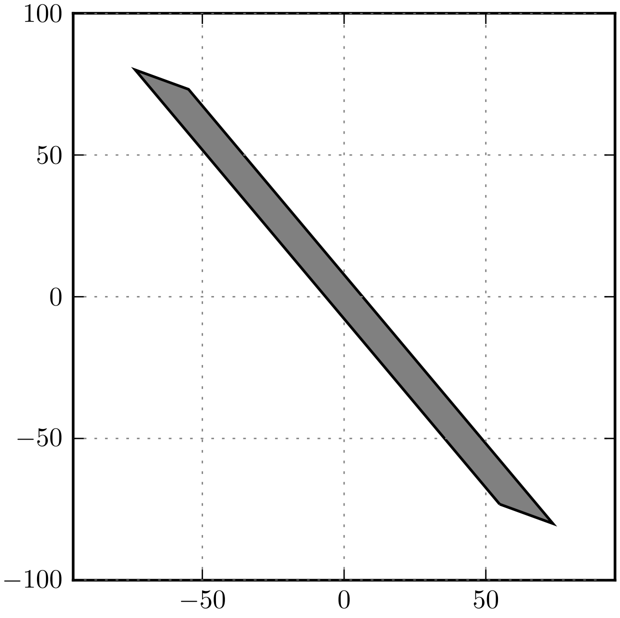

Figure 5.11: Geometry used in validation

Table 5.2: *UDEC* parameters for slumping block validation

Parameter	Value
Block type	Rigid
Rounding	2% smallest dimension
Density	$2,700$ kg/m^3
Joint shear stiffness	$6.56e10$ N/m
Joint normal stiffness	$6.56e10$ N/m
Damping Type	Stiffness Proportional
Damping Frequency	4.0 hz
Damping Portion	0.1%

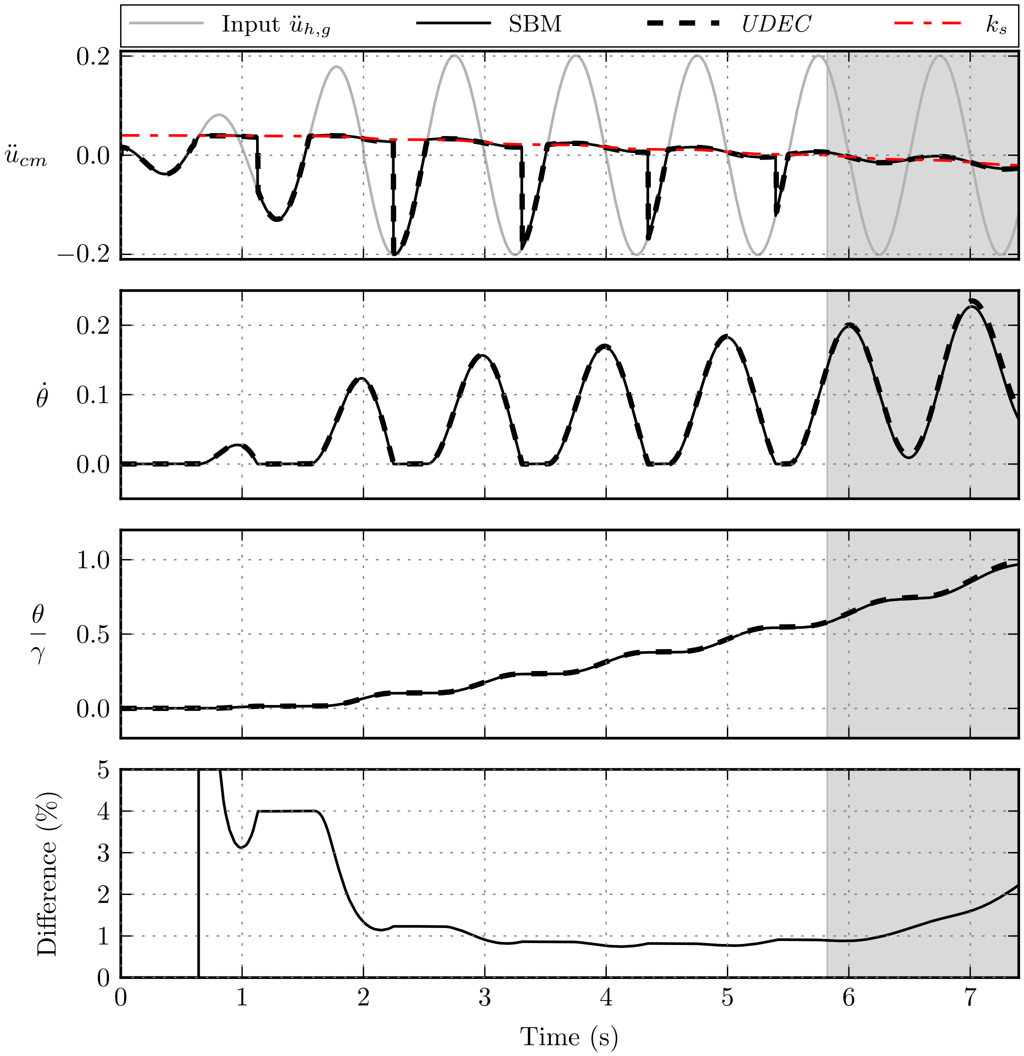

Figure 5.12: Validation of slumping block model (SBM) with DEM. Shaded region indicates when $k_s \leq 0$.

The calculated responses for the simplified and DEM models are shown in Figure 5.12. The agreement between the two simulations is excellent. The top plot shows the horizontal acceleration response of the block's center of mass relative to the input time history. Note that the block's acceleration is actually opposite of the base motion, but for comparison purposes the negative base ground motion is plotted to provide an intuitive understanding that the ground motion and block's inertial acceleration are related. This plot can be interpreted very much like a classic sliding block analysis. When the block's response is not tracing the input motion, the block is in a slumping motion. The acceleration at the onset of motion is exactly the slumping yield acceleration. However, unlike sliding block models, the center of mass acceleration does not remain constant throughout block motion because of the rotational component of motion. In addition, the horizontal acceleration of the block after the onset of motion does not represent the current yield acceleration. This concept can be seen by comparing the block's horizontal acceleration to the dashed line which represents the rotation dependent slumping yield acceleration based on Equation 3.25. At about 5.8 seconds (gray shaded region), k_s falls below zero and the block stays in continuous motion.

The second plot shows the angular velocity of the block which has positive values only when the block is in motion. The shape of this curve is similar to that of both sliding and toppling blocks with the difference being that for a sliding block this would be relative horizontal velocity. The scenario where $k_s < 0$ is indicated by $\dot{\theta} > 0$ for the rest of the simulation.

The third plot shows the normalized angular displacement where a value of unity indicates that the block has fully rotated backward. Similar to a sliding block, the displacement of the block accumulates with each cycle of motion.

In the lower plot, the difference between the two analyses $((\theta_{SBM} - \theta_{UDEC})/\theta_{SBM} \times 100\%)$ is shown. At the beginning of the analyses the difference is large because of the accuracy in integrating the small increments of motion. As the motion during each cycle becomes larger, the difference goes down to about 1%. Once the k_s of the block drops below zero, the difference begins to rise again. It is suspected that this difference could be attributed to the rounded corners, springs, and damping used in *UDEC*.

5.3.3 *Comparison to Sliding Block Analysis*

As indicated in the previous section, the slumping block model shares characteristics with both the sliding block and toppling rock block models. To illustrate the similarities with the sliding block model, three simulations were performed with blocks of the same geometry but different scales. The full results of both translational and rotational motion are shown in Figure 5.13. The translational motion is shown in the top three axes while the rotational motion is shown in the bottom three axes. As expected, the influence of the different block scales results in a dramatic difference in rotational response. The smaller block experiences large angular accelerations and thus slumps rather quickly compared to the larger blocks. However, the horizontal translational behavior of all the blocks travel similar paths. Since all blocks have the same geometry, the initial k_s's are equal. However, the drop in subsequent k_s as the blocks rotate is more dramatic for the small block versus large block since the small block experiences more rotation. Although subtle, the duration of motion for each cycle of motion for the small size blocks are slightly larger than the large block. The beginning of each cycle of motion is marked by the beginning of relative block motion from a state of zero relative block motion with respect to the base plane. This is the result of the slumping block's motion being maintained as long as there is angular motion and since the small blocks have a higher angular velocity, the motion lasts longer.

As the angular velocity decreases and the change in k_s is minimal, the translational response of the block approaches the sliding block response. This similarity is generally the case for blocks that are large relative to the magnitude and duration of the ground motion since the rotational response of the block is small and the path of the center of mass is linear (Figure 5.14). The path of the center of mass for each block is shown and compared to that of the sliding block model, assuming slumping movement parallel to the base plane. The horizontal motion is similar in total magnitude but the vertical motion is not as accurate because the true path of the center of mass is not parallel to the base plane (as was shown previously).

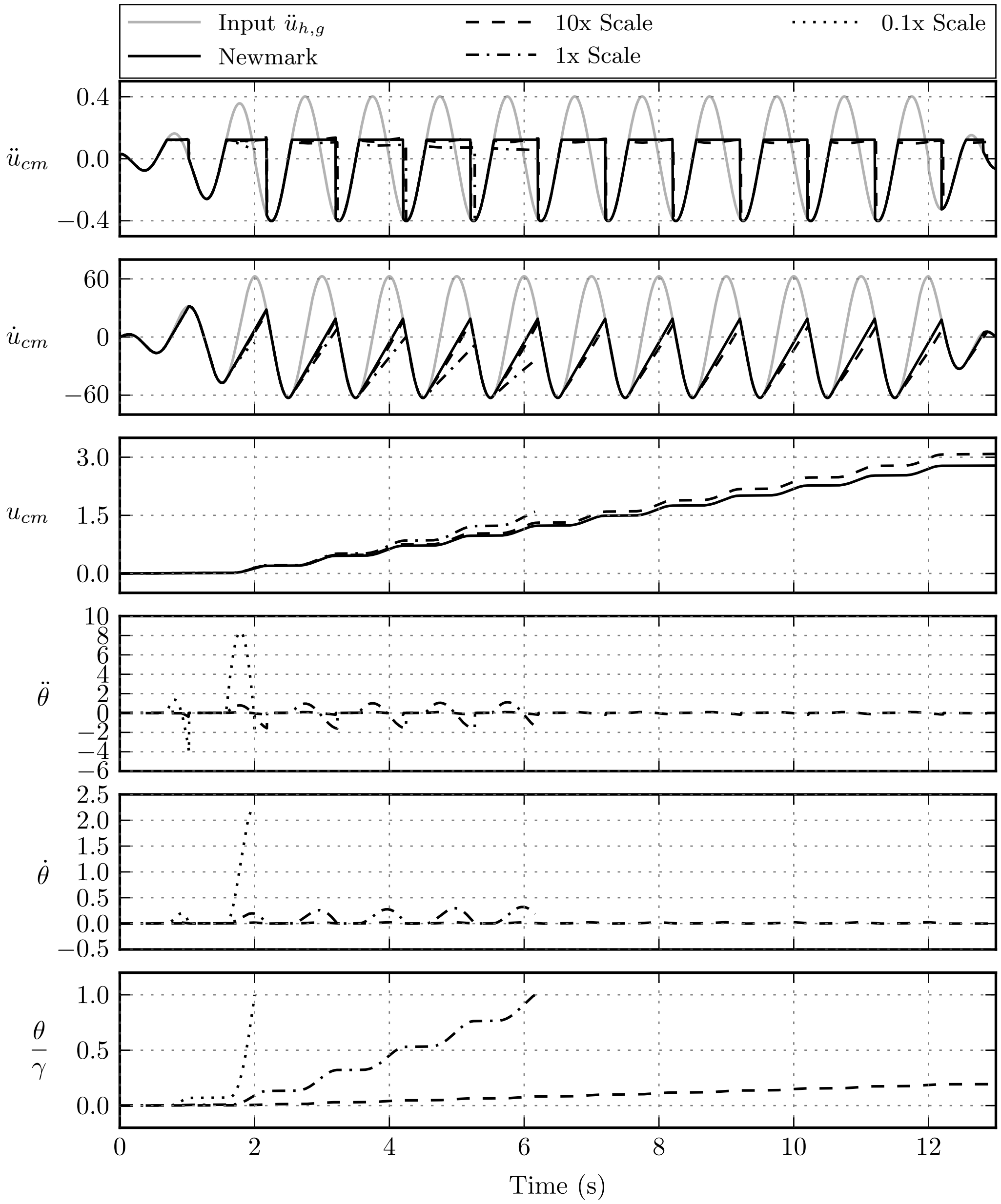

Figure 5.13: Comparison between slumping and sliding block models.

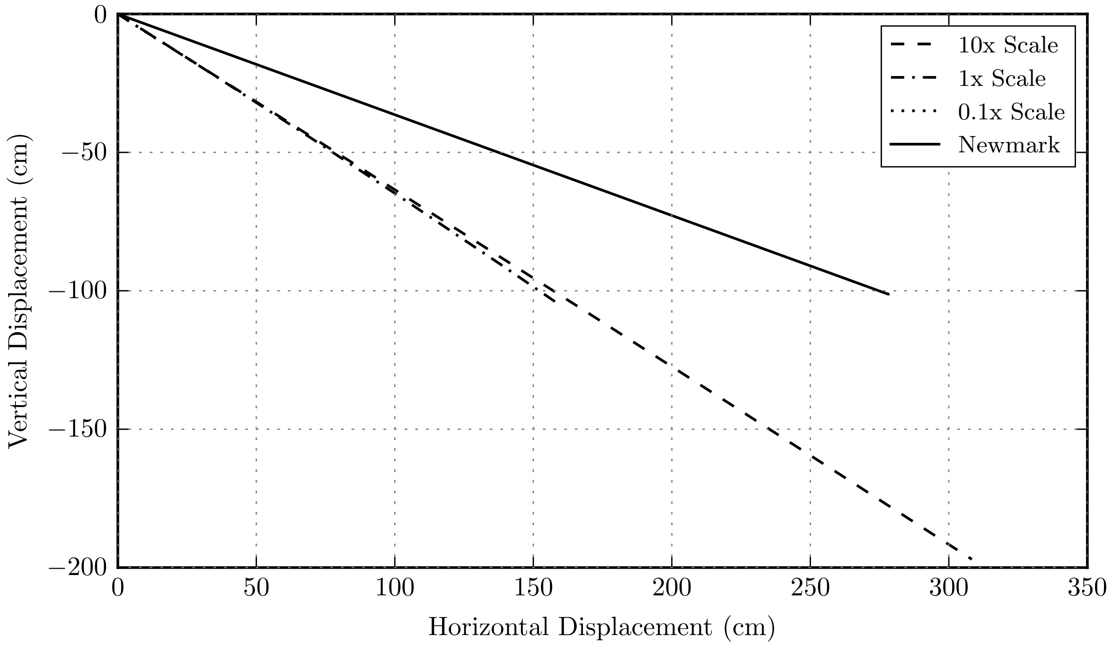

Figure 5.14: Comparison between slumping and sliding block models.

This comparison indicates that an approximation of the slumping block response could be made by performing a sliding block analysis with the appropriate yield acceleration. The similarity is only with respect to the block's horizontal response which is at its center of mass since the sliding block model can only describe one degree of freedom of the motion. However, as shown in Equation (5.7b), translational and rotational motion are related by the boundary conditions which direct the block's motion on a unique path. This relationship can be used to calculate the vertical and rotational component of the block's motion from the horizontal response provided by the sliding block model to yield an approximation of the full motion. However, once the total motion was calculated, the duration of motion would need to be truncated if the normalized rotation of the block exceeded 1.0. The error in this approximation would increase as the block's rotational velocity or displacement becomes relatively large and the path of the center of mass deviates from a linear path.

Other block models (Crawford and Curran, 1982) show displacement dependent reduction in yield acceleration for a sliding block with rate-dependent friction. The slumping block achieves similar behavior purely through geometry. The signature of the sliding block with rate dependent friction and slumping block are similar. Care should be exercised that the true motion of the rock mass is determined so that an appropriate model (e.g. slumping block or rate dependent friction sliding block) is used when back calculating friction coefficients from field and laboratory observations.

5.3.4 Dimensionless Analysis of Slumping Blocks

As mentioned previously, the equation of motion for the slumping block (Equation 5.12) is similar to the toppling block Equation (Equation 4.2). For convenience, they are restated here in their simplified forms

$$\ddot{\theta} = p^2 \cos(\theta_c - \theta) k_{inc} \tag{Slumping}$$

$$\ddot{\theta} = q^2 k_{inc}. \tag{Toppling}$$

Both p and q have the same units ($1/s$) and represent a natural frequency of the block. The slumping block does not oscillate in the traditional sense but the parameter q still represents a natural response to periodic loading and will be used to normalize the time dimension. Given these mathematical similarities, the extensive rocking block literature can be used as a guide for investigating the behavior of slumping blocks. A dimensionless analysis of rocking blocks performed by Dimitrakopoulos and DeJong (2012) yielded the following dimensionless parameters, $\frac{\ddot{\theta}}{p^2 PGA}$, $\frac{\dot{\theta}}{p PGA}$, $\frac{\theta}{PGA}$, ω_g/p, k_r/PGA, pt, which should be applicable to the slumping block. For applicability to the slumping block, q and k_s are substituted for p and k_r, respectively.

Four sets of evaluations were performed to demonstrate the behavior described in the previous sections with results presented with dimensionless parameters. The block parameters used in these evaluations and the corresponding figure references are shown in Table 5.3. As was indicated in the previous section, scale does not change the behavior of k_s and q^2

Table 5.3: Block parameters used in dimensionless evaluations

Varied Parameter	Block	Scale (cm)	Slope (deg)	ϕ (deg)	$\frac{s_2}{s_1}$	γ (deg)
	Default	100	20.0	35.0	0.1	30.0
Scale (Figure 5.15)	0.1x Scale	10				
	1x Scale	100				
	10x Scale	1000				
Slope and Friction (Figure 5.16)	Block 2		0.0	20.0		
	Block 3		10.0	25.0		
	Block 1		20.0	35.0		
Aspect Ratio (Figure 5.17)	Block 1				0.1	
	Block 6				0.3	
	Block 7				0.5	
Relative Fracture Angle (Figure 5.18)	Block 1					30.0
	Block 4					40.0
	Block 5					50.0

with respect to θ, therefore the responses of the three different sized blocks are identical in dimensionless space (Figure 5.15). Similarly, the slope and friction angles and block aspect ration ($\frac{S_2}{S_1}$) have only a modest affect on k_s and q^2 with respect to θ thus the responses are practically similar (Figures 5.16 and 5.17, respectively). However, for the simulations where γ is varied the block responses deviate substantially from each other as the blocks rotate and θ increases (Figure 5.18). From this analysis it can be concluded that self-similar slumping block behavior is best evaluated when the block shape is held relatively constant.

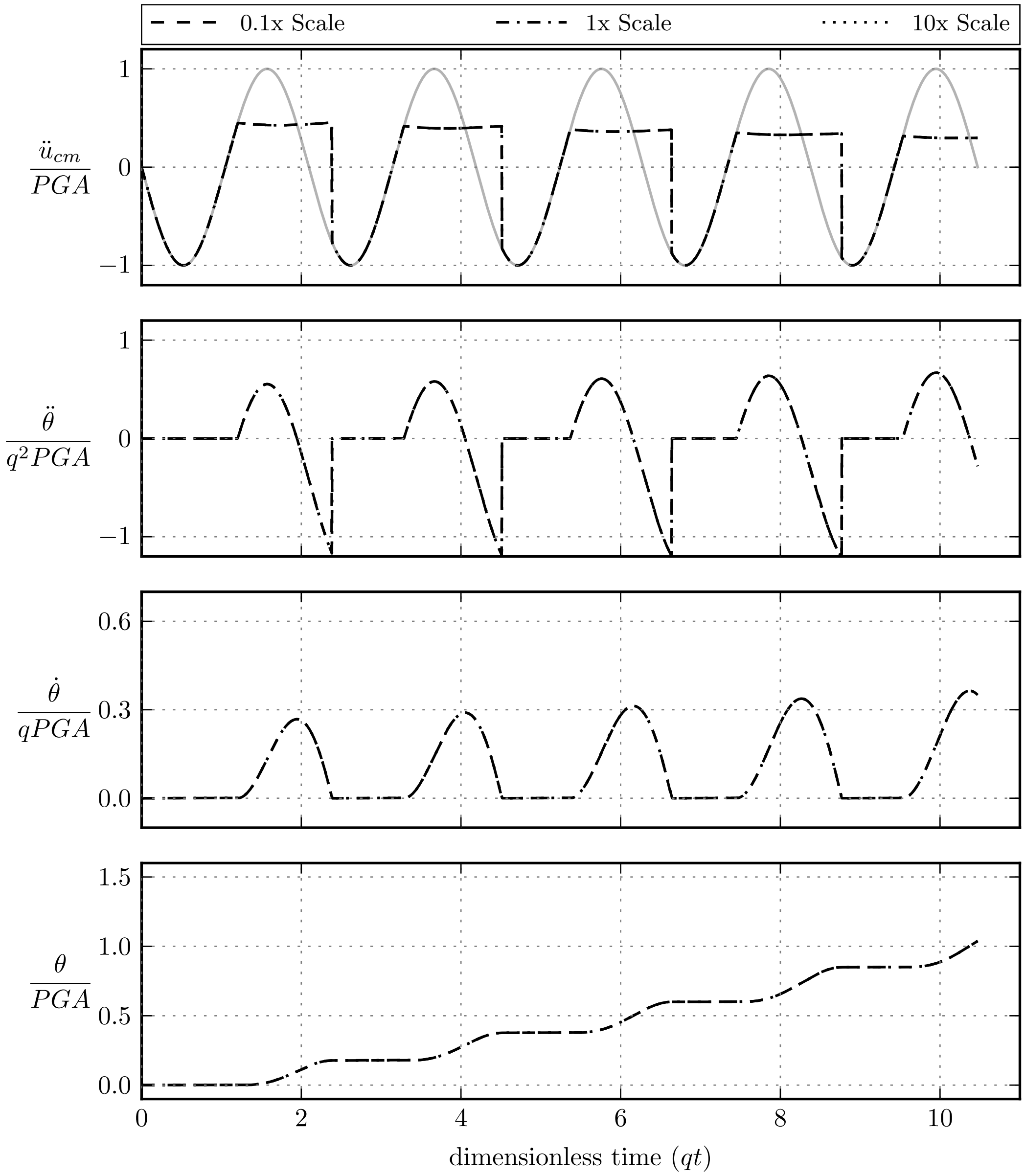

Figure 5.15: Dimensionless evaluation of the effects of block scale.

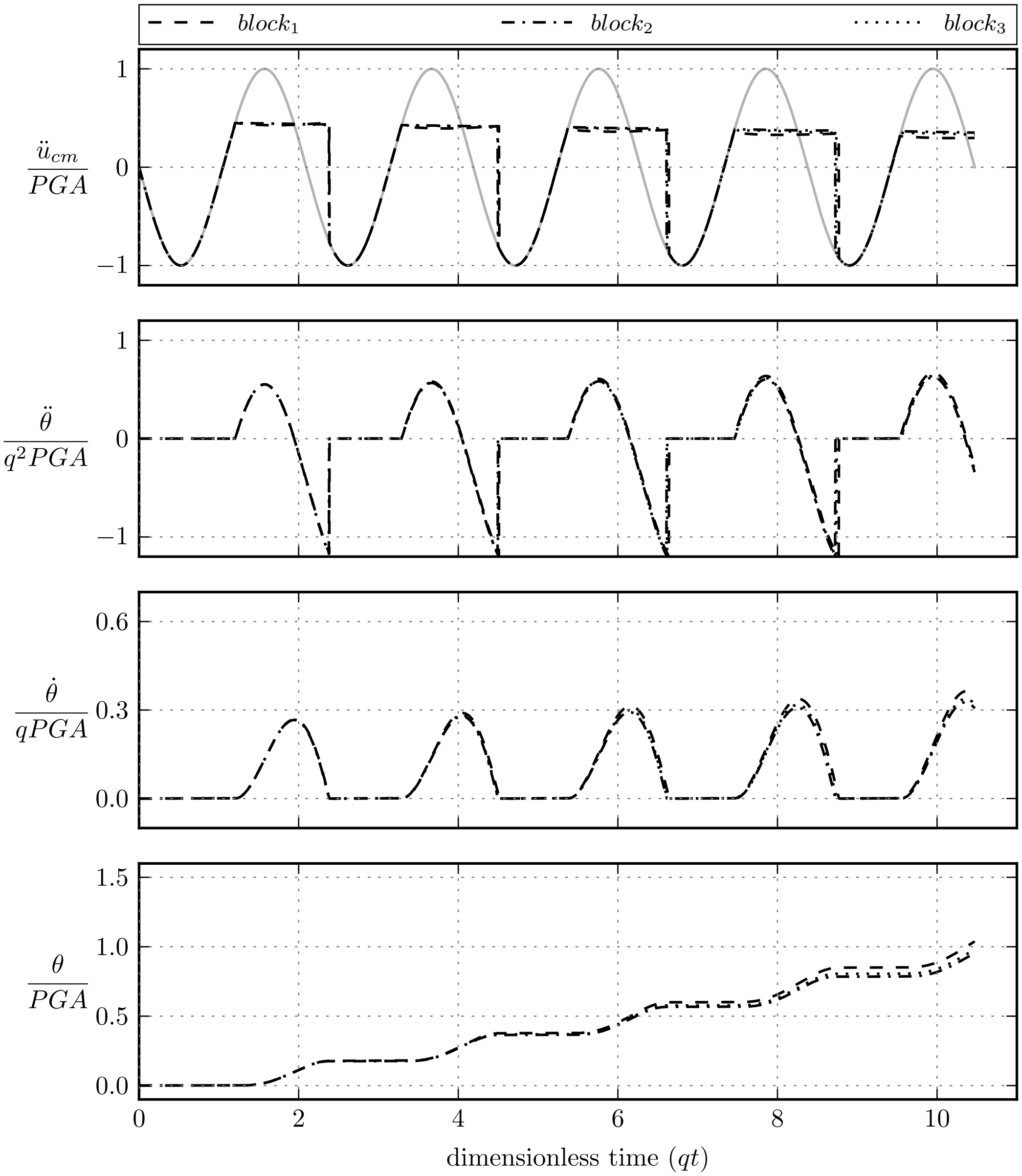

Figure 5.16: Dimensionless evaluation of the effects of slope and friction angle.

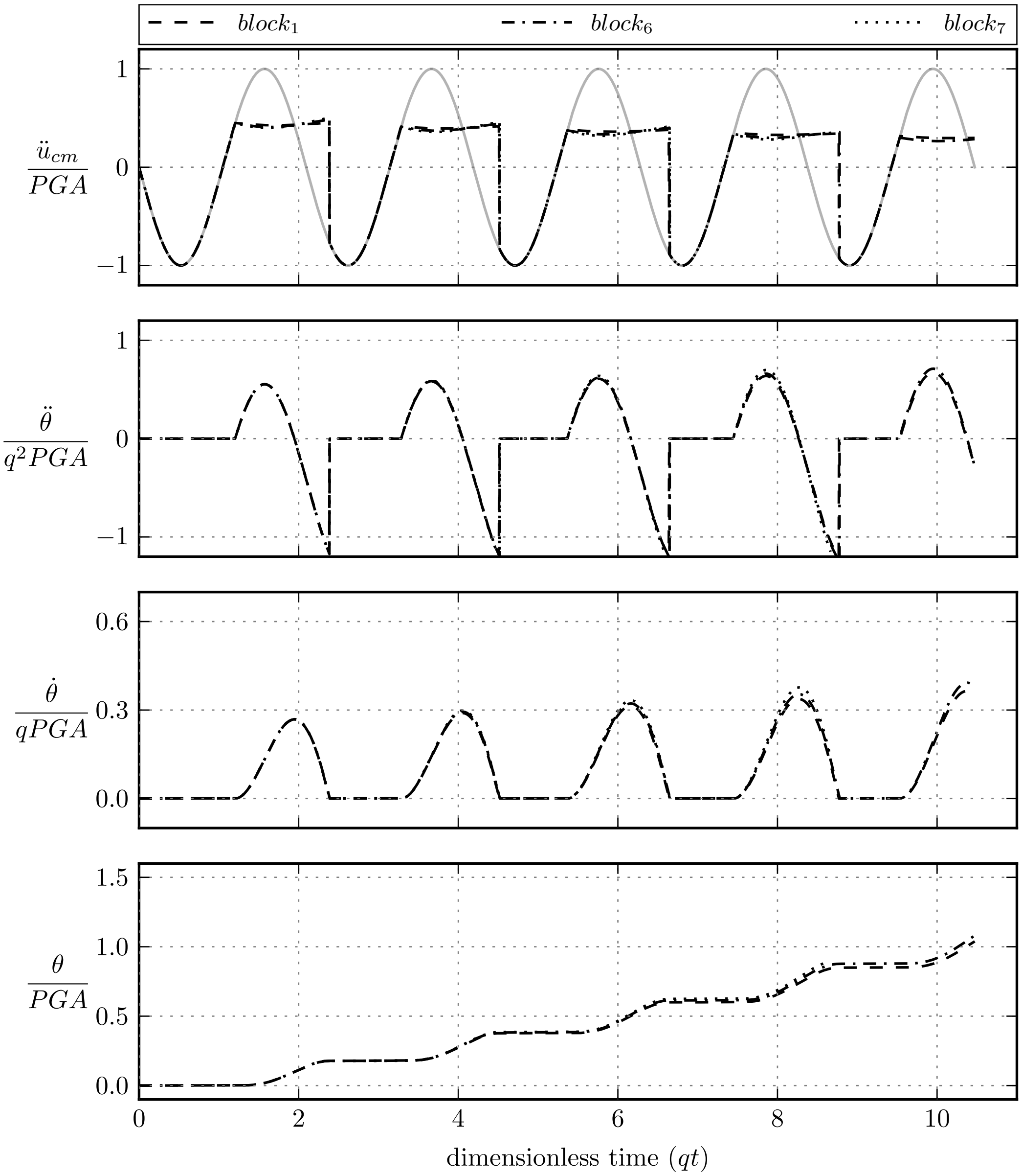

Figure 5.17: Dimensionless evaluation of the effects of aspect ratio.

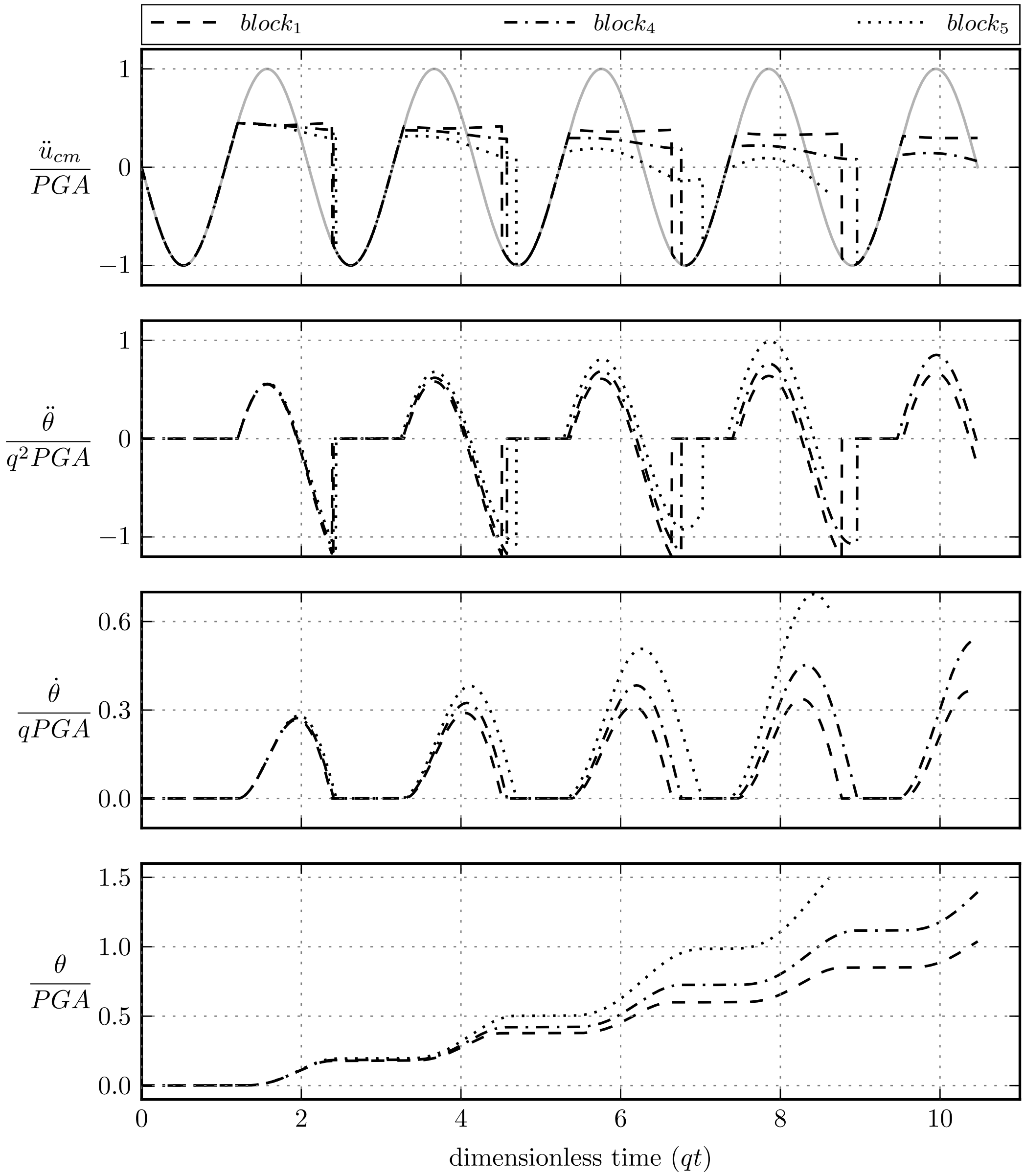

Figure 5.18: Dimensionless evaluation of the effects of relative fracture angle, γ.

5.4 Slumping Response to Random Earthquake Ground Motions

The response of slumping blocks to earthquake ground motions and the ability to predict that response is investigated in this section. Given the varying characteristics of ground motions, such as seemingly random accelerations in the time-domain and the non-linearity of slumping block equations, it is expected that the response of a slumping block will differ from one ground motion to the next. In addition, natural variations in the slumping geometry and fracture friction are also expected to increase the variability of responses. However, there are many problems in seismic engineering (e.g. sliding blocks, rocking blocks, and liquefaction) that are better understood if viewed statistically. Therefore, the statistical response of slumping blocks to numerous ground motions is evaluated.

5.4.1 Solving for Critical k_s

If the parameter q^2 is assumed to be constant, then the equation of motion is similar in structure to that of the rocking block. This means it is likely that the dimensionless parameters, ω_m/p and k_s/PGA be used to evaluate rocking blocks, can be used to evaluate slumping blocks. As with sliding and toppling blocks, it is desirable to determine the minimum peak acceleration magnitude that will cause slumping behavior. Generally, this is accomplished by performing a series of simulations in which the peak amplitude of a signal, such as a sine wave that lasts for one cycle, is increased until a given failure criteria is reached. This approach is sound, except for the case of earthquake ground motions where it is desired to keep the input signal fixed. In this case, k_s must be systematically reduced until a block exhibits the desired threshold response in a similar approach that was pioneered for earth dams by Makdisi and Seed (1978). When this approach is applied for sliding block models, the threshold response (displacement) becomes asymptotic relative to changes in the critical acceleration ratio (k_y/PGA) (Strenk and Wartman, 2011). In Chapter 4, this behavior has also been shown to be true for the rocking block for normalized angular displacement (θ/θ_n)

versus the critical acceleration ratio (k_r/PGA). For the slumping block, the normalized angular displacement ($\theta_n = \theta/\gamma$) versus critical acceleration ratio (k_s/PGA) is evaluated.

To search for this asymptote, it is necessary to make small changes in k_s between successive simulations. However, these small steps can result in a large number of simulations. Optimization is gained by taking large steps in k_s while the threshold response is small and then decreasing the steps in k_s as the change in threshold response becomes relatively large. Initial simulations are performed at high values of k_s/PGA to establish a trend, in this case $k_s/PGA = [0.99, 0.95]$. From this point, spline interpolation of $\log(\theta_n)$ vs k_s/PGA is used to predict the next target simulation point based on preset target θ_n values between 0.01 and 2.0. It is inevitable that the asymptote will be "overshot" and in the case of slumping blocks this means an indication of failure at a lower k_s/PGA than critical. In this scenario, it is useful to "backup" the simulation by increasing k_s in very small increments (0.001g) until the block exhibits a non-failure response again. Lastly, since some changes in k_s may result in large unexpected changes in the threshold response, it is prudent to "fill-in" simulations between these large jumps for better definition of this curve. Figure 5.19 demonstrates this concept by example. The initial points represent the initial stepping by reducing k_s/PGA until a failure point is reached. Once failure is detected, k_s/PGA is increased in very small increments producing more failure points until a non-failure point is found. Finally, simulations at the green circle points are performed to provided better definition of the curve. The horizontal and vertical dashed lines mark the parameters which represent the interpreted boundary between failure and stability. The kink in the leftmost curve represents a situation where the block's yield acceleration drops below zero and a run-out failure occurs.

5.4.2 Solving for Critical k_s at Threshold Behaviors

Before a critical k_s can be determined, failure must first be defined by a specific threshold criteria. For a slumping block there are two natural criteria that could be used.

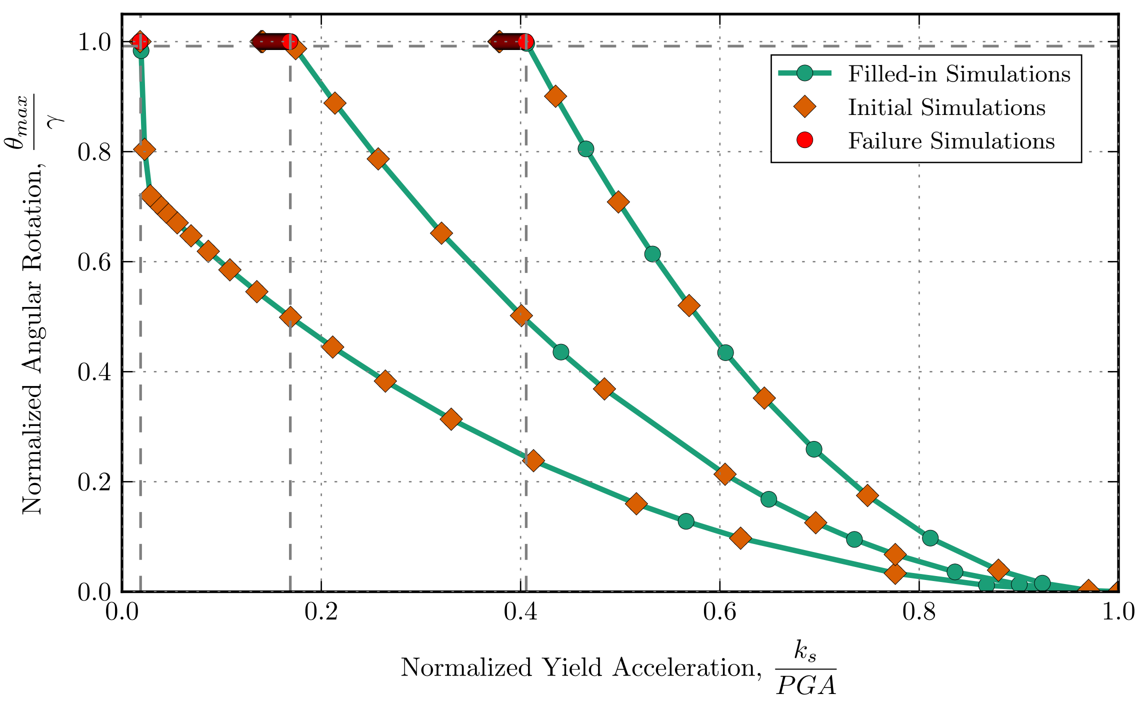

Figure 5.19: Solution scheme to determine critical k_s/PGA

Full rotation:

The criteria of full rotation arises from the fact that when the block rotates through an angle equal to γ, the block is no longer in contact with the back fracture plane and is sliding solely on the base fracture plane. In this scenario, a reevaluation of pseudo static failure mode (new α_1 and α_3) indicates that the critical mode of failure is sliding, so slumping displacement criteria no longer apply. For this threshold behavior, the failure criteria is defined as the scenario where $\theta/\gamma \geq 1$ and is shown in Figure 5.20a.

Heel displacement:

The criteria of heel displacement is based on the scenario where the block is situated on a slope such as shown in Figure 5.20b. In this case, the length of the base fracture is equal to the base of the block and is thus is not long enough for the block to

> undergo full rotation. Once the block rotates such that the heel of the block displaces a distance equal to the block's base length then the block will be in contact with the fractures only along its back contacts. This configuration is considered to be unstable and an indicator of failure. For this threshold behavior, the failure criteria is defined as the scenario where $d_{heel}/l_{back} \leq 1$ and is shown in Figure 5.20b. Note that the heel displacement criteria always requires less displacement of the slumping block than that of the full rotation criteria.

In order to determine the critical k_s for these threshold criteria, a procedure is used similar to that used in Makdisi and Seed (1978) and Chapter 4. The parameter k_s is reduced until the block reaches the full rotation threshold criteria.

5.4.3 Solving for Critical k_s for Various Block Shapes

It is desirable that k_s be reduced while minimizing the impacts on the block response characteristics discussed previously. However, reducing k_s using block parameters and friction angle can cause the functional shape of k_s and q^2 to change. To measure these effects, a new parameter is introduced that measures the reduction in k_s and is defined as

$$k_{s,red} = \frac{k_{s,\theta=\gamma} - k_{s,\theta=0}}{\gamma}. \tag{5.14}$$

The parameters which represent different block shapes and responses, q^2 and $k_{s,red}$, should also be varied independently while minimizing changes in k_s. An analysis is performed to evaluate which block parameters, including joint friction angle, have the most influence over the motion parameters k_s, q^2, and $k_{s,red}$. The block parameters are varied individually to gauge their influence on the motion parameters. The results of this analysis are shown in Figure 5.21. From this figure it can be seen that ϕ and slope affect k_s and $k_{s,red}$, but have very little influence over q^2. Since ϕ appears to have the most influence over k_s, it will be used to reduce k_s. The parameters α_3 and scale the most influence over the values of q^2. Since scale has a directly proportional relationship with q^2, it will be used to vary q^2. Although ϕ

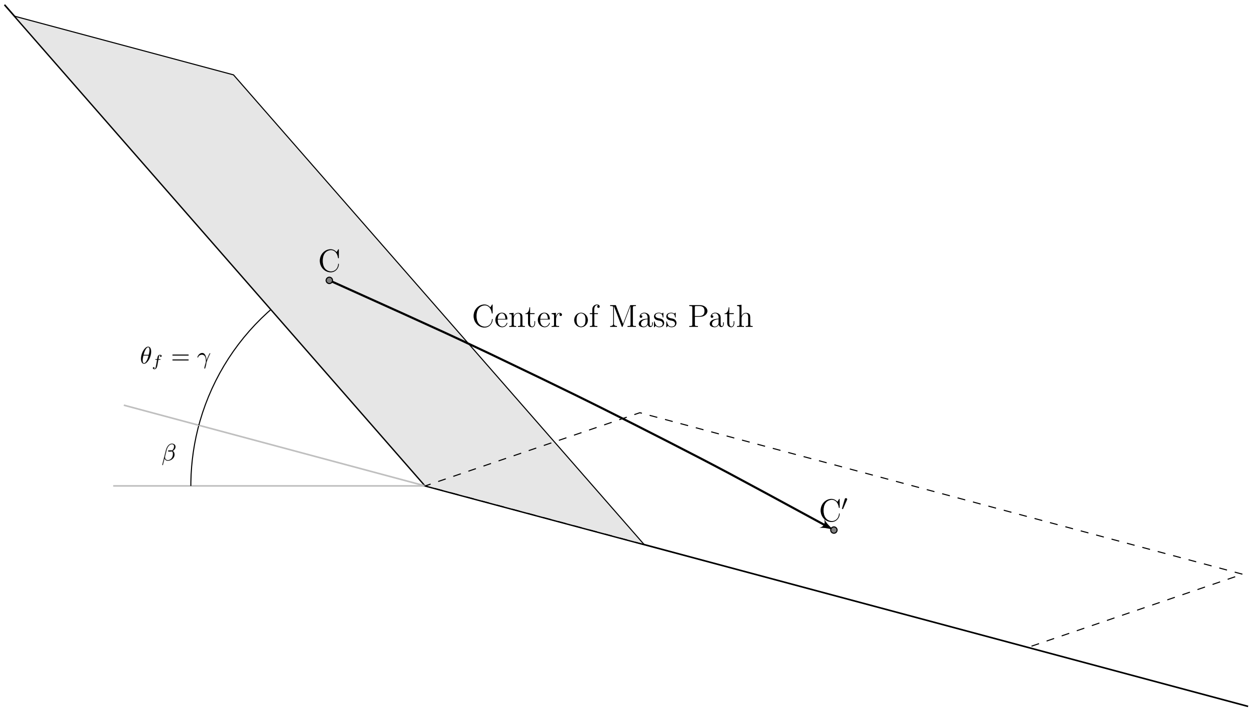

(a) Full rotation

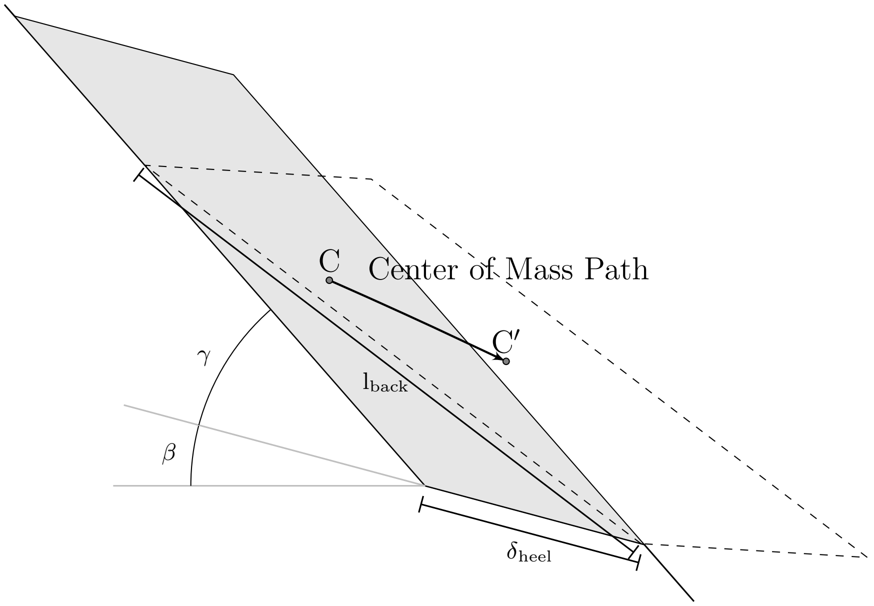

(b) Heel displacement

Figure 5.20: Slumping block failure criteria.

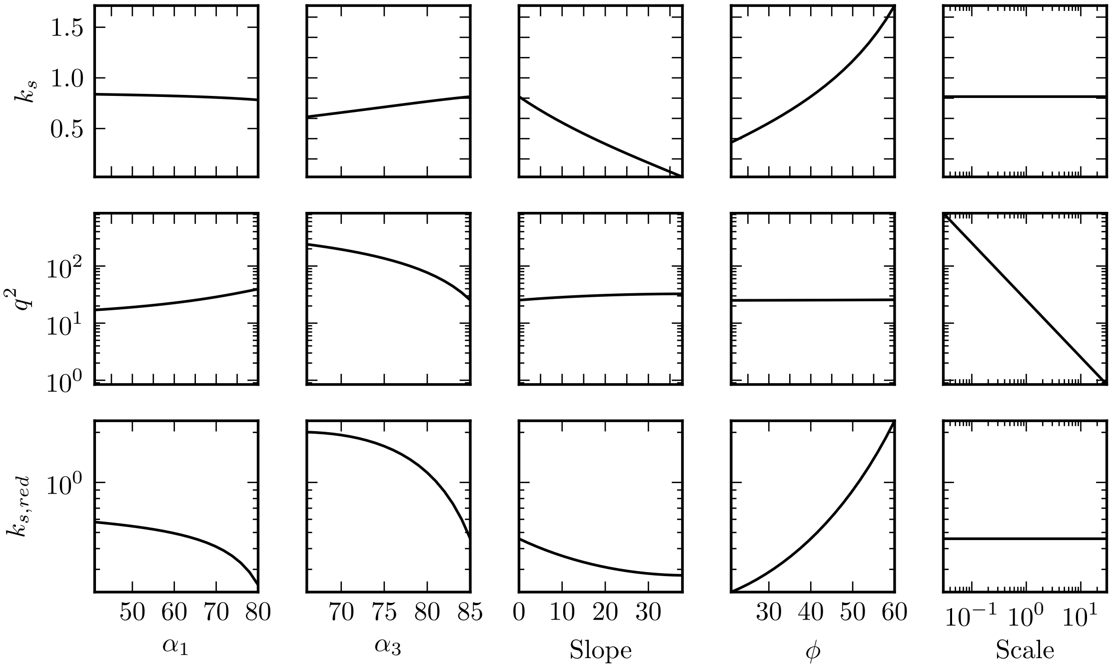

Figure 5.21: Influence of geometric parameters and joint friction angle on initial motion parameters.

changes $k_{s,red}$, that change is related to k_s. For this reason, α_3 is used to independently vary $k_{s,red}$.

5.4.4 Earthquake Ground Motion Simulations

Earthquake Time Histories

Unique earthquake time histories (537 horizontal motions) were selected from various sources. Additional information about the ground motions (e.g. magnitude, distance, PGA) is provided in Appendix A. In general, several suites of ground motions were selected as follows:

PEER

This set of motions consist of 427 horizontal components. They include all the motions from the PEER strong ground motion database (PEER, 2010) with a site shear wave velocity greater than 600m/s. The shear wave velocity boundary was chosen with the idea that the time histories would be more related to rock-like geologic profiles.

Baker

Broadband and pulse-like motions (40 each) were selected based on sets 2 and 3 of the motions developed by Baker et al. (2011). The purpose of these motion sets is to assess whether the spectral shape of a ground motion produces a unique signature in the results.

Spectrally Matched

This set of 30 motions were spectrally matched and developed by Astaneh (2013) and are unpublished. The purpose of this motion set is to assess whether spectrally matched motions produce a different response pattern than unmatched motions.

All motions were derived from the PEER database and thus are associated to a NGA reference number. Four combinations of each ground motion set were evaluated and consisted of two horizontal components and horizontal time history polarity. The possible combinations are summarized in Table 5.4 below. Since it has been shown in Chapter 4 that vertical motion does not have a substantial statistical influence, vertical motions were not evaluated.

Geometries

A range of values for block scale $||\mathbf{r}_1|| = [10.0, 1.0, 0.1](cm)$ and $\alpha_3 = [65, 75, 85](deg)$ were chosen to represent a broad range of block sizes and boundary conditions. The slope angle (β) and block property (α_1) were fixed at zero and 62.0, respectively since they have minimal influence over the equation of motion parameters. In terms of the parameters in the equation of motion, the variation of these geometries produce $q = 1.53$ to 53.81 (1/sec) and $k_s = 0.0001$

Table 5.4: Possible earthquake simulation combinations.

Combination	Component	Polarity
1	1	Forward
2	2	Forward
3	1	Reverse
4	2	Reverse

to 1.22 (g). For each value of q^2 and α_3, simulations for each of the four permutations per ground motion were performed.

Simulations

For each time history and geometry permutation, the search algorithm described previously was used to determine the critical k_s that results in full rotation. The total number of permutations totaled $10,713$ requiring a total number of simulations of $186,811$ to determine the critical k_s. For practical purposes, the lower limit of k_s/PGA was set to 0.01. This limit is assumed to not be critical since values of k_s/PGA below 0.01 essentially indicate inevitable failures. The relationships of $\frac{k_s}{PGA}$ versus $\frac{\theta}{\gamma}$ were recorded for each simulations. In addition, the entire time dependent response of each simulation was recorded. The results of these simulations were parsed and loaded into a MYSQL database for further processing and visualization. In some cases for very large blocks (low q^2), the limit set on k_s/PGA ended the simulations before the critical k_s could be determined. In these scenarios the results of these simulations were recorded but omitted from the evaluation of "failed" blocks. Table 5.5 summarizes some basic statistics about the number of permutations that determined a critical k_s/k_{max}.

Table 5.5: Slumping simulation summary statistics

	PEER	Baker Broadband	Baker Pulse	Spectrally Matched
Total simulations	7300	1433	1440	540
Unique NGA motions	222	40	40	30
Unique earthquakes	222	40	40	30
Unique horizontal motions	427	80	80	30

5.4.5 Simulation Results

Hexabin plots (2D histograms) of the simulation results for both failure criteria and all ground motion sources are plotted in terms of the dimensionless parameters discussed previously (k_s/PGA and ω_m/q) as shown in Figures 5.22 and 5.23. For each plot, the safe zone (the zone where combinations of block and ground motion parameters result in no slumping failure) is located above the data/lines. The data does not coalesce along a linear line for two reasons:

1. The ground motion parameters $\omega_m = 2\pi/T_m$ and PGA are being used as proxies for motion frequency and amplitude which is an approximation for an earthquake.

2. Similarly to rocking blocks, as Makris and Roussos (2000) indicated, small blocks (large q^2) react more to acceleration pulses while large blocks (small q^2) react more to accumulated acceleration (i.e. velocity pulses).

3. The block parameters k_s and q^2 at zero rotation ($\theta = 0$) are being used as proxies for the block's characteristics. As mentioned previously, the initial values of k_s and q^2

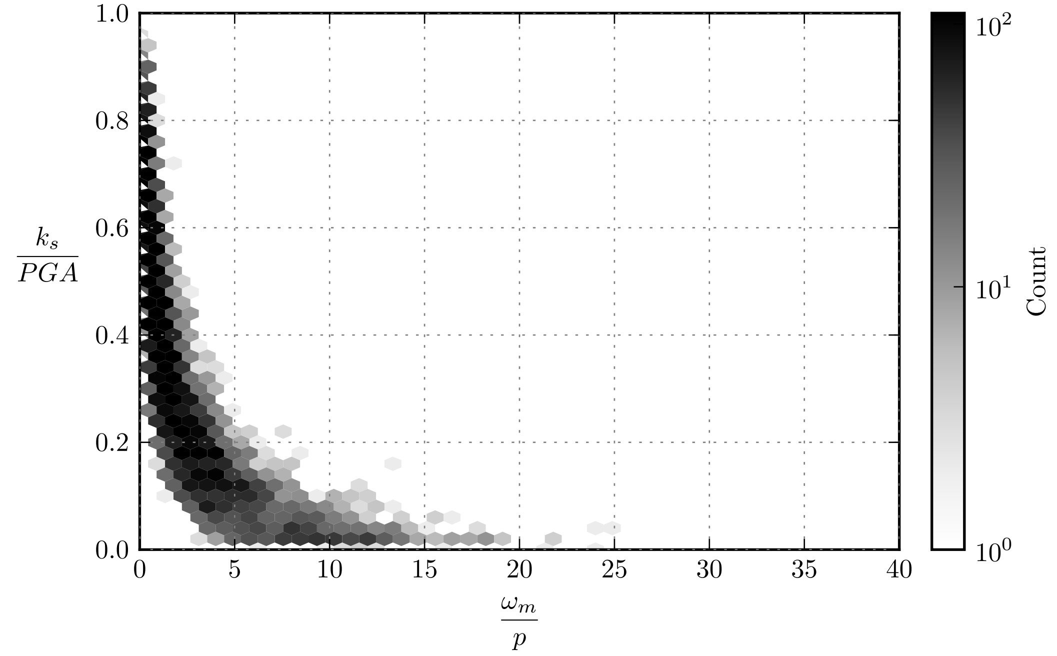

(a) Linear space

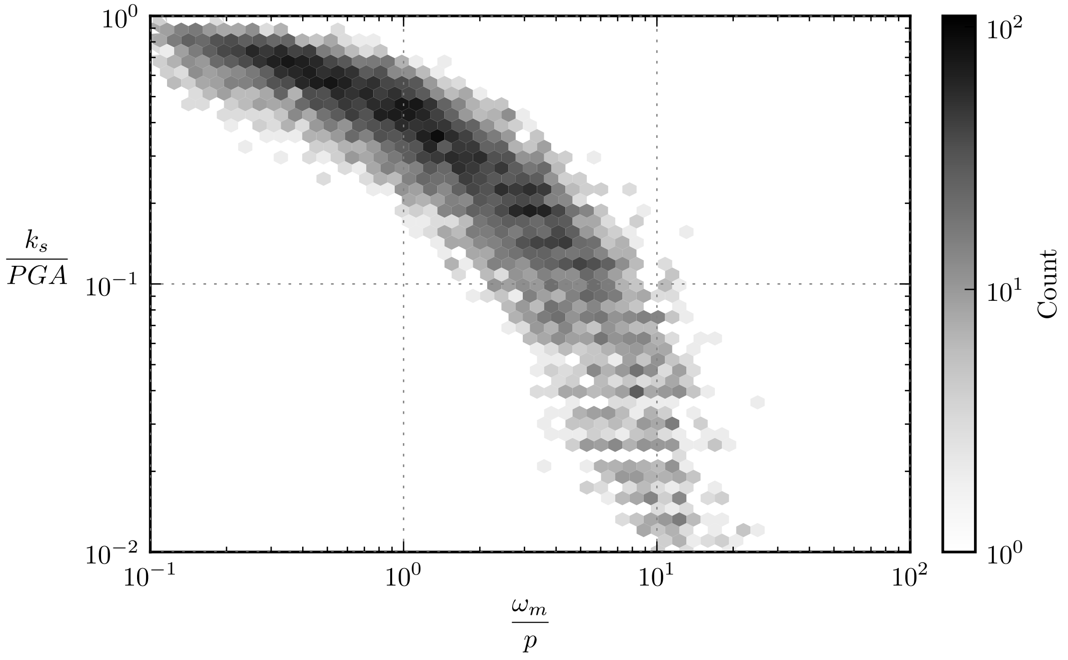

(b) Log space

Figure 5.22: Simulation results for slumping block failure based on full rotation using dimensionless parameters.

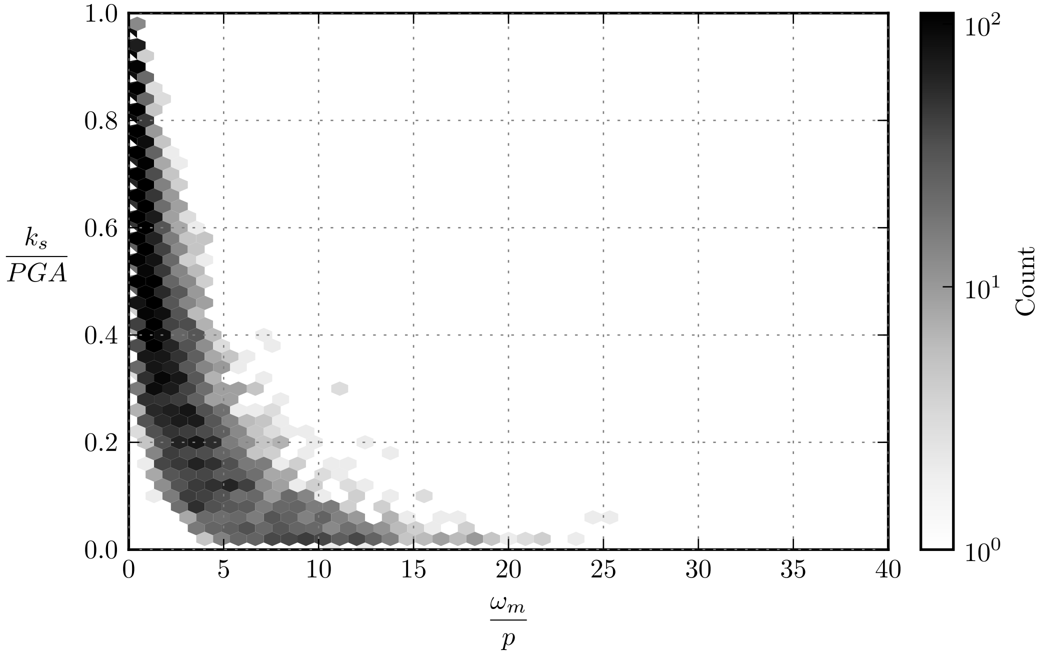

(a) Linear space

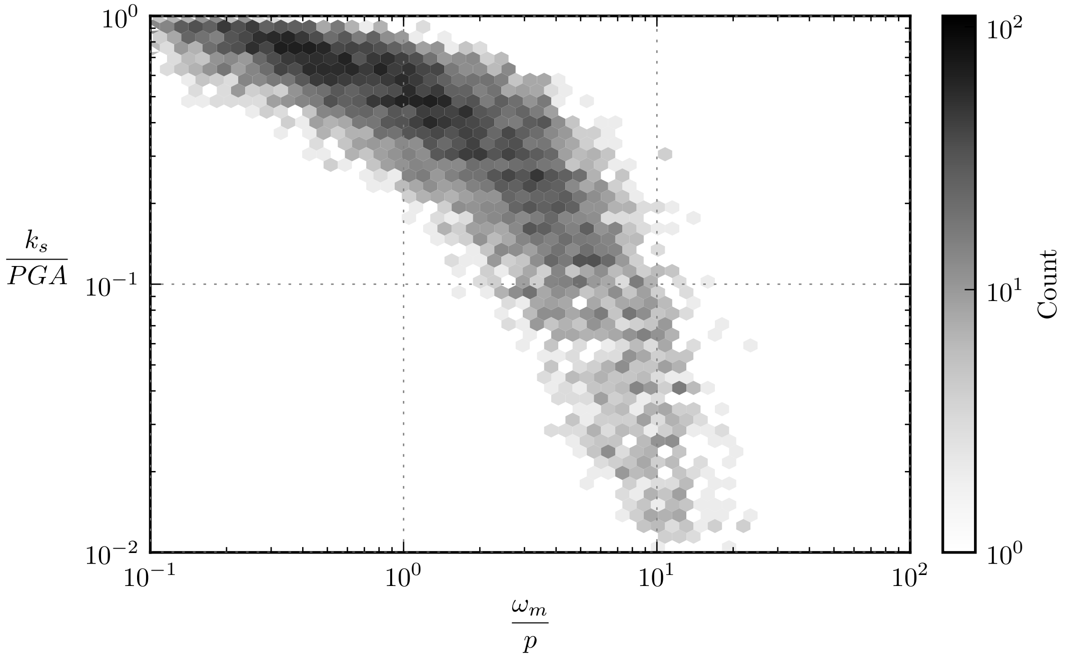

(b) Log space

Figure 5.23: Simulation results for slumping block failure based on heel displacement using dimensionless parameters.

are consistent between various blocks, however as θ increases the parameters become non-linear, and the consistency breaks down.

5.4.6 Reinterpretation of Simulation Data

In Chapter 4 for rock block toppling problems, it was shown that the dimensionless parameters could be rearranged such that the earthquake parameters and block parameters were segregated. Since, the toppling block and slumping block have similar equations of motion, the simulation data is now replotted with the rearranged parameters $k_s g/q$ (deemed the critical block velocity because of its units) and $T_m PGA/2\pi, PGV, 2\pi PGD/T_m$. Simulation data for full rotation failure is shown in Figures 5.24 through 5.26, and simulation data for heel displacement failure is shown in Figures 5.27 through 5.29.

For each ground motion parameter (GMP), a hexabin plot of the data with the bin counts colored in a log scale is shown. Histograms of each ground motion set and associated critical block parameters are plotted along the abscissa and ordinate axis to further illuminate the density of the data.

The variability of the results visually appear to increase with the increase in each GMP. For this reason a weighted linear least squares (WLS) fit was performed on each data set for each GMP. Since the variance is unknown, the weights used for each fit were determined by an iterative evaluation of the fitted variance. First the data was split into bins and the variance of each bin calculated as shown in Figures 5.24a to 5.26a and Figures 5.24a to 5.26a. From these plots, the relationship between the GMP and variance was determined to be linear relative to PGA and PGV and quadratic relative to PGD. After applying weights, the mean WLS fit is plotted as a solid line, while the 2.5% and 97.5% probability of failure lines are dashed. The resulting regression equations are shown in each figure.

To further evaluate this, the results of the earthquake simulations segregated by ground motion set are shown in Figure 5.30 along with the WLS fit for all the data. It visually appears that differences in the ground motion set does not impact the likelihood of failure. As with toppling blocks, these evaluations highlight that it is the ground motion shape and

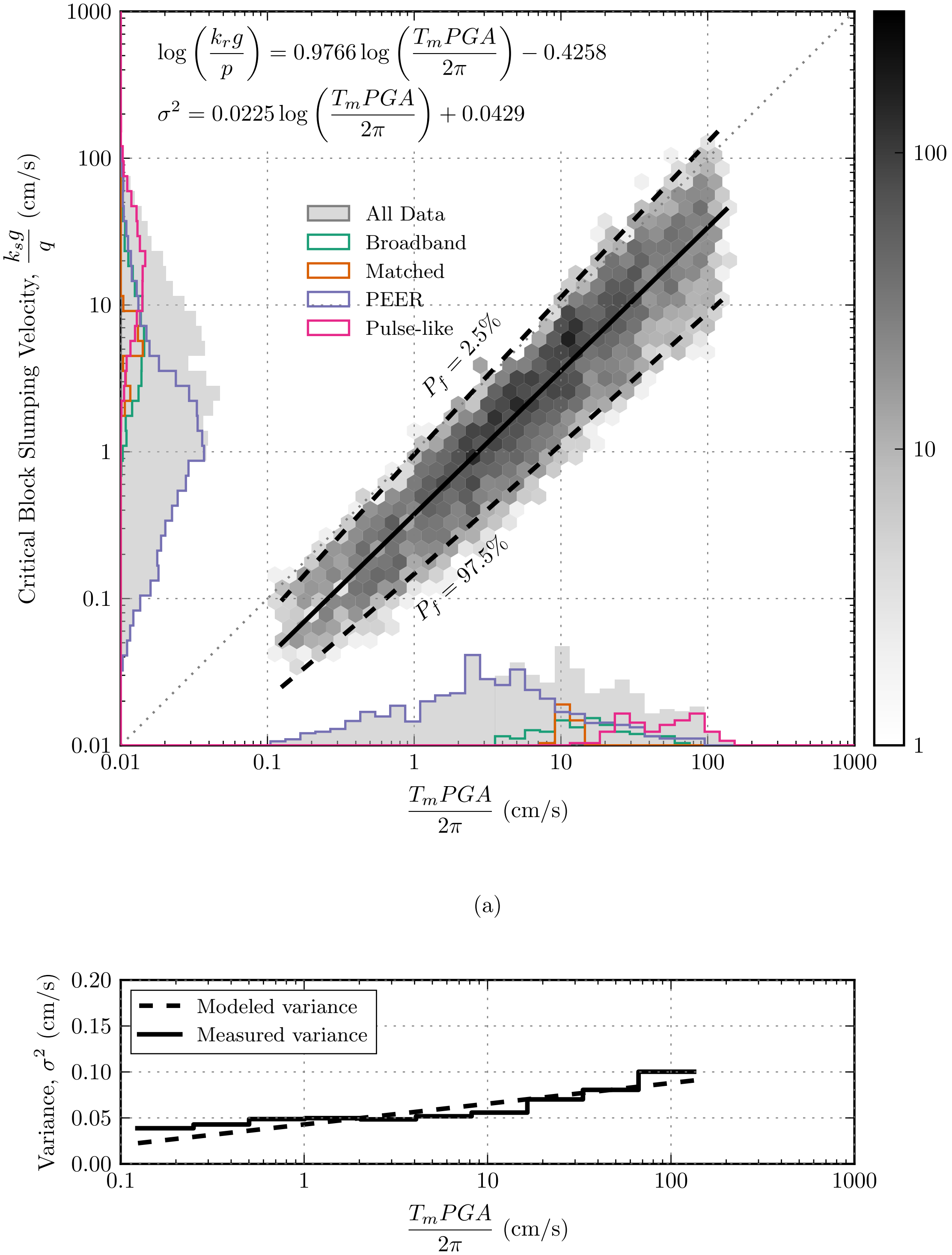

(a)

(b)

Figure 5.24: Earthquake simulation results (full rotation failure) for PGA and T_m.

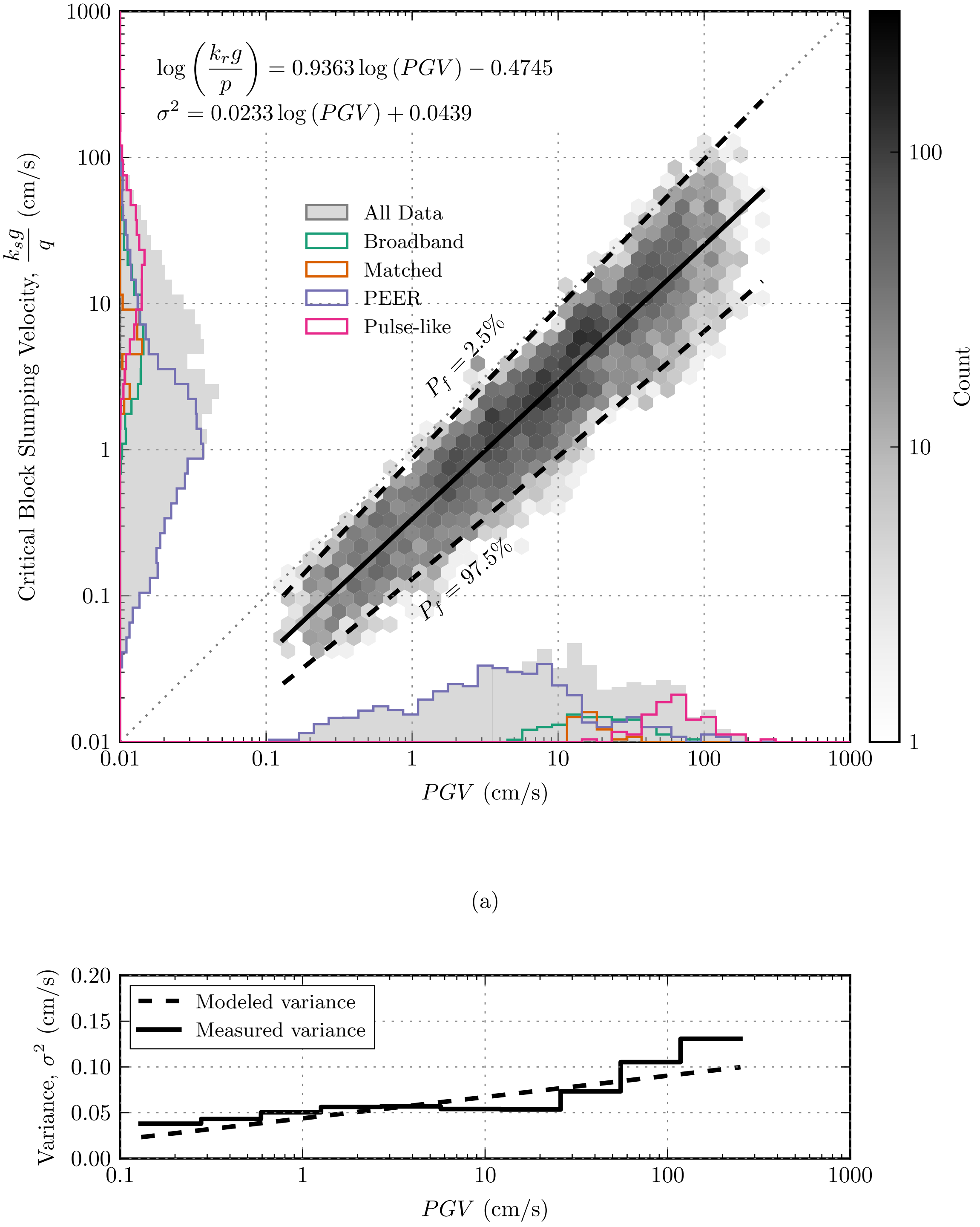

(a)

(b)

Figure 5.25: Earthquake simulation results (full rotation failure) for PGV.

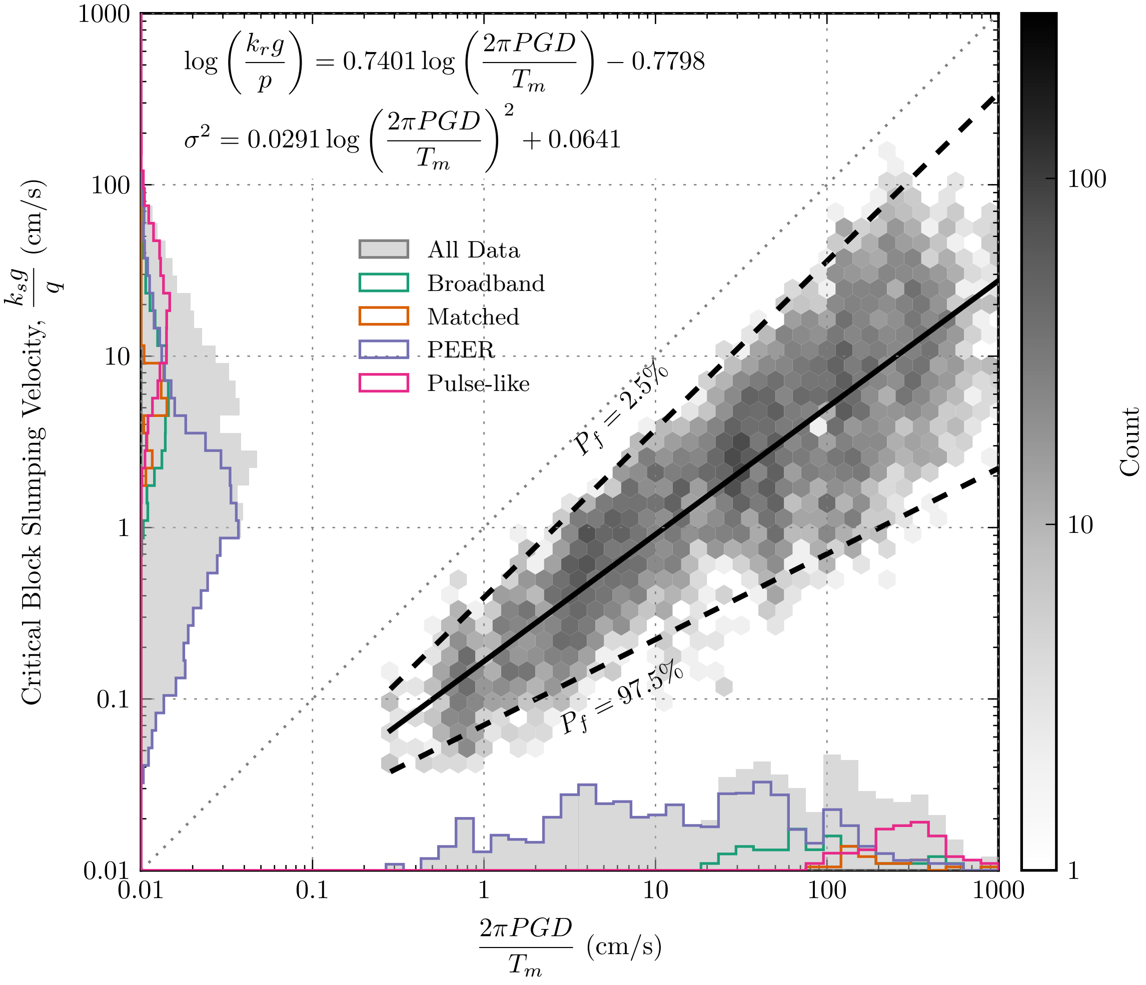

(a)

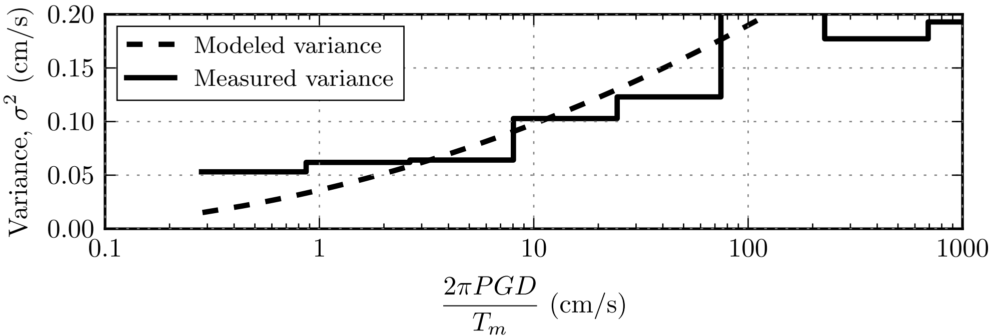

(b)

Figure 5.26: Earthquake simulation results (full rotation failure) for PGD and T_m.

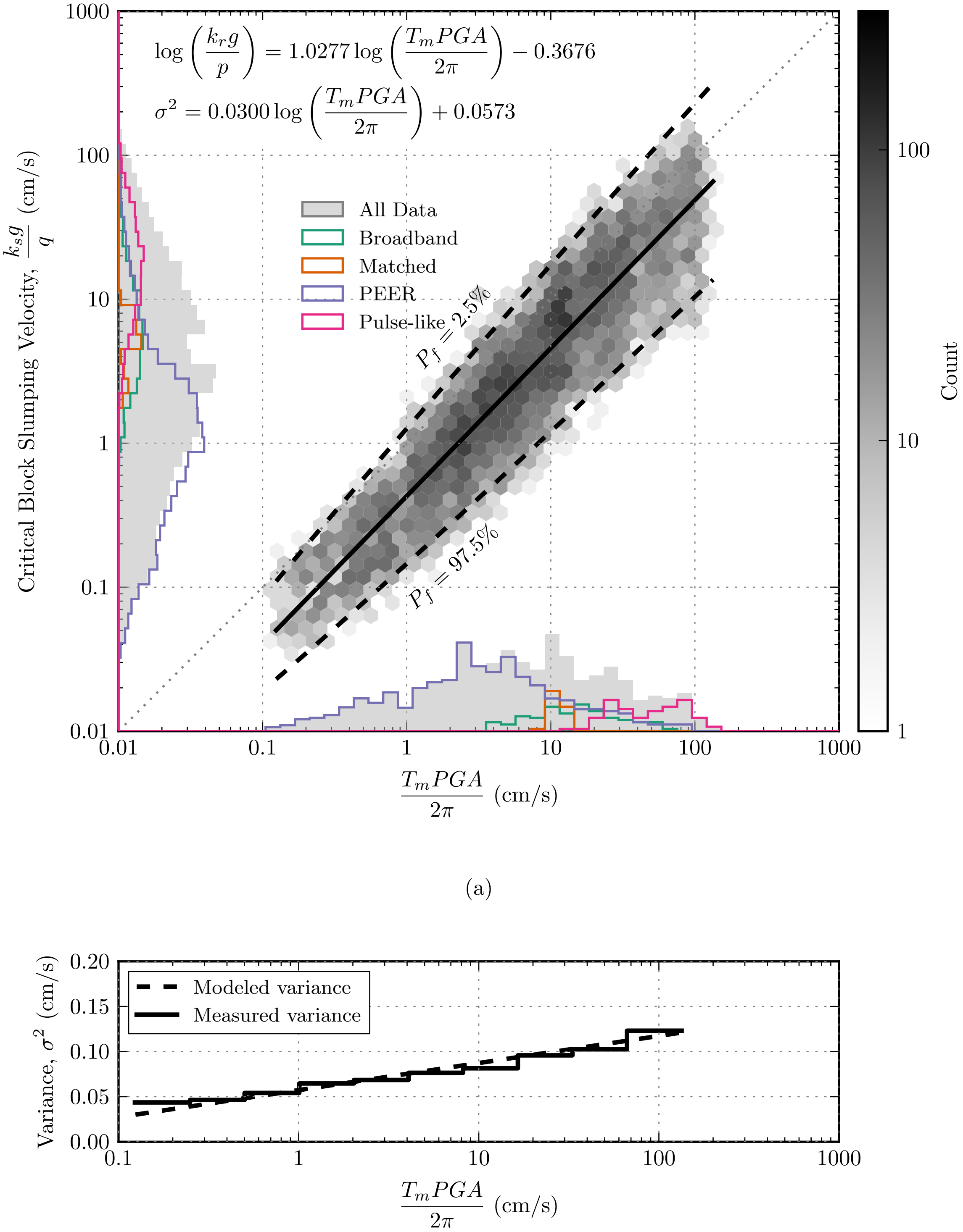

(a)

(b)

Figure 5.27: Earthquake simulation results (heel displacement failure) for PGA and T_m.

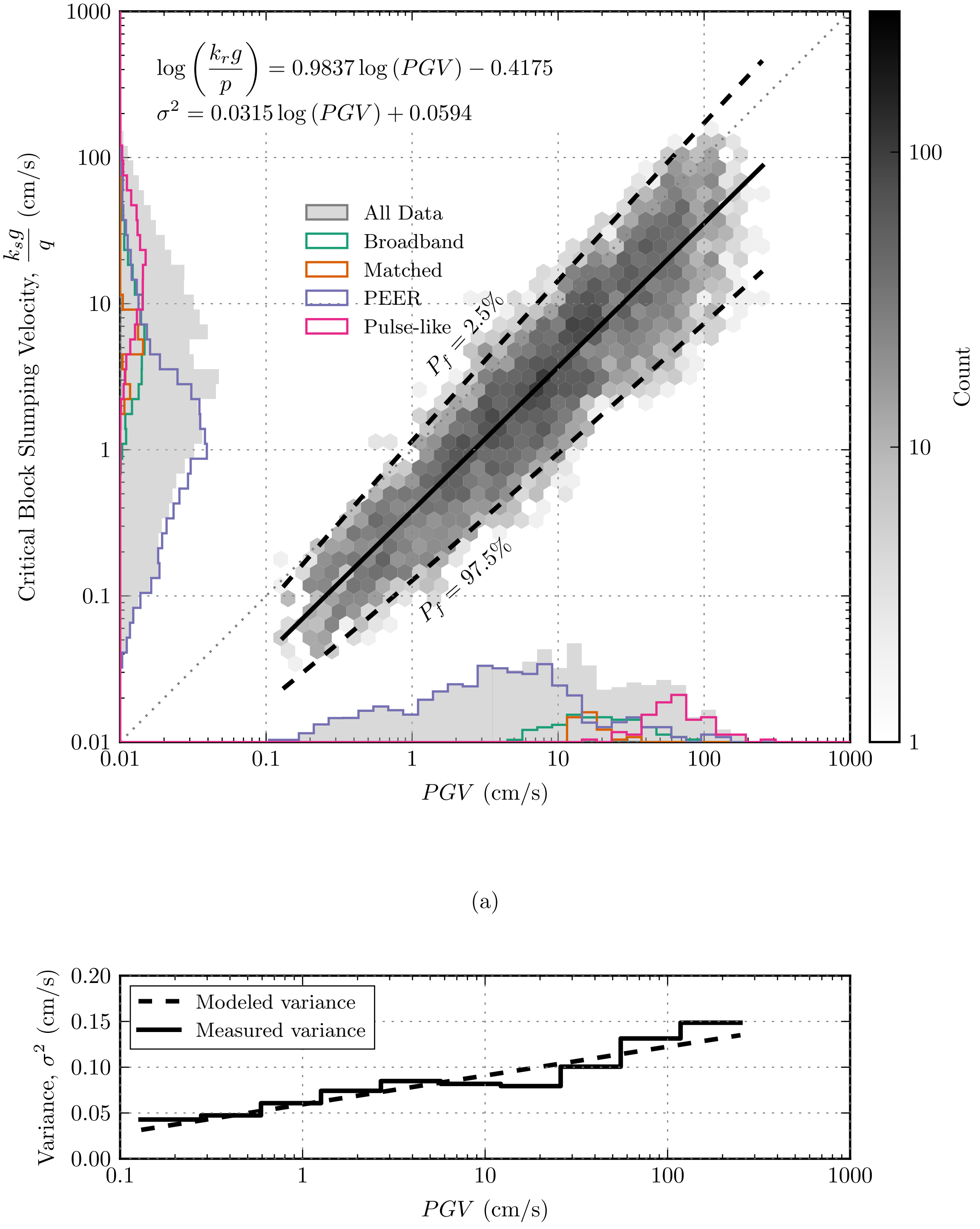

(a)

(b)

Figure 5.28: Earthquake simulation results (heel displacement failure) for PGV.

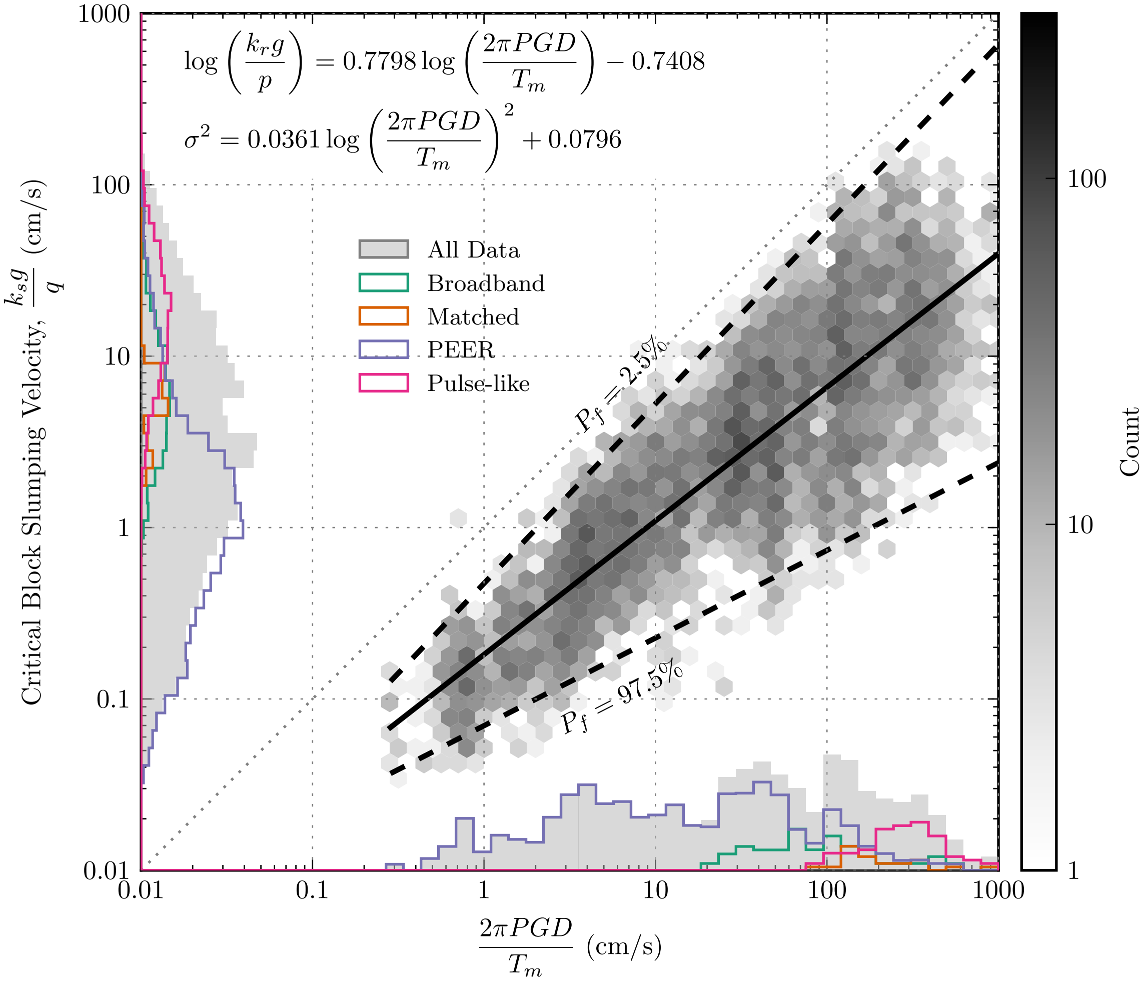

(a)

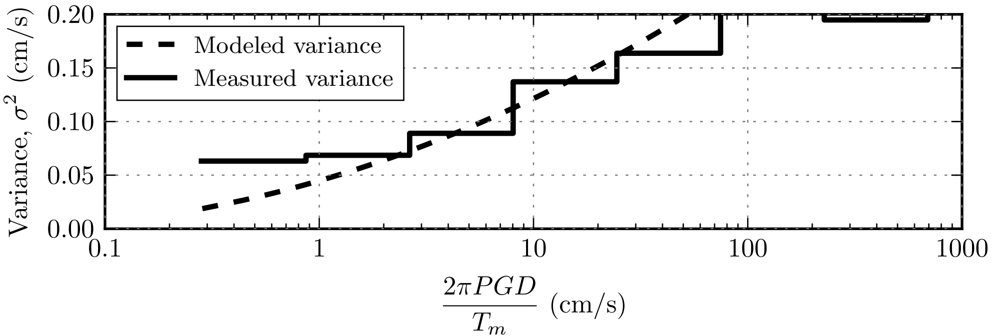

(b)

Figure 5.29: Earthquake simulation results (heel displacement failure) for PGD and T_m.

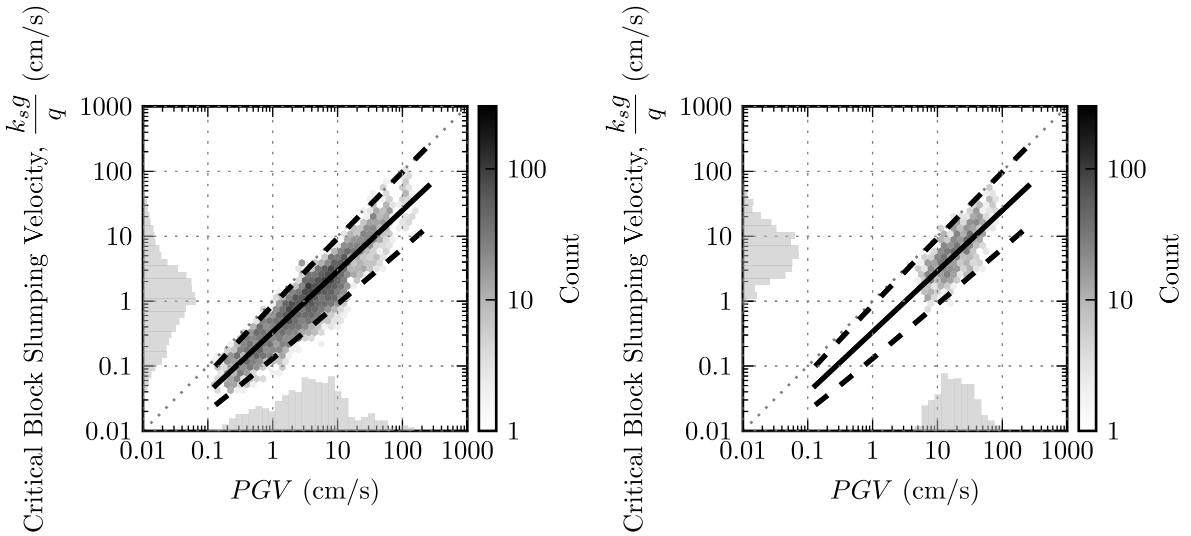

(a) PEER ground motion set

(b) Broadband ground motion set

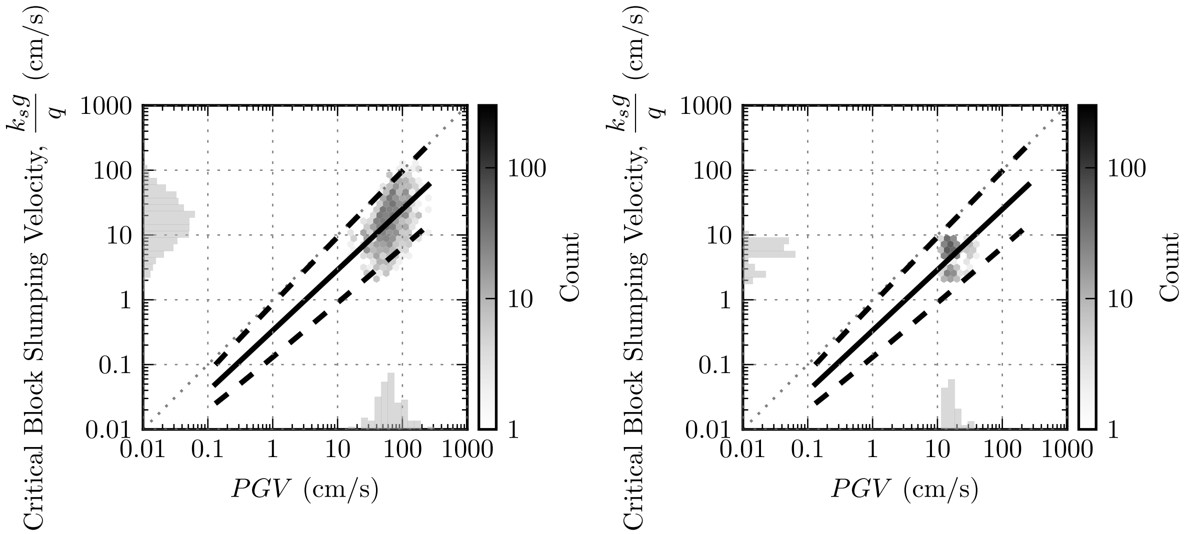

(c) Pulse-like ground motion set

(d) Matched ground motion set

Figure 5.30: Earthquake simulation results for each ground motion set.

limited mean frequency content that focus the results in the linear relationship shown by the earthquake simulations.

These plots confirm that the critical block size can be linearly related to the ground motion parameters from a statistical standpoint. In fact, the boundary of nearly zero percent probability of failure occurs when $k_s g/q \approx T_m PGA/2\pi \approx PGV \approx 2\pi PGD/T_m$. From these distributions, it can be seen from the narrower confidence intervals that PGV and $T_m PGA/2\pi$ are the best predictors of the boundary between safe blocks and blocks that will overturn. However, the PGV relationship requires one less parameter and has virtually the same skill predicting the critical block shape giving it an advantage over PGA. The parameter $2\pi PGD/T_m$ also shows a linear trend, but as can be seen, there is much more scatter and the heteroskedacity is visually significant.

5.5 Multiple Block Systems Represented by Slumping Blocks

The slumping block model has several key characteristics that are potentially useful in representing the behavior of more complex block shapes and fractured rock slopes in a simplified manner. These characteristics of the slumping block model are yield acceleration, moment of inertia, and boundary conditions that influence the path of motion. Several researchers have explicitly evaluated multiple block systems (Enoki et al., 2005; Michalowski, 2007; Stamatopoulos et al., 2011), however the generality of their methods were not expanded on. Here, three examples of multiple block systems are evaluated with the simple slumping block model and compared to a known solution to illustrate this connection. The examples are inspired by the conceptual slopes in Figure 5.1. Since it has been shown in Chapter 3 that *UDEC* can provide a reasonable approximation to single block systems subject to earthquake loading its use will be extended to multiple blocks. This step is supported by Eberhardt (2003), Havenith et al. (2003), and Hatzor et al. (2004) whom have used DEM modeling to evaluate seismic response of rock slopes. The target solution for these examples of multi-block systems will be approximated through the use of DEM modeling.

5.5.1 *DEM (UDEC) Model as Target Solution*

For this example, the vertically stacked blocks are modeled in *UDEC*. The parameters of the model are listed in Table 5.6. The translational and angular motion (velocity and displacement) of the lowermost block is recorded throughout the simulation. Acceleration is calculated by numerically calculating the derivative of velocity by finite difference. Central difference estimation is used except at the beginning and end of the time history and at any discontinuities which occur when the motion stops and starts.

Table 5.6: *UDEC* parameters for vertically and horizontally stacked block simulations

Parameter	Value
Block type	Rigid
Rounding	2% smallest dimension
Density	$2,700$ kg/m^3
Joint shear stiffness	$6.56e10$ N/m
Joint normal stiffness	$6.56e10$ N/m
Joint friction angle	40.0°
Damping Type	Stiffness Proportional
Damping Frequency	4.0 hz
Damping Portion	0.1%

5.5.2 *Vertically Stacked Rock Blocks*

The first example consists of a prototypical slumping block that is sliced into three equally shaped blocks by a joint structure parallel to the base fracture. This joint structure produces blocks that are vertically stacked on top of each other as shown in Figure 5.31. The input parameters for the larger block before it is split and the individual blocks are summarized

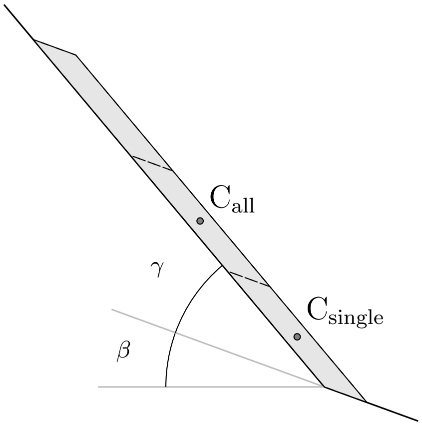

Figure 5.31: Geometry of three vertically stacked blocks

in Table 5.7. The rotations and vertical motion of the base and back fractures are fixed to zero movement while horizontal translation is used to simulate an input ground motion. The input ground motion is prescribed as a one hertz sine wave that has a linear increase in amplitude for the first two full cycles and then maintains a constant amplitude of 0.5g to the end of the simulation.

Table 5.7: Input parameters for the global geometry and lowermost block in the vertically stacked block simulation.

Parameter	Global Geometry	Individual Block Geometry
Slope	20°	20°
γ	30°	30°
S_1	$1.0m$	$0.33m$
S_2	$0.1m$	$0.1m$
ϕ	40°	40°

Simplified Model

In order to model this system with the simplified model, the following system behaviors need to be determined:

Pseudo-static yield acceleration of key block:

The yield acceleration of the vertically stacked blocks is controlled by the lowermost block. The lower block is the key block which must displace before the system as a whole can move. Although the individual geometry of the lower block suggests slumping, the yield acceleration cannot be determined from the equations of a single block presented in Chapter 3. The blocks above the lower block change the free body diagram of the lower block relative to a lone block and act as a surcharge loading to the lower block. This surcharge acts to drive the system toward failure thus lowering the pseudo-static yield acceleration. A similar conclusion was made by Michalowski (2007) for multiple block systems. For this simulation, the yield acceleration was determined by matching the acceleration at which movement begins in the *UDEC* simulation by trial & error adjustment of ϕ. A $\phi = 31°$ used with the geometry of the lower block produces a yield acceleration of approximately 0.12g that provides a good visual match to the *UDEC* solution.

Controlling inertial properties:

The rate at which the system displaces is dependent on the blocks that control the dominant rotation in the system. In this case, it is again the lower block that undergoes the most displacement and thus its moment of inertia will control the rate at which displacement accrues in this system. Therefore, the lower block's geometry is used in the slumping block approximation.

Boundary conditions:

The boundary conditions relative to the key block consist of the back and base fractures. Throughout deformation of the blocky system, the orientations of these fractures remain constant and thus there is no additional influence expected.

Results

The results of both the *UDEC* solution and simplified model solution are shown in Figure 5.32. It can be seen that with the use of the appropriate slumping yield acceleration (i.e. friction angle and block geometries), the simplified slumping block simulation approximates the *UDEC* solution very well. In the first cycle of block motion, the acceleration of the *UDEC* block has a different shape compared to the slumping block simulation, but on average has approximately the same yield acceleration. During the first half of the second cycle the bottom block is slumping while the block above it is also slumping. In the second half of the cycle, the upper block stops slumping but the lower block continues slumping. This transition is visually represented by the discontinuity in the lower block's horizontal acceleration. In the third acceleration cycle, the bottom block fully rotates onto its back and then is pushed by the blocks above it over the remainder of this cycle. In the next cycle, the middle block rotates onto its back and itself is being pushed by the upper block. Eventually all three blocks are on their backs and undergo classic sliding failure. The transition for each block from slumping to forced sliding can be seen by the jump in the lower block's horizontal acceleration. Ultimately, when all the blocks are on their backs, their horizontal acceleration during sliding exhibits the classic sliding block characteristics.

5.5.3 Three Horizontally Stacked Rock Blocks

The second example consists of a prototypical slumping block that is sliced into three equally shaped blocks by a joint structure parallel to the back fracture. This joint structure produces blocks that are horizontally stacked next to each other as shown in Figure 5.33. The input parameters for the combined block shape before they are sliced equally are summarized in Table 5.8. The rotations of the base and back fractures are fixed to zero movement while

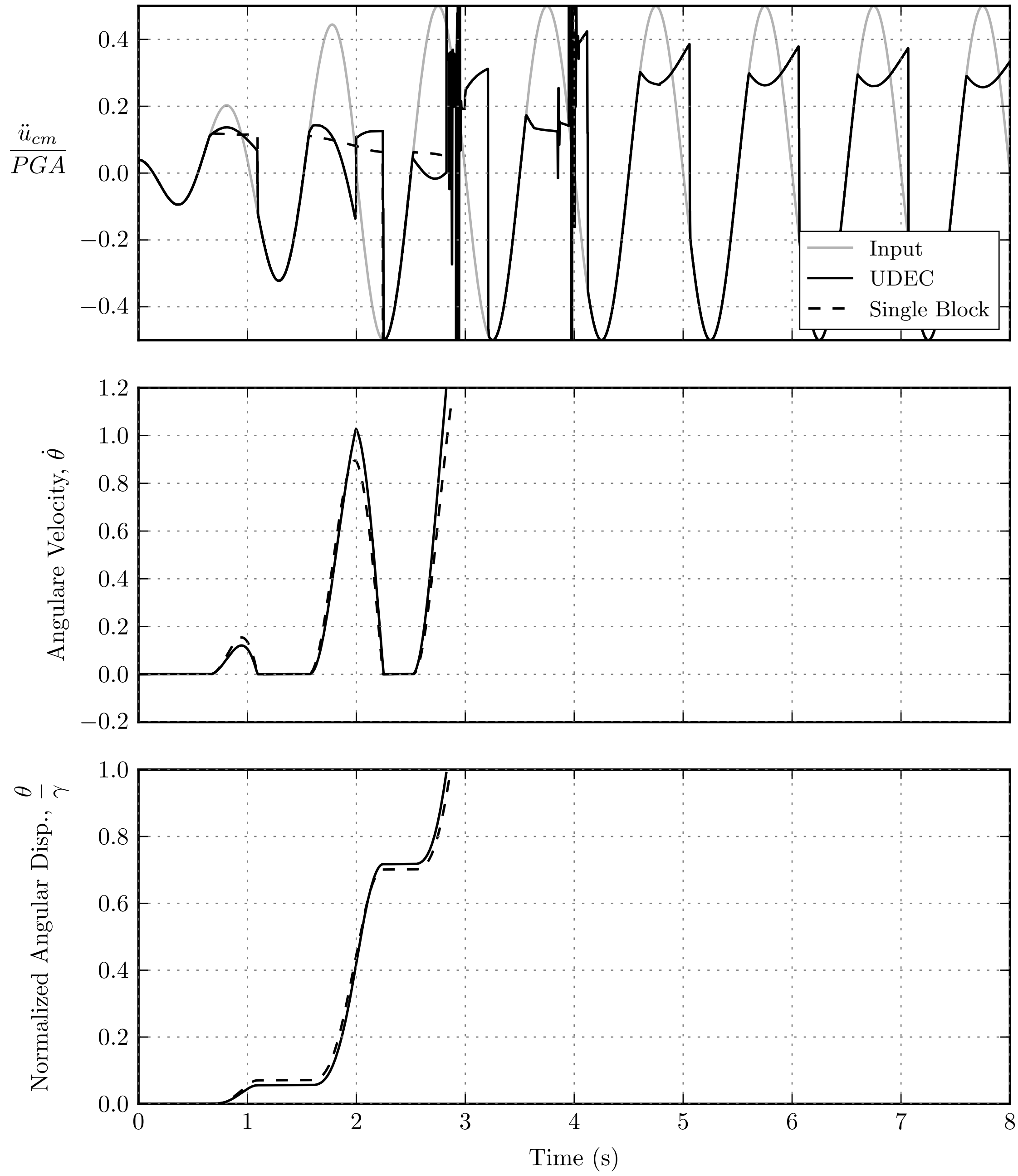

Figure 5.32: Example 1: Comparison of *UDEC* to simplified model for three vertically stacked blocks.

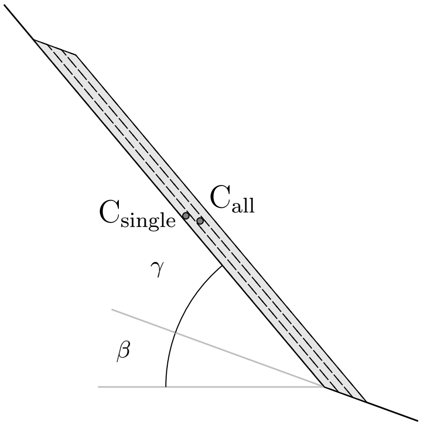

Figure 5.33: Geometry of three horizontally stacked blocks.

horizontal translation is used to simulate an input ground motion. The input ground motion is the same as for the previous example.

Table 5.8: Input parameters for the combined geometry in the three horizontally stacked block simulation.

Parameter	Global Geometry
Slope	10°
α_1	20°
α_3	30°
Scale	$1.5m$
ϕ	40°

Simplified Model

In order to model this system with the simplified model the following system behavior needs to be determined:

Pseudo-static yield acceleration of key block:

The yield acceleration of the horizontally stacked blocks is controlled by the combined shape of the stacked blocks. The geometry of these blocks and interface friction angle suggests slumping and the yield acceleration can be determined from the standard yield equations of a single block presented in Chapter 3.

Controlling inertial properties:

The rate at which the system displaces is dependent on the blocks that contribute to the dominant rotation in the system. In this case, it is the combined shape of the three blocks that undergo the most displacement and thus its moment of inertia will control the rate at which displacement accrues in this system.

Boundary conditions:

The boundary conditions relative to all the blocks consist of the orientation of the back and base fracture. Throughout deformation of this blocky system, the orientations of the fractures remain constant.

Results

The results of both the *UDEC* solution and simplified model solution are shown in Figure 5.34. It can be seen that by using the combined geometry of the blocks and interface friction angle, the slumping block simulation approximates the *UDEC* solution very well. The combined movement of the blocks throughout the earthquake mimics a single block. However, there is some small relative inter-block movement/sliding occurring which causes the multi-block system to deviate from single slumping block motion. To accommodate this relative motion, the friction angle in the simplified simulation was reduced to $\phi = 39°$ in the slumping block simulations. Once the blocks have rotated fully onto their backs they change to a sliding mode which is indicated in the *UDEC* simulation where the forward block's horizontal acceleration jumps up to the sliding yield acceleration.

5.5.4 Ten Horizontally Stacked Rock Blocks

The third example consists of a ten prototypical slumping blocks that are stacked horizontally. This configuration produces blocks arranged as shown in Figure 5.35. The input parameters for the individual blocks, which all have equal dimension, that form the combined shape are summarized in Table 5.9. The rotations of the base and back fractures are fixed to zero movement while horizontal translation is used to simulate an input ground motion. The input ground motion is the same as for the previous example. Note that the outer-most block will be influenced by movement of blocks behind it.

Table 5.9: Input parameters for the individual blocks that form the ten horizontally stacked block simulation.

Parameter	Individual Block Geometry
Slope	10°
α_1	20°
α_3	30°
Scale	$1.5m$
ϕ	40°

Simplified Model

In order to model this system with the simplified model the following system behavior needs to be determined:

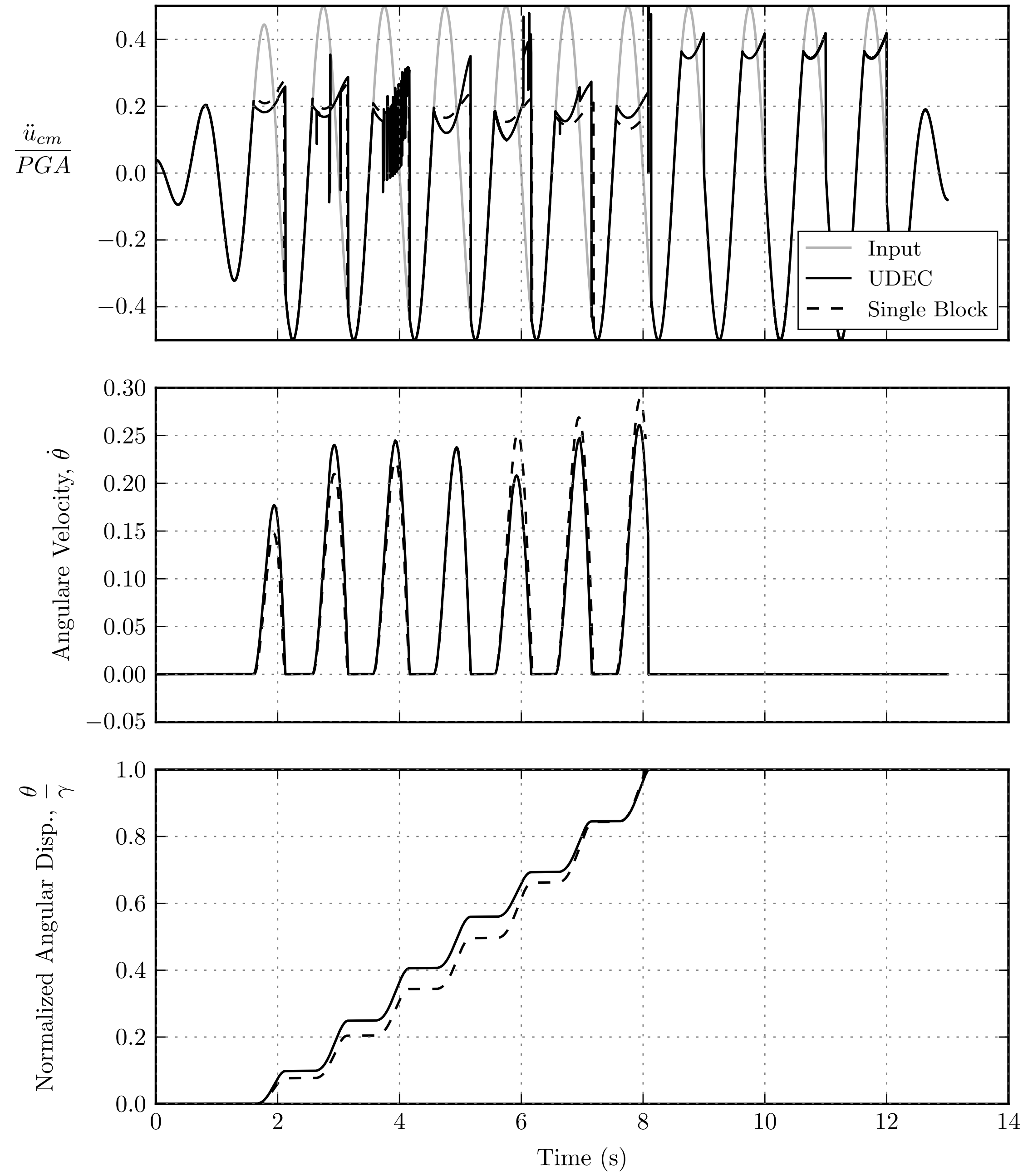

Figure 5.34: Example 2: Comparison of *UDEC* to simplified model for three horizontally stacked blocks

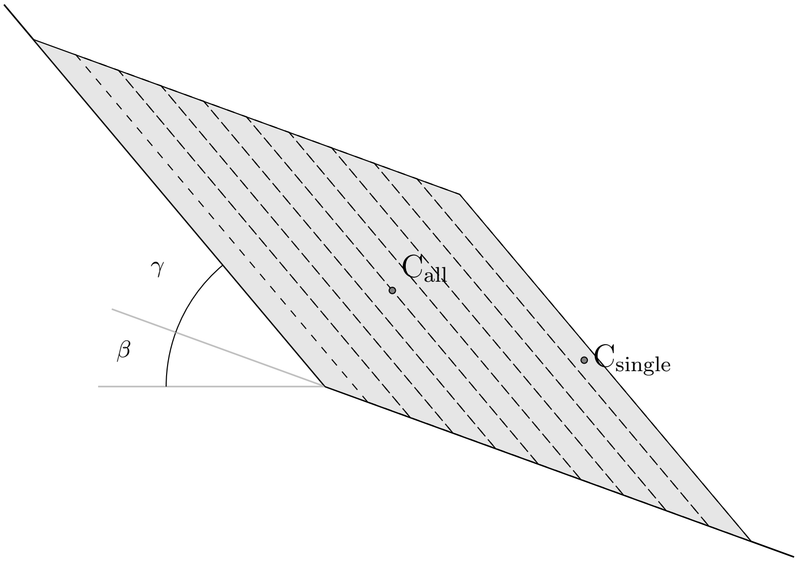

Figure 5.35: Geometry of ten horizontally stacked blocks.

Pseudo-static yield acceleration of outer-most block:

The yield acceleration of the horizontally stacked blocks is controlled by the outer-most block. This block is the key block which must move before the system as a whole can move. The geometry of this block and interface friction angle suggests the slumping yield acceleration can be determined from the standard yield equations of a single slumping block presented in Chapter 3.

Controlling inertial properties:

The rate at which the system displaces is dependent on the blocks that represent the dominant rotation in the system. It appears that the inertial properties of the outer-most block would control the rate at which displacement accrues in this system. However, through iterative evaluation, a reasonable approximation of the inertial property of the system is achieved by using the geometry of the outer-most, single block that is scaled up by a factor of two.

Boundary conditions:

> The boundary conditions relative to the key block consist of the orientation of the block behind it and the base fracture. Throughout deformation of the system, the orientation of the base fracture remains constant. However, the block behind the key block undergoes rotational deformation causing its orientation to change. This change in orientation causes the yield acceleration to remain relatively constant as opposed to a single slumping block whose yield acceleration decreases. To accommodate this change, the equations of motion for the slumping block are modified such that the orientation of the back fracture changes as a linear function of (0.2 times) the key block's own rotation.

Results

The results of both the *UDEC* solution and simplified model solution are shown in Figure 5.36. Slumping block simulations are shown for a basic block equivalent to the outer-most block and combinations of modified boundary conditions and moment of inertia. The modification to the boundary condition causes the outer-most block's yield acceleration to be more constant instead of decreasing. The modification of the inertia properties causes the angular velocity to be dramatically reduced. It can be seen that with both modifications accounting for the effective inertial properties of the system and the changing boundary conditions, the slumping block simulation approximates the *UDEC* solution reasonably well.

The deviations from the single slumping block are based on unique characteristics of block motion for this system. The blocks undergo slumping motion like the three block system but there is significantly more relative inter-block movement. This movement causes the system's shape to change in a pure shear like manner. The change in shape effectively retards the angular motion (i.e. exhibits a lower q) and changes the yield acceleration as a function of movement. Since q^2 contains the boundary conditions and inertial properties, ultimately the best approximation would be obtained by choosing a functional form of q^2 that is non-linear and specific to the problem. This signifies that the motion of complex rock

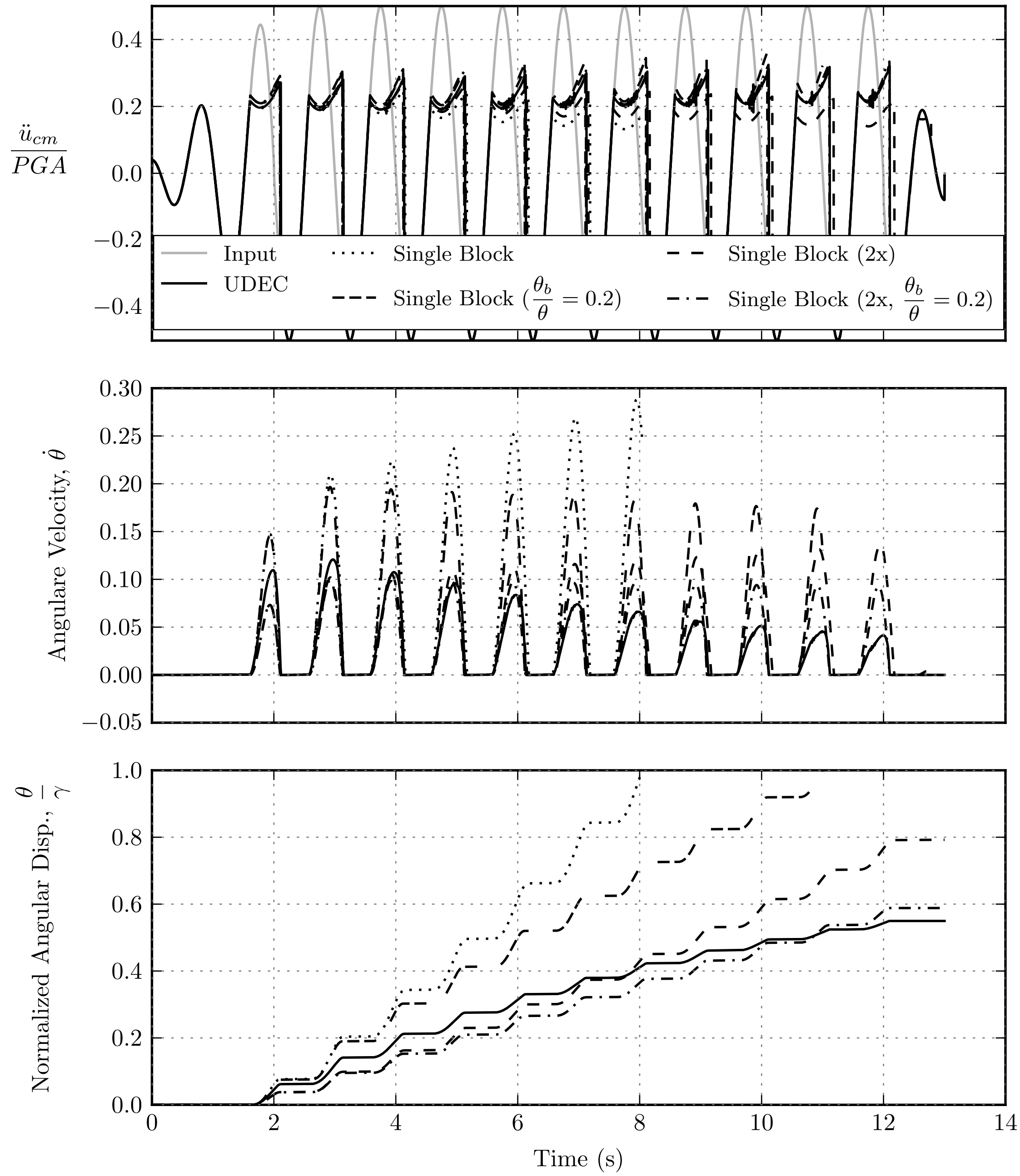

Figure 5.36: Example 3: Comparison of *UDEC* to simplified model for ten horizontally stacked blocks. θ is the rotation of the block and θ_b is the rotation of the block behind it. 2x refers to a block that is twice as big as the single block.

slopes could be approximated by the general slumping equation of motion $\ddot{\theta} = q^2 k_{inc}$ with appropriate q^2 and k_s. Translational motion would be related to the angular motion using a function unique to the failure path of the problem.

5.6 Discussion and Conclusion

In this chapter, a non-linear, time history model and algorithm has been developed to evaluate earthquake-induced slumping of rock blocks. The model incorporates the size of the rock block, rotational motion of the rock block and the boundary conditions that guide its failure path. There is direct applicability of this model to the failure of slumping rock blocks from slopes. It is shown that the block's geometric characteristics (shape and size), fracture strength, and ground motion characteristics (magnitude and duration) control the likelihood of slumping failure.

Evaluation of the equation of motion parameters throughout the slumping motion allowed parameters to be lumped together simplifying the equations of motion. In the simplified form, the equations of motion are strikingly similar to the rocking block equations. The dimensionless rocking block parameters ($\frac{\ddot{\theta}}{p^2 PGA}$, $\frac{\dot{\theta}}{pPGA}$, $\frac{\theta}{PGA}$, ω_g/p, k_r/PGA, and pt) are applicable to the slumping block when the slumping block's dynamic frequency parameter q, yield acceleration k_s, and ground motion frequency ω_g are substituted for the rocking block's frequency parameter p, yield acceleration k_r, and ground motion mean frequency $\omega_m = 2\pi/T_m$. This finding suggests that the extensive knowledge in the dynamic rocking block literature can be analogously applied to the slumping block problem.

Two natural failure criteria were determined from the geometric configuration of the slumping block. These consist of either full rotation of the block onto its back or sufficient rotation such that the heel of the block travels a distance along the base fracture equal to its base length. Both criteria are in terms of a rotation normalized by the block shape. These criterion provide a stable basis for describing the normalized behavior of slumping blocks during earthquakes. However, for a given block shape and normalized rotation, as the scale of the block increases, the relative displacement on the fracture planes also increases. This feature of a rotational system means that a normalized rotational displacement may not be an appropriate failure criteria and highlights the importance to define what is considered the critical displacement of a slumping rock block. For instance, if absolute joint interface displacement is critical (e.g. post peak behavior) then the sliding block model estimate of displacement is a poor index of a rotating slope's damage potential since the actual deformation on the rock joints is dependent on the amount of rotational motion and block size.

Sliding block models are shown to represent well the horizontal motion of the slumping block's center of mass along the center of mass displacement path, which incidentally is not parallel to the base fracture plane as is the case in sliding block models. The observation is similar to the observations discussed in Jibson et al. (2000) and Dreyfus et al. (2013) which stated that the sliding block models correlates well with non-planar slopes. However, this is a source of error when estimating rotating systems with the sliding block which only calculates translational displacement. Since the block is always rotating backward, the center of mass displacement would not accurately represent the displacement as measured at the top, toe, or anywhere else along the slip plane of a slope or block. Since slope displacements are rarely made at the center of mass, this is a possible explanation for the conclusion made by Meehan and Vahedifard (2013) who showed that sliding block displacement relationships predominately underestimate the displacement of landslides. It is possible that the full motion could be better described and predictive equations made more accurate by utilizing the relationship between the slumping mass rotation and translation created by boundary conditions.

A parametric analysis consisting of exciting a broad range of slumping block geometries by over 647 recorded earthquake ground motion time histories was conducted. An investigation into the results of this analysis leads to the following conclusions:

1. A probabilistic design chart is presented relating block geometry and yield characteristics to ground motion parameters and predicting the boundary between failure and

safety. Peak ground acceleration and ground motion frequency content are required to define the failure boundary. Since acceleration can be integrated to determine displacements, PGV alone can also define the failure boundary since it is the integral of PGA and ground motion frequency. The predictive ability of PGA and mean period, $\mathrm{T_m}$ (Rathje et al., 1998) or PGV are virtually identical and thus either are recommended. A rule of thumb can be adopted that the safe boundary is defined by $pgaT_m/2\pi = pgv = k_s g/q$ in the units of cm/s. The limiting factor in this prediction is likely the uncertainty in the ground motion and definition of geometric parameters themselves. Alternatively, PGD can be used. However, since displacement requires two integrations, the frequency content is accounted for twice and thus needs to be divided by the mean period. The downside of PGD is that it has much less predictive capabilities than the other ground motion parameters.

2. The design chart shows that the two natural failure criteria for the slumping block have very similar failure boundary.

3. Failure of the slumping block is best evaluated from a statistical point of view. The response of slumping block can be sensitive to various individual ground motions with similar ground motion parameters, however the likelihood of failure is best estimated using a suite of ground motions.

4. For relatively large blocks, one of two scenarios must be met to induce failure. Either the ground motion must be relatively large in amplitude or duration, or the yield acceleration of the block must be near zero. Since ground motions considered in typical designs have a maximum limit, this implies that there is a critical upper bound block size that can only fail if its static factor of safety is near unity. This conclusion is similar to (moore2012) who discussed the deterioration of rock slope from successive earthquakes. However, it should be noted that this conclusion likely does not apply for joint interfaces that are prone to post-peak behavior and small displacements that lead

to catastrophic failure. Small blocks, on the other hand, have a much lower threshold of ground motion intensity and duration to initiate failure owing to their high q^2 values. This size dependent behavior indicates that the size of failed slumping blocks would increase as the ground motion intensity and duration increases as was shown to be the case for toppling blocks (see Chapter 4).

5. The chart supports the trends noted by Jibson and Harp (2012) that short (high frequency) motions cause small failures.

Several examples were presented of slopes composed of multiple blocks. During yield, each of these slopes exhibits characteristics of slumping behavior: translation and back rotation. Investigation into these examples leads to the following conclusions:

1. The slumping block model could be used and potentially calibrated to model and represent more complex slide masses composed of multi discrete blocks that yield and deform with slump-like characteristics.

2. The model gives insights into the behaviors occurring during the failure of slumping masses including how the moment of inertia, boundary conditions or fracture geometry, and yield acceleration of the mass influences the deformation behavior.

3. It is expected that each unique block or blocky system will have a unique acceleration shape or signature depending on its specific configuration.

Chapter 6

RECOMMENDATIONS FOR FUTURE RESEARCH

The research presented in this dissertation has opened many doors to further research in seismic rock slope engineering. There are immediately obvious research paths that go beyond this research that will be discussed below. While details always matter, future researchers are advised to not get too distracted by the seemingly infinite rock slope geometries, joint geometries, and many other factors encountered in the field, but rather stay focused on the big picture. An attempt was made by the author to parametrically evaluate as much of this variability, however this quickly proved to be futile. Reducing the rock slope problem into simple models as was done in this thesis was required to illuminate the path ahead.

6.1 Pseudo-Static Failure Modes

Pseudo-static failure mode charts were developed in Chapter 3 that expanded the modes of failure and block geometries for seismically-induced rock failure evaluations. These charts should be adapted to stereonet-based methods so that the practicing rock slope engineer can evaluate large quantities of data produced from field studies and LIDAR-based mapping of rock slopes. Modification factors representing the influences of groundwater, neighboring blocks, three dimensionality, and various strength conditions along joints should be developed.

6.2 Seismically-Induced Toppling Failure

In Chapter 4, constraints inherent in a rock slope brought some level of calm to the chaotic rocking block problem. The constraint of a block coming to rest after impact into its seat should be experimentally investigated. It is easily imagined that rock fracture undulations may causes changes to the block's motion, perhaps keeping it in motion. In addition, toppling methods could be very sensitive to rounding or crushing of the rotation edge. This sensitivity could likely be related to rock type and rock mass strength allowing adjustment factors to be developed for various geologic conditions.

The critical toppling block velocity, $k_r g/p$ proved to be very powerful, such that it may be able to predict outcomes for the rocking block problem. The algorithms used in this research could be easily adapted to explore the rocking block problem. A regional hazard analysis should be undertaken using the critical toppling block velocity where toppling modes are known to dominate. These maps could be used in early warning systems such as the PAGER system developed by the USGS. Furthermore, using existing maps and data, locations could be identified for further site-specific evaluations.

6.3 Seismically-Induced Slumping Failure

In Chapter 5, a connection was made between the rocking block literature and slumping block. This allowed for the expansive rocking block literature to be leveraged. It is envisioned that slumping block frequency parameters (q) and slumping yield accelerations ($\mathrm{k_s}$) could be determined for various rock slopes. Rock slopes with the various combination of joint geometries and strengths could be split into various bins with similar parametric values. The influences of groundwater and other environmental factors could be included as well. These inclusions would allow for rock slope engineers and/or public agencies to make broad generalizations about seismic rock slope stability.

Further exploration of various failure definitions are warranted given the sensitivity of joint strength to absolute deformation. In addition, different engineering applications may have different thresholds for critical behavior. It is expected that investigating different displacement thresholds will lead to families of threshold curves.

A limitation of the sliding block model was shown for systems that have a rotational component. A study between the sliding block and slumping block model should be conducted to explore other potential deficiencies in the sliding block model and whether those deficiencies lead to the inaccuracies seen with the sliding block.

Finally, the slumping block model is not limited to rock slopes and could be easily used to explore soil slopes. Some relationships to existing soil slope models were presented. Similar to rock slopes, various soil slopes could be characterized by the parameters established for slumping blocks.

6.4 Seismically-Induced Confined Toppling Failure

A similar study as was performed for the slumping block in Chapter 5 should be undertaken for confined toppling failure. Given that the confined toppling equations are very similar to the slumping equations, positive outcomes are highly probable. It is suspected that the confined toppling model would map well onto rock slopes that undergo complex modes of toppling, such as flexural toppling.

BIBLIOGRAPHY

P. Alfaro, J. Delgado, F. García-Tortosa, L. Lenti, J. López, C. López-Casado, and S. Martino. Widespread landslides induced by the Mw 5.1 earthquake of 11 May 2011 in Lorca, SE Spain. *Engineering Geology*, 137–138(0):40–52, June 2012.

R. Allen and X. Duan. Effects of linearizing on rocking-block toppling. *Journal of Structural Engineering*, 121(7):1146–1149, 1995.

C. Andersson, C. Führer, and J. Åkesson. Assimulo: A unified framework for ODE solvers. *Mathematics and Computers in Simulation*, 116:26–43, October 2015.

A. Anooshehpoor and J. N. Brune. Verification of precarious rock methodology using shake table tests of rock models. *Soil Dynamics and Earthquake Engineering*, 22(9-12): 917–922, October 2002.

A. Anooshehpoor, T. H. Heaton, B. Shi, and J. N. Brune. Estimates of the ground accelerations at point reyes station during the 1906 san francisco earthquake. *Bulletin of the Seismological Society of America*, 89(4):845–853, August 1999.

A. Anooshehpoor, J. N. Brune, and Y. Zeng. Methodology for obtaining constraints on ground motion from precariously balanced rocks. *Bulletin of the Seismological Society of America*, 94(1):285–303, February 2004.

K. N. Applegate and J. P. Wartman. Dynamic rock-slope stability during sliding failure. *Network for Earthquake Engineering Simulation (distributor), Dataset*, 2011.

K. N. Applegate and J. P. Wartman. Dynamic rock-slope stability during sliding failure - phase 2. *Network for Earthquake Engineering Simulation (distributor), Dataset*, 2012.

K. N. Applegate and J. P. Wartman. Dynamic rock-slope stability during rotational failure. *Network for Earthquake Engineering Simulation (distributor), Dataset*, 2013.

J. P. Ashby. *Sliding and toppling modes of failure in models and jointed rock slopes.* PhD thesis, Imperial College of London, 1971.

S. A. Ashford, N. Sitar, J. Lysmer, and N. Deng. Topographic effects on the seismic response of steep slopes. *Bulletin of the Seismological society of america*, 87(3):701, 1997.

M. Aslam, W. Godden, and D. Scalise. Rocking and overturning response of rigid bodies to earthquake motions. Technical Report LBL-7539, Department of Energy, Lawrence Berkeley National Laboratory, 1978.

B. Astaneh. Personal communication: Spectrally matched ground motion set, July 2013.

Ö. Aydan, Y. Shimizu, and Y. Ichikawa. The effective failure modes and stability of slopes in rock mass with two discontinuity sets. *Rock Mechanics and Rock Engineering*, 22(3):163–188, July 1989.

Ö. Aydan, Y. Ohta, and M. Hamada. Geotechnical evaluation of slope and ground failures during the 8 October 2005 Muzaffarabad earthquake, Pakistan. *Journal of Seismology*, 13(3):399–413, March 2009.

J. W. Baker, T. Lin, S. K. Shahi, and N. Jayaram. New ground motion selection procedures and selected motions for the PEER transportation research program. Technical Report PEER Report 2011/03, Pacific Earthquake Engineering Research Center, 2011.

D. Bakun-Mazor, Y. H. Hatzor, and S. D. Glaser. Dynamic sliding of tetrahedral wedge: The role of interface friction. *International Journal for Numerical and Analytical Methods in Geomechanics*, 2011.

S. Bartlett and T. L. Youd. Empirical analysis of horizontal ground displacement generated by liquefaction-induced lateral spreads. Technical Report Technical Report NCEER-92-0021, National Center for Earthquake Engineering Research, August 1992.

R. Bhasin and A. M. Kaynia. Static and dynamic simulation of a 700-m high rock slope in western Norway. *Engineering Geology*, 71(3-4):213–226, February 2004.

B. A. Bradley, M. C. Quigley, R. J. Van Dissen, and N. J. Litchfield. Ground motion and seismic source aspects of the Canterbury earthquake sequence. *Earthquake Spectra*, 30(1):1–15, February 2014.

J. Bray and T. Travasarou. Pseudostatic coefficient for use in simplified seismic slope stability evaluation. *Journal of Geotechnical and Geoenvironmental Engineering*, 135 (9):1336–1340, 2009.

J. W. Bray and R. E. Goodman. The theory of base friction models. In *International Journal of Rock Mechanics and Mining Sciences & Geomechanics Abstracts*, volume 18, pages 453–468, 1981.

J. N. Brune, J. W. Bell, and A. Anooshehpoor. Precariously balanced rocks and seismic risk. *Endeavour*, 20(4):168–172, 1996.

C. Chang, W. Chen, and J. Yao. Seismic Displacements in Slopes by Limit Analysis. *Journal of Geotechnical Engineering*, 110(7):860–874, 1984.

G. Chiaro, T. Kiyota, R. M. Pokhrel, K. Goda, T. Katagiri, and K. Sharma. Reconnaissance report on geotechnical and structural damage caused by the 2015 Gorkha Earthquake, Nepal. *Soils and Foundations*, 55(5):1030–1043, October 2015.

A. K. Chopra. *Dynamics of structures: theory and applications to earthquake engineering*. Prentice Hall, Upper Saddle River, NJ, 2000.

Z. Chuhan, O. A. Pekau, J. Feng, and W. Guanglun. Application of distinct element method in dynamic analysis of high rock slopes and blocky structures. *Soil Dynamics and Earthquake Engineering*, 16(6):385–394, August 1997.

L. S. Cluff. Peru earthquake of May 31, 1970; engineering geology observations. *Bulletin of the Seismological Society of America*, 61(3):511–533, 1971.

J. S. Coggan, D. Stead, and J. M. Eyre. Evaluation of techniques for quarry slope stability assessment. *Transactions. Section B, Applied earth science /*, 107:B139, 1998.

A. Crawford and J. Curran. The influence of rate- and displacement-dependent shear resistance on the response of rock slopes to seismic loads. *International Journal of Rock Mechanics and Mining Sciences & Geomechanics Abstracts*, 19(1):1–8, February 1982.

J. Dafni and J. P. Wartman. Centrifuge modeling of dynamic response in slopes. In *8th International Conference on Physical Modelling in Geotechnicas*, Perth, Australia, January 2014.

M. J. Dejong. *Seismic assesment strategies for masonary structures*. PhD thesis, Massachusetts Institute of Technology, 2009.

A. Di Egidio and A. Contento. Base isolation of slide-rocking non-symmetric rigid blocks under impulsive and seismic excitations. *Engineering Structures*, 31(11): 2723–2734, November 2009.

E. G. Dimitrakopoulos and M. J. DeJong. Revisiting the rocking block: closed-form solutions and similarity laws. *Proceedings of the Royal Society A: Mathematical, Physical and Engineering Science*, April 2012.

D. Dreyfus, E. M. Rathje, and R. W. Jibson. The influence of different simplified sliding-block models and input parameters on regional predictions of seismic landslides triggered by the Northridge earthquake. *Engineering Geology*, 163:41–54, August 2013.

E. Eberhardt. From cause to effect: using numerical modelling to understand rock slope instability mechanisms. In S. G. Evans, G. S. Mugnozza, A. Strom, and R. L. Hermanns, editors, *Landslides from Massive Rock Slope Failure*, number 49 in NATO Science Series, pages 85–101. Springer Netherlands, January 2006.

E. Eberhardt. Rock slope stability analysis - utilization of advanced numerical techniques, April 2003.

E. Eberhardt. Twenty-ninth Canadian Geotechnical Colloquium: The role of advanced numerical methods and geotechnical field measurements in understanding complex deep-seated rock slope failure mechanisms. *Canadian Geotechnical Journal*, 45(4): 484–510, April 2008.

H. Einstein, D. Veneziano, G. Baecher, and K. O'Reilly. The effect of discontinuity persistence on rock slope stability. *International Journal of Rock Mechanics and Mining Sciences & Geomechanics Abstracts*, 20(5):227–236, October 1983.

M. Enoki, B. X. Luong, N. Okabe, and K. Itou. Dynamic theory of rigid-plasticity. *Soil Dynamics and Earthquake Engineering*, 25(7-10):635–647, August 2005.

E. Fredriksson, C. Andersson, and J. Akesson. Discontinuities handled with events in Assimulo. In *Proceedings of the 10th International Modelica Conference*, pages 827–836, Lund, Sweden, March 2014.

G. Gazetas, E. Garini, J. B. Berrill, and M. Apostolou. Sliding and overturning potential of Christchurch 2011 earthquake records. *Earthquake Engineering & Structural Dynamics*, pages n/a–n/a, February 2012.

F. Gelagoti, R. Kourkoulis, I. Anastasopoulos, and G. Gazetas. Rocking-isolated frame structures: margins of safety against toppling collapse and simplified design approach. *Soil Dynamics and Earthquake Engineering*, 32(1):87–102, 2012.

R. E. Goodman. *Introduction to Rock Mechanics*. Wiley, 2nd edition, 1989.

R. E. Goodman and D. S. Kieffer. Behavior of rock in slopes. *Journal of Geotechnical and Geoenvironmental Engineering*, 126(8):675–684, August 2000.

R. E. Goodman and H. B. Seed. Earthquake-induced displacements in sand embankments. *Journal of Soil Mechanics & Foundations Div*, 92(SM2), March 1966.

W. C. Haneberg. Simplified dynamic analysis of vibration-induced rock toppling. *Environmental & Engineering Geoscience*, 15(1):41–45, 2009.

E. L. Harp and R. W. Jibson. Anomalous concentrations of seismically triggered rock falls in Pacoima canyon: are they caused by highly susceptible slopes or local amplification of seismic shaking? *BULLETIN OF THE SEISMOLOGICAL SOCIETY OF AMERICA*, 92(8):3180–3189, December 2002.

E. L. Harp and M. A. Noble. An engineering rock classification to evaluate seismic rock-fall susceptibility and its application to the Wasatch Front. *Bulletin - Association of Engineering Geologists.*, 30(3):291, 1993.

E. L. Harp and R. C. Wilson. Shaking intensity thresholds for rock falls and slides: Evidence from 1987 Whittier Narrows and superstition hills earthquake strong-motion records. *Bulletin of the Seismological Society of America*, 85(6):1739–1757, December 1995.

Y. H. Hatzor, A. A. Arzi, Y. Zaslavsky, and A. Shapira. Dynamic stability analysis of jointed rock slopes using the DDA method: King Herod's Palace, Masada, Israel. *International journal of rock mechanics and mining sciences*, 41(5):813–832, 2004.

Y. H. H. Hatzor. Dynamic rock slope stability analysis at Masada national monument using Block Theory and DDA. In *Proceedings of the 37th U.S. Rock Mechanics Symposium: Rock Mechanics for Industry*, volume 1, pages 63–70. American Rock Mechanics Association, January 1999.

Y. H. Hatzor. Keyblock stability in seismically active rock slopes-Snake Path cliff, Masada. *Journal of geotechnical and geoenvironmental engineering*, 129(8):697–710, 2003.

H. B. Havenith, A. Strom, F. Calvetti, and D. Jongmans. Seismic triggering of landslides. Part B: Simulation of dynamic failure processes. *Natural Hazards and Earth System Science*, 2003.

K. Hewitt, J. J. Clague, and J. F. Orwin. Legacies of catastrophic rock slope failures in mountain landscapes. *Earth-Science Reviews*, 87(1–2):1–38, February 2008.

K.-G. Hinzen. Simulation of toppling columns in archaeoseismology. *Bulletin of the Seismological Society of America*, 99(5):2855–2875, October 2009.

E. Hoek, J. Read, A. Karzulovic, and Z. Y. Chen. Rock slopes in civil and mining engineering. In *Proceedings, GeoEng*, 2000.

E. Hoek and J. Bray. *Rock slope engineering.* Institution of Mining and Metallurgy, London, 1977.

S. J. Hogan. On the dynamics of rigid-block motion under harmonic forcing. *Proceedings of the Royal Society of London. Series A: Mathematical and Physical Sciences*, 425(1869):441–476, 1989.

G. Housner. The behavior of inverted pendulum structures during earthquakes. *Bulletin of the Seismological Society of America*, 53(2):403–417, 1963.

Y. Ishiyama. Review and discussion on overturning of bodies by earthquake motion. Technical Report BRI reseach paper 85, Ministry of Construction, Building Research Institute, 1980.

Y. Ishiyama. Motions of rigid bodies and criteria for overturning by earthquake excitations. *Earthquake Engineering & Structural Dynamics*, 10(5):635–650, 1982.

R. W. Jibson. Predicting earthquake-induced landslide displacements using Newmark's sliding block analysis. *Transportation Research Record*, pages 9–17, 1993.

R. W. Jibson. Regression models for estimating coseismic landslide displacement. *Engineering Geology*, 91(2-4):209–218, 2007.

R. W. Jibson. Methods for assessing the stability of slopes during earthquakes–A retrospective. *Engineering Geology*, 122(1-2):43–50, September 2011.

R. W. Jibson and E. L. Harp. Extraordinary distance limits of landslides triggered by the 2011 Mineral, Virginia, earthquake. *Bulletin of the Seismological Society of America*, 102(6):2368–2377, December 2012.

R. W. Jibson, E. L. Harp, and J. A. Michael. A method for producing digital probabilistic seismic landslide hazard maps. *Engineering Geology*, 58(3–4):271–289, December 2000.

R. W. Jibson, E. L. Harp, W. Schulz, and D. K. Keefer. Large rock avalanches triggered by the M 7.9 Denali Fault, Alaska, earthquake of 3 November 2002. *Engineering Geology*, 83(1-3):144–160, February 2006.

D. K. Keefer. Landslides caused by earthquakes. *Bulletin of the Geological Society of America*, 95(4):406, April 1984.

D. K. Keefer. The susceptibility of rock slopes to earthquake-induced failure. *Bulletin of the Association of Engineering Geologists*, 33(3):353–361, 1993.

D. K. Keefer. Landslides generated by earthquakes: immediate and long-term effects. In J. F. Shroder, editor, *Treatise on Geomorphology*, volume 5, pages 250–266. Elsevier, San Diego, 2013.

D. K. Keefer and M. C. Larsen. Assessing landslide hazards. *Science*, 316(5828):1136 –1138, May 2007.

D. K. Keefer, J. Wartman, C. Navarro Ochoa, A. Rodriguez-Marek, and G. F. Wieczorek. Landslides caused by the M 7.6 Tecomán, Mexico earthquake of January 21, 2003. *Engineering Geology*, 86(2-3):183–197, August 2006.

D. S. Kieffer. *Rock slumping: A compound failure mode of jointed hard rock slopes.* PhD thesis, University of California, Berkeley, 1998.

A. N. Kounadis, G. J. Papadopoulos, and D. M. Cotsovos. Overturning instability of a two-rigid block system under ground excitation. *ZAMM - Journal of Applied Mathematics and Mechanics / Zeitschrift für Angewandte Mathematik und Mechanik*, April 2012.

S. L. Kramer and M. W. Smith. Modified Newmark model for seismic displacements of compliant slopes. *Journal of Geotechnical and Geoenvironmental Engineering*, 123 (7):635, July 1997.

S. L. Kramer. *Geotechnical earthquake engineering*. Prentice Hall, Upper Saddle River, N.J., 1996.

F. Lanaro, L. Jing, O. Stephansson, and G. Barla. DEM modelling of laboratory tests of block toppling. *International Journal of Rock Mechanics and Mining Sciences*, 34 (3-4), 1997.

G. Lanzo, G. Di Capua, R. E. Kayen, D. Scott Kieffer, E. Button, G. Biscontin, and J. P. Stewart. Seismological and geotechnical aspects of the Mw=6.3 l'Aquila earthquake in central Italy on 6 April 2009, April 2010.

H. I. Ling and D. Leshchinsky. Seismic performance of simple slopes. *Soils and foundations*, 35(2):85–94, 1995.

H. I. Ling, D. Leshchinsky, and Y. Mohri. Soil slopes under combined horizontal and vertical seismic accelerations. *Earthquake Engineering & Structural Dynamics*, 26(12): 1231–1241, 1997.

P. Majumdar and S. Roy. Friction controlled three stage ladder sliding motion in a non-conservative system: from pre-detachment to post-detachment. *The African Review of Physics*, 7, 2012.

F. I. Makdisi and H. B. Seed. Simplified procedure for estimating dam and embankment earthquake-induced deformations. *Journal of the Geotechnical Engineering Division*, 104(7):849–867, July 1978.

N. Makris and D. Konstantinidis. Rocking response and overturning of equipment under horizontal pulse-type motions. Technical Report PEER-1998/05, University of California, Berkeley, Pacific Earthquake Engineering Research Center, 1998.

N. Makris and D. Konstantinidis. The rocking spectrum and the limitations of practical design methodologies. *Earthquake engineering & structural dynamics*, 32(2):265–289, 2003.

N. Makris and Y. S. Roussos. Rocking response of rigid blocks under near-source ground motions. *Géotechnique*, 50(3):243–262, January 2000.

C. I. Massey, M. J. McSaveney, T. Taig, L. Richards, N. J. Litchfield, D. A. Rhoades, G. H. McVerry, B. Lukovic, D. W. Heron, W. Ries, and R. J. Van Dissen. Determining rockfall risk in Christchurch using rockfalls triggered by the 2010-2011 Canterbury earthquake sequence. *Earthquake Spectra*, 30(1):155–181, February 2014.

C. Massey, M. McSaveney, D. Heron, and B. Lukovic. Canterbury earthquakes 2010/11 Port Hills slope stability: Pilot study for assessing life-safety risk from rockfalls (boulder rolls). Technical Report 2011/311, GNS Science, March 2012.

B. J. McDowell. Site investigations for residential development on the port hills, christchurch. Technical report, University of Canterbury, 1989.

C. L. Meehan and F. Vahedifard. Evaluation of simplified methods for predicting earthquake-induced slope displacements in earth dams and embankments. *Engineering Geology*, 152(1):180–193, January 2013.

R. Michalowski. Displacements of multiblock geotechnical structures subjected to seismic excitation. *Journal of Geotechnical and Geoenvironmental Engineering*, 133(11): 1432–1439, 2007.

R. E. S. Moss, E. M. Thompson, D. S. Kieffer, B. Tiwari, Y. M. A. Hashash, I. Acharya, B. R. Adhikari, D. Asimaki, K. B. Clahan, B. D. Collins, S. Dahal, R. W. Jibson, D. Khadka, A. Macdonald, C. L. M. Madugo, H. B. Mason, M. Pehlivan, D. Rayamajhi, and S. Uprety. Geotechnical effects of the 2015 magnitude 7.8 Gorkha, Nepal, earthquake and aftershocks. *Seismological Research Letters*, 86(6):1514–1523, November 2015.

W. Murphy. The role of topographic amplification on the initiation of rock slopes failures during earthquakes. In S. G. Evans, G. S. Mugnozza, A. Strom, and R. L. Hermanns, editors, *Landslides from Massive Rock Slope Failure*, volume 49, pages 139–154. Springer Netherlands, Dordrecht, 2006.

N. Newmark. Effects of earthquakes on dams and embankments. *Geotechnique*, 15(2): 139–160, 1965.

M. Özer and G. F. Alışverişci. Dynamic response analysis of rocking rigid blocks subjected to half-sine pulse type base excitations. In *Vibration Problems ICOVP 2005*, volume 111, pages 389–394. Springer Netherlands, Dordrecht, 2005.

A. Pagliaroli, G. Lanzo, and B. D'Elia. Numerical evaluation of topographic effects at the Ricastro ridge in southern Italy. *Journal of Earthquake Engineering*, 15(3): 404–432, March 2011.

S. Pal, A. M. Kaynia, R. K. Bhasin, and D. K. Paul. Earthquake stability analysis of rock slopes: a case study. *Rock Mechanics and Rock Engineering*, April 2011.

PEER. Technical report for the PEER ground motion database web application, 2010.

O. Pekau and C. Yuzhu. Failure analysis of fractured dams during earthquakes by DEM. *Engineering Structures*, 26(10):1483–1502, August 2004.

F. Peña, P. B. Lourenço, and A. Campos-Costa. Experimental dynamic behavior of free-standing multi-block structures under seismic loadings. *Journal of Earthquake Engineering*, 12(6):953–979, August 2008.

G. Plafker, G. E. Ericksen, and J. F. Concha. Geological aspects of the May 31, 1970, Peru earthquake. *Bulletin of the Seismological Society of America*, 61(3):543–578, 1971.

R. Plaut, W. Fielder, and L. Virgin. Fractal behavior of an asymmetric rigid block overturning due to harmonic motion of a tilted foundation. *Chaos, Solitons & Fractals*, 7(2):177–196, February 1996.

A. Pompei, A. Scalia, and M. A. Sumbatyan. Dynamics of rigid block due to horizontal ground motion. *Journal of Engineering Mechanics*, 124(7):713, July 1998.

E. G. Prater. Yield acceleration for seismic stability of slopes. *Journal of the Geotechnical Engineering Division*, 105(5):682–687, May 1979.

M. D. Purvance. *Overturning of slender blocks: numerical investigation and application to precariously balanced rocks in southern california*. PhD thesis, University of Nevada, Reno, May 2005.

E. Rathje, N. Abrahamson, and J. Bray. Simplified frequency content estimates of earthquake ground motions. *Journal of Geotechnical and Geoenvironmental Engineering*, 124(2):150–159, 1998.

E. M. Rathje and G. Antonakos. A unified model for predicting earthquake-induced sliding displacements of rigid and flexible slopes. *Engineering Geology*, In Press, Corrected Proof, 2011.

C. Rodríguez, J. Bommer, and R. Chandler. Earthquake-induced landslides: 1980–1997. *Soil Dynamics and Earthquake Engineering*, 18(5):325–346, July 1999.

C. Sagaseta. On the modes of instability of a rigid block on an inclined plane. *Rock Mechanics and Rock Engineering*, 19:261–266, 1986.

S. K. Sarma. Seismic displacement analysis of earth dams. *Journal of the Geotechnical Engineering Division*, 107(12):1735–1739, December 1981.

T. Sawada and S. G. Nomachi. Displacement of earthquake-induced slope in logarithmic spiral local failure. *Memoirs of the Tomakomai Technical College*, 21, 1985.

G. Saygili and E. Rathje. Empirical predictive models for earthquake-induced sliding displacements of slopes. *Journal of Geotechnical and Geoenvironmental Engineering*, 134(6):790–803, 2008.

S. A. Schumm and R. J. Chorley. The fall of threatening rock. *American Journal of Science*, 262(9):1041–1054, 1964.

H. B. Seed and R. E. Goodman. Earthquake stability of slopes of cohesionless soils. *Journal of Soil Mechanics & Foundations Div*, 90(SM6):43–73, November 1964.

H. W. Shenton III. Criteria for initiation of slide, rock, and slide-rock rigid-body modes. *Journal of Engineering Mechanics*, 122(7):690, July 1996.

B. Shi, A. Anooshehpoor, Y. Zeng, and J. Brune. Rocking and overturning of precariously balanced rocks by earthquakes. *Bulletin of the Seismological Society of America*, 86(5):1364–1371, 1996.

R. Siddharthan and M. El-Gamal. Permanent rotational deformation of dry cohesionless slopes under seismic excitations. *Transportation Research Record: Journal of the Transportation Research Board*, 1633(-1):45–50, January 1998.

N. Sitar, M. MacLaughlin, and D. Doolin. Influence of kinematics on landslide mobility and failure mode. *Journal of Geotechnical and Geoenvironmental Engineering*, 131(6): 716–728, June 2005.

S. E. Smith, M. M. MacLaughlin, S. L. Adams, J. P. Wartman, K. N. Applegate, M. D. Gibson, L. D. Arnold, and D. K. Keefer. Interface properties of synthetic rock specimens: experimental and numerical investigation. *Unpublished Manuscript*, 2013.

L. Sorrentino, R. Masiani, and L. D. Decanini. Overturning of rocking rigid bodies under transient ground motions. *Structural Engineering and Mechanics*, 22(3):293–310, 2006.

C. Stamatopoulos, C. Mavromihalis, and S. Sarma. Correction for geometry changes during motion of sliding-block seismic displacement. *Journal of Geotechnical and Geoenvironmental Engineering*, 137(10):926–938, 2011.

D. Stead, E. Eberhardt, and J. Coggan. Developments in the characterization of complex rock slope deformation and failure using numerical modelling techniques. *Engineering Geology*, 83(1-3):217–235, February 2006.

P. M. Strenk and J. Wartman. Uncertainty in seismic slope deformation model predictions. *Engineering Geology*, 122(1-2):61–72, September 2011.

C. Tang, J. Zhu, X. Qi, and J. Ding. Landslides induced by the Wenchuan earthquake and the subsequent strong rainfall event: A case study in the Beichuan area of China. *Engineering Geology*, 122(1–2):22–33, September 2011.

T. Taniguchi. Non-linear response analyses of rectangular rigid bodies subjected to horizontal and vertical ground motion. *Earthquake engineering & structural dynamics*, 31(8):1481–1500, 2002.

T. Taniguchi. Experimental and analytical study of free lift-off motion induced slip behavior of rectangular rigid bodies. *Journal of Pressure Vessel Technology*, 126(1): 53–58, February 2004.

F. Tonon. Analysis of single rock blocks for general failure modes under conservative and non-conservative forces. *International Journal for Numerical and Analytical Methods in Geomechanics*, 31(14):1567–1608, December 2007.

M. D. Voegele. Rational design of tunnel supports: an interactive graphics based analysis of the support requirements of excavations in jointed rock masses. Technical report, University of Minnesota, 1979.

E. Voyagaki, I. Psycharis, and G. Mylonakis. Complex response of a rocking block to a full-cycle pulse. *Journal of Engineering Mechanics*, 0(0):04014024, September 2013a.

E. Voyagaki, I. N. Psycharis, and G. Mylonakis. Rocking response and overturning criteria for free standing rigid blocks to single-lobe pulses. *Soil Dynamics and Earthquake Engineering*, 46:85–95, March 2013b.

J. Wang, G. Lin, and J. Liu. Static and dynamic stability analysis using 3D-DDA with incision body scheme. *Earthquake Engineering and Engineering Vibration*, 5(2): 273–283, December 2006.

J. Wartman, J. D. Bray, and R. B. Seed. Inclined plane studies of the Newmark sliding block procedure. *Journal of Geotechnical and Geoenvironmental Engineering*, 129(8): 673–684, August 2003.

J. P. Wartman. Reconnaissance photos from 2007 Pisco, Peru earthquake, 2007.

R. C. Wilson and D. K. Keefer. Dynamic analysis of a slope failure from the 6 August 1979 Coyote Lake, California, earthquake. *Bulletin of the Seismological Society of America*, 73(3):863 –877, June 1983.

T. Winkler, K. Meguro, and F. Yamazaki. Response of rigid body assemblies to dynamic excitation. *Earthquake Engineering & Structural Dynamics*, 24(10):1389–1408, October 1995.

C. M. Wong and W. K. Tso. Steady state rocking response of rigid blocks part 2: experiment. *Earthquake Engineering & Structural Dynamics*, 18(1):107–120, January 1989.

J.-H. Wu. Seismic landslide simulations in discontinuous deformation analysis. *Computers and Geotechnics*, 37(5):594–601, July 2010.

Q. Xu, X.-M. Fan, R.-Q. Huang, and C. V. Westen. Landslide dams triggered by the Wenchuan Earthquake, Sichuan Province, south west China. *Bulletin of Engineering Geology and the Environment*, 68(3):373–386, August 2009.

G. Yagoda-Biran and Y. Hatzor. A new failure mode chart for toppling and sliding with consideration of earthquake inertia force. *International Journal of Rock Mechanics and Mining Sciences*, 64:122–131, December 2013.

C.-S. Yim, A. K. Chopra, and J. Penzien. Rocking response of rigid blocks to earthquakes. *Earthquake Engineering & Structural Dynamics*, 8(6):565–587, 1980.

L. You and R. L. Michalowski. Displacement charts for slopes subjected to seismic loads. *Computers and Geotechnics*, 25(1):45–55, July 1999.

X. Zeng and C. He. Rotating block method for seismic displacement of slopes of saturated clay. In *IACGE 2013: Challenges and Recent Advances in Geotechnical and Seismic Research and Practices: Proceedings of the Second International Conference on Geotechnical and Earthquake Engineering, October 25-27, 2013, Chengdu, China*, page 27. ASCE Publications, 2013.

X. Zeng and R. S. Steedman. Rotating block method for seismic displacement of gravity walls. *Journal of geotechnical and geoenvironmental engineering*, 126(8):709–717, 2000.

J. Zhang and N. Makris. Rocking response of free-standing blocks under cycloidal pulses. *Journal of Engineering Mechanics*, 127(5), May 2001.

Appendix A

GROUND MOTIONS

Ground motions used throughout this thesis are documented in this Appendix. 800 unique earthquake time histories were selected from various sources. The sources for the suites of ground motions that were collected are summarized as follows:

PEER

This set of motions consist of 427 horizontal components and 104 associated vertical motions (when available). They include all the motions from the PEER strong ground motion database (NGA-West 1) PEER (2010) with a site shear wave velocity greater than 600m/s.

Baker

40 Broadband and 40 pulse-like motions were selected based on sets 2 and 3 of the motions developed by Baker et al. (2011).

Spectrally Matched

This set of 30 spectrally-matched motions were selected. These motions were developed by Astaneh (2013) and are unpublished.

All motions are derived from the PEER database and thus are associated with a NGA reference number and meta data. In addition to the NGA metadata, various properties of the acceleration time histories were calculated for use in analyses. These properties include PGA, PGV, PGD, time history duration, T_m (Rathje et al., 1998), and T_c and shape factor "d" (Kramer, 1996). Definitions of these parameters is shown in the main glossary. Histograms of these parameters for each motion within the four sets are presented in Figure A.1. The metadata from these histograms are presented in Tables A.1, A.2, A.3, and A.4.

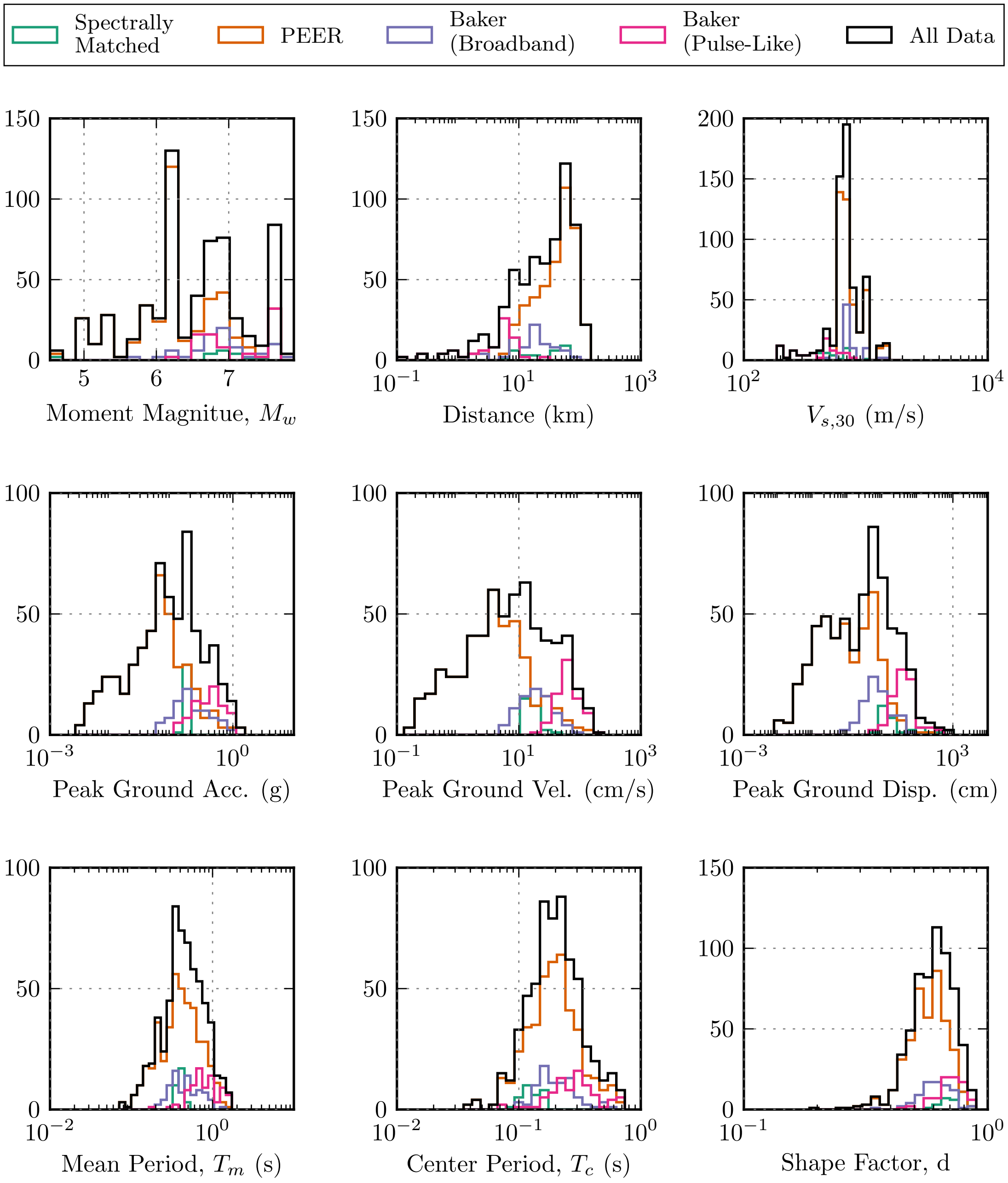

Figure A.1: Histograms of ground motion metadata

Table A.1: PEER ground motion metadata

Earthquake (Year)	Station	NGA Number	Fault Type	M_w	Distance (km)	$V_{s,30}$ (m/s)	Component	PGA (g)	PGV (cm/s)	PGD (cm)	T_m (s)	Duration (s)
Anza (Horse Canyon)-01	Anza - Terwilliger Valley	226	SS	5.19	12.7	685	Component1	0.13	3.92	0.17	0.16	10.22
Anza (Horse Canyon)-01	Anza - Terwilliger Valley	226	SS	5.19	12.7	685	Component2	0.08	1.67	0.06	0.13	10.22
Anza (Horse Canyon)-01	Anza - Terwilliger Valley	226	SS	5.19	12.7	685	Vertical	-	-	-	-	10.22
Anza-02	Anza - Tripp Flats Training	1919	N-OBL	4.92	27.8	685	Component1	0.12	2.86	0.14	0.12	56.00
Anza-02	Idyllwild - Hwy 243 & Pine Crest	1942	N-OBL	4.92	35.0	685	Component1	0.05	1.19	0.08	0.14	48.00
Anza-02	Idyllwild - Hwy 243 & Pine Crest	1942	N-OBL	4.92	35.0	685	Component2	0.07	1.75	0.07	0.15	48.00
Anza-02	Idyllwild - Hwy 243 & Pine Crest	1942	N-OBL	4.92	35.0	685	Vertical	-	-	-	-	48.00
Anza-02	Idyllwild - Keenwild Fire Sta.	1943	N-OBL	4.92	32.0	845	Component1	0.04	0.46	0.06	0.12	46.00
Anza-02	Lake Elsinore - Graham & Poe	1949	N-OBL	4.92	79.0	623	Component1	0.02	0.29	0.01	0.10	37.00
Anza-02	Lake Elsinore - Graham & Poe	1949	N-OBL	4.92	79.0	623	Component2	0.02	0.22	0.01	0.11	37.00
Anza-02	Lake Elsinore - Graham & Poe	1949	N-OBL	4.92	79.0	623	Vertical	-	-	-	-	37.00
Anza-02	Nuevo - 11th & McKinley	1961	N-OBL	4.92	82.0	685	Component1	0.03	1.16	0.07	0.18	48.00
Anza-02	Nuevo - 11th & McKinley	1961	N-OBL	4.92	82.0	685	Component2	0.03	1.18	0.08	0.23	48.00
Anza-02	Nuevo - 11th & McKinley	1961	N-OBL	4.92	82.0	685	Vertical	-	-	-	-	48.00
Anza-02	Riverside - Van Buren&Trautwein	1972	N-OBL	4.92	87.0	685	Component1	0.01	0.27	0.02	0.13	36.00
Anza-02	Riverside - Van Buren&Trautwein	1972	N-OBL	4.92	87.0	685	Component2	0.01	0.25	0.02	0.14	36.00
Anza-02	Riverside - Van Buren&Trautwein	1972	N-OBL	4.92	87.0	685	Vertical	-	-	-	-	36.00
Anza-02	Sage - Fire Station	1974	N-OBL	4.92	41.0	623	Component1	0.06	0.39	0.02	0.07	42.00
Anza-02	Sage - Fire Station	1974	N-OBL	4.92	41.0	623	Component2	0.05	0.73	0.04	0.08	42.00
Anza-02	Sage - Fire Station	1974	N-OBL	4.92	41.0	623	Vertical	-	-	-	-	42.00
Anza-02	San Bernardino - Del Rosa Wk Sta	1975	N-OBL	4.92	101.0	685	Component1	0.01	0.55	0.04	0.33	42.00
Anza-02	Seven Oaks Dam Downstream Surf.	1985	N-OBL	4.92	87.0	685	Component1	0.01	0.27	0.04	0.16	42.00
Big Bear City	Anza - Tripp Flats Training	2119	SS	4.92	78.0	685	Component1	0.01	0.21	0.01	0.16	45.00
Big Bear City	Paradise Springs - Camp Office	2134	SS	4.92	88.0	623	Component1	0.00	0.14	0.01	0.20	40.75
Big Bear City	San Bernardino - Del Rosa Wk Sta	2138	SS	4.92	40.0	685	Component1	0.01	0.41	0.08	0.33	45.00
Big Bear City	San Bernardino - Sycamore FS	2148	SS	4.92	54.0	623	Component1	0.01	0.20	0.03	0.22	41.00
Big Bear City	Seven Oaks Dam Downstream Surf.	2149	SS	4.92	33.0	685	Component1	0.03	0.77	0.08	0.15	50.00
Big Bear-01	Pear Blossom - Pallet Creek	922	SS	6.46	96.0	685	Component1	0.03	2.01	0.21	0.44	60.01
Big Bear-01	Pear Blossom - Pallet Creek	922	SS	6.46	96.0	685	Component2	0.03	1.84	0.27	0.35	60.01
Big Bear-01	Pear Blossom - Pallet Creek	922	SS	6.46	96.0	685	Vertical	-	-	-	-	60.01
Big Bear-01	Rancho Cucamonga - Deer Can	925	SS	6.46	59.0	822	Component1	0.05	3.42	0.61	0.40	60.01
Big Bear-01	Rancho Cucamonga - Deer Can	925	SS	6.46	59.0	822	Component2	0.03	1.96	0.45	0.38	60.01
Big Bear-01	Rancho Cucamonga - Deer Can	925	SS	6.46	59.0	822	Vertical	-	-	-	-	60.01
Big Bear-01	Sage - Fire Station	928	SS	6.46	64.0	623	Component1	0.17	3.00	0.22	0.12	60.01
Big Bear-01	Sage - Fire Station	928	SS	6.46	64.0	623	Component2	0.17	2.66	0.29	0.12	60.01

Continued on next page

Table A.1: PEER ground motion metadata (continued)

Earthquake (Year)	Station	NGA Number	Fault Type	M_w	Distance (km)	$V_{s,30}$ (m/s)	Component	PGA (g)	PGV (cm/s)	PGD (cm)	T_m (s)	Duration (s)
Big Bear-01	Sage - Fire Station	928	SS	6.46	64.0	623	Vertical	-	-	-	-	60.01
Big Bear-01	Silent Valley - Poppet Flat	934	SS	6.46	35.0	685	Component1	0.06	2.03	3.30	0.21	40.00
Big Bear-01	Silent Valley - Poppet Flat	934	SS	6.46	35.0	685	Component2	0.07	2.13	2.75	0.17	40.00
Big Bear-01	Silent Valley - Poppet Flat	934	SS	6.46	35.0	685	Vertical	-	-	-	-	40.00
Big Bear-01	Winchester Bergman Ran	938	SS	6.46	59.0	685	Component1	0.08	1.77	2.05	0.13	40.00
Big Bear-01	Winchester Bergman Ran	938	SS	6.46	59.0	685	Component2	0.06	1.16	3.83	0.11	40.00
Big Bear-01	Winchester Bergman Ran	938	SS	6.46	59.0	685	Vertical	-	-	-	-	40.00
Big Bear-02	San Bernardino - Del Rosa Wk Sta	1891	SS	4.53	32.0	685	Component1	0.01	0.29	0.03	0.28	42.00
Big Bear-02	Seven Oaks Dam Downstream Surf.	1903	SS	4.53	24.8	685	Component1	0.06	1.66	0.10	0.15	48.00
Chi-Chi, Taiwan	HWA003	1257	RV-OBL	7.62	56.0	1526	Component1	0.14	19.13	8.93	1.10	65.00
Chi-Chi, Taiwan	HWA003	1257	RV-OBL	7.62	56.0	1526	Component2	0.05	10.55	5.45	1.11	65.00
Chi-Chi, Taiwan	HWA024	1273	RV-OBL	7.62	43.0	630	Component1	0.02	7.47	7.37	0.86	90.00
Chi-Chi, Taiwan	HWA024	1273	RV-OBL	7.62	43.0	630	Component2	0.02	4.55	5.43	0.70	90.00
Chi-Chi, Taiwan	HWA029	1278	RV-OBL	7.62	54.0	614	Component1	0.10	14.05	6.74	1.00	87.00
Chi-Chi, Taiwan	HWA029	1278	RV-OBL	7.62	54.0	614	Component2	0.03	7.19	12.90	0.98	87.00
Chi-Chi, Taiwan	HWA038	1287	RV-OBL	7.62	43.0	643	Component1	0.03	8.79	4.97	0.89	90.00
Chi-Chi, Taiwan	HWA038	1287	RV-OBL	7.62	43.0	643	Component2	0.04	5.54	5.25	0.65	90.00
Chi-Chi, Taiwan	HWA046	1293	RV-OBL	7.62	52.0	618	Component1	0.09	9.00	14.02	0.55	89.00
Chi-Chi, Taiwan	HWA046	1293	RV-OBL	7.62	52.0	618	Component2	0.08	9.80	18.09	0.53	89.00
Chi-Chi, Taiwan	HWA057	1302	RV-OBL	7.62	51.0	679	Component1	0.08	8.40	16.24	0.34	90.00
Chi-Chi, Taiwan	HWA057	1302	RV-OBL	7.62	51.0	679	Component2	0.05	6.27	9.33	0.42	90.00
Chi-Chi, Taiwan	ILA031	1325	RV-OBL	7.62	83.0	649	Component1	0.06	10.06	9.95	0.42	78.00
Chi-Chi, Taiwan	ILA031	1325	RV-OBL	7.62	83.0	649	Component2	0.03	7.28	9.76	0.52	78.00
Chi-Chi, Taiwan	ILA063	1347	RV-OBL	7.62	61.0	997	Component1	0.09	8.12	12.99	0.42	79.00
Chi-Chi, Taiwan	ILA063	1347	RV-OBL	7.62	61.0	997	Component2	0.08	12.61	8.81	0.47	79.00
Chi-Chi, Taiwan	KAU003	1352	RV-OBL	7.62	114.0	914	Component1	0.02	6.48	9.03	1.23	129.00
Chi-Chi, Taiwan	KAU003	1352	RV-OBL	7.62	114.0	914	Component2	0.02	5.41	10.83	1.29	129.00
Chi-Chi, Taiwan	TAP065	1440	RV-OBL	7.62	122.0	1023	Component1	0.04	9.87	6.98	1.48	60.00
Chi-Chi, Taiwan	TAP065	1440	RV-OBL	7.62	122.0	1023	Component2	0.01	5.62	6.38	1.21	60.00
Chi-Chi, Taiwan	TAP077	1446	RV-OBL	7.62	119.0	1023	Component1	0.04	6.86	6.03	0.97	83.00
Chi-Chi, Taiwan	TAP077	1446	RV-OBL	7.62	119.0	1023	Component2	0.03	12.02	9.09	1.46	83.00
Chi-Chi, Taiwan	TCU076	1511	RV-OBL	7.62	2.8	615	Component1	0.30	62.65	31.49	0.50	90.00
Chi-Chi, Taiwan	TCU076	1511	RV-OBL	7.62	2.8	615	Component2	0.28	34.07	17.40	0.63	90.00
Chi-Chi, Taiwan	TCU085	1518	RV-OBL	7.62	58.0	1000	Component1	0.06	7.51	13.89	0.64	79.00
Chi-Chi, Taiwan	TCU085	1518	RV-OBL	7.62	58.0	1000	Component2	0.04	9.40	12.33	0.80	79.00
Chi-Chi, Taiwan	TCU138	1551	RV-OBL	7.62	9.8	653	Component1	0.22	40.87	26.10	0.96	150.00

Continued on next page

Table A.1: PEER ground motion metadata (continued)

Earthquake (Year)	Station	NGA Number	Fault Type	M_w	Distance (km)	$V_{s,30}$ (m/s)	Component	PGA (g)	PGV (cm/s)	PGD (cm)	T_m (s)	Duration (s)
Chi-Chi, Taiwan	TCU138	1551	RV-OBL	7.62	9.8	653	Component2	0.19	40.96	36.44	0.70	150.00
Chi-Chi, Taiwan	TTN024	1576	RV-OBL	7.62	60.0	645	Component1	0.03	3.75	5.32	0.52	90.00
Chi-Chi, Taiwan	TTN024	1576	RV-OBL	7.62	60.0	645	Component2	0.02	4.01	3.36	0.53	90.00
Chi-Chi, Taiwan	TTN042	1587	RV-OBL	7.62	65.0	845	Component1	0.06	5.93	4.55	0.57	100.00
Chi-Chi, Taiwan	TTN042	1587	RV-OBL	7.62	65.0	845	Component2	0.06	5.38	5.97	0.57	100.00
Chi-Chi, Taiwan-02	CHY062	2185	RV	5.90	100.0	603	Component1	0.01	0.74	0.07	0.35	45.00
Chi-Chi, Taiwan-02	CHY062	2185	RV	5.90	100.0	603	Component2	0.00	0.29	0.04	0.42	45.00
Chi-Chi, Taiwan-02	HWA024	2231	RV	5.90	64.0	630	Component1	0.00	0.32	0.04	0.39	33.00
Chi-Chi, Taiwan-02	HWA024	2231	RV	5.90	64.0	630	Component2	0.00	0.18	0.03	0.32	33.00
Chi-Chi, Taiwan-02	HWA029	2236	RV	5.90	48.0	614	Component1	0.02	1.88	0.37	0.80	35.00
Chi-Chi, Taiwan-02	HWA029	2236	RV	5.90	48.0	614	Component2	0.01	1.58	0.45	0.77	35.00
Chi-Chi, Taiwan-02	HWA038	2245	RV	5.90	56.0	643	Component1	0.01	0.75	0.14	0.52	38.00
Chi-Chi, Taiwan-02	HWA038	2245	RV	5.90	56.0	643	Component2	0.01	0.68	0.11	0.39	38.00
Chi-Chi, Taiwan-02	HWA046	2251	RV	5.90	56.0	618	Component1	0.03	2.47	0.30	0.48	37.00
Chi-Chi, Taiwan-02	HWA046	2251	RV	5.90	56.0	618	Component2	0.03	1.92	0.26	0.45	37.00
Chi-Chi, Taiwan-02	HWA057	2258	RV	5.90	55.0	679	Component1	0.03	1.36	0.21	0.31	39.00
Chi-Chi, Taiwan-02	HWA057	2258	RV	5.90	55.0	679	Component2	0.02	1.10	0.17	0.35	39.00
Chi-Chi, Taiwan-02	ILA031	2280	RV	5.90	100.0	649	Component1	0.02	0.85	0.10	0.38	41.00
Chi-Chi, Taiwan-02	ILA031	2280	RV	5.90	100.0	649	Component2	0.01	0.94	0.15	0.50	41.00
Chi-Chi, Taiwan-02	ILA063	2296	RV	5.90	80.0	997	Component1	0.01	0.71	0.13	0.34	40.00
Chi-Chi, Taiwan-02	ILA063	2296	RV	5.90	80.0	997	Component2	0.01	0.90	0.26	0.38	40.00
Chi-Chi, Taiwan-02	TAP077	2336	RV	5.90	140.0	1023	Component1	0.01	1.28	0.29	0.81	42.00
Chi-Chi, Taiwan-02	TAP077	2336	RV	5.90	140.0	1023	Component2	0.01	0.87	0.24	0.83	42.00
Chi-Chi, Taiwan-02	TCU076	2389	RV	5.90	29.2	615	Component1	0.07	5.21	0.70	0.45	44.99
Chi-Chi, Taiwan-02	TCU076	2389	RV	5.90	29.2	615	Component2	0.04	3.17	0.39	0.45	44.99
Chi-Chi, Taiwan-02	TCU085	2396	RV	5.90	78.0	1000	Component1	0.01	0.67	0.15	0.58	34.99
Chi-Chi, Taiwan-02	TCU085	2396	RV	5.90	78.0	1000	Component2	0.01	0.40	0.07	0.61	34.99
Chi-Chi, Taiwan-02	TCU129	2423	RV	5.90	28.3	664	Component1	0.09	3.88	0.32	0.22	47.01
Chi-Chi, Taiwan-02	TCU129	2423	RV	5.90	28.3	664	Component2	0.03	2.75	0.32	0.48	47.01
Chi-Chi, Taiwan-02	TCU138	2427	RV	5.90	37.0	653	Component1	0.04	3.76	0.66	0.57	47.00
Chi-Chi, Taiwan-02	TCU138	2427	RV	5.90	37.0	653	Component2	0.04	2.82	0.38	0.43	47.00
Chi-Chi, Taiwan-02	TTN024	2438	RV	5.90	99.0	645	Component1	0.00	0.34	0.08	0.41	43.00
Chi-Chi, Taiwan-02	TTN024	2438	RV	5.90	99.0	645	Component2	0.00	0.26	0.05	0.36	43.00
Chi-Chi, Taiwan-02	TTN042	2447	RV	5.90	99.0	845	Component1	0.01	0.60	0.08	0.35	39.00
Chi-Chi, Taiwan-02	TTN042	2447	RV	5.90	99.0	845	Component2	0.01	0.44	0.05	0.37	39.00
Chi-Chi, Taiwan-03	CHY062	2483	RV	6.20	79.0	603	Component1	0.02	2.20	0.59	0.69	49.96

Continued on next page

Table A.1: PEER ground motion metadata (continued)

Earthquake (Year)	Station	NGA Number	Fault Type	M_w	Distance (km)	$V_{s,30}$ (m/s)	Component	PGA (g)	PGV (cm/s)	PGD (cm)	T_m (s)	Duration (s)
Chi-Chi, Taiwan-03	CHY062	2483	RV	6.20	79.0	603	Component2	0.01	1.89	0.87	1.20	49.96
Chi-Chi, Taiwan-03	HWA024	2528	RV	6.20	62.0	630	Component1	0.01	0.57	0.06	0.50	31.00
Chi-Chi, Taiwan-03	HWA024	2528	RV	6.20	62.0	630	Component2	0.00	0.41	0.08	0.48	31.00
Chi-Chi, Taiwan-03	HWA029	2532	RV	6.20	70.0	614	Component1	0.00	0.51	0.10	0.57	34.00
Chi-Chi, Taiwan-03	HWA029	2532	RV	6.20	70.0	614	Component2	0.00	0.23	0.04	0.36	34.00
Chi-Chi, Taiwan-03	HWA038	2541	RV	6.20	57.0	643	Component1	0.01	0.57	0.11	0.56	43.95
Chi-Chi, Taiwan-03	HWA038	2541	RV	6.20	57.0	643	Component2	0.01	0.54	0.10	0.49	43.95
Chi-Chi, Taiwan-03	HWA046	2547	RV	6.20	82.0	618	Component1	0.01	0.44	0.06	0.43	35.93
Chi-Chi, Taiwan-03	HWA046	2547	RV	6.20	82.0	618	Component2	0.01	0.38	0.05	0.40	35.93
Chi-Chi, Taiwan-03	HWA057	2553	RV	6.20	81.0	679	Component1	0.01	0.23	0.03	0.28	40.99
Chi-Chi, Taiwan-03	HWA057	2553	RV	6.20	81.0	679	Component2	0.00	0.13	0.01	0.26	40.99
Chi-Chi, Taiwan-03	TCU076	2627	RV	6.20	14.7	615	Component1	0.52	59.31	9.62	0.71	96.00
Chi-Chi, Taiwan-03	TCU076	2627	RV	6.20	14.7	615	Component2	0.25	26.41	5.12	0.77	96.00
Chi-Chi, Taiwan-03	TCU085	2633	RV	6.20	104.0	1000	Component1	0.01	0.33	0.06	0.49	37.00
Chi-Chi, Taiwan-03	TCU085	2633	RV	6.20	104.0	1000	Component2	0.00	0.22	0.04	0.56	37.00
Chi-Chi, Taiwan-03	TCU129	2658	RV	6.20	12.8	664	Component1	0.95	39.68	7.81	0.39	104.03
Chi-Chi, Taiwan-03	TCU129	2658	RV	6.20	12.8	664	Component2	0.19	24.32	4.85	0.86	104.03
Chi-Chi, Taiwan-03	TCU138	2661	RV	6.20	22.2	653	Component1	0.13	12.89	3.43	0.74	35.00
Chi-Chi, Taiwan-03	TCU138	2661	RV	6.20	22.2	653	Component2	0.13	19.72	4.34	0.86	35.00
Chi-Chi, Taiwan-03	TTN024	2676	RV	6.20	91.0	645	Component1	0.01	0.40	0.05	0.35	35.00
Chi-Chi, Taiwan-03	TTN024	2676	RV	6.20	91.0	645	Component2	0.00	0.30	0.05	0.34	35.00
Chi-Chi, Taiwan-03	TTN042	2687	RV	6.20	94.0	845	Component1	0.01	0.58	0.09	0.33	41.98
Chi-Chi, Taiwan-03	TTN042	2687	RV	6.20	94.0	845	Component2	0.01	0.70	0.21	0.42	41.98
Chi-Chi, Taiwan-04	CHY062	2726	SS	6.20	61.0	603	Component1	0.04	1.79	0.36	0.39	52.00
Chi-Chi, Taiwan-04	CHY062	2726	SS	6.20	61.0	603	Component2	0.01	1.14	0.50	0.74	52.00
Chi-Chi, Taiwan-04	HWA024	2772	SS	6.20	46.0	630	Component1	0.01	0.60	0.10	0.32	43.95
Chi-Chi, Taiwan-04	HWA024	2772	SS	6.20	46.0	630	Component2	0.01	0.44	0.12	0.30	43.95
Chi-Chi, Taiwan-04	HWA029	2777	SS	6.20	85.0	614	Component1	0.01	0.60	0.12	0.52	40.00
Chi-Chi, Taiwan-04	HWA029	2777	SS	6.20	85.0	614	Component2	0.00	0.40	0.15	0.42	40.00
Chi-Chi, Taiwan-04	HWA038	2786	SS	6.20	48.0	643	Component1	0.02	0.92	0.20	0.44	48.00
Chi-Chi, Taiwan-04	HWA038	2786	SS	6.20	48.0	643	Component2	0.01	1.06	0.19	0.41	48.00
Chi-Chi, Taiwan-04	HWA046	2792	SS	6.20	101.0	618	Component1	0.01	0.54	0.05	0.39	38.00
Chi-Chi, Taiwan-04	HWA046	2792	SS	6.20	101.0	618	Component2	0.01	0.36	0.04	0.36	38.00
Chi-Chi, Taiwan-04	HWA057	2799	SS	6.20	101.0	679	Component1	0.00	0.22	0.03	0.25	45.00
Chi-Chi, Taiwan-04	HWA057	2799	SS	6.20	101.0	679	Component2	0.00	0.19	0.03	0.29	45.00
Chi-Chi, Taiwan-04	KAU003	2805	SS	6.20	116.0	914	Component1	0.01	0.83	0.17	0.82	65.00

Continued on next page

Table A.1: PEER ground motion metadata (continued)

Earthquake (Year)	Station	NGA Number	Fault Type	M_w	Distance (km)	$V_{s,30}$ (m/s)	Component	PGA (g)	PGV (cm/s)	PGD (cm)	T_m (s)	Duration (s)
Chi-Chi, Taiwan-04	KAU003	2805	SS	6.20	116.0	914	Component2	0.01	0.80	0.21	0.71	65.00
Chi-Chi, Taiwan-04	TCU138	2897	SS	6.20	34.0	653	Component1	0.04	10.66	6.25	1.03	58.00
Chi-Chi, Taiwan-04	TCU138	2897	SS	6.20	34.0	653	Component2	0.05	6.94	2.98	0.94	58.00
Chi-Chi, Taiwan-04	TTN024	2918	SS	6.20	63.0	645	Component1	0.02	1.37	0.17	0.33	46.00
Chi-Chi, Taiwan-04	TTN024	2918	SS	6.20	63.0	645	Component2	0.01	0.92	0.15	0.36	46.00
Chi-Chi, Taiwan-04	TTN042	2929	SS	6.20	69.0	845	Component1	0.02	1.49	0.28	0.32	45.00
Chi-Chi, Taiwan-04	TTN042	2929	SS	6.20	69.0	845	Component2	0.03	1.63	0.20	0.38	45.00
Chi-Chi, Taiwan-05	CHY062	2966	RV	6.20	95.0	603	Component1	0.03	4.05	0.85	0.42	58.99
Chi-Chi, Taiwan-05	CHY062	2966	RV	6.20	95.0	603	Component2	0.02	1.82	0.64	0.60	58.99
Chi-Chi, Taiwan-05	HWA003	2996	RV	6.20	50.0	1526	Component1	0.03	1.51	0.24	0.30	28.00
Chi-Chi, Taiwan-05	HWA003	2996	RV	6.20	50.0	1526	Component2	0.02	3.46	1.21	0.63	28.00
Chi-Chi, Taiwan-05	HWA024	3011	RV	6.20	49.0	630	Component1	0.03	3.36	0.63	0.58	50.00
Chi-Chi, Taiwan-05	HWA024	3011	RV	6.20	49.0	630	Component2	0.03	2.44	0.40	0.43	50.00
Chi-Chi, Taiwan-05	HWA029	3016	RV	6.20	52.0	614	Component1	0.03	2.85	0.35	0.52	52.99
Chi-Chi, Taiwan-05	HWA029	3016	RV	6.20	52.0	614	Component2	0.03	1.22	0.23	0.34	52.99
Chi-Chi, Taiwan-05	HWA038	3025	RV	6.20	41.0	643	Component1	0.04	4.27	0.79	0.58	56.99
Chi-Chi, Taiwan-05	HWA038	3025	RV	6.20	41.0	643	Component2	0.04	3.48	0.58	0.36	56.99
Chi-Chi, Taiwan-05	HWA046	3031	RV	6.20	64.0	618	Component1	0.03	1.52	0.21	0.34	48.00
Chi-Chi, Taiwan-05	HWA046	3031	RV	6.20	64.0	618	Component2	0.03	2.00	0.18	0.33	48.00
Chi-Chi, Taiwan-05	HWA057	3037	RV	6.20	63.0	679	Component1	0.03	1.36	0.11	0.22	57.99
Chi-Chi, Taiwan-05	HWA057	3037	RV	6.20	63.0	679	Component2	0.02	1.25	0.14	0.24	57.99
Chi-Chi, Taiwan-05	ILA031	3058	RV	6.20	111.0	649	Component1	0.03	1.41	0.12	0.29	51.99
Chi-Chi, Taiwan-05	ILA031	3058	RV	6.20	111.0	649	Component2	0.01	0.68	0.14	0.26	51.99
Chi-Chi, Taiwan-05	TAP077	3139	RV	6.20	152.0	1023	Component1	0.01	1.36	0.42	0.86	44.00
Chi-Chi, Taiwan-05	TAP077	3139	RV	6.20	152.0	1023	Component2	0.01	0.94	0.27	0.65	44.00
Chi-Chi, Taiwan-05	TCU044	3171	RV	6.20	65.0	668	Component1	0.05	3.15	0.69	0.33	56.99
Chi-Chi, Taiwan-05	TCU044	3171	RV	6.20	65.0	668	Component2	0.04	2.03	0.70	0.24	56.99
Chi-Chi, Taiwan-05	TCU085	3194	RV	6.20	92.0	1000	Component1	0.02	0.86	0.16	0.40	48.98
Chi-Chi, Taiwan-05	TCU085	3194	RV	6.20	92.0	1000	Component2	0.01	0.47	0.08	0.42	48.98
Chi-Chi, Taiwan-05	TCU129	3217	RV	6.20	39.0	664	Component1	0.53	12.99	1.15	0.20	75.00
Chi-Chi, Taiwan-05	TCU129	3217	RV	6.20	39.0	664	Component2	0.07	3.50	0.37	0.19	75.00
Chi-Chi, Taiwan-05	TCU138	3220	RV	6.20	48.0	653	Component1	0.15	6.00	0.76	0.20	62.00
Chi-Chi, Taiwan-05	TCU138	3220	RV	6.20	48.0	653	Component2	0.22	7.43	1.31	0.21	62.00
Chi-Chi, Taiwan-05	TTN042	3251	RV	6.20	85.0	845	Component1	0.06	2.71	0.70	0.34	57.00
Chi-Chi, Taiwan-05	TTN042	3251	RV	6.20	85.0	845	Component2	0.04	3.11	0.46	0.40	57.00
Chi-Chi, Taiwan-06	CHY062	3292	RV	6.30	83.0	603	Component1	0.05	3.65	0.55	0.56	50.99

Continued on next page

Table A.1: PEER ground motion metadata (continued)

Earthquake (Year)	Station	NGA Number	Fault Type	M_w	Distance (km)	$V_{s,30}$ (m/s)	Component	PGA (g)	PGV (cm/s)	PGD (cm)	T_m (s)	Duration (s)
Chi-Chi, Taiwan-06	CHY062	3292	RV	6.30	83.0	603	Component2	0.01	2.48	0.61	0.95	50.99
Chi-Chi, Taiwan-06	HWA003	3325	RV	6.30	56.0	1526	Component1	0.04	8.09	2.16	1.25	31.00
Chi-Chi, Taiwan-06	HWA003	3325	RV	6.30	56.0	1526	Component2	0.03	4.82	1.45	1.07	31.00
Chi-Chi, Taiwan-06	HWA024	3337	RV	6.30	52.0	630	Component1	0.02	3.60	1.06	0.94	44.95
Chi-Chi, Taiwan-06	HWA024	3337	RV	6.30	52.0	630	Component2	0.01	1.80	0.35	0.64	44.95
Chi-Chi, Taiwan-06	HWA029	3342	RV	6.30	53.0	614	Component1	0.04	3.88	0.75	0.77	51.99
Chi-Chi, Taiwan-06	HWA029	3342	RV	6.30	53.0	614	Component2	0.01	1.70	0.47	0.65	51.99
Chi-Chi, Taiwan-06	HWA038	3350	RV	6.30	46.0	643	Component1	0.03	4.22	1.15	1.12	54.98
Chi-Chi, Taiwan-06	HWA038	3350	RV	6.30	46.0	643	Component2	0.02	3.70	1.10	0.86	54.98
Chi-Chi, Taiwan-06	HWA046	3355	RV	6.30	60.0	618	Component1	0.03	2.31	0.31	0.50	49.00
Chi-Chi, Taiwan-06	HWA046	3355	RV	6.30	60.0	618	Component2	0.03	2.58	0.36	0.44	49.00
Chi-Chi, Taiwan-06	HWA057	3360	RV	6.30	60.0	679	Component1	0.03	1.48	0.29	0.34	49.99
Chi-Chi, Taiwan-06	HWA057	3360	RV	6.30	60.0	679	Component2	0.02	0.89	0.21	0.38	49.99
Chi-Chi, Taiwan-06	ILA063	3390	RV	6.30	84.0	997	Component1	0.01	0.97	0.16	0.36	48.00
Chi-Chi, Taiwan-06	ILA063	3390	RV	6.30	84.0	997	Component2	0.01	0.69	0.18	0.43	48.00
Chi-Chi, Taiwan-06	TCU044	3453	RV	6.30	48.0	668	Component1	0.03	3.40	0.87	0.57	48.99
Chi-Chi, Taiwan-06	TCU044	3453	RV	6.30	48.0	668	Component2	0.02	2.55	0.78	0.63	48.99
Chi-Chi, Taiwan-06	TCU076	3472	RV	6.30	25.9	615	Component1	0.12	11.37	4.94	0.50	57.00
Chi-Chi, Taiwan-06	TCU076	3472	RV	6.30	25.9	615	Component2	0.26	7.69	2.73	0.37	57.00
Chi-Chi, Taiwan-06	TCU085	3479	RV	6.30	83.0	1000	Component1	0.01	0.60	0.13	0.54	43.99
Chi-Chi, Taiwan-06	TCU085	3479	RV	6.30	83.0	1000	Component2	0.00	0.40	0.15	0.53	43.99
Chi-Chi, Taiwan-06	TCU129	3507	RV	6.30	24.8	664	Component1	0.33	16.76	5.49	0.33	71.02
Chi-Chi, Taiwan-06	TCU129	3507	RV	6.30	24.8	664	Component2	0.10	9.64	2.32	0.57	71.02
Chi-Chi, Taiwan-06	TCU138	3509	RV	6.30	34.0	653	Component1	0.06	7.86	2.68	0.75	71.00
Chi-Chi, Taiwan-06	TCU138	3509	RV	6.30	34.0	653	Component2	0.07	8.44	4.07	0.81	71.00
Chi-Chi, Taiwan-06	TTN024	3531	RV	6.30	87.0	645	Component1	0.02	1.14	0.29	0.49	46.99
Chi-Chi, Taiwan-06	TTN024	3531	RV	6.30	87.0	645	Component2	0.01	1.28	0.28	0.57	46.99
Chi-Chi, Taiwan-06	TTN042	3542	RV	6.30	86.0	845	Component1	0.03	2.65	0.74	0.57	61.00
Chi-Chi, Taiwan-06	TTN042	3542	RV	6.30	86.0	845	Component2	0.03	2.36	0.45	0.62	61.00
Coalinga-01	Slack Canyon	369	RV	6.36	27.5	685	Component1	0.17	16.10	4.16	0.74	30.00
Coalinga-01	Slack Canyon	369	RV	6.36	27.5	685	Component2	0.15	13.29	2.70	0.84	30.00
Coalinga-01	Slack Canyon	369	RV	6.36	27.5	685	Vertical	-	-	-	-	30.00
Coalinga-02	Sulphur Baths (temp)	387	RV	5.09	19.9	617	Component1	0.01	0.49	0.04	0.41	39.99
Coalinga-02	Sulphur Baths (temp)	387	RV	5.09	19.9	617	Component2	0.00	0.32	0.03	0.40	39.99
Coalinga-02	Sulphur Baths (temp)	387	RV	5.09	19.9	617	Vertical	-	-	-	-	39.99
Coalinga-03	Sulphur Baths (temp)	393	RV	5.38	13.3	617	Component1	0.04	5.13	2.29	0.93	40.00

Continued on next page

Table A.1: PEER ground motion metadata (continued)

Earthquake (Year)	Station	NGA Number	Fault Type	M_w	Distance (km)	$V_{s,30}$ (m/s)	Component	PGA (g)	PGV (cm/s)	PGD (cm)	T_m (s)	Duration (s)
Coalinga-03	Sulphur Baths (temp)	393	RV	5.38	13.3	617	Component2	0.04	4.48	1.64	0.79	40.00
Coalinga-03	Sulphur Baths (temp)	393	RV	5.38	13.3	617	Vertical	-	-	-	-	40.00
Coalinga-04	Sulphur Baths (temp)	403	RV	5.18	15.4	617	Component1	0.06	2.17	0.21	0.24	40.00
Coalinga-04	Sulphur Baths (temp)	403	RV	5.18	15.4	617	Component2	0.07	1.45	0.15	0.22	40.00
Coalinga-04	Sulphur Baths (temp)	403	RV	5.18	15.4	617	Vertical	-	-	-	-	40.00
Coalinga-05	Sulphur Baths (temp)	414	RV	5.77	11.4	617	Component1	0.14	5.47	0.79	0.29	40.00
Coalinga-05	Sulphur Baths (temp)	414	RV	5.77	11.4	617	Component2	0.13	6.25	0.66	0.30	40.00
Coalinga-05	Sulphur Baths (temp)	414	RV	5.77	11.4	617	Vertical	-	-	-	-	40.00
Coalinga-06	Sulphur Baths (temp)	417	RV	4.89	11.8	617	Component1	0.04	1.56	0.21	0.27	40.00
Coalinga-06	Sulphur Baths (temp)	417	RV	4.89	11.8	617	Component2	0.03	0.96	0.16	0.27	40.00
Coalinga-06	Sulphur Baths (temp)	417	RV	4.89	11.8	617	Vertical	-	-	-	-	40.00
Coalinga-07	Sulphur Baths (temp)	419	RV	5.21	12.1	617	Component1	0.15	8.49	1.27	0.39	40.00
Coalinga-07	Sulphur Baths (temp)	419	RV	5.21	12.1	617	Component2	0.23	10.90	0.76	0.29	40.00
Coalinga-07	Sulphur Baths (temp)	419	RV	5.21	12.1	617	Vertical	-	-	-	-	40.00
Coalinga-08	Sulphur Baths (temp)	424	SS	5.23	18.3	617	Component1	0.01	0.64	0.06	0.31	40.00
Coalinga-08	Sulphur Baths (temp)	424	SS	5.23	18.3	617	Component2	0.02	0.63	0.06	0.29	40.00
Coalinga-08	Sulphur Baths (temp)	424	SS	5.23	18.3	617	Vertical	-	-	-	-	40.00
Coyote Lake	Gilroy Array #1	146	SS	5.74	10.7	1428	Component1	0.10	3.37	0.48	0.19	26.83
Coyote Lake	Gilroy Array #1	146	SS	5.74	10.7	1428	Component2	0.13	8.25	1.52	0.30	26.83
Coyote Lake	Gilroy Array #1	146	SS	5.74	10.7	1428	Vertical	-	-	-	-	26.83
Coyote Lake	Gilroy Array #6	150	SS	5.74	3.1	663	Component1	0.43	49.23	7.67	0.67	27.09
Coyote Lake	Gilroy Array #6	150	SS	5.74	3.1	663	Component2	0.32	24.48	3.84	0.40	27.09
Coyote Lake	Gilroy Array #6	150	SS	5.74	3.1	663	Vertical	-	-	-	-	27.09
Denali, Alaska	Carlo (temp)	2107	SS	7.90	51.0	964	Component1	0.10	7.56	3.88	0.32	86.00
Denali, Alaska	Carlo (temp)	2107	SS	7.90	51.0	964	Vertical	-	-	-	-	86.00
Denali, Alaska	R109 (temp)	2111	SS	7.90	43.0	964	Component1	0.06	6.15	3.51	0.51	73.04
Denali, Alaska	R109 (temp)	2111	SS	7.90	43.0	964	Vertical	-	-	-	-	73.04
Duzce, Turkey	Lamont 1060	1613	SS	7.14	25.9	782	Component1	0.05	5.31	5.98	0.41	43.99
Duzce, Turkey	Lamont 1060	1613	SS	7.14	25.9	782	Component2	0.09	7.53	6.52	0.29	42.33
Gilroy	Gilroy Array #6	2021	SS	4.90	14.5	663	Component1	0.10	3.16	0.16	0.18	45.00
Gilroy	Gilroy Array #6	2021	SS	4.90	14.5	663	Component2	0.10	2.30	0.14	0.20	45.00
Gilroy	Gilroy Array #6	2021	SS	4.90	14.5	663	Vertical	-	-	-	-	45.00
Gilroy	Golden Gate Bridge	2022	SS	4.90	120.0	642	Component1	0.01	0.71	0.09	0.43	45.00
Gilroy	Golden Gate Bridge	2022	SS	4.90	120.0	642	Component2	0.01	0.52	0.07	0.41	45.00
Gilroy	Golden Gate Bridge	2022	SS	4.90	120.0	642	Vertical	-	-	-	-	45.00
Hector Mine	Anza - Tripp Flats Training	1764	SS	7.13	102.0	685	Component1	0.03	4.34	4.69	0.59	72.00

Continued on next page

Table A.1: PEER ground motion metadata (continued)

Earthquake (Year)	Station	NGA Number	Fault Type	M_w	Distance (km)	$V_{s,30}$ (m/s)	Component	PGA (g)	PGV (cm/s)	PGD (cm)	T_m (s)	Duration (s)
Hector Mine	Banning - Twin Pines Road	1767	SS	7.13	83.0	685	Component1	0.02	4.65	5.26	0.62	67.84
Hector Mine	Banning - Twin Pines Road	1767	SS	7.13	83.0	685	Component2	0.02	4.02	5.16	0.68	67.84
Hector Mine	Banning - Twin Pines Road	1767	SS	7.13	83.0	685	Vertical	-	-	-	-	67.84
Hector Mine	Heart Bar State Park	1786	SS	7.13	61.0	685	Component1	0.08	11.56	9.85	0.39	60.00
Hector Mine	Heart Bar State Park	1786	SS	7.13	61.0	685	Component2	0.08	8.42	8.57	0.28	60.00
Hector Mine	Heart Bar State Park	1786	SS	7.13	61.0	685	Vertical	-	-	-	-	60.00
Hector Mine	Hector	1787	SS	7.13	11.7	685	Component1	0.27	28.56	22.52	0.61	45.31
Hector Mine	Hector	1787	SS	7.13	11.7	685	Component2	0.15	12.01	6.92	0.39	45.31
Hector Mine	Joshua Tree N.M. - Keys View	1795	SS	7.13	50.0	685	Component1	0.08	7.68	7.61	0.44	71.68
Hector Mine	Joshua Tree N.M. - Keys View	1795	SS	7.13	50.0	685	Component2	0.09	6.86	2.56	0.34	71.68
Hector Mine	Joshua Tree N.M. - Keys View	1795	SS	7.13	50.0	685	Vertical	-	-	-	-	71.68
Hector Mine	San Bernardino - Del Rosa Wk Sta	1824	SS	7.13	97.0	685	Component1	0.02	10.74	10.21	0.98	20.00
Hector Mine	Twentynine Palms	1836	SS	7.13	42.0	685	Component1	0.07	6.99	7.70	0.35	60.00
Hector Mine	Twentynine Palms	1836	SS	7.13	42.0	685	Component2	0.07	4.57	6.21	0.26	60.00
Hector Mine	Twentynine Palms	1836	SS	7.13	42.0	685	Vertical	-	-	-	-	60.00
Hollister-04	SAGO South - Surface	501	SS	5.45	12.2	685	Component1	0.04	5.33	1.27	0.79	40.00
Hollister-04	SAGO South - Surface	501	SS	5.45	12.2	685	Component2	0.09	9.27	1.70	0.76	40.00
Hollister-04	SAGO South - Surface	501	SS	5.45	12.2	685	Vertical	-	-	-	-	40.00
Irpinia, Italy-01	Arienzo	283	N	6.90	53.0	1000	Component1	0.03	2.86	0.77	0.51	24.66
Irpinia, Italy-01	Arienzo	283	N	6.90	53.0	1000	Component2	0.04	2.36	0.48	0.41	24.66
Irpinia, Italy-01	Arienzo	283	N	6.90	53.0	1000	Vertical	-	-	-	-	24.66
Irpinia, Italy-01	Auletta	284	N	6.90	9.6	1000	Component1	0.06	5.16	3.19	0.46	34.29
Irpinia, Italy-01	Auletta	284	N	6.90	9.6	1000	Component2	0.06	6.11	3.68	0.49	34.29
Irpinia, Italy-01	Auletta	284	N	6.90	9.6	1000	Vertical	-	-	-	-	34.29
Irpinia, Italy-01	Bagnoli Irpinio	285	N	6.90	8.2	1000	Component1	0.14	22.07	9.26	0.67	36.86
Irpinia, Italy-01	Bagnoli Irpinio	285	N	6.90	8.2	1000	Component2	0.20	31.87	9.59	0.97	36.86
Irpinia, Italy-01	Bagnoli Irpinio	285	N	6.90	8.2	1000	Vertical	-	-	-	-	36.86
Irpinia, Italy-01	Bisaccia	286	N	6.90	21.3	1000	Component1	0.10	23.48	14.75	1.17	38.26
Irpinia, Italy-01	Bisaccia	286	N	6.90	21.3	1000	Component2	0.08	12.49	2.93	1.04	38.26
Irpinia, Italy-01	Bisaccia	286	N	6.90	21.3	1000	Vertical	-	-	-	-	38.26
Irpinia, Italy-01	Calitri	289	N	6.90	17.6	600	Component1	0.13	16.45	4.72	0.77	35.21
Irpinia, Italy-01	Calitri	289	N	6.90	17.6	600	Component2	0.18	18.37	4.89	0.76	35.21
Irpinia, Italy-01	Calitri	289	N	6.90	17.6	600	Vertical	-	-	-	-	35.21
Irpinia, Italy-01	Sturno	292	N	6.90	10.8	1000	Component1	0.25	36.40	11.38	0.68	39.34
Irpinia, Italy-01	Sturno	292	N	6.90	10.8	1000	Component2	0.36	51.84	32.03	0.87	39.34
Irpinia, Italy-01	Sturno	292	N	6.90	10.8	1000	Vertical	-	-	-	-	39.34

Continued on next page

Table A.1: PEER ground motion metadata (continued)

Earthquake (Year)	Station	NGA Number	Fault Type	M_w	Distance (km)	$V_{s,30}$ (m/s)	Component	PGA (g)	PGV (cm/s)	PGD (cm)	T_m (s)	Duration (s)
Irpinia, Italy-02	Auletta	295	N	6.20	29.9	1000	Component1	0.02	2.37	0.72	0.79	31.97
Irpinia, Italy-02	Auletta	295	N	6.20	29.9	1000	Component2	0.02	2.32	0.84	0.66	31.97
Irpinia, Italy-02	Auletta	295	N	6.20	29.9	1000	Vertical	-	-	-	-	31.97
Irpinia, Italy-02	Bagnoli Irpinio	296	N	6.20	19.6	1000	Component1	0.05	4.52	0.52	0.54	42.03
Irpinia, Italy-02	Bagnoli Irpinio	296	N	6.20	19.6	1000	Component2	0.06	3.51	0.68	0.67	42.02
Irpinia, Italy-02	Bagnoli Irpinio	296	N	6.20	19.6	1000	Vertical	-	-	-	-	42.02
Irpinia, Italy-02	Bisaccia	297	N	6.20	14.7	1000	Component1	0.08	10.44	4.61	1.05	37.69
Irpinia, Italy-02	Bisaccia	297	N	6.20	14.7	1000	Component2	0.07	14.39	5.43	1.23	37.69
Irpinia, Italy-02	Bisaccia	297	N	6.20	14.7	1000	Vertical	-	-	-	-	37.69
Irpinia, Italy-02	Calitri	300	N	6.20	8.8	600	Component1	0.18	23.19	6.73	0.92	49.50
Irpinia, Italy-02	Calitri	300	N	6.20	8.8	600	Component2	0.16	25.64	6.62	0.84	49.50
Irpinia, Italy-02	Calitri	300	N	6.20	8.8	600	Vertical	-	-	-	-	49.50
Irpinia, Italy-02	Sturno	303	N	6.20	20.4	1000	Component1	0.07	3.40	0.93	0.36	30.26
Irpinia, Italy-02	Sturno	303	N	6.20	20.4	1000	Component2	0.08	4.45	0.74	0.43	30.26
Irpinia, Italy-02	Sturno	303	N	6.20	20.4	1000	Vertical	-	-	-	-	30.26
Kobe, Japan	MZH	1109	SS	6.90	70.0	609	Component1	0.07	4.35	1.54	0.50	78.00
Kobe, Japan	MZH	1109	SS	6.90	70.0	609	Component2	0.05	4.74	1.87	0.55	78.00
Kobe, Japan	MZH	1109	SS	6.90	70.0	609	Vertical	-	-	-	-	78.00
Kobe, Japan	Nishi-Akashi	1111	SS	6.90	7.1	609	Component1	0.51	37.29	9.53	0.49	40.96
Kobe, Japan	Nishi-Akashi	1111	SS	6.90	7.1	609	Component2	0.50	36.62	11.27	0.53	40.96
Kobe, Japan	Nishi-Akashi	1111	SS	6.90	7.1	609	Vertical	-	-	-	-	40.96
Kobe, Japan	OKA	1112	SS	6.90	87.0	609	Component1	0.08	4.84	2.12	0.38	78.00
Kobe, Japan	OKA	1112	SS	6.90	87.0	609	Component2	0.06	3.20	1.62	0.35	78.00
Kobe, Japan	OKA	1112	SS	6.90	87.0	609	Vertical	-	-	-	-	78.00
Kobe, Japan	TOT	1117	SS	6.90	120.0	609	Component1	0.08	10.90	3.71	0.71	78.00
Kobe, Japan	TOT	1117	SS	6.90	120.0	609	Component2	0.08	7.58	4.58	0.66	78.00
Kobe, Japan	TOT	1117	SS	6.90	120.0	609	Vertical	-	-	-	-	78.00
Kocaeli, Turkey	Izmit	1165	SS	7.51	7.2	811	Component1	0.22	29.78	17.13	0.58	30.00
Kocaeli, Turkey	Izmit	1165	SS	7.51	7.2	811	Component2	0.15	22.60	9.82	0.63	30.00
Kocaeli, Turkey	Izmit	1165	SS	7.51	7.2	811	Vertical	-	-	-	-	30.00
Landers	Lucerne	879	SS	7.28	2.2	685	Component1	0.73	146.54	262.73	0.30	48.12
Landers	Lucerne	879	SS	7.28	2.2	685	Component2	0.79	32.41	69.78	0.16	48.12
Landers	Lucerne	879	SS	7.28	2.2	685	Vertical	-	-	-	-	48.12
Landers	Silent Valley - Poppet Flat	891	SS	7.28	51.0	685	Component1	0.05	3.78	4.07	0.26	55.00
Landers	Silent Valley - Poppet Flat	891	SS	7.28	51.0	685	Component2	0.04	4.96	7.82	0.34	55.00
Landers	Silent Valley - Poppet Flat	891	SS	7.28	51.0	685	Vertical	-	-	-	-	55.00

Continued on next page

Table A.1: PEER ground motion metadata (continued)

Earthquake (Year)	Station	NGA Number	Fault Type	M_w	Distance (km)	$V_{s,30}$ (m/s)	Component	PGA (g)	PGV (cm/s)	PGD (cm)	T_m (s)	Duration (s)
Landers	Twentynine Palms	897	SS	7.28	41.0	685	Component1	0.08	3.59	3.35	0.22	50.00
Landers	Twentynine Palms	897	SS	7.28	41.0	685	Component2	0.06	4.91	5.72	0.23	50.00
Landers	Twentynine Palms	897	SS	7.28	41.0	685	Vertical	-	-	-	-	50.00
Loma Prieta	Gilroy Array #1	765	RV-OBL	6.93	9.6	1428	Component1	0.41	31.58	6.31	0.29	39.95
Loma Prieta	Gilroy Array #1	765	RV-OBL	6.93	9.6	1428	Component2	0.47	33.87	8.03	0.39	39.95
Loma Prieta	Gilroy Array #1	765	RV-OBL	6.93	9.6	1428	Vertical	-	-	-	-	39.95
Loma Prieta	Gilroy Array #6	769	RV-OBL	6.93	18.3	663	Component1	0.13	12.75	4.78	0.54	39.95
Loma Prieta	Gilroy Array #6	769	RV-OBL	6.93	18.3	663	Component2	0.17	14.16	3.75	0.46	39.95
Loma Prieta	Gilroy Array #6	769	RV-OBL	6.93	18.3	663	Vertical	-	-	-	-	39.95
Loma Prieta	Golden Gate Bridge	771	RV-OBL	6.93	80.0	642	Component1	0.23	38.05	11.45	0.96	38.08
Loma Prieta	Golden Gate Bridge	771	RV-OBL	6.93	80.0	642	Component2	0.12	17.84	2.90	0.74	38.08
Loma Prieta	Golden Gate Bridge	771	RV-OBL	6.93	80.0	642	Vertical	-	-	-	-	38.08
Loma Prieta	Monterey City Hall	782	RV-OBL	6.93	44.0	685	Component1	0.07	3.49	1.40	0.32	39.95
Loma Prieta	Monterey City Hall	782	RV-OBL	6.93	44.0	685	Component2	0.06	5.81	2.91	0.38	39.95
Loma Prieta	Monterey City Hall	782	RV-OBL	6.93	44.0	685	Vertical	-	-	-	-	39.95
Loma Prieta	Piedmont Jr High	788	RV-OBL	6.93	73.0	895	Component1	0.08	8.18	2.90	0.67	39.95
Loma Prieta	Piedmont Jr High	788	RV-OBL	6.93	73.0	895	Component2	0.07	9.14	3.31	0.63	39.95
Loma Prieta	Piedmont Jr High	788	RV-OBL	6.93	73.0	895	Vertical	-	-	-	-	39.95
Loma Prieta	Point Bonita	789	RV-OBL	6.93	83.0	1316	Component1	0.07	11.41	3.97	0.88	39.95
Loma Prieta	Point Bonita	789	RV-OBL	6.93	83.0	1316	Component2	0.07	12.87	3.96	1.09	39.95
Loma Prieta	Point Bonita	789	RV-OBL	6.93	83.0	1316	Vertical	-	-	-	-	39.95
Loma Prieta	SAGO South - Surface	791	RV-OBL	6.93	34.0	685	Component1	0.07	10.46	6.44	0.84	39.95
Loma Prieta	SAGO South - Surface	791	RV-OBL	6.93	34.0	685	Component2	0.07	9.64	6.42	0.93	39.95
Loma Prieta	SAGO South - Surface	791	RV-OBL	6.93	34.0	685	Vertical	-	-	-	-	39.95
Loma Prieta	SF - Pacific Heights	795	RV-OBL	6.93	76.0	1250	Component1	0.06	12.84	3.45	1.04	28.00
Loma Prieta	SF - Pacific Heights	795	RV-OBL	6.93	76.0	1250	Component2	0.05	9.21	2.89	0.91	28.00
Loma Prieta	SF - Pacific Heights	795	RV-OBL	6.93	76.0	1250	Vertical	-	-	-	-	28.00
Loma Prieta	SF - Rincon Hill	797	RV-OBL	6.93	74.0	873	Component1	0.08	6.75	2.57	0.68	39.95
Loma Prieta	SF - Rincon Hill	797	RV-OBL	6.93	74.0	873	Component2	0.09	10.43	3.89	0.84	39.95
Loma Prieta	SF - Rincon Hill	797	RV-OBL	6.93	74.0	873	Vertical	-	-	-	-	39.95
Loma Prieta	San Jose - Santa Teresa Hills	801	RV-OBL	6.93	14.7	672	Component1	0.27	26.17	13.21	0.31	50.02
Loma Prieta	San Jose - Santa Teresa Hills	801	RV-OBL	6.93	14.7	672	Component2	0.23	20.87	6.24	0.36	50.02
Loma Prieta	San Jose - Santa Teresa Hills	801	RV-OBL	6.93	14.7	672	Vertical	-	-	-	-	50.02
Loma Prieta	So. San Francisco, Sierra Pt.	804	RV-OBL	6.93	63.0	1021	Component1	0.06	7.11	5.17	0.61	39.99
Loma Prieta	So. San Francisco, Sierra Pt.	804	RV-OBL	6.93	63.0	1021	Component2	0.11	8.75	4.61	0.54	39.99
Loma Prieta	So. San Francisco, Sierra Pt.	804	RV-OBL	6.93	63.0	1021	Vertical	-	-	-	-	39.99

Continued on next page

Table A.1: PEER ground motion metadata (continued)

Earthquake (Year)	Station	NGA Number	Fault Type	M_w	Distance (km)	$V_{s,30}$ (m/s)	Component	PGA (g)	PGV (cm/s)	PGD (cm)	T_m (s)	Duration (s)
Lytle Creek	Cedar Springs, Allen Ranch	43	RV-OBL	5.33	19.2	813	Component1	0.07	1.80	0.11	0.16	38.12
Lytle Creek	Cedar Springs, Allen Ranch	43	RV-OBL	5.33	19.2	813	Component2	0.05	1.20	0.06	0.15	38.12
Lytle Creek	Devil's Canyon	45	RV-OBL	5.33	20.1	685	Component1	0.15	3.33	0.18	0.17	13.61
Lytle Creek	Devil's Canyon	45	RV-OBL	5.33	20.1	685	Component2	0.08	1.73	0.10	0.15	13.61
Lytle Creek	Santa Anita Dam	49	RV-OBL	5.33	43.0	685	Component1	0.04	1.64	0.09	0.18	5.92
Lytle Creek	Santa Anita Dam	49	RV-OBL	5.33	43.0	685	Component2	0.01	0.27	0.01	0.13	5.92
Morgan Hill	Gilroy Array #1	455	SS	6.19	14.9	1428	Component1	0.07	2.85	1.25	0.21	29.98
Morgan Hill	Gilroy Array #1	455	SS	6.19	14.9	1428	Component2	0.10	2.88	1.04	0.24	29.98
Morgan Hill	Gilroy Array #1	455	SS	6.19	14.9	1428	Vertical	-	-	-	-	29.98
Morgan Hill	Gilroy Array #6	459	SS	6.19	9.9	663	Component1	0.22	11.40	2.46	0.33	29.98
Morgan Hill	Gilroy Array #6	459	SS	6.19	9.9	663	Component2	0.29	36.69	6.14	0.63	29.98
Morgan Hill	Gilroy Array #6	459	SS	6.19	9.9	663	Vertical	-	-	-	-	29.98
Morgan Hill	San Justo Dam (L Abut)	471	SS	6.19	32.0	623	Component1	0.08	6.51	2.62	0.47	28.32
Morgan Hill	San Justo Dam (L Abut)	471	SS	6.19	32.0	623	Component2	0.07	5.10	1.85	0.46	28.32
Morgan Hill	San Justo Dam (L Abut)	471	SS	6.19	32.0	623	Vertical	-	-	-	-	28.32
Morgan Hill	San Justo Dam (R Abut)	472	SS	6.19	32.0	623	Component1	0.08	6.98	3.08	0.60	28.32
Morgan Hill	San Justo Dam (R Abut)	472	SS	6.19	32.0	623	Component2	0.06	5.82	2.18	0.55	28.32
Morgan Hill	San Justo Dam (R Abut)	472	SS	6.19	32.0	623	Vertical	-	-	-	-	28.32
N. Palm Springs	Anza - Red Mountain	511	RV-OBL	6.06	38.0	685	Component1	0.10	5.18	0.62	0.22	11.01
N. Palm Springs	Anza - Red Mountain	511	RV-OBL	6.06	38.0	685	Component2	0.13	3.43	0.46	0.21	11.01
N. Palm Springs	Anza - Red Mountain	511	RV-OBL	6.06	38.0	685	Vertical	-	-	-	-	11.01
N. Palm Springs	Anza - Tule Canyon	512	RV-OBL	6.06	52.0	685	Component1	0.11	6.54	0.71	0.45	20.39
N. Palm Springs	Anza - Tule Canyon	512	RV-OBL	6.06	52.0	685	Component2	0.10	7.51	0.71	0.43	20.39
N. Palm Springs	Anza - Tule Canyon	512	RV-OBL	6.06	52.0	685	Vertical	-	-	-	-	20.39
N. Palm Springs	Lake Mathews Dike Toe	525	RV-OBL	6.06	67.0	685	Component1	0.06	1.51	0.08	0.13	20.30
N. Palm Springs	Lake Mathews Dike Toe	525	RV-OBL	6.06	67.0	685	Component2	0.05	0.75	0.03	0.12	20.30
N. Palm Springs	Lake Mathews Dike Toe	525	RV-OBL	6.06	67.0	685	Vertical	-	-	-	-	20.30
N. Palm Springs	Murrieta Hot Springs	528	RV-OBL	6.06	55.0	685	Component1	0.05	1.82	0.30	0.15	24.00
N. Palm Springs	Murrieta Hot Springs	528	RV-OBL	6.06	55.0	685	Component2	0.05	1.23	0.32	0.14	24.00
N. Palm Springs	Murrieta Hot Springs	528	RV-OBL	6.06	55.0	685	Vertical	-	-	-	-	24.00
N. Palm Springs	Santa Rosa Mountain	536	RV-OBL	6.06	39.0	685	Component1	0.11	2.56	0.11	0.15	10.39
N. Palm Springs	Santa Rosa Mountain	536	RV-OBL	6.06	39.0	685	Component2	0.10	2.23	0.10	0.14	10.39
N. Palm Springs	Santa Rosa Mountain	536	RV-OBL	6.06	39.0	685	Vertical	-	-	-	-	10.39
N. Palm Springs	Silent Valley - Poppet Flat	537	RV-OBL	6.06	17.0	685	Component1	0.14	3.94	0.56	0.15	24.00
N. Palm Springs	Silent Valley - Poppet Flat	537	RV-OBL	6.06	17.0	685	Component2	0.11	3.95	0.79	0.18	24.00
N. Palm Springs	Silent Valley - Poppet Flat	537	RV-OBL	6.06	17.0	685	Vertical	-	-	-	-	24.00

Continued on next page

Table A.1: PEER ground motion metadata (continued)

Earthquake (Year)	Station	NGA Number	Fault Type	M_w	Distance (km)	$V_{s,30}$ (m/s)	Component	PGA (g)	PGV (cm/s)	PGD (cm)	T_m (s)	Duration (s)
N. Palm Springs	Winchester Bergman Ran	541	RV-OBL	6.06	49.0	685	Component1	0.07	1.94	0.20	0.13	24.00
N. Palm Springs	Winchester Bergman Ran	541	RV-OBL	6.06	49.0	685	Component2	0.09	1.76	0.30	0.13	24.00
N. Palm Springs	Winchester Bergman Ran	541	RV-OBL	6.06	49.0	685	Vertical	-	-	-	-	24.00
Norcia, Italy	Bevagna	155	N	5.90	31.0	1000	Component1	0.02	1.03	0.09	0.33	23.84
Norcia, Italy	Bevagna	155	N	5.90	31.0	1000	Component2	0.04	2.18	0.41	0.39	23.81
Norcia, Italy	Bevagna	155	N	5.90	31.0	1000	Vertical	-	-	-	-	23.82
Northridge-01	Anacapa Island	943	RV	6.69	69.0	822	Component1	0.07	3.17	1.23	0.26	40.00
Northridge-01	Anacapa Island	943	RV	6.69	69.0	822	Component2	0.04	1.76	0.31	0.30	40.00
Northridge-01	Anacapa Island	943	RV	6.69	69.0	822	Vertical	-	-	-	-	40.00
Northridge-01	Antelope Buttes	946	RV	6.69	47.0	822	Component1	0.05	3.58	2.32	0.35	28.00
Northridge-01	Antelope Buttes	946	RV	6.69	47.0	822	Component2	0.07	4.26	2.78	0.39	28.00
Northridge-01	Antelope Buttes	946	RV	6.69	47.0	822	Vertical	-	-	-	-	28.00
Northridge-01	Burbank - Howard Rd.	957	RV	6.69	16.9	822	Component1	0.12	9.52	2.25	0.44	29.99
Northridge-01	Burbank - Howard Rd.	957	RV	6.69	16.9	822	Component2	0.16	8.48	1.81	0.32	29.99
Northridge-01	Burbank - Howard Rd.	957	RV	6.69	16.9	822	Vertical	-	-	-	-	29.99
Northridge-01	LA - Griffith Park Observatory	994	RV	6.69	23.8	1016	Component1	0.29	26.57	3.89	0.43	46.94
Northridge-01	LA - Griffith Park Observatory	994	RV	6.69	23.8	1016	Component2	0.16	13.55	2.40	0.51	46.94
Northridge-01	LA - Griffith Park Observatory	994	RV	6.69	23.8	1016	Vertical	-	-	-	-	46.94
Northridge-01	LA - Wonderland Ave	1011	RV	6.69	20.3	1223	Component1	0.11	8.66	1.78	0.33	29.99
Northridge-01	LA - Wonderland Ave	1011	RV	6.69	20.3	1223	Component2	0.17	11.80	2.78	0.46	29.99
Northridge-01	LA - Wonderland Ave	1011	RV	6.69	20.3	1223	Vertical	-	-	-	-	29.99
Northridge-01	LA Dam	1013	RV	6.69	5.9	629	Component1	0.51	63.68	21.26	0.88	26.57
Northridge-01	LA Dam	1013	RV	6.69	5.9	629	Component2	0.35	50.81	15.09	0.80	26.57
Northridge-01	LA Dam	1013	RV	6.69	5.9	629	Vertical	-	-	-	-	26.57
Northridge-01	Lake Hughes #12A	1020	RV	6.69	21.4	602	Component1	0.17	11.81	4.63	0.25	40.00
Northridge-01	Lake Hughes #12A	1020	RV	6.69	21.4	602	Component2	0.26	8.87	4.17	0.22	40.00
Northridge-01	Lake Hughes #12A	1020	RV	6.69	21.4	602	Vertical	-	-	-	-	40.00
Northridge-01	Lake Hughes #4 - Camp Mend	1021	RV	6.69	32.0	822	Component1	0.06	6.61	4.43	0.36	32.00
Northridge-01	Lake Hughes #4 - Camp Mend	1021	RV	6.69	32.0	822	Component2	0.08	6.16	2.11	0.27	32.00
Northridge-01	Lake Hughes #4 - Camp Mend	1021	RV	6.69	32.0	822	Vertical	-	-	-	-	32.00
Northridge-01	Lake Hughes #9	1023	RV	6.69	25.4	671	Component1	0.17	8.30	4.54	0.25	40.00
Northridge-01	Lake Hughes #9	1023	RV	6.69	25.4	671	Component2	0.22	9.83	2.77	0.25	40.00
Northridge-01	Lake Hughes #9	1023	RV	6.69	25.4	671	Vertical	-	-	-	-	40.00
Northridge-01	Leona Valley #1	1027	RV	6.69	37.0	685	Component1	0.09	7.75	1.75	0.49	32.00
Northridge-01	Leona Valley #1	1027	RV	6.69	37.0	685	Component2	0.07	7.08	2.12	0.50	32.00
Northridge-01	Leona Valley #1	1027	RV	6.69	37.0	685	Vertical	-	-	-	-	32.00

Continued on next page

Table A.1: PEER ground motion metadata (continued)

Earthquake (Year)	Station	NGA Number	Fault Type	M_w	Distance (km)	$V_{s,30}$ (m/s)	Component	PGA (g)	PGV (cm/s)	PGD (cm)	T_m (s)	Duration (s)
Northridge-01	Leona Valley #3	1029	RV	6.69	37.0	685	Component1	0.08	8.49	2.18	0.51	32.00
Northridge-01	Leona Valley #3	1029	RV	6.69	37.0	685	Component2	0.11	8.07	1.82	0.54	32.00
Northridge-01	Leona Valley #3	1029	RV	6.69	37.0	685	Vertical	-	-	-	-	32.00
Northridge-01	Littlerock - Brainard Can	1033	RV	6.69	47.0	822	Component1	0.07	6.03	1.33	0.57	40.00
Northridge-01	Littlerock - Brainard Can	1033	RV	6.69	47.0	822	Component2	0.06	6.28	1.24	0.54	40.00
Northridge-01	Littlerock - Brainard Can	1033	RV	6.69	47.0	822	Vertical	-	-	-	-	40.00
Northridge-01	Mt Wilson - CIT Seis Sta	1041	RV	6.69	36.0	822	Component1	0.23	7.25	0.70	0.23	40.00
Northridge-01	Mt Wilson - CIT Seis Sta	1041	RV	6.69	36.0	822	Component2	0.13	5.68	0.45	0.23	40.00
Northridge-01	Mt Wilson - CIT Seis Sta	1041	RV	6.69	36.0	822	Vertical	-	-	-	-	40.00
Northridge-01	Pacoima Dam (downstr)	1050	RV	6.69	7.0	2016	Component1	0.42	45.08	4.98	0.46	20.00
Northridge-01	Pacoima Dam (downstr)	1050	RV	6.69	7.0	2016	Component2	0.43	30.91	4.37	0.50	20.00
Northridge-01	Pacoima Dam (downstr)	1050	RV	6.69	7.0	2016	Vertical	-	-	-	-	20.00
Northridge-01	Pacoima Dam (upper left)	1051	RV	6.69	7.0	2016	Component1	1.58	54.77	6.28	0.33	40.00
Northridge-01	Pacoima Dam (upper left)	1051	RV	6.69	7.0	2016	Component2	1.29	103.47	22.83	0.44	40.00
Northridge-01	Pacoima Dam (upper left)	1051	RV	6.69	7.0	2016	Vertical	-	-	-	-	40.00
Northridge-01	Rancho Cucamonga - Deer Can	1060	RV	6.69	80.0	822	Component1	0.07	4.15	0.56	0.32	40.00
Northridge-01	Rancho Cucamonga - Deer Can	1060	RV	6.69	80.0	822	Component2	0.05	5.84	0.77	0.37	40.00
Northridge-01	Rancho Cucamonga - Deer Can	1060	RV	6.69	80.0	822	Vertical	-	-	-	-	40.00
Northridge-01	Sandberg - Bald Mtn	1074	RV	6.69	42.0	822	Component1	0.09	12.20	4.74	0.67	40.00
Northridge-01	Sandberg - Bald Mtn	1074	RV	6.69	42.0	822	Component2	0.10	8.86	4.58	0.56	40.00
Northridge-01	Sandberg - Bald Mtn	1074	RV	6.69	42.0	822	Vertical	-	-	-	-	40.00
Northridge-01	Vasquez Rocks Park	1091	RV	6.69	23.6	996	Component1	0.15	18.41	2.90	0.41	40.00
Northridge-01	Vasquez Rocks Park	1091	RV	6.69	23.6	996	Component2	0.14	11.06	2.88	0.38	40.00
Northridge-01	Vasquez Rocks Park	1091	RV	6.69	23.6	996	Vertical	-	-	-	-	40.00
Northridge-01	Wrightwood - Jackson Flat	1096	RV	6.69	65.0	822	Component1	0.06	5.02	0.72	0.55	60.00
Northridge-01	Wrightwood - Jackson Flat	1096	RV	6.69	65.0	822	Component2	0.04	3.49	0.75	0.60	60.00
Northridge-01	Wrightwood - Jackson Flat	1096	RV	6.69	65.0	822	Vertical	-	-	-	-	60.00
Northridge-06	Anacapa Island	1691	RV	5.28	83.0	822	Component1	0.01	0.41	0.05	0.22	40.01
Northridge-06	Anacapa Island	1691	RV	5.28	83.0	822	Component2	0.01	0.36	0.13	0.30	40.01
Northridge-06	Anacapa Island	1691	RV	5.28	83.0	822	Vertical	-	-	-	-	40.01
Northridge-06	Burbank - Howard Rd.	1696	RV	5.28	19.3	822	Component1	0.08	4.11	0.26	0.33	4.99
Northridge-06	Burbank - Howard Rd.	1696	RV	5.28	19.3	822	Component2	0.07	2.93	0.21	0.33	4.99
Northridge-06	LA - Griffith Park Observatory	1709	RV	5.28	21.8	1016	Component1	0.03	2.34	0.81	0.43	25.71
Northridge-06	LA - Griffith Park Observatory	1709	RV	5.28	21.8	1016	Component2	0.06	2.42	0.68	0.32	25.71
Northridge-06	LA - Wonderland Ave	1715	RV	5.28	17.2	1223	Component1	0.05	1.85	0.07	0.20	5.74
Northridge-06	LA - Wonderland Ave	1715	RV	5.28	17.2	1223	Component2	0.05	2.49	0.13	0.29	5.74

Continued on next page

Table A.1: PEER ground motion metadata (continued)

Earthquake (Year)	Station	NGA Number	Fault Type	M_w	Distance (km)	$V_{s,30}$ (m/s)	Component	PGA (g)	PGV (cm/s)	PGD (cm)	T_m (s)	Duration (s)
Northridge-06	LA - Wonderland Ave	1715	RV	5.28	17.2	1223	Vertical	-	-	-	-	5.74
Northridge-06	Lake Hughes #12A	1717	RV	5.28	39.0	602	Component1	0.02	0.53	0.29	0.17	40.01
Northridge-06	Lake Hughes #12A	1717	RV	5.28	39.0	602	Component2	0.02	0.56	0.40	0.15	40.01
Northridge-06	Lake Hughes #12A	1717	RV	5.28	39.0	602	Vertical	-	-	-	-	40.01
Northridge-06	Littlerock - Brainard Can	1718	RV	5.28	54.0	822	Component1	0.01	0.64	0.14	0.35	40.01
Northridge-06	Littlerock - Brainard Can	1718	RV	5.28	54.0	822	Component2	0.01	0.51	0.08	0.31	40.01
Northridge-06	Littlerock - Brainard Can	1718	RV	5.28	54.0	822	Vertical	-	-	-	-	40.01
Northridge-06	Mill Creek, Angeles Nat For	1720	RV	5.28	41.0	685	Component1	0.05	3.47	0.22	0.36	7.99
Northridge-06	Mill Creek, Angeles Nat For	1720	RV	5.28	41.0	685	Component2	0.07	3.37	0.21	0.37	7.99
Northridge-06	Rancho Cucamonga - Deer Can	1727	RV	5.28	82.0	822	Component1	0.01	0.51	0.12	0.24	40.01
Northridge-06	Rancho Cucamonga - Deer Can	1727	RV	5.28	82.0	822	Component2	0.01	0.44	0.08	0.23	40.01
Northridge-06	Rancho Cucamonga - Deer Can	1727	RV	5.28	82.0	822	Vertical	-	-	-	-	40.01
Oroville-01	Oroville Seismograph Station	106	N	5.89	8.0	623	Component1	0.09	3.70	0.17	0.19	12.20
Oroville-01	Oroville Seismograph Station	106	N	5.89	8.0	623	Component2	0.07	2.84	0.22	0.20	12.20
Oroville-03	DWR Garage	113	N	4.70	6.1	623	Component1	0.14	1.10	0.04	0.07	13.32
Oroville-03	DWR Garage	113	N	4.70	6.1	623	Component2	0.11	0.62	0.01	0.07	13.32
San Fernando	Cedar Springs, Allen Ranch	59	RV	6.61	90.0	813	Component1	0.02	1.69	0.48	0.47	14.66
San Fernando	Cedar Springs, Allen Ranch	59	RV	6.61	90.0	813	Component2	0.01	0.91	0.48	0.52	14.66
San Fernando	Fairmont Dam	63	RV	6.61	30.0	685	Component1	0.07	4.67	0.68	0.31	30.00
San Fernando	Fairmont Dam	63	RV	6.61	30.0	685	Component2	0.11	6.43	1.07	0.37	30.00
San Fernando	Fairmont Dam	63	RV	6.61	30.0	685	Vertical	-	-	-	-	30.00
San Fernando	Isabella Dam (Aux Abut)	67	RV	6.61	131.0	685	Component1	0.01	1.42	1.87	0.49	42.41
San Fernando	Isabella Dam (Aux Abut)	67	RV	6.61	131.0	685	Component2	0.01	1.29	1.39	0.71	42.41
San Fernando	Lake Hughes #12	71	RV	6.61	19.3	602	Component1	0.37	16.88	1.69	0.23	36.60
San Fernando	Lake Hughes #12	71	RV	6.61	19.3	602	Component2	0.17	3.72	0.64	0.14	36.60
San Fernando	Lake Hughes #4	72	RV	6.61	25.1	822	Component1	0.19	5.60	0.91	0.20	36.89
San Fernando	Lake Hughes #4	72	RV	6.61	25.1	822	Component2	0.16	6.37	0.88	0.18	36.89
San Fernando	Lake Hughes #9	73	RV	6.61	22.6	671	Component1	0.16	4.49	1.24	0.22	34.89
San Fernando	Lake Hughes #9	73	RV	6.61	22.6	671	Component2	0.09	2.25	0.79	0.17	34.89
San Fernando	Pacoima Dam (upper left abut)	77	RV	6.61	1.8	2016	Component1	1.23	112.49	35.41	0.48	41.64
San Fernando	Pacoima Dam (upper left abut)	77	RV	6.61	1.8	2016	Component2	0.70	56.45	18.18	0.30	41.64
San Fernando	Santa Anita Dam	87	RV	6.61	31.0	685	Component1	0.15	4.70	2.31	0.19	29.66
San Fernando	Santa Anita Dam	87	RV	6.61	31.0	685	Component2	0.06	3.93	1.75	0.20	29.66
San Fernando	Tehachapi Pump	89	RV	6.61	64.0	669	Component1	0.05	2.02	0.37	0.21	12.55
San Fernando	Tehachapi Pump	89	RV	6.61	64.0	669	Component2	0.04	1.72	0.27	0.21	12.55
San Francisco	Golden Gate Park	23	RV	5.28	11.0	874	Component1	0.10	3.91	0.19	0.22	39.73

Continued on next page

Table A.1: PEER ground motion metadata (continued)

Earthquake (Year)	Station	NGA Number	Fault Type	M_w	Distance (km)	$V_{s,30}$ (m/s)	Component	PGA (g)	PGV (cm/s)	PGD (cm)	T_m (s)	Duration (s)
San Francisco	Golden Gate Park	23	RV	5.28	11.0	874	Component2	0.11	4.58	0.43	0.21	39.73
San Francisco	Golden Gate Park	23	RV	5.28	11.0	874	Vertical	-	-	-	-	39.73
Sierra Madre	Cogswell Dam - Right Abutment	1642	RV	5.61	22.0	685	Component1	0.30	14.85	1.95	0.29	40.00
Sierra Madre	Mt Wilson - CIT Seis Sta	1645	RV	5.61	10.4	822	Component1	0.28	12.93	22.54	0.25	40.00
Sierra Madre	Mt Wilson - CIT Seis Sta	1645	RV	5.61	10.4	822	Component2	0.20	7.99	8.05	0.21	40.00
Sierra Madre	Mt Wilson - CIT Seis Sta	1645	RV	5.61	10.4	822	Vertical	-	-	-	-	40.02
Sierra Madre	Vasquez Rocks Park	1649	RV	5.61	40.0	996	Component1	0.10	2.97	0.33	0.22	40.00
Sierra Madre	Vasquez Rocks Park	1649	RV	5.61	40.0	996	Component2	0.13	2.53	0.65	0.18	40.00
Sierra Madre	Vasquez Rocks Park	1649	RV	5.61	40.0	996	Vertical	-	-	-	-	40.00
Tabas, Iran	Tabas	143	RV	7.35	2.1	767	Component1	0.84	97.85	40.47	0.48	32.84
Tabas, Iran	Tabas	143	RV	7.35	2.1	767	Component2	0.85	121.22	95.04	0.46	32.84
Tabas, Iran	Tabas	143	RV	7.35	2.1	767	Vertical	-	-	-	-	32.84
Whittier Narrows-01	LA - Wonderland Ave	643	RV-OBL	5.99	27.6	1223	Component1	0.04	1.71	0.17	0.21	18.16
Whittier Narrows-01	LA - Wonderland Ave	643	RV-OBL	5.99	27.6	1223	Component2	0.05	1.46	0.15	0.24	18.16
Whittier Narrows-01	LA - Wonderland Ave	643	RV-OBL	5.99	27.6	1223	Vertical	-	-	-	-	18.16
Whittier Narrows-01	Malibu - Las Flores Canyon	657	RV-OBL	5.99	49.0	623	Component1	0.07	2.23	0.13	0.23	15.20
Whittier Narrows-01	Malibu - Las Flores Canyon	657	RV-OBL	5.99	49.0	623	Component2	0.05	2.20	0.33	0.22	15.20
Whittier Narrows-01	Malibu - Las Flores Canyon	657	RV-OBL	5.99	49.0	623	Vertical	-	-	-	-	15.20
Whittier Narrows-01	Mill Creek, Angeles Nat For	661	RV-OBL	5.99	37.0	685	Component1	0.09	3.94	0.52	0.34	26.26
Whittier Narrows-01	Mill Creek, Angeles Nat For	661	RV-OBL	5.99	37.0	685	Component2	0.07	3.24	0.31	0.29	26.26
Whittier Narrows-01	Mill Creek, Angeles Nat For	661	RV-OBL	5.99	37.0	685	Vertical	-	-	-	-	26.26
Whittier Narrows-01	Mt Wilson - CIT Seis Sta	663	RV-OBL	5.99	22.7	822	Component1	0.12	3.33	0.37	0.18	39.99
Whittier Narrows-01	Mt Wilson - CIT Seis Sta	663	RV-OBL	5.99	22.7	822	Component2	0.19	4.62	0.21	0.16	39.99
Whittier Narrows-01	Mt Wilson - CIT Seis Sta	663	RV-OBL	5.99	22.7	822	Vertical	-	-	-	-	39.99
Whittier Narrows-01	Vasquez Rocks Park	703	RV-OBL	5.99	50.0	996	Component1	0.06	2.11	0.12	0.20	39.99
Whittier Narrows-01	Vasquez Rocks Park	703	RV-OBL	5.99	50.0	996	Component2	0.06	2.34	0.11	0.19	39.99
Whittier Narrows-01	Vasquez Rocks Park	703	RV-OBL	5.99	50.0	996	Vertical	-	-	-	-	39.99
Whittier Narrows-02	Mt Wilson - CIT Seis Sta	715	RV-OBL	5.27	19.9	822	Component1	0.16	5.72	0.24	0.20	22.00
Whittier Narrows-02	Mt Wilson - CIT Seis Sta	715	RV-OBL	5.27	19.9	822	Component2	0.14	4.57	0.20	0.17	22.00
Whittier Narrows-02	Mt Wilson - CIT Seis Sta	715	RV-OBL	5.27	19.9	822	Vertical	-	-	-	-	22.00
Yountville	Golden Gate Bridge	1851	SS	5.00	63.0	642	Component1	0.01	0.29	0.04	0.28	41.00

Table A.2: Baker: Broadband ground motion metadata

Earthquake (Year)	Station	NGA Number	Fault Type	M_w	Distance (km)	$V_{s,30}$ (m/s)	Component	PGA (g)	PGV (cm/s)	PGD (cm)	T_m (s)	Duration (s)
Chi-Chi, Taiwan	TCU045	1485	RV-OBL	7.62	26.0	705	Normal	0.60	44.12	38.37	0.49	90.00
Chi-Chi, Taiwan	TCU045	1485	RV-OBL	7.62	26.0	705	Parallel	0.29	33.72	35.07	0.51	90.00
Chi-Chi, Taiwan	TCU045	1485	RV-OBL	7.62	26.0	705	Vertical	-	-	-	-	90.00
Chi-Chi, Taiwan	TCU129	1549	RV-OBL	7.62	1.8	664	Normal	1.01	60.16	50.54	0.34	90.00
Chi-Chi, Taiwan	TCU129	1549	RV-OBL	7.62	1.8	664	Parallel	0.64	35.79	28.15	0.34	90.00
Chi-Chi, Taiwan	TCU129	1549	RV-OBL	7.62	1.8	664	Vertical	-	-	-	-	90.00
Chi-Chi, Taiwan	TCU138	1551	RV-OBL	7.62	9.8	653	Normal	0.20	40.66	36.11	0.69	150.00
Chi-Chi, Taiwan	TCU138	1551	RV-OBL	7.62	9.8	653	Parallel	0.23	40.80	26.64	0.96	150.00
Chi-Chi, Taiwan	TCU138	1551	RV-OBL	7.62	9.8	653	Vertical	-	-	-	-	150.00
Chi-Chi, Taiwan	WNT	1596	RV-OBL	7.62	1.8	502	Normal	0.96	69.16	31.44	0.33	60.00
Chi-Chi, Taiwan	WNT	1596	RV-OBL	7.62	1.8	502	Parallel	0.63	41.19	18.35	0.33	60.00
Chi-Chi, Taiwan	WNT	1596	RV-OBL	7.62	1.8	502	Vertical	-	-	-	-	60.00
Chi-Chi, Taiwan-03	TCU138	2661	RV	6.20	22.2	653	Normal	0.13	19.72	4.34	0.86	35.00
Chi-Chi, Taiwan-03	TCU138	2661	RV	6.20	22.2	653	Parallel	0.13	12.89	3.43	0.74	35.00
Chi-Chi, Taiwan-03	TCU138	2661	RV	6.20	22.2	653	Vertical	-	-	-	-	35.00
Chi-Chi, Taiwan-06	TCU129	3507	RV	6.30	24.8	664	Normal	0.34	16.50	5.53	0.33	71.02
Chi-Chi, Taiwan-06	TCU129	3507	RV	6.30	24.8	664	Parallel	0.19	10.35	1.72	0.22	71.02
Chi-Chi, Taiwan-06	TCU129	3507	RV	6.30	24.8	664	Vertical	-	-	-	-	71.02
Chi-Chi, Taiwan-06	TCU138	3509	RV	6.30	34.0	653	Normal	0.06	9.02	4.25	0.83	71.00
Chi-Chi, Taiwan-06	TCU138	3509	RV	6.30	34.0	653	Parallel	0.05	7.37	2.42	0.73	71.00
Chi-Chi, Taiwan-06	TCU138	3509	RV	6.30	34.0	653	Vertical	-	-	-	-	71.00
Coyote Lake	Gilroy Array #6	150	SS	5.74	3.1	663	Normal	0.45	51.54	7.10	0.63	27.09
Coyote Lake	Gilroy Array #6	150	SS	5.74	3.1	663	Parallel	0.33	27.14	4.49	0.42	27.09
Coyote Lake	Gilroy Array #6	150	SS	5.74	3.1	663	Vertical	-	-	-	-	27.09
Denali, Alaska	Carlo (temp)	2107	SS	7.90	51.0	964	Normal	0.09	10.38	5.38	0.56	86.00
Denali, Alaska	Carlo (temp)	2107	SS	7.90	51.0	964	Parallel	0.10	7.58	3.72	0.32	86.00
Denali, Alaska	Carlo (temp)	2107	SS	7.90	51.0	964	Vertical	-	-	-	-	86.00
Duzce, Turkey	Lamont 531	1618	SS	7.14	8.0	660	Normal	0.16	12.66	8.00	0.34	41.50
Duzce, Turkey	Lamont 531	1618	SS	7.14	8.0	660	Parallel	0.12	12.95	9.05	0.47	41.50
Duzce, Turkey	Lamont 531	1618	SS	7.14	8.0	660	Vertical	-	-	-	-	41.50
Duzce, Turkey	Mudurnu	1619	SS	7.14	34.0	660	Normal	0.11	10.19	9.31	0.42	28.82
Duzce, Turkey	Mudurnu	1619	SS	7.14	34.0	660	Parallel	0.07	15.79	14.45	0.51	28.82
Duzce, Turkey	Mudurnu	1619	SS	7.14	34.0	660	Vertical	-	-	-	-	28.82
Hector Mine	Heart Bar State Park	1786	SS	7.13	61.0	685	Normal	0.07	7.16	3.34	0.37	60.00
Hector Mine	Heart Bar State Park	1786	SS	7.13	61.0	685	Parallel	0.09	13.52	11.73	0.31	60.00

Continued on next page

Table A.2: Baker: Broadband ground motion metadata (continued)

Earthquake (Year)	Station	NGA Number	Fault Type	M_w	Distance (km)	$V_{s,30}$ (m/s)	Component	PGA (g)	PGV (cm/s)	PGD (cm)	T_m (s)	Duration (s)
Hector Mine	Heart Bar State Park	1786	SS	7.13	61.0	685	Vertical	-	-	-	-	60.00
Hector Mine	Hector	1787	SS	7.13	11.7	685	Normal	0.34	37.02	13.49	0.59	45.31
Hector Mine	Hector	1787	SS	7.13	11.7	685	Parallel	0.31	33.05	22.03	0.68	45.31
Hector Mine	Hector	1787	SS	7.13	11.7	685	Vertical	-	-	-	-	45.31
Helena, Montana-01	Carroll College	1	SS	6.00	2.9	660	Normal	0.15	6.24	1.18	0.26	40.00
Helena, Montana-01	Carroll College	1	SS	6.00	2.9	660	Parallel	0.18	16.28	2.28	0.45	40.00
Helena, Montana-01	Carroll College	1	SS	6.00	2.9	660	Vertical	-	-	-	-	40.00
Imperial Valley-06	Cerro Prieto	164	SS	6.53	15.2	660	Normal	0.15	18.39	7.93	0.57	63.74
Imperial Valley-06	Cerro Prieto	164	SS	6.53	15.2	660	Parallel	0.17	11.42	4.32	0.40	63.74
Imperial Valley-06	Cerro Prieto	164	SS	6.53	15.2	660	Vertical	-	-	-	-	63.74
Irpinia, Italy-01	Bagnoli Irpinio	285	N	6.90	8.2	1000	Normal	0.19	29.34	10.24	0.89	36.86
Irpinia, Italy-01	Bagnoli Irpinio	285	N	6.90	8.2	1000	Parallel	0.13	23.35	9.51	0.77	36.86
Irpinia, Italy-01	Bagnoli Irpinio	285	N	6.90	8.2	1000	Vertical	-	-	-	-	36.86
Irpinia, Italy-01	Bisaccia	286	N	6.90	21.3	1000	Normal	0.12	17.80	10.86	0.96	38.26
Irpinia, Italy-01	Bisaccia	286	N	6.90	21.3	1000	Parallel	0.06	15.83	10.00	1.35	38.26
Irpinia, Italy-01	Bisaccia	286	N	6.90	21.3	1000	Vertical	-	-	-	-	38.26
Kocaeli, Turkey	Gebze	1161	SS	7.51	10.9	792	Normal	0.24	51.96	44.02	0.66	28.00
Kocaeli, Turkey	Gebze	1161	SS	7.51	10.9	792	Parallel	0.14	28.19	25.38	0.54	28.00
Kocaeli, Turkey	Gebze	1161	SS	7.51	10.9	792	Vertical	-	-	-	-	28.00
Kocaeli, Turkey	Izmit	1165	SS	7.51	7.2	811	Normal	0.15	22.60	9.82	0.63	30.00
Kocaeli, Turkey	Izmit	1165	SS	7.51	7.2	811	Parallel	0.22	29.78	17.13	0.58	30.00
Kocaeli, Turkey	Izmit	1165	SS	7.51	7.2	811	Vertical	-	-	-	-	30.00
Loma Prieta	Belmont - Envirotech	748	RV-OBL	6.93	44.0	628	Normal	0.14	19.95	6.10	0.78	39.95
Loma Prieta	Belmont - Envirotech	748	RV-OBL	6.93	44.0	628	Parallel	0.10	7.63	3.26	0.67	39.95
Loma Prieta	Belmont - Envirotech	748	RV-OBL	6.93	44.0	628	Vertical	-	-	-	-	39.95
Loma Prieta	Gilroy - Gavilan Coll.	763	RV-OBL	6.93	10.0	730	Normal	0.29	30.79	6.53	0.35	39.95
Loma Prieta	Gilroy - Gavilan Coll.	763	RV-OBL	6.93	10.0	730	Parallel	0.41	26.62	4.81	0.34	39.95
Loma Prieta	Gilroy - Gavilan Coll.	763	RV-OBL	6.93	10.0	730	Vertical	-	-	-	-	39.95
Loma Prieta	Gilroy Array #1	765	RV-OBL	6.93	9.6	1428	Normal	0.43	38.57	7.21	0.35	39.95
Loma Prieta	Gilroy Array #1	765	RV-OBL	6.93	9.6	1428	Parallel	0.44	28.75	6.28	0.36	39.95
Loma Prieta	Gilroy Array #1	765	RV-OBL	6.93	9.6	1428	Vertical	-	-	-	-	39.95
Loma Prieta	Gilroy Array #6	769	RV-OBL	6.93	18.3	663	Normal	0.16	17.44	5.81	0.53	39.95
Loma Prieta	Gilroy Array #6	769	RV-OBL	6.93	18.3	663	Parallel	0.18	11.45	2.69	0.44	39.95
Loma Prieta	Gilroy Array #6	769	RV-OBL	6.93	18.3	663	Vertical	-	-	-	-	39.95
Loma Prieta	Golden Gate Bridge	771	RV-OBL	6.93	80.0	642	Normal	0.14	28.60	7.09	0.97	38.08
Loma Prieta	Golden Gate Bridge	771	RV-OBL	6.93	80.0	642	Parallel	0.18	29.92	9.53	0.82	38.08

Continued on next page

Table A.2: Baker: Broadband ground motion metadata (continued)

Earthquake (Year)	Station	NGA Number	Fault Type	M_w	Distance (km)	$V_{s,30}$ (m/s)	Component	PGA (g)	PGV (cm/s)	PGD (cm)	T_m (s)	Duration (s)
Loma Prieta	Golden Gate Bridge	771	RV-OBL	6.93	80.0	642	Vertical	-	-	-	-	38.08
Loma Prieta	San Jose - Santa Teresa Hills	801	RV-OBL	6.93	14.7	672	Normal	0.27	25.71	12.64	0.31	50.02
Loma Prieta	San Jose - Santa Teresa Hills	801	RV-OBL	6.93	14.7	672	Parallel	0.22	21.92	6.34	0.36	50.02
Loma Prieta	San Jose - Santa Teresa Hills	801	RV-OBL	6.93	14.7	672	Vertical	-	-	-	-	50.02
Loma Prieta	UCSC	809	RV-OBL	6.93	18.5	714	Normal	0.37	12.04	5.52	0.19	25.00
Loma Prieta	UCSC	809	RV-OBL	6.93	18.5	714	Parallel	0.31	11.57	4.84	0.24	25.00
Loma Prieta	UCSC	809	RV-OBL	6.93	18.5	714	Vertical	-	-	-	-	25.00
Loma Prieta	UCSC Lick Observatory	810	RV-OBL	6.93	18.4	714	Normal	0.41	17.68	4.85	0.28	39.95
Loma Prieta	UCSC Lick Observatory	810	RV-OBL	6.93	18.4	714	Parallel	0.51	19.46	4.34	0.24	39.95
Loma Prieta	UCSC Lick Observatory	810	RV-OBL	6.93	18.4	714	Vertical	-	-	-	-	39.95
Northridge-01	Burbank - Howard Rd.	957	RV	6.69	16.9	822	Normal	0.11	8.13	1.69	0.43	29.99
Northridge-01	Burbank - Howard Rd.	957	RV	6.69	16.9	822	Parallel	0.14	6.90	2.64	0.32	29.99
Northridge-01	Burbank - Howard Rd.	957	RV	6.69	16.9	822	Vertical	-	-	-	-	29.99
Northridge-01	LA - Chalon Rd	989	RV	6.69	20.5	740	Normal	0.19	18.57	2.16	0.51	31.07
Northridge-01	LA - Chalon Rd	989	RV	6.69	20.5	740	Parallel	0.23	29.21	5.71	0.63	31.07
Northridge-01	LA - Chalon Rd	989	RV	6.69	20.5	740	Vertical	-	-	-	-	31.07
Northridge-01	LA - Wonderland Ave	1011	RV	6.69	20.3	1223	Normal	0.16	11.45	2.66	0.45	29.99
Northridge-01	LA - Wonderland Ave	1011	RV	6.69	20.3	1223	Parallel	0.12	11.72	1.76	0.36	29.99
Northridge-01	LA - Wonderland Ave	1011	RV	6.69	20.3	1223	Vertical	-	-	-	-	29.99
Northridge-01	LA 00	1012	RV	6.69	19.1	706	Normal	0.38	22.07	5.06	0.37	60.02
Northridge-01	LA 00	1012	RV	6.69	19.1	706	Parallel	0.33	31.81	4.13	0.47	60.02
Northridge-01	LA 00	1012	RV	6.69	19.1	706	Vertical	-	-	-	-	60.02
Northridge-01	LA Dam	1013	RV	6.69	5.9	629	Normal	0.58	77.09	20.10	0.82	26.57
Northridge-01	LA Dam	1013	RV	6.69	5.9	629	Parallel	0.42	40.75	16.01	0.88	26.57
Northridge-01	LA Dam	1013	RV	6.69	5.9	629	Vertical	-	-	-	-	26.57
Northridge-01	Pacoima Dam (downstr)	1050	RV	6.69	7.0	2016	Normal	0.50	48.99	6.37	0.49	20.00
Northridge-01	Pacoima Dam (downstr)	1050	RV	6.69	7.0	2016	Parallel	0.25	18.91	2.77	0.46	20.00
Northridge-01	Pacoima Dam (downstr)	1050	RV	6.69	7.0	2016	Vertical	-	-	-	-	20.00
Northridge-01	Santa Susana Ground	1078	RV	6.69	16.7	715	Normal	0.23	14.34	3.20	0.29	57.25
Northridge-01	Santa Susana Ground	1078	RV	6.69	16.7	715	Parallel	0.27	21.63	7.57	0.38	57.25
Northridge-01	Santa Susana Ground	1078	RV	6.69	16.7	715	Vertical	-	-	-	-	57.25
Northridge-01	Vasquez Rocks Park	1091	RV	6.69	23.6	996	Normal	0.16	17.79	2.20	0.41	40.00
Northridge-01	Vasquez Rocks Park	1091	RV	6.69	23.6	996	Parallel	0.15	13.65	3.89	0.38	40.00
Northridge-01	Vasquez Rocks Park	1091	RV	6.69	23.6	996	Vertical	-	-	-	-	40.00
San Fernando	Lake Hughes #4	72	RV	6.61	25.1	822	Normal	0.15	8.44	1.91	0.26	36.89
San Fernando	Lake Hughes #4	72	RV	6.61	25.1	822	Parallel	0.19	5.55	0.91	0.20	36.89

Continued on next page

Table A.2: Baker: Broadband ground motion metadata (continued)

Earthquake (Year)	Station	NGA Number	Fault Type	M_w	Distance (km)	$V_{s,30}$ (m/s)	Component	PGA (g)	PGV (cm/s)	PGD (cm)	T_m (s)	Duration (s)
San Fernando	Lake Hughes #4	72	RV	6.61	25.1	822	Vertical	-	-	-	-	36.89
San Fernando	Pasadena - Old Seismo Lab	80	RV	6.61	21.5	969	Normal	0.09	6.96	1.05	0.29	30.00
San Fernando	Pasadena - Old Seismo Lab	80	RV	6.61	21.5	969	Parallel	0.19	10.68	2.37	0.32	30.00
San Fernando	Pasadena - Old Seismo Lab	80	RV	6.61	21.5	969	Vertical	-	-	-	-	30.00
Sitka, Alaska	Sitka Observatory	1626	SS	7.68	35.0	660	Normal	0.09	7.18	5.27	0.30	55.03
Sitka, Alaska	Sitka Observatory	1626	SS	7.68	35.0	660	Parallel	0.09	14.71	21.08	0.30	55.03
Sitka, Alaska	Sitka Observatory	1626	SS	7.68	35.0	660	Vertical	-	-	-	-	55.24
Taiwan SMART1(45)	SMART1 E02	572	RV	7.30	52.0	660	Normal	0.12	12.52	5.37	0.47	32.93
Taiwan SMART1(45)	SMART1 E02	572	RV	7.30	52.0	660	Parallel	0.15	14.14	6.32	0.47	32.93
Taiwan SMART1(45)	SMART1 E02	572	RV	7.30	52.0	660	Vertical	-	-	-	-	32.93
Victoria, Mexico	Cerro Prieto	265	SS	6.33	14.4	660	Normal	0.63	31.29	12.72	0.51	24.45
Victoria, Mexico	Cerro Prieto	265	SS	6.33	14.4	660	Parallel	0.60	19.71	9.75	0.40	24.45
Victoria, Mexico	Cerro Prieto	265	SS	6.33	14.4	660	Vertical	-	-	-	-	24.45

Table A.3: Baker: Pulse-like ground motion metadata

Earthquake (Year)	Station	NGA Number	Fault Type	M_w	Distance (km)	$V_{s,30}$ (m/s)	Component	PGA (g)	PGV (cm/s)	PGD (cm)	T_m (s)	Duration (s)
Chi-Chi, Taiwan	CHY028	1197	RV-OBL	7.62	3.1	543	Normal	0.66	77.65	15.09	0.59	90.00
Chi-Chi, Taiwan	CHY028	1197	RV-OBL	7.62	3.1	543	Parallel	0.85	66.92	22.72	0.58	90.00
Chi-Chi, Taiwan	CHY028	1197	RV-OBL	7.62	3.1	543	Vertical	-	-	-	-	90.00
Chi-Chi, Taiwan	CHY101	1244	RV-OBL	7.62	10.0	259	Normal	0.38	75.28	49.02	1.02	90.00
Chi-Chi, Taiwan	CHY101	1244	RV-OBL	7.62	10.0	259	Parallel	0.43	114.49	68.96	0.99	90.00
Chi-Chi, Taiwan	CHY101	1244	RV-OBL	7.62	10.0	259	Vertical	-	-	-	-	90.00
Chi-Chi, Taiwan	TCU049	1489	RV-OBL	7.62	3.8	487	Normal	0.29	46.08	65.26	0.64	90.00
Chi-Chi, Taiwan	TCU049	1489	RV-OBL	7.62	3.8	487	Parallel	0.25	58.91	50.00	0.63	90.00
Chi-Chi, Taiwan	TCU049	1489	RV-OBL	7.62	3.8	487	Vertical	-	-	-	-	90.00
Chi-Chi, Taiwan	TCU052	1492	RV-OBL	7.62	0.7	579	Normal	0.38	165.54	204.59	1.59	90.00
Chi-Chi, Taiwan	TCU052	1492	RV-OBL	7.62	0.7	579	Parallel	0.39	113.06	229.65	1.50	90.00
Chi-Chi, Taiwan	TCU052	1492	RV-OBL	7.62	0.7	579	Vertical	-	-	-	-	90.00
Chi-Chi, Taiwan	TCU053	1493	RV-OBL	7.62	6.0	455	Normal	0.22	40.87	57.53	0.67	90.00
Chi-Chi, Taiwan	TCU053	1493	RV-OBL	7.62	6.0	455	Parallel	0.14	41.31	48.86	0.87	90.00
Chi-Chi, Taiwan	TCU053	1493	RV-OBL	7.62	6.0	455	Vertical	-	-	-	-	90.00
Chi-Chi, Taiwan	TCU054	1494	RV-OBL	7.62	5.3	461	Normal	0.16	60.38	61.12	0.82	90.00
Chi-Chi, Taiwan	TCU054	1494	RV-OBL	7.62	5.3	461	Parallel	0.19	39.13	51.48	0.90	90.00
Chi-Chi, Taiwan	TCU054	1494	RV-OBL	7.62	5.3	461	Vertical	-	-	-	-	90.00
Chi-Chi, Taiwan	TCU068	1505	RV-OBL	7.62	0.3	487	Normal	0.56	184.60	350.03	1.52	90.00
Chi-Chi, Taiwan	TCU068	1505	RV-OBL	7.62	0.3	487	Parallel	0.43	250.79	409.33	1.27	90.00
Chi-Chi, Taiwan	TCU068	1505	RV-OBL	7.62	0.3	487	Vertical	-	-	-	-	90.00
Chi-Chi, Taiwan	TCU075	1510	RV-OBL	7.62	0.9	573	Normal	0.33	88.57	86.85	0.76	90.00
Chi-Chi, Taiwan	TCU075	1510	RV-OBL	7.62	0.9	573	Parallel	0.27	37.61	28.18	0.67	90.00
Chi-Chi, Taiwan	TCU075	1510	RV-OBL	7.62	0.9	573	Vertical	-	-	-	-	90.00
Chi-Chi, Taiwan	TCU076	1511	RV-OBL	7.62	2.8	615	Normal	0.31	67.81	33.52	0.51	90.00
Chi-Chi, Taiwan	TCU076	1511	RV-OBL	7.62	2.8	615	Parallel	0.42	58.71	33.51	0.61	90.00
Chi-Chi, Taiwan	TCU076	1511	RV-OBL	7.62	2.8	615	Vertical	-	-	-	-	90.00
Chi-Chi, Taiwan	TCU082	1515	RV-OBL	7.62	5.2	473	Normal	0.23	57.80	71.99	0.85	90.00
Chi-Chi, Taiwan	TCU082	1515	RV-OBL	7.62	5.2	473	Parallel	0.19	43.08	55.75	1.03	90.00
Chi-Chi, Taiwan	TCU082	1515	RV-OBL	7.62	5.2	473	Vertical	-	-	-	-	90.00
Chi-Chi, Taiwan	TCU087	1519	RV-OBL	7.62	7.0	562	Normal	0.13	43.68	64.53	1.08	90.00
Chi-Chi, Taiwan	TCU087	1519	RV-OBL	7.62	7.0	562	Parallel	0.12	36.26	24.34	1.34	90.00
Chi-Chi, Taiwan	TCU087	1519	RV-OBL	7.62	7.0	562	Vertical	-	-	-	-	90.00
Chi-Chi, Taiwan	TCU101	1528	RV-OBL	7.62	2.1	504	Normal	0.21	68.35	73.33	0.71	49.00
Chi-Chi, Taiwan	TCU101	1528	RV-OBL	7.62	2.1	504	Parallel	0.24	51.78	39.28	0.77	49.00

Continued on next page

Table A.3: Baker: Pulse-like ground motion metadata (continued)

Earthquake (Year)	Station	NGA Number	Fault Type	M_w	Distance (km)	$V_{s,30}$ (m/s)	Component	PGA (g)	PGV (cm/s)	PGD (cm)	T_m (s)	Duration (s)
Chi-Chi, Taiwan	TCU101	1528	RV-OBL	7.62	2.1	504	Vertical	-	-	-	-	49.00
Chi-Chi, Taiwan	TCU102	1529	RV-OBL	7.62	1.5	714	Normal	0.30	109.03	88.45	1.36	90.00
Chi-Chi, Taiwan	TCU102	1529	RV-OBL	7.62	1.5	714	Parallel	0.16	77.55	51.13	1.70	90.00
Chi-Chi, Taiwan	TCU102	1529	RV-OBL	7.62	1.5	714	Vertical	-	-	-	-	90.00
Chi-Chi, Taiwan	TCU103	1530	RV-OBL	7.62	6.1	494	Normal	0.13	62.13	86.16	1.28	90.00
Chi-Chi, Taiwan	TCU103	1530	RV-OBL	7.62	6.1	494	Parallel	0.17	27.70	20.30	0.96	90.00
Chi-Chi, Taiwan	TCU103	1530	RV-OBL	7.62	6.1	494	Vertical	-	-	-	-	90.00
Chi-Chi, Taiwan	TCU122	1546	RV-OBL	7.62	9.4	475	Normal	0.22	42.43	44.05	0.70	90.00
Chi-Chi, Taiwan	TCU122	1546	RV-OBL	7.62	9.4	475	Parallel	0.26	34.40	33.97	0.68	90.00
Chi-Chi, Taiwan	TCU122	1546	RV-OBL	7.62	9.4	475	Vertical	-	-	-	-	90.00
Chi-Chi, Taiwan	WGK	1595	RV-OBL	7.62	10.0	244	Normal	0.30	67.62	33.74	1.03	59.00
Chi-Chi, Taiwan	WGK	1595	RV-OBL	7.62	10.0	244	Parallel	0.49	74.42	66.57	0.89	59.00
Chi-Chi, Taiwan	WGK	1595	RV-OBL	7.62	10.0	244	Vertical	-	-	-	-	53.00
Imperial Valley-06	EC County Center FF	170	SS	6.53	7.3	192	Normal	0.18	54.47	38.46	1.21	39.98
Imperial Valley-06	EC County Center FF	170	SS	6.53	7.3	192	Parallel	0.22	42.95	20.89	1.01	39.98
Imperial Valley-06	EC County Center FF	170	SS	6.53	7.3	192	Vertical	-	-	-	-	39.98
Imperial Valley-06	EC Meloland Overpass FF	171	SS	6.53	0.1	186	Normal	0.38	115.02	40.30	1.73	39.98
Imperial Valley-06	EC Meloland Overpass FF	171	SS	6.53	0.1	186	Parallel	0.27	27.31	14.56	0.83	39.98
Imperial Valley-06	EC Meloland Overpass FF	171	SS	6.53	0.1	186	Vertical	-	-	-	-	39.98
Imperial Valley-06	El Centro Array #4	179	SS	6.53	7.1	209	Normal	0.36	77.84	58.69	1.37	39.00
Imperial Valley-06	El Centro Array #4	179	SS	6.53	7.1	209	Parallel	0.47	40.12	20.58	0.66	39.00
Imperial Valley-06	El Centro Array #4	179	SS	6.53	7.1	209	Vertical	-	-	-	-	39.00
Imperial Valley-06	El Centro Array #5	180	SS	6.53	4.0	206	Normal	0.38	91.49	61.92	1.25	39.28
Imperial Valley-06	El Centro Array #5	180	SS	6.53	4.0	206	Parallel	0.53	48.99	37.23	0.66	39.28
Imperial Valley-06	El Centro Array #5	180	SS	6.53	4.0	206	Vertical	-	-	-	-	39.28
Imperial Valley-06	El Centro Array #6	181	SS	6.53	1.4	203	Normal	0.44	111.82	66.44	1.37	39.03
Imperial Valley-06	El Centro Array #6	181	SS	6.53	1.4	203	Parallel	0.40	64.67	24.74	0.90	39.03
Imperial Valley-06	El Centro Array #6	181	SS	6.53	1.4	203	Vertical	-	-	-	-	39.03
Imperial Valley-06	El Centro Array #7	182	SS	6.53	0.6	211	Normal	0.46	108.78	45.49	1.31	36.82
Imperial Valley-06	El Centro Array #7	182	SS	6.53	0.6	211	Parallel	0.33	44.53	24.05	0.95	36.82
Imperial Valley-06	El Centro Array #7	182	SS	6.53	0.6	211	Vertical	-	-	-	-	36.82
Imperial Valley-06	El Centro Array #8	183	SS	6.53	3.9	206	Normal	0.47	48.56	36.72	0.48	37.56
Imperial Valley-06	El Centro Array #8	183	SS	6.53	3.9	206	Parallel	0.59	51.95	30.76	0.61	37.56
Imperial Valley-06	El Centro Array #8	183	SS	6.53	3.9	206	Vertical	-	-	-	-	37.56
Imperial Valley-06	El Centro Differential Array	184	SS	6.53	5.1	202	Normal	0.42	59.60	38.68	0.49	38.96
Imperial Valley-06	El Centro Differential Array	184	SS	6.53	5.1	202	Parallel	0.44	51.39	27.77	0.57	38.96

Continued on next page

Table A.3: Baker: Pulse-like ground motion metadata (continued)

Earthquake (Year)	Station	NGA Number	Fault Type	M_w	Distance (km)	$V_{s,30}$ (m/s)	Component	PGA (g)	PGV (cm/s)	PGD (cm)	T_m (s)	Duration (s)
Imperial Valley-06	El Centro Differential Array	184	SS	6.53	5.1	202	Vertical	-	-	-	-	38.96
Kobe, Japan	KJMA	1106	SS	6.90	1.0	312	Normal	0.85	95.76	24.53	0.71	48.00
Kobe, Japan	KJMA	1106	SS	6.90	1.0	312	Parallel	0.55	53.39	10.26	0.51	48.00
Kobe, Japan	KJMA	1106	SS	6.90	1.0	312	Vertical	-	-	-	-	48.00
Kobe, Japan	Takarazuka	1119	SS	6.90	0.3	312	Normal	0.65	72.53	20.76	0.68	40.96
Kobe, Japan	Takarazuka	1119	SS	6.90	0.3	312	Parallel	0.70	82.96	26.55	0.72	40.96
Kobe, Japan	Takarazuka	1119	SS	6.90	0.3	312	Vertical	-	-	-	-	40.96
Kocaeli, Turkey	Gebze	1161	SS	7.51	10.9	792	Normal	0.24	51.18	43.51	0.65	28.00
Kocaeli, Turkey	Gebze	1161	SS	7.51	10.9	792	Parallel	0.14	28.67	26.48	0.55	28.00
Kocaeli, Turkey	Gebze	1161	SS	7.51	10.9	792	Vertical	-	-	-	-	28.00
Landers	Lucerne	879	SS	7.28	2.2	685	Normal	0.70	140.33	249.61	0.30	48.12
Landers	Lucerne	879	SS	7.28	2.2	685	Parallel	0.81	48.31	113.10	0.17	48.12
Landers	Lucerne	879	SS	7.28	2.2	685	Vertical	-	-	-	-	48.12
Landers	Yermo Fire Station	900	SS	7.28	23.6	354	Normal	0.24	56.41	48.38	0.85	44.00
Landers	Yermo Fire Station	900	SS	7.28	23.6	354	Parallel	0.18	17.24	9.35	0.69	44.00
Landers	Yermo Fire Station	900	SS	7.28	23.6	354	Vertical	-	-	-	-	44.00
Loma Prieta	Gilroy - Gavilan Coll.	763	RV-OBL	6.93	10.0	730	Normal	0.29	30.78	6.49	0.35	39.95
Loma Prieta	Gilroy - Gavilan Coll.	763	RV-OBL	6.93	10.0	730	Parallel	0.41	26.60	4.86	0.34	39.95
Loma Prieta	Gilroy - Gavilan Coll.	763	RV-OBL	6.93	10.0	730	Vertical	-	-	-	-	39.95
Loma Prieta	LGPC	779	RV-OBL	6.93	3.9	478	Normal	0.94	96.96	62.58	0.74	25.00
Loma Prieta	LGPC	779	RV-OBL	6.93	3.9	478	Parallel	0.54	72.12	30.55	0.71	25.00
Loma Prieta	LGPC	779	RV-OBL	6.93	3.9	478	Vertical	-	-	-	-	25.00
Morgan Hill	Coyote Lake Dam (SW Abut)	451	SS	6.19	0.5	597	Normal	0.81	62.29	10.15	0.49	29.95
Morgan Hill	Coyote Lake Dam (SW Abut)	451	SS	6.19	0.5	597	Parallel	1.08	70.16	14.07	0.50	29.95
Morgan Hill	Coyote Lake Dam (SW Abut)	451	SS	6.19	0.5	597	Vertical	-	-	-	-	29.95
Northridge-01	Jensen Filter Plant	982	RV	6.69	5.4	373	Normal	0.52	67.39	41.97	0.91	28.61
Northridge-01	Jensen Filter Plant	982	RV	6.69	5.4	373	Parallel	1.07	64.42	21.16	0.55	28.61
Northridge-01	Jensen Filter Plant	982	RV	6.69	5.4	373	Vertical	-	-	-	-	28.61
Northridge-01	Jensen Filter Plant Generator	983	RV	6.69	5.4	526	Normal	0.52	67.35	42.64	0.92	28.61
Northridge-01	Jensen Filter Plant Generator	983	RV	6.69	5.4	526	Parallel	1.07	65.25	23.34	0.55	28.61
Northridge-01	Jensen Filter Plant Generator	983	RV	6.69	5.4	526	Vertical	-	-	-	-	28.61
Northridge-01	Newhall - Fire Sta	1044	RV	6.69	5.9	269	Normal	0.72	120.09	35.07	0.71	40.00
Northridge-01	Newhall - Fire Sta	1044	RV	6.69	5.9	269	Parallel	0.65	49.88	16.28	0.46	40.00
Northridge-01	Newhall - Fire Sta	1044	RV	6.69	5.9	269	Vertical	-	-	-	-	40.00
Northridge-01	Newhall - W Pico Canyon Rd.	1045	RV	6.69	5.5	286	Normal	0.43	87.73	55.12	1.59	24.99
Northridge-01	Newhall - W Pico Canyon Rd.	1045	RV	6.69	5.5	286	Parallel	0.28	74.72	21.77	1.27	24.99

Continued on next page

Table A.3: Baker: Pulse-like ground motion metadata (continued)

Earthquake (Year)	Station	NGA Number	Fault Type	M_w	Distance (km)	$V_{s,30}$ (m/s)	Component	PGA (g)	PGV (cm/s)	PGD (cm)	T_m (s)	Duration (s)
Northridge-01	Newhall - W Pico Canyon Rd.	1045	RV	6.69	5.5	286	Vertical	-	-	-	-	24.99
Northridge-01	Rinaldi Receiving Sta	1063	RV	6.69	6.5	282	Normal	0.87	167.10	28.96	0.80	19.91
Northridge-01	Rinaldi Receiving Sta	1063	RV	6.69	6.5	282	Parallel	0.42	62.54	21.54	0.52	19.91
Northridge-01	Rinaldi Receiving Sta	1063	RV	6.69	6.5	282	Vertical	-	-	-	-	19.91
Northridge-01	Sylmar - Converter Sta	1084	RV	6.69	5.4	251	Normal	0.59	130.29	53.94	1.15	40.00
Northridge-01	Sylmar - Converter Sta	1084	RV	6.69	5.4	251	Parallel	0.80	93.29	53.30	0.98	40.00
Northridge-01	Sylmar - Converter Sta	1084	RV	6.69	5.4	251	Vertical	-	-	-	-	40.00
Northridge-01	Sylmar - Converter Sta East	1085	RV	6.69	5.2	371	Normal	0.83	113.57	41.01	0.73	40.00
Northridge-01	Sylmar - Converter Sta East	1085	RV	6.69	5.2	371	Parallel	0.53	80.15	28.70	0.77	40.00
Northridge-01	Sylmar - Converter Sta East	1085	RV	6.69	5.2	371	Vertical	-	-	-	-	40.00
Northridge-01	Sylmar - Olive View Med FF	1086	RV	6.69	5.3	441	Normal	0.73	122.85	32.13	0.96	40.00
Northridge-01	Sylmar - Olive View Med FF	1086	RV	6.69	5.3	441	Parallel	0.60	54.40	10.66	0.59	40.00
Northridge-01	Sylmar - Olive View Med FF	1086	RV	6.69	5.3	441	Vertical	-	-	-	-	40.00

Table A.4: Spectrally Matched ground motion metadata

Earthquake (Year)	Station	NGA Number	Fault Type	M_w	Distance (km)	$V_{s,30}$ (m/s)	Component	PGA (g)	PGV (cm/s)	PGD (cm)	T_m (s)	Duration (s)
Chi-Chi, Taiwan	CHY010	1184	RV-OBL	7.62	20.0	550	Component1	0.16	15.21	12.10	0.46	132.00
Chi-Chi, Taiwan	HWA006	1259	RV-OBL	7.62	48.0	491	Component1	0.19	18.86	135.18	0.36	45.20
Chi-Chi, Taiwan	HWA020	1270	RV-OBL	7.62	45.0	502	Component1	0.18	20.59	20.02	0.37	89.00
Chi-Chi, Taiwan	HWA035	1284	RV-OBL	7.62	48.0	501	Component1	0.17	18.24	38.38	0.42	90.00
Chi-Chi, Taiwan	HWA056	1301	RV-OBL	7.62	41.0	511	Component1	0.16	17.49	17.96	0.42	86.03
Chi-Chi, Taiwan	HWA058	1303	RV-OBL	7.62	46.0	564	Component1	0.17	14.15	20.76	0.40	90.00
Chi-Chi, Taiwan	ILA050	1338	RV-OBL	7.62	67.0	497	Component1	0.18	15.07	17.90	0.40	56.00
Chi-Chi, Taiwan	ILA067	1350	RV-OBL	7.62	39.0	680	Component1	0.15	13.81	14.35	0.44	90.00
Chi-Chi, Taiwan	TCU071	1507	RV-OBL	7.62	5.3	625	Component1	0.18	16.39	13.32	0.37	90.00
Chi-Chi, Taiwan	TCU089	1521	RV-OBL	7.62	8.9	680	Component1	0.17	13.93	11.64	0.42	79.00
Chi-Chi, Taiwan-03	TCU089	2635	RV	6.20	9.8	680	Component1	0.19	11.78	7.58	0.41	96.00
Chi-Chi, Taiwan-06	CHY046	3281	RV	6.30	54.0	442	Component1	0.16	16.16	6.98	0.50	71.00
Duzce, Turkey	Lamont 531	1618	SS	7.14	8.0	660	Component1	0.19	19.90	99.95	0.43	49.70
Hector Mine	Heart Bar State Park	1786	SS	7.13	61.0	685	Component1	0.19	15.20	69.15	0.40	60.00
Hector Mine	Joshua Tree N.M. - Keys View	1795	SS	7.13	50.0	685	Component1	0.19	14.51	174.04	0.40	79.60
Hector Mine	Twentynine Palms	1836	SS	7.13	42.0	685	Component1	0.19	29.59	1049.23	0.34	72.70
Irpinia, Italy-01	Auletta	284	N	6.90	9.6	1000	Component1	0.16	13.87	8.63	0.42	43.14
Kocaeli, Turkey	Izmit	1165	SS	7.51	7.2	811	Component1	0.18	15.31	8.91	0.38	43.23
Loma Prieta	APEEL 3E Hayward CSUH	734	RV-OBL	6.93	53.0	517	Component1	0.16	11.83	9.45	0.45	44.15
Loma Prieta	Anderson Dam (Downstream)	739	RV-OBL	6.93	20.3	489	Component1	0.19	13.68	12.18	0.40	61.05
Loma Prieta	Gilroy Array #6	769	RV-OBL	6.93	18.3	663	Component1	0.17	17.00	9.33	0.47	43.55
Loma Prieta	Monterey City Hall	782	RV-OBL	6.93	44.0	685	Component1	0.18	16.22	7.48	0.38	47.20
Loma Prieta	Sunol - Forest Fire Station	807	RV-OBL	6.93	48.0	401	Component1	0.18	14.02	8.04	0.41	43.95
Northridge-01	Glendora - N Oakbank	975	RV	6.69	54.0	446	Component1	0.20	14.59	24.01	0.42	30.00
Northridge-01	LA - W 15th St	1008	RV	6.69	29.7	405	Component1	0.19	12.72	55.98	0.43	40.00
Northridge-01	Lake Hughes #4 - Camp Mend	1021	RV	6.69	32.0	822	Component1	0.19	36.42	569.32	0.36	42.20
Northridge-01	N Hollywood - Coldwater Can	1042	RV	6.69	12.5	446	Component1	0.19	29.32	335.30	0.45	41.10
Oroville-03	Duffy Residence (OR5)	114	N	4.70	10.5	438	Component1	0.16	17.26	8.31	0.34	37.12
Oroville-03	Summit Ave (OR6)	119	N	4.70	7.6	478	Component1	0.17	18.56	9.55	0.37	30.62
Tabas, Iran	Dayhook	139	RV	7.35	13.9	660	Component1	0.19	20.50	143.30	0.38	41.20